

MOLECULAR NEUROIMAGING IN ALZHEIMER'S DISEASE: TARGETING
BUTYRYLCHOLINESTERASE (BCHE) FOR POSITRON EMISSION
TOMOGRAPHY (PET) AND SINGLE PHOTON EMISSION COMPUTED
TOMOGRAPHY (SPECT) IMAGING OF THE BRAIN

by

Drew Roderick DeBay

Submitted in partial fulfilment of the requirements
for the degree of Doctor of Philosophy

at

Dalhousie University
Halifax, Nova Scotia
August 2019

© Copyright by Drew Roderick DeBay, 2019

To Danielle, Eleanore and Arlo.

Table of Contents

List of Tables	x
List of Figures	xi
Abstract	xv
List of Abbreviations and Symbols Used	xvi
Acknowledgements	xxvii
Chapter 1 Introduction	1
1.1 Publication Status	1
1.2 Overview	1
1.3 Alzheimer's Disease (AD)	2
1.4 Current Biomarkers in AD	3
1.4.1 β -Amyloid ($A\beta$) as an AD Biomarker	3
1.4.2 Tau as an AD Biomarker.....	6
1.4.3 Neurodegeneration (N) as an AD Biomarker	8
1.5 The Cholinergic System and the AD Cholinergic Hypothesis	8
1.5.1 Cholinesterases: BChE and AChE	9
1.5.2 Cholinesterase Distribution in Normal and AD brain.....	12
1.5.3 Butyrylcholinesterase (BChE) as an AD Biomarker.....	12
1.5.4 BChE as an Imaging Biomarker.....	17
1.5.5 The Functional Role of BChE in AD.....	19
1.6 Neuroimaging Techniques	22
1.6.1 Nuclear Medicine Imaging	22
1.6.1.1 Radioactive Decay	22
1.6.1.2 Principles of Positron Emission Tomography (PET).....	25
1.6.1.3 PET Scanners.....	26
1.6.1.4 Principles of Single Photon Emission Computed Tomography (SPECT).....	28
1.6.1.5 SPECT Scanners.....	29
1.6.1.6 Radionuclide Production.....	30

1.6.2 Computed Tomography (CT).....	32
1.6.3 Principles of Magnetic Resonance Imaging (MRI).....	33
1.6.4 Strengths and Weaknesses of Neuroimaging Modalities	36
1.7 Analysis Techniques in Nuclear Medicine.....	38
1.7.1 Quantitation of Static Images in PET and SPECT	38
1.7.2 Dynamic Imaging Evaluation in PET and SPECT.....	40
1.7.3 PET Kinetic Modelling.....	41
1.7.3.1 Arterial Input Function (AIF).....	42
1.7.3.2 Generalized Three Tissue Compartment Model (3TCM).....	43
1.7.3.3 One Tissue Compartmental Model (1TCM).....	45
1.7.3.4 Simplified Reference Tissue Model (SRTM).....	48
1.7.3.5 Logan Graphical Analysis	50
1.8 Central Nervous System (CNS) Radiotracer Development	53
1.8.1 Radioligand Design Criteria	53
1.8.2 Physicochemical Profile	55
1.8.3 Radioligand Classification.....	57
1.8.3.1 Receptor Radioligands	57
1.8.3.2 Hydrolytic Enzyme Radioligands: Substrate, Reversible and Irreversible Inhibitors.....	59
1.9 Thesis Objective & Hypothesis	66
1.10 Chapter Overviews.....	67
Chapter 2 Preliminary <i>In Vivo</i> Neuroimaging Evaluation of Lead Candidate Radioligand <i>N</i>-Methylpiperidin-4-yl 4- [¹²³I]iodobenzoate: A Butyrylcholinesterase (BChE)-Specific Radiotracer for Alzheimer's Disease (AD)	69
2.1 Publication Status	69
2.2 Overview	69
2.3 Abstract	70
2.4 Introduction	70
2.5 Materials and Methods.....	73
2.5.1 Synthesis/Biochemical Materials	73

2.5.2 Enzyme Specificity	73
2.5.3 Synthesis and Labelling of Radiotracer	74
2.5.4 Animals	75
2.5.5 SPECT-CT Imaging	75
2.5.6 MR Imaging.....	76
2.5.7 Image Processing	76
2.5.8 SPECT/CT/MRI Coregistration and Dynamic SPECT Regional Analysis	77
2.5.9 BChE Histochemistry	78
2.5.10 Statistical Analysis	79
2.6 Results	79
2.6.1 Synthesis of <i>N</i> -Methylpiperidin-4-yl 4-[¹²³ I]iodobenzoate	79
2.6.2 Cholinesterase Specificity for 1-Methylpiperidin-4-yl 4-Iodobenzoate .	79
2.6.3 Sequential SPECT Imaging	81
2.6.4 Whole Brain Retention of Radioligand	81
2.6.5 Comparative Histochemical- and SPECT-Visualized Regional Butyrylcholinesterase Activity	83
2.6.6 Cortical and Subcortical Retention Comparisons	85
2.7 Discussion.....	90
2.8 Conclusions.....	92
2.9 Acknowledgements	92
Chapter 3 <i>In Vivo</i> Screening of BChE Radioligands using 2D Dynamic Planar Scintigraphy	94
3.1 Publication Status	94
3.2 Overview	94
3.3 Abstract	95
3.4 Introduction	98
3.5 Materials and Methods.....	99
3.5.1 Physicochemical Evaluation of [¹²³ I] Radioligands.....	100
3.5.2 <i>In Vitro</i> Enzyme Kinetics	100
3.5.3 Radiosynthesis.....	100

3.5.3.1 (<i>p</i> -[¹²³ I]iodophenyl)methyl 6-oxo-1H-pyridine-2-carboxylate (TRV7005).....	100
3.5.3.2 (<i>p</i> -[¹²³ I]iodophenyl)methyl 1-methyl-6-oxo-1H-pyridine-2-carboxylate (TRV7006)	101
3.5.3.3 (<i>p</i> -[¹²³ I]iodophenyl)methyl 6-methoxy-2-pyridinecarboxylate (TRV7019).....	102
3.5.3.4 benzyl 6-[(<i>p</i> -[¹²³ I]iodophenyl)methoxy]-2-pyridinecarboxylate (TRV7040).....	103
3.5.3.5 <i>p</i> -[¹²³ I]iodophenylamino benzoate (TRV5001)	103
3.5.3.6 <i>N</i> -Methylpiperidin-4-yl 4-[¹²³ I]iodobenzoate (TRV6001)	104
3.5.4 Animals	104
3.5.5 2D dynamic Planar Scintigraphy.....	106
3.5.5.1 Dynamic Scintigraphy Acquisition.....	106
3.5.5.2 3D SPECT/CT Imaging of TRV7040	107
3.5.5.3 2D Dynamic Planar Scintigraphy Imaging and Statistical Analyses	108
3.6 Results	110
3.6.1 Physicochemical Profile of [¹²³ I] Radioligands	110
3.6.2 <i>In Vitro</i> Enzyme Kinetic Profile of [¹²³ I] Radioligands.....	111
3.6.3 Radiosynthesis.....	111
3.6.4 2D Dynamic Planar Scintigraphy	114
3.6.4.1 TRV7005.....	116
3.6.4.2 TRV7006.....	120
3.6.4.3 TRV7019.....	124
3.6.4.4 TRV7040.....	128
3.6.4.5 TRV5001.....	132
3.6.4.6 TRV6001.....	136
3.7 Comparison of Kinetics Between Radioligands	143
3.8 Discussion.....	146
3.9 Acknowledgements	150

Chapter 4 Synthesis and <i>In Vivo</i> Evaluation of 1-methyl-4-piperidinyl- <i>p</i>-¹⁸F]fluorobenzoate: A Butyrylcholinesterase Radioligand for PET Imaging of the Brain in Alzheimer’s Disease	151
4.1 Publication Status	151
4.2 Overview	151
4.3 Abstract	152
4.4 Introduction	155
4.5 Materials and Methods	158
4.5.1 Synthesis, Enzyme Kinetics and Labelling of Radiotracer	158
4.5.2 Synthesis of <i>N</i> -methylpiperidin-4-yl <i>p</i> -fluorobenzoate	159
4.5.3 Synthesis of <i>N</i> -methylpiperidin-4-yl <i>p</i> -nitrobenzoate	160
4.5.4 <i>In Vitro</i> Evaluation of <i>N</i> -methylpiperidin-4-yl <i>p</i> -fluorobenzoate as a Cholinesterase Substrate	160
4.5.5 Synthesis of <i>N</i> -methylpiperidin-4-yl <i>p</i> - ¹⁸ F]fluorobenzoate	161
4.5.6 Animals	162
4.5.7 PET/CT Imaging	163
4.5.8 PET Image Processing and Analysis	164
4.5.9 Kinetic Modeling and Statistical Analysis	165
4.6 Results	168
4.6.1 Physicochemical and <i>In Vitro</i> Kinetic Profile of <i>N</i> -Methylpiperidin-4-yl <i>p</i> -fluorobenzoate	168
4.6.2 Radiochemical Synthesis of <i>N</i> -Methylpiperidin-4-yl <i>p</i> - ¹⁸ F]Fluorobenzoate	170
4.6.3 Image-derived Arterial Input Function (IDAIF)	170
4.6.4 Dynamic PET Imaging	172
4.6.5 PET Kinetic Modeling	179
4.6.5.1 1TCM Evaluation of TRV6501	179
4.6.5.2 SRTM Evaluation of TRV6501	184
4.6.5.3 Logan Graphical Analysis of TRV6501	187
4.6.5.4 Suitability of Models to Describe TRV6501 <i>In Vivo</i> Kinetics: Goodness of Fit Metrics	191
4.7 Discussion	193

4.8 Acknowledgements	199
Chapter 5 Cerebral Perfusion in the 5XFAD Mouse Model of Alzheimer's Disease	201
5.1 Publication Status	201
5.2 Overview	201
5.3 Abstract	201
5.4 Introduction	203
5.4.1 Brain Perfusion Agents	204
5.4.2 Imaging Brain Perfusion in AD	207
5.5 Methods	209
5.5.1 Animals	209
5.5.2 ^{99m} Tc-Exametazime Synthesis	210
5.5.3 SPECT-CT Imaging	210
5.5.4 MR Imaging.....	211
5.5.5 Image Processing	211
5.5.6 SPECT/CT/MRI Coregistration and SPECT Regional Analysis.....	212
5.5.7 Statistical Analysis	213
5.6 Results	213
5.6.1 ^{99m} Tc-Exametazime Perfusion SPECT	213
5.6.1.1 Whole Brain Perfusion	214
5.6.1.2 Regional Perfusion	214
5.7 Discussion.....	218
5.8 Acknowledgements	219
Chapter 6 Butyrylcholinesterase-Knockout Reduces Fibrillar β-amyloid and Conserves Cerebral Glucose Metabolism in 5XFAD Mouse Model of Alzheimer's Disease	221
6.1 Publication Status	221
6.2 Overview	221
6.3 Abstract	221
6.4 Introduction	222

6.5 Experimental Methods	226
6.5.1 Animals	226
6.5.2 Genotyping.....	227
6.5.3 PET/CT Imaging	228
6.5.4 MR Imaging.....	229
6.5.5 Image Processing	230
6.5.6 Whole Brain and Regional ¹⁸ FDG Uptake Analysis	231
6.5.7 Thioflavin-S Histofluorescence	232
6.5.8 Microscopy Analysis	233
6.5.9 Statistical Analysis	234
6.6 Results	234
6.6.1 Brain Fibrillar A β Deposition	235
6.6.2 Whole Brain ¹⁸ FDG SUV Comparisons	237
6.6.3 [¹⁸ F]FDG Regional SUV Comparisons.....	240
6.7 Discussion.....	243
6.8 Acknowledgements	247
Chapter 7 Conclusions	248
7.1 Overview	248
7.2 General Conclusions.....	248
7.3 Current Perspectives and Future of BChE Imaging of the Brain in AD: Towards Clinical Translation.....	251
7.4 Significance.....	257
References	259
Appendix A Copyright Permission Letters	278

List of Tables

Table 1.1 Diagnostic performance summary of current AD biomarkers	5
Table 1.2 Common radionuclides in nuclear medicine	24
Table 1.3 Medical imaging techniques and associated performance characteristics	37
Table 1.4 Multiparameter optimization (MPO) properties of CNS drugs	56
Table 1.5 Summary of <i>in vitro</i> radioligand kinetic parameters	65
Table 3.1 2D dynamic planar scintigraphy subject demographics	105
Table 3.2 Physicochemical profile of lead BChE radioligands	112
Table 3.3 <i>In vitro</i> enzyme kinetic parameters and radiosynthesis results of BChE radioligands	113
Table 3.4 Goodness of fit metrics for each [¹²³ I] radioligand	115
Table 3.5 Kinetic summary measures of radioligand clearance for each [¹²³ I] radioligand	142
Table 3.6 Pooled <i>in vivo</i> kinetic summary measures for BChE radioligands	145
Table 4.1 Physicochemical and <i>in vitro</i> kinetic profile of TRV6501	169
Table 4.2 TRV6501 Single Tissue Compartment Model (1TCM) kinetic parameter estimates	183
Table 4.3 TRV6501 Simplified Reference Tissue Model (SRTM) kinetic parameter estimates	186
Table 4.4 TRV6501 goodness of fit metrics for 1TCM, SRTM and Logan graphical analysis	192

List of Figures

Figure 1.1 Crystal structure of human BChE	11
Figure 1.2 A β and BChE in cognitively normal, with A β and AD brains	14
Figure 1.3 Receiver-Operating Characteristic Plot summarizing diagnostic performance of A β and BChE in the brain	15
Figure 1.4 Photomicrographs of BChE in non-AD dementias	16
Figure 1.5 Fibrillar A β plaque load in 5XFAD/BChE-KO mice	21
Figure 1.6 Generalized three-tissue compartment model (3TCM)	44
Figure 1.7 One tissue compartment model (1TCM)	46
Figure 1.8 Simplified reference tissue model (SRTM)	49
Figure 1.9 Logan graphical analysis technique	52
Figure 1.10 PET and SPECT radioligand design criteria.	54
Figure 2.1 UV absorbance curves showing TRV6001 specificity for BChE	80
Figure 2.2 Representative TRV6001 SPECT/CT brain images for 5XFAD and WT mice	82
Figure 2.3 Representative BChE histochemical staining in 5XFAD and WT mouse brain	84
Figure 2.4 TRV6001 SPECT/CT/MRI brain images in 5XFAD and WT mice	86
Figure 2.5 Regional TRV6001 time-activity curves in 5XFAD and WT mice	87
Figure 2.6 TRV6001 cortical retention index for 5XFAD and WT mice	89
Figure 3.1 Exponential fits of radioligand clearance	109
Figure 3.2 TRV7005 dynamic planar scintigraphy scans for a representative 5XFAD mouse	117

Figure 3.3 TRV7005 dynamic planar scintigraphy scans for a representative WT mouse	118
Figure 3.4 Whole brain time-activity curves for TRV7005	119
Figure 3.5 TRV7006 dynamic planar scintigraphy scans for a representative WT mouse	121
Figure 3.6 TRV7006 dynamic planar scintigraphy scans for a representative BChE-KO mouse	122
Figure 3.7 Whole brain time-activity curves for TRV7006	123
Figure 3.8 TRV7019 dynamic planar scintigraphy scans for a representative 5XFAD mouse	125
Figure 3.9 TRV7019 dynamic planar scintigraphy scans for a representative WT mouse	126
Figure 3.10 Whole brain time-activity curves for TRV7019	127
Figure 3.11 TRV7040 dynamic planar scintigraphy scans for a representative 5XFAD mouse	129
Figure 3.12 TRV7040 dynamic planar scintigraphy scans for a representative WT mouse	130
Figure 3.13 TRV7040 3D SPECT scan of a 5XFAD mouse	131
Figure 3.14 TRV5001 dynamic planar scintigraphy scans for a representative 5XFAD mouse	133
Figure 3.15 TRV5001 dynamic planar scintigraphy scans for a representative WT mouse	134
Figure 3.16 Whole brain time-activity curves for TRV5001	135
Figure 3.17 TRV6001 dynamic planar scintigraphy scans for a representative WT mouse	137
Figure 3.18 TRV6001 dynamic planar scintigraphy scans for a representative 5X-BChE-KO mouse	138
Figure 3.19 Whole brain time-activity curves for TRV6001	139

Figure 3.20 Whole brain time-activity curves for TRV7005, TRV7006, TRV7019, TRV5001 and TRV6001 radiotracers	140
Figure 3.21 Kinetic summary measures of tracer clearance for TRV7005, TRV7006, TRV7019, TRV5001 and TRV6001	141
Figure 3.22 Time-activity curves and kinetic summary measure comparison between radioligands	144
Figure 4.1 Image-derived arterial input function for TRV6501	171
Figure 4.2 TRV6501 dynamic PET images for a 5XFAD mouse	173
Figure 4.3 TRV6501 dynamic PET imaging for a WT/BChE-KO mouse	174
Figure 4.4 TRV6501 whole brain time-activity curves for a 5XFAD mouse	175
Figure 4.5 TRV6501 whole brain time-activity curves for a WT/BChE-KO mouse	176
Figure 4.6 TRV6501 time-activity curves (%ID/mL) for 5XFAD and WT/BChE mice	177
Figure 4.7 TRV6501 time-activity curves (%C _{max}) for 5XFAD and WT/BChE mice	178
Figure 4.8 TRV6501 time-activity curves with corresponding 1TCM and SRTM curves for 5XFAD mice	180
Figure 4.9 TRV6501 time-activity curves with corresponding 1TCM and SRTM curves for WT/BChE-KO mice	181
Figure 4.10 TRV6501 1TCM kinetic parameter estimates	182
Figure 4.11 TRV6501 SRTM kinetic parameter estimates	185
Figure 4.12 TRV6501 whole brain Logan plots	188
Figure 4.13 TRV6501 Logan plot linear regressions	189
Figure 4.14 Logan plot estimates of V _T for TRV6501	190
Figure 5.1 Chemical structure of ^{99m} Tc-Exametazime (^{99m} Tc-HMPAO)	205
Figure 5.2 ^{99m} Tc-Exametazime SPECT/CT images for 5XFAD and WT	215

Figure 5.3 Whole brain perfusion SUVs for 5XFAD and WT	216
Figure 5.4 Regional brain perfusion SUV and SUVrs for 5XFAD and WT	217
Figure 6.1 Fibrillar A β burden in 5XFAD and 5XFAD/BChE-KO	236
Figure 6.2 [^{18}F]FDG PET images in 5XFAD and 5XFAD/BChE-KO	238
Figure 6.3 Whole brain [^{18}F]FDG SUV comparisons between mouse strains	239
Figure 6.4 Regional [^{18}F]FDG SUV comparisons between mouse strains	242

Abstract

Currently, there are no effective means to definitively diagnose Alzheimer's disease (AD) during life. Molecular imaging of β -amyloid ($A\beta$) or tau neurofibrillary tangle (NFT) pathology in the AD brain, though informative, has limited diagnostic value because similar changes are found in brains of ~30% of cognitively normal individuals and in other neurodegenerative disorders.

We have recently shown that the enzyme butyrylcholinesterase (BChE), typically present in high levels in the AD cerebral cortex (yet largely absent in normal brain), is a highly sensitive and specific biomarker for the disease and could therefore provide enhanced accuracy as an AD diagnostic. Consequently, we have developed BChE radioligands for positron emission tomography (PET) and single photon emission computed tomography (SPECT) imaging of the brain in AD. Rigorous *in vivo* evaluation of such radiotracers in AD animal models is essential in order to establish a radioligand's product profile, ultimately advancing the most promising candidates towards clinical trials in humans.

The current work develops and implements a multimodal neuroimaging analysis framework using PET, SPECT magnetic resonance imaging (MRI) and computed tomography (CT) to evaluate putative BChE radioligands. One such BChE radioligand for SPECT imaging, *N*-Methylpiperidin-4-yl 4- ^{123}I iodobenzoate (TRV6001), was found to cross the blood brain barrier and recapitulate the known histochemical distribution of BChE in an experimental model, effectively distinguishing an AD mouse brain from that of a wild-type control. An essential neuroimaging analysis framework has been developed and implemented, providing an *in vivo* radioligand development toolkit for the rapid screening of lead BChE radiotracer candidates.

Brain imaging of BChE in humans may enhance the accuracy and timely detection of AD not yet possible with current brain imaging methods and could provide a unique opportunity to facilitate evaluation of emerging next generation therapies for AD.

List of Abbreviations and Symbols Used

Symbol/Abbreviation	Definition
%ID	percent injected dose
[E _{total}]	total concentration of enzyme
[S]	substrate concentration (tracer)
°	degree
°C	degree Celsius
μA	microampere
μCi	microcurie
μL	microlitre
μm	micrometer
μmol	micromole
¹⁸ F	¹⁸ fluorine
1TCM	single tissue compartment model
2D	two dimensional
2TCM	two tissue compartmental model
3D	three dimensional
3R	3 microtubule binding domain repeats
3TCM	three tissue compartment model
4R	4 microtubule binding domain repeats
5XFAD	B6SJL-Tg(APP ^{Sw} FIL ^{on} , PSEN1* ^{M146 L*L286 V}) 6799Vas/Mmjax mouse model
A	amygdala
ACh	acetylcholine
AChE	acetylcholinesterase

AD	Alzheimer's disease
ADNI	Alzheimer's Disease Neuroimaging Initiative
AIF	arterial input function
Amg	amygdala
ANOVA	analysis of variance
A_o	initial activity
APP	amyloid precursor protein
ASL	arterial spin labelling
A_t	activity at time t
AUC	area under curve
$A\beta$	β -amyloid plaque
B	bound receptor-ligand complex
B_1	RF electromagnetic field
BBB	blood-brain barrier
BChE	butyrylcholinesterase enzyme
<i>BCHE</i>	butyrylcholinesterase gene
BChE-het	heterozygous butyrylcholinesterase
BChE-KO	butyrylcholinesterase knockout
BG	basal ganglia
B_{max}	receptor density (target protein concentration)
B_0	external magnetic field strength
BOLD	blood oxygen level dependent
BP	binding potential
BP_{ND}	non-displaceable binding potential
BS	brainstem

b-SSFP	balanced steady-state free precession
BW	bandwidth
BW	body weight
C	clinical
C	concentration
C	caudal
$C(t)$	radioligand concentration in the brain over time
C/P	caudate/putamen
C_A	asymptotic tracer concentration
$C_a(t)$	concentration of radiotracer in arterial blood compartment as a function of time
$c_a(\tau)$	input curve
$C_s(t)$	concentration of specifically bound radiotracer as a function of time
CBD	corticobasal degeneration
CC	cerebral cortex
CC/EC	corpus callosum/external capsule
CCA	common carotid artery
Cerebel	cerebellum
Cerebel-gm	cerebellar gray matter
$C_f(t)$	concentration of freely circulating radiotracer in the reference region as a function of time
$C_f(t)$	concentration of freely circulating radiotracer over time
ChAT	choline acetyltransferase
CHT1	high affinity choline transporter
ClogD	dissociation coefficient

ClogP	partition coefficient
C_{\max}	peak concentration
$C_{ns}(t)$	concentration of non-specifically bound radiotracer as a function of time
CNS	central nervous system
$C_p(t)$	concentration of plasma bound radiotracer as a function of time
$C_{PET}(t)$	concentration of radioactivity observed by PET as a function of time
CPP	cerebral perfusion pressure
CSF	cerebrospinal fluid
CT	computed tomography
$C_T(t)$	instantaneous tissue concentration as a function of time
CTA	computed tomography angiography
cts	counts
d	deuterium
D	dorsal
DAT	dopamine transporter
DLB	dementia with Lewy bodies
DNA	deoxyribonucleic acid
E	free enzyme
e^-	electron
EC	electron capture
ECD	ethyl cysteinate dimer
EE	enzymatic efficiency
EI	enzyme-inhibitor complex

EI*	inactivated form of enzyme
ER	emergency room
ES	enzyme-substrate complex
F	free ligand
F	female
FAD	familial Alzheimer's disease
FDA	Food and Drug Administration
FDG	fluorodeoxyglucose
FID	free induction decay
fMRI	functional magnetic resonance imaging
FOV	field of view
FTD-tau	frontotemporal dementia with tau
g	gram
GBq	giga-becquerel
GM	grey matter
GP	globus pallidus
H	hippocampal formation
h	hour
HBD	hydrogen bond donors
HC	hippocampus
HPLC	high-performance liquid chromatography
hypo	hypothalamus
I	inhibitor
IC ₅₀	inhibitor concentration at 50 percent enzyme activity
ID	injected dose

IDAIF	image-derived arterial input function
IT	isomeric transition (gamma ray)
IUPAC	International Unit of Pure and Applied Chemistry
k	rate constant
K_1	perfusion rate constant (one tissue compartment model)
K_1	perfusion rate constant (three tissue compartment model)
K_1'	radiotracer perfusion rate constant in the reference region
k_2	rate constant of radioligand transfer from tissue compartment to arterial plasma (one tissue compartment model)
k_2	rate constant of radioligand transfer from free tracer to arterial plasma compartments (two tissue compartment model)
k_2	rate constant of radioligand transfer from free tracer to arterial plasma compartments (three tissue compartment model)
k_2'	rate constant of radioligand transfer from free tracer to arterial plasma compartments for the reference region
k_{2a}	apparent overall rate constant of radioligand transfer from tissue to arterial plasma (simplified tissue compartment model)
k_3	rate constant of radioligand transfer from free tracer to target-specific binding compartments (three tissue compartment model)
k_3	rate constant of radioligand transfer from free tracer to target-specific binding compartments (two tissue compartment model)
k_4	rate constant of radioligand transfer from target-specific binding and free tracer compartments (three tissue compartment model)

k_4	rate constant of radioligand transfer from target-specific binding and free tracer compartments (two tissue compartment model)
k_5	rate constant of radioligand transfer from free tracer and non-specific binding compartments (three tissue compartment model)
k_6	rate constant of radioligand transfer from non-specific binding to free tracer compartments coefficient 6 (three tissue compartment model)
kBq	kilobecquerel
k_{cat}	rate of first committed chemical step
$k_{clearance}$	rate of tracer clearance from the brain
K_D	radioligand equilibrium dissociation constant
keV	kiloelectron volts
k_f	forward reaction rate
Kg	kilogram
k_i	reaction rate constant generating inactivated form of enzyme
$K_i irreversible$	inhibitor concentration required to reach one half of the maximum enzymatic reaction rate
$K_i reversible$	inhibition equilibrium constant
K_m	Michaelis constant
k_{off}	dissociation rate constant
k_{on}	association rate constant
k_r	reverse reaction rate
kVp	kilovoltage peak
LOR	line of response
LSD	least significant difference

M	molar
m	slope
M	male
mAChR	muscarinic Ach receptor
MAO	monoamine oxidase
MBq	megabecquerel
MCI	mild cognitive impairment
mCi	millicurie
MeV	megaelectron volt
MIP	maximum intensity projection
mL	millilitre
MLEM	Maximum-Likelihood Expectation Maximization
mm	millimeter
mM	millimolar
MPO	multiparameter optimization
MP-RAGE	magnetization prepared gradient echo
MR	magnetic resonance
MRI	magnetic resonance imaging
MRS	magnetic resonance spectroscopy
mT	millitesla
MW	molecular weight
N	neurodegeneration
n	neutron
n	number of subjects
nAChR	nicotinic ACh receptor

NC	neocortex
ND	not determined
NFT	neurofibrillary tangle
nm	nanometer
nM	nanomolar
NMR	nuclear magnetic resonance
ns	nanosecond
p	level of significance
p	bombarding proton
p	proton
P	product
PB	phosphate buffer
PC	pre-clinical
PCR	polymerase chain reaction
PET	positron emission tomography
PI	post-injection
pK _a	acid dissociation constant
PRiMA	proline-rich membrane anchor
PS1	presenilin 1
PSP	progressive supranuclear palsy
P-tau	phosphorylated tau
R	receptor
R	rostral
<i>R_l</i>	relative tracer delivery constant
rCBF	regional cerebral blood flow

RF	radiofrequency
ROC	receiver operating characteristic
ROI	regions of interest
rpm	rotations per minute
S	free substrate
SEM	standard error of the mean
SLM	super list mode
SNR	signal-to-noise ratio
SPECT	single photon emission computed tomography
SRTM	simplified reference tissue model
SUV	standardized uptake value
SUVr	relative standardized uptake value
T	tesla
t	time
T ₁	spin-lattice relaxation
t _{1/2}	physical half life
T ₂	spin-spin relaxation
TAC	time-activity curve
TE	echo time
Th	thalamus
Thal	thalamus
Th-S	thioflavin-S
TLC	thin-layer chromatography
Total cts	total counts of radioactive decay
TPSA	topological polar surface area

TR	repetition time
TSPO	translocator protein
T-tau	total tau
UV	ultraviolet
V	ventral
VACht	vesicular acetylcholine transporter
VaD	vascular dementia
v_B	physiological blood volume fraction
V_{\max}	maximum enzymatic reaction rate
VOI	volume of interest
VOI_{in}	inner volume of interest
VOI_{out}	outer volume of interest
V_T	volume of distribution
V_T	volume of distribution (reference tissue)
WB	whole brain
WM	white matter
WT	wild type
X	parent nucleus
Y	daughter nucleus
β^+	Positron (β^+ decay)
γ	gyromagnetic ratio
λ	decay constant
ν	Neutrino
ω_0	precessional (Larmour) frequency

Acknowledgements

I would first like to express my most sincere gratitude to Dr. Sultan Darvesh, whose infectious enthusiasm for scientific endeavour has fueled these PhD research pursuits. His mentorship has been invaluable, I have learned much, and a considerable amount has been accomplished over the last five years.

My passion for medical imaging has origins that predate the current graduate work. I would be remiss not to acknowledge the mentorship and guidance provided by Dr. Chris Bowen who, over the years, has taught me much of what I know in the field.

I am grateful for the guidance provided to me by my PhD advisory committee including Dr. Bill Baldrige, Dr. Kazue Semba, Dr. Steve Burrell, Dr. Chris Bowen and to my PhD external examiner Dr. Robert Bartha for his expertise and interest in the work.

For collaborators on the ADNI neuroimaging project, I would like to extend my thanks to Dr. John Fisk, Dr. Sandra Black, Dr. Xiaowei Song and Dr. Steve Burrell.

To the Darvesh research group, it has been a tremendous experience to work alongside Andrew Reid, Meghan Cash, Ian Pottie, Ian Macdonald, Selena Maxwell and David Luke on various research pursuits over the years. I am also extremely honoured to have worked with Professor Earl Martin over my tenure with the group. Special thanks to Dr. Erin Mazerolle, Dr. Kirk Feindel and Dr. Kim Brewer for helpful medical imaging research discussions over the years and to Christa Davis for her technical expertise.

Most importantly, I would like to acknowledge the love and support from my family and friends. In particular, to my wife Danielle, thank you for your unwavering patience and support you have shown me throughout this journey.

Chapter 1 Introduction

1.1 Publication Status

D.R. DeBay and S. Darvesh. *Butyrylcholinesterase as a Biomarker in Alzheimer's Disease and Dementia* in *The Neuroscience of Dementia* (Eds: Martin and Preedy, Elsevier). In press. Aspects of this introductory chapter appear in upcoming book chapter.

1.2 Overview

Alzheimer's disease (AD) is the most common neurodegenerative disorder that causes dementia and is a significant cause of morbidity and mortality. The etiology of AD remains unknown and a definitive diagnosis for the disease is not yet achievable during life. Consequently, intense focus has been placed on establishing reliable AD biomarkers that both improve the certainty of an AD diagnosis during life and improve our understanding of the pathogenesis of the disease. The cholinergic system is one of the first neuronal networks that degenerates in AD and importantly, the serine hydrolase enzyme butyrylcholinesterase (BChE) associates with pathological hallmarks of the disease. We have recently shown that BChE is a highly sensitive and specific AD biomarker and an important diagnostic target for molecular imaging in the AD brain that could ultimately enhance the accuracy and timely detection of the disease. To this end, the Darvesh group has developed several lead candidate radioligands that target and bind to BChE. The current thesis sought to develop and implement a rigorous neuroimaging analysis framework, offering the first direct *in vivo* evaluation of these radioligands for Positron Emission Tomography (PET) and Single Photon Emission Computed Tomography (SPECT) imaging in the brain.

In this chapter we review the current understanding of AD and associated biomarkers, emphasizing BChE, the cholinergic system and current state of molecular imaging of the cholinergic system. The principles of nuclear medicine neuroimaging modalities including positron emission tomography (PET) and single photon emission tomography (SPECT) will be reviewed in addition to complementary structural imaging techniques such as Magnetic Resonance Imaging (MRI) and Computed Tomography (CT). The relevant theory in the analyses of imaging data in nuclear medicine will be covered followed by concepts of central nervous system (CNS) radiotracer development. Finally, the overall thesis objective and hypothesis will be highlighted followed by an overview of each thesis chapter.

1.3 Alzheimer's Disease (AD)

Alzheimer's disease (AD) is a progressive neurodegenerative disorder of insidious onset and is the most common cause of dementia (Scheltens et al., 2016). The prevalence of AD and concomitant socioeconomic economic burdens, are predicted to dramatically rise over the next decades (Scheltens et al., 2016). AD remains a clinical diagnosis based on acquired impairment in cognitive domains (memory, language, visuospatial or executive functions) that interfere with activities of daily living (McKhann et al., 2011). Considerable overlap of symptomatology exists between AD and other non-AD dementias, making the reliability of a clinical diagnosis of AD insufficient (sensitivity=81%, specificity=70%) (Knopman et al., 2001). A definitive diagnosis of AD requires the clinically observed presence of dementia during life and disease-defining hallmarks at autopsy, namely, extracellular neuritic plaques containing β -amyloid ($A\beta$) and intracellular neurofibrillary tangles (NFTs) containing hyperphosphorylated tau

(Montine et al., 2012). A β and NFTs are necessary criteria but not alone sufficient for an AD diagnosis, as they lack specificity since up to 30% of cognitively normal older individuals also have A β and NFTs in the brain (Jansen et al., 2015; Snowden & Nun, 2003). Nevertheless, characterizing A β biomarkers, for example, in the living brain has helped improve the accuracy of AD diagnosis during life (Johnson, Minoshima, Bohnen, Donohoe, Foster, Herscovitch, Karlawish, Rowe, Carrillo, Hartley, Hedrick, Pappas, Thies, et al., 2013).

1.4 Current Biomarkers in AD

A shift in research focus towards a biological (biomarker-based) definition of AD has been suggested recently. This includes a focus on the A, T, (N) framework; that is, amyloid (A), tau (T) and neurodegeneration (N) (Jack et al., 2018) which is currently evaluated with quantitative molecular imaging approaches using Positron Emission Tomography (PET) and Single Photon Emission Computed Tomography (SPECT) in addition to structural imaging and cerebrospinal fluid (CSF)-based biomarkers.

1.4.1 β -Amyloid (A β) as an AD Biomarker

Amyloid plaques are composed of extracellular aggregates of A β peptide, with 39-43 amino acid residues resulting from γ - and β -secretase proteolytic cleavage of the amyloid precursor protein (APP) (Villemagne, 2016). An imbalance of production and clearance of A β ₄₂ oligomer in particular has been implicated in AD, whereby A β ₄₂ and soluble fragments aggregate into large fibrils and insoluble extracellular plaques. This amyloid cascade has been suggested to be an early event that initiates the pathogenesis of AD (Selkoe & Hardy, 2016).

The pursuit of A β molecular imaging has taken cues from the chemistry of established histopathological dyes (Villemagne, 2016). One such dye is thioflavin T which, upon binding to A β , fluoresces. A derivative of thioflavin T, *N*-methyl-[¹¹C]2-(4'-methylaminophenyl)-6-hydroxybenzothiazole (¹¹C-PiB) (Klunk et al., 2004), was the first to show high affinity and selectivity for A β plaques (Villemagne, 2016). Subsequently, three additional [¹⁸F] labelled A β tracers have been approved for brain imaging by the Food and Drug Administration (FDA), to capitalize on the longer half-life of [¹⁸F] ($t_{1/2}$, 110 min) and consequently, more widespread utility globally. These tracers include [¹⁸F]florbetapir, [¹⁸F]flutemetamol and [¹⁸F]florbetaban (Villemagne, 2016). These agents represent a major leap forward for molecular imaging of A β during life as an adjunct test in AD. However, the lack of specificity of A β in AD limits their diagnostic value as 30% of cognitively normal elderly individuals have A β pathology at autopsy (Snowdon & Nun, 2003). A β imaging as an AD biomarker provides an average sensitivity of 90% and specificity of 85% (Morris et al., 2016) (Table 1.1).

Cerebrospinal fluid (CSF) A β biomarkers have also been evaluated in AD, reflecting the homeostatic balance between A β production and clearance in the brain. In AD, a marked decrease in CSF A β_{42} and A β_{42} / A β_{40} ratio has been shown consistently with a mean decrease to approximately 56% of cognitively normal individuals (Olsson et al., 2016). It has been suggested that this is due to A β_{42} aggregates becoming sequestered in A β plaques in the brain resulting in lower amounts remaining in the CSF (Blennow & Zetterberg, 2018).

Diagnostic Modality	Sensitivity (%)	Specificity (%)	Reference
^a Clinical Diagnosis	81	70	(Knopmann et al., 2001)
^b MRI Atrophy	83	89	(Bloudek et al., 2011)
^c ¹⁸ F-DG-PET	90	89	(Bloudek et al., 2011)
^d SPECT perfusion	80	85	(Bloudek et al., 2011)
^e A β -PET	90	85	(Morris et al., 2016)
^f tau-PET	100	86	(Wang et al., 2016)
^g CSF A β ₄₂	80	82	(Bloudek et al., 2011)
^h CSF P-tau	80	83	(Bloudek et al., 2011)
ⁱ CSF T-tau	82	90	(Bloudek et al., 2011)
^j BChE neuropathology	100	100	(Macdonald et al., 2017)

Table 1.1 Diagnostic performance summary (sensitivity and specificity) of current AD biomarkers (AD vs. cognitively normal meta-analyses). ^aclinical diagnosis using neuropathology “gold standard”, ^bmagnetic resonance imaging (MRI)-based hippocampal atrophy, ^c[¹⁸F]fluorodeoxyglucose ([¹⁸F]FDG)-Positron Emission Tomography (PET) temporoparietal hypometabolism, ^dSingle Photon Emission Computed Tomography (SPECT) perfusion using pooled [^{99m}Tc]-HMPAO, [^{99m}Tc]-ECD or [¹²³I]IMP imaging, ^eamyloid (A β)-PET using pooled [¹⁸F]florbetapir, [¹⁸F]flutemetamol or [¹⁸F]florbetaban imaging, ^ftau-PET using radiotracer ¹⁸F-AV1451, ^gcerebrospinal fluid (CSF) A β ₄₂, ^hCSF phosphorylated (P)-tau, ⁱCSF total (T)-tau, ^jbutyrylcholinesterase (BChE) neuropathological quantification. Adapted from (Morris et al., 2016), (Bloudek et al., 2011) and (Macdonald et al., 2017).

1.4.2 Tau as an AD Biomarker

In addition to A β , tau neurofibrillary tangles (NFTs) are required for the diagnosis of AD, though they are not exclusive to this disease. Tau (tubulin-associated unit) is a microtubule-stabilizing protein, important for the neuronal cytoskeleton and for axonal transport (Iqbal et al., 2016). Six isoforms of tau exist in humans, classified by the microtubule binding domain repeats, namely, 3 or 4 repeats (3R and 4R, respectively) (Iqbal et al., 2016). Abnormal tauopathies occur when hyperphosphorylation of tau generates conformational changes (misfolding and aggregation) which, in turn, prevents normal microtubule binding. This promotes axonal destabilization, transport impairment and degeneration, ultimately leading to neuronal dysfunction (Iqbal et al., 2016). Insoluble paired helical filaments, a major component of NFTs, also arise from tau hyperphosphorylation and are a common feature in the AD brain (Iqbal et al., 2016).

Tauopathies with both 3R and 4R isoforms include Alzheimer's disease, Down Syndrome and Chronic traumatic encephalopathy. Tauopathies that accumulate the 4R isoform, include progressive supranuclear palsy (PSP), corticobasal degeneration (CBD) and argyrophilic grain disease, while Pick's disease expresses a 3R isoform (Villemagne & Okamura, 2016). Despite this widespread and varied presence of tau in numerous tauopathies, tau biomarkers continue to be considered for AD diagnosis.

Tau as an imaging biomarker is in a very early stage of development. A benzimidazole derivative, 7-(6-[¹⁸F]fluoropyridin-3yl)-5H-pyrido[4,3-b]indole, ([¹⁸F]-AV1451) has shown high affinity for tau and minimal binding to white matter in the brain (Villemagne & Okamura, 2016). However, "off-target" binding has been identified in non-tau regions of the brain including retention seen in the basal ganglia, anterior

midbrain, venous sinuses and the choroid plexus (Villemagne & Okamura, 2016). Brain imaging of tau with [¹⁸F] –AV1451 has been shown to distinguish AD from cognitively normal controls (sensitivity=100%, specificity=86%) (Wang et al., 2016) (Table 1.1). The presence of NFTs in a number of non-AD tauopathies represents a major limitation for the use of such agents for specific AD diagnosis.

Over the last two decades, assays for CSF tau have been developed, including the total tau (T-tau) assay, recognizing all 6 isoforms of tau. T-tau is a reflection of an overall state of neurodegeneration rather than a direct marker of pathophysiological process in AD (Blennow & Zetterberg, 2018). In AD, T-tau is elevated 2.5-fold that of cognitively normal individuals reflecting heightened neurodegeneration (Olsson et al., 2016). However, increased T-tau is also observed in several other neurodegenerative disorders (Zetterberg, 2017). Of particular relevance in AD, the measurement of CSF phosphorylated tau (P-tau) targets tau protein residues possessing the same post-translational phosphorylation observed in the AD brain, namely, hyperphosphorylation at threonine-181, threonine-231 and serine-199 residues (Blennow & Zetterberg, 2018). Individuals with AD show increased CSF P-tau concentrations approximately 1.9-fold compared to cognitively normal individuals (Olsson et al., 2016); however, to date, only modest associations with direct measures of neurofibrillary pathology have been documented (Zetterberg, 2017).

Taken together, current fluid biomarkers in AD have been consolidated into an Alzheimer's CSF profile, namely, decreased CSF A β ₄₂ concentrations with increased CSF levels of T-tau and P-tau, generating moderate diagnostic performance in AD (Table 1.1).

1.4.3 Neurodegeneration (N) as an AD Biomarker

Neurodegenerative biomarkers in AD includes detection of brain atrophy in the medial temporal lobe with Magnetic Resonance Imaging (MRI) (Frisoni et al., 2010) as well as measurement of impaired cerebral metabolism and perfusion in temporo-parietal regions with ¹⁸Fluorodeoxyglucose Positron Emission Tomography (FDG-PET) (Mosconi, 2005) and ^{99m}Tc-Exametazime, Single Photon Emission Computed Tomography (SPECT) (Yeo et al., 2013), respectively. Moderate diagnostic performance has been achieved with these modalities (sensitivity=83%, specificity=89%) for MRI , (sensitivity=83%, specificity=86%) for FDG-PET and (sensitivity=80%, specificity=85%) for SPECT (Bloudek et al., 2011) (Table 1.1). Neurodegenerative biomarkers do not inform the cause for neurodegeneration and the lack of AD specificity provides limited predictive value for a definitive AD diagnosis. Consequently, though considerable progress has been made characterizing these AD biomarkers, they currently must be used in conjunction with clinical history and cognitive testing, to support the clinical diagnosis of AD (Johnson, Minoshima, Bohnen, Donohoe, Foster, Herscovitch, Karlawish, Rowe, Carrillo, Hartley, Hedrick, Pappas, Thies, et al., 2013).

The limitations of A β , tau and neurodegeneration biomarkers notwithstanding, the AT(N) classification system has provided the opportunity to formalize our current understanding of AD progression at a biological level. Biomarker development beyond AT(N) will be important to augment existing approaches for AD diagnosis.

1.5 The Cholinergic System and the AD Cholinergic Hypothesis

The cholinergic system is responsible for several functions in the central nervous system (CNS) including cognition and behaviour. The major cholinergic pathways in the

brain originate in the cholinergic complex of the basal forebrain and forms the major cholinergic projections to cortical and subcortical regions important in memory and other cognitive functions (Mesulam, 2013). The observation that the central cholinergic system is one of the first neuronal networks affected in AD (Davies & Maloney, 1976) led to development of the cholinergic hypothesis of memory dysfunction. The cholinergic hypothesis posits that loss of cholinergic function significantly contributes to the cognitive decline associated with AD (Coyle et al., 1983).

Neurons that release the neurotransmitter acetylcholine (ACh) are said to be cholinergic. Components of the cholinergic system include the ACh-synthesizing enzyme choline acetyltransferase (ChAT), high affinity choline transporters (CHT1) whose functions include uptake of choline at the pre-synaptic terminal of neurons, vesicular acetylcholine transporter (VAChT) to transport ACh to the pre-synaptic cleft and cholinergic muscarinic (mAChR) and nicotinic (nAChR) ACh receptors for synaptic signaling and ACh metabolizing enzymes acetylcholinesterase (AChE) and butyrylcholinesterase (BChE) (Giacobini & Pepeu, 2006). This chapter focuses on cholinesterases with a particular emphasis on BChE.

1.5.1 Cholinesterases: BChE and AChE

BChE and AChE are enzymes that co-regulate cholinergic neurotransmission in the brain by controlling the concentration of the neurotransmitter ACh (Darvesh, Hopkins, et al., 2003; Silver, 1974). BChE is an enzyme of the hydrolase class, utilizing a serine residue at its catalytic center (Silver, 1974). While AChE is highly specific for hydrolyzing ACh, BChE shows broader substrate repertoire and can hydrolyze a wide variety of esters and related compounds (Lockridge, 2015). In addition to enzymatic

activity, BChE is involved in the development of the nervous system (Layer, 1983), detoxification and drug metabolism (Lockridge, 2015). Importantly, BChE has been shown to interact with other proteins, such as β -amyloid (Mesulam & Geula, 1994) and NFTs (Moran et al., 1994).

BChE is a 574 amino acid residue glycoprotein (Figure 1.1). As a hydrolase enzyme, BChE has the serine (S198:human BCHE numbering of mature enzyme), glutamate (E325) and histidine (H438) residues at the catalytic site (Lockridge et al., 1987). This catalytic triad is located near the bottom of a 20Å deep active site gorge, where substrates such as choline esters, react with serine to generate a tetrahedral intermediate that collapses to expel alcohol to form an acylated enzyme that undergoes hydrolysis to release the enzyme and product (Nicolet et al., 2003; Sussman et al., 1991). The active site gorge of BChE is large (~500 Å) relative to AChE (~300 Å) and can accommodate larger substrate and inhibitor ligands than AChE (Saxena et al., 1997).

BChE exists in different molecular forms, that have significance in health and disease. BChE monomers and oligomers are comprised of identical catalytic subunits (Massoulié et al., 1993) and include the G₁ monomeric (globular) form, the G₂ dimeric form comprised of two monomers joined by a disulfide bridge at identical cysteine 571 residues (Lockridge et al., 1987), and the G₄ globular tetramer, containing two G₂ forms held together by hydrophobic interactions (Lockridge et al., 1987). Asymmetric G₄ membrane-bound tetramers also exist that are tethered to membranes either by a proline-rich membrane anchor (PRiMA) (Massoulié et al., 1993) or by triple helical collagen-tailed anchor in single (A₄), double (A₈) or triple tetramer configurations (Massoulié et al., 1993). The G₁ form of the enzyme, is prevalent in embryonic development, while the

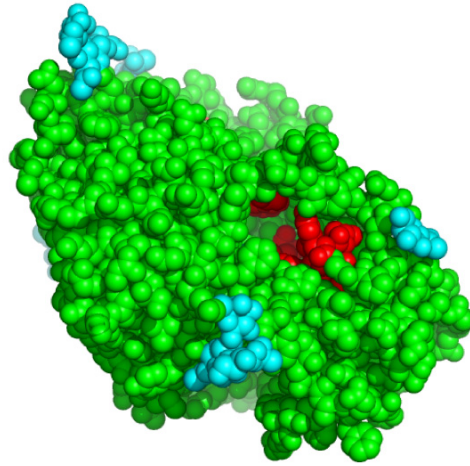


Figure 1.1 3-Dimensional rendering of the monomeric crystal structure of human butyrylcholinesterase (BChE) enzyme. BChE is a 574 amino acid glycoprotein with an active site (red) containing catalytic triad serine (S198), glutamate (E325) and histidine (H438). Other BChE amino acids shown in green and glycosylated regions in blue. Image generated in PyMOL (<https://pymol.org>) using crystal structure (Nicolet et al., 2003) from PDB (Protein Data Bank, <https://www.rcsb.org>).

G₄ form predominates in the mature healthy brain (Arendt et al., 1992). Interestingly, there is a reversal of the molecular form to embryonic G₁ form of the enzyme in the AD brain.

1.5.2 Cholinesterase Distribution in Normal and AD brain

In the healthy brain, AChE is found in neurons and neuropil while BChE is found in distinct neurons in regions such as the amygdala, hippocampus and thalamus as well as in glia and white matter (Darvesh, Hopkins, et al., 2003). However, BChE is found at relatively low concentrations in the cerebral cortex in the normal brain (Macdonald et al., 2017). In the AD brain, AChE levels are observed to be reduced (Perry, Tomlinson, et al., 1978) while those of BChE are markedly increased (Perry, Tomlinson, et al., 1978) or remain relatively constant (Darvesh et al., 2010). Importantly, while there is very little BChE activity in the cerebral cortex in cognitively normal individuals, this distribution changes in AD. In AD, BChE preferentially associates with A β plaques and NFTs in the cerebral cortex in a highly AD-specific manner (Figure 1.2) (Darvesh et al., 2010; Macdonald et al., 2017; Mesulam & Geula, 1994), the significance of which is not entirely clear. In AD, the brain ratio of BChE to AChE increases from BChE/AChE=0.2 in normal brain to BChE/AChE=11.0 in the AD brain (Perry, 1980). Additionally, BChE in the cerebral cortex is also virtually absent in other forms of dementia (Macdonald et al., 2017).

1.5.3 Butyrylcholinesterase (BChE) as an AD Biomarker

The preferential association of BChE with AD neuropathology positions BChE as a viable diagnostic target in AD. We have recently published a paper comparing human

brain tissue at autopsy from AD brains, cognitively normal older individuals and cognitively normal older individuals with A β plaques (Macdonald et al., 2017). The diagnostic performance of A β vs. BChE quantification in predicting AD was evaluated, using clinicopathological criteria as the gold standard. A virtual absence of BChE in non-AD orbitofrontal cortex was seen and significantly elevated BChE was observed in AD brains only (Figure 1.2). BChE quantification in these brains provided better overall diagnostic performance (sensitivity/specificity = 100%/100%, receiver operating characteristic (ROC) area under curve (AUC) = 1.0, diagnostic accuracy =100%) outperforming A β quantification (sensitivity/specificity = 100%/85.7%, ROC AUC = 0.98, diagnostic accuracy =90%) (Figure 1.3) (Macdonald et al., 2017). Importantly, BChE was virtually absent in other common dementias including corticobasal degeneration (CBD), frontotemporal dementia with tau (FTD-tau), dementia with Lewy bodies (DLB) and vascular dementia (VaD) (Figure 1.4) (Macdonald et al., 2017). The superior specificity of BChE distinguishes plaques associated with AD from those found in the cognitively normal individuals with A β plaques. BChE is a sensitive and specific biomarker with high predictive value in AD and a valuable diagnostic target that could enhance the current AD biomarker armamentarium.

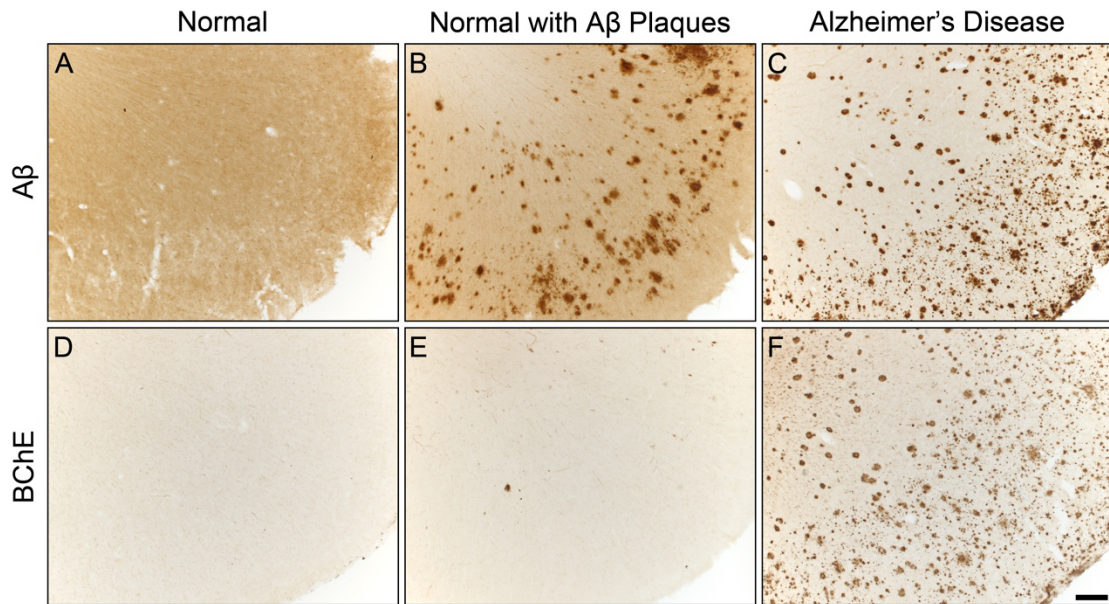


Figure 1.2 Orbitofrontal cortex photomicrographs from cognitively normal (**A,D**), cognitively normal with A β plaques (**B,E**), and AD (**C,F**) brains stained for A β (**A,B,C**) immunohistochemistry, and butyrylcholinesterase (BChE, **D,E,F**) histochemistry. Note, lack of BChE staining in normal orbitofrontal cortex (**D**), paucity of BChE activity in cognitively normal with A β plaques (**E**), and significant BChE activity in AD (**F**). Scale bar = 500 μ m. Representative photomicrographs adapted from (Macdonald et al., 2017).

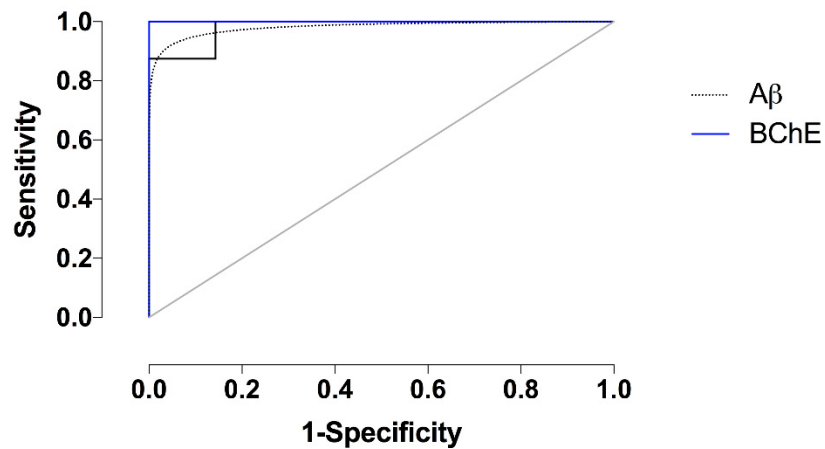


Figure 1.3 Receiver-Operating Characteristic Plot (sensitivity vs. 1-specificity) of β -amyloid ($A\beta$) and butyrylcholinesterase (BChE) quantification metrics of the orbitofrontal cortex. Empirical data shown as solid lines and fitted curves as dashed lines of the same colour. Chance association shown as diagonal line indicates no discriminative capability of a diagnostic test. The area under the curve (AUC) serves as summary measure of the diagnostic accuracy of each metric. BChE demonstrated high diagnostic accuracy with sensitivity/specificity = 100%/100%, diagnostic accuracy of 100% and ROC AUC of 1.0. $A\beta$ demonstrated sensitivity/specificity = 100%/85.7%, diagnostic accuracy of 0.90 and ROC AUC of 0.98. Adapted from (Macdonald et al., 2017).

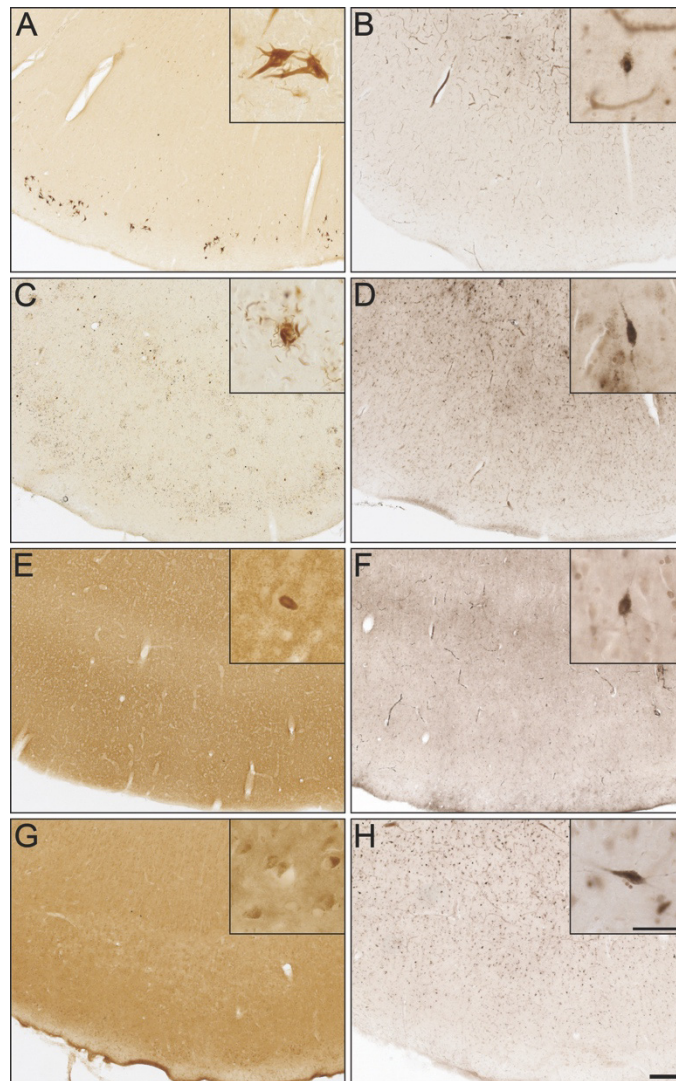


Figure 1.4 Photomicrographs of post-mortem human entorhinal cortex from corticobasal degeneration (**A,B**), frontotemporal dementia with tau (**C,D**), dementia with Lewy bodies (**E,F**) and vascular dementia (**G,H**) stained for tau 3R (**A**), tau 4R (**C**), α -synuclein (**E**), $A\beta$ (**G**) and butyrylcholinesterase (BChE) activity (**B,D,F,H**). Note, insets are higher magnification photomicrographs demonstrating examples of the pathology observed in each of the neurodegenerative diseases including neurofibrillary tangles (**A**), neuropil threads and degenerating neurites (**C**), Lewy bodies (**E**) and intraneuronal inclusions (**G**). Note, BChE staining was limited to a few scattered cortical neurons (insets **B,D,F,H**) and did not label pathological structures in these neurodegenerative diseases. Scale bars = 250 μ m, insets 50 μ m. (Macdonald et al., 2017).

1.5.4 BChE as an Imaging Biomarker

Molecular imaging of the cholinergic system has generated a number of radioligands that target VAChT, cholinergic receptors mAChR, nAChR, as well as AChE and BChE cholinesterases. Different strategies have been adopted for imaging of cholinesterases in the brain. The metabolic trapping principle (Kikuchi et al., 2007) is a concept that has been successfully used for imaging of AChE, whereby a radioligand that crosses the blood-brain barrier acts as a substrate for AChE and is hydrolyzed by AChE into hydrophilic products that are trapped inside the brain, labelling areas where the AChE enzyme is present (Kikuchi et al., 2007). The enzymatic trapping principle shows promise for BChE radioligands. This approach relies on incorporating the radionuclide in the portion of a BChE ligand that remains attached to the longer-lived acyl enzyme intermediate, providing a more stable radiolabeled complex to accurately localize BChE in the brain (Darvesh, 2013).

Several PET agents targeting AChE (Namba et al., 2002) and BChE (Kikuchi et al., 2004; Kuhl et al., 2006; Snyder et al., 2001) have been tested for human brain imaging of cholinesterases in neurodegenerative disorders. In particular, AChE imaging with *N*-[¹¹C]methylpiperidin-4-yl acetate (¹¹C-MP4A) and *N*-[¹¹C]methylpiperidin-4-yl proprionate (¹¹C-MP4P) are established radiotracers in the assessment of AChE. AChE PET imaging was able to successfully characterize AChE activity *in vivo* as a therapeutic monitoring tool after treatment with cholinesterase inhibitor donepezil in the AD brain (Ota et al., 2010).

The quest for visualization of BChE associated with AD plaques is still an ongoing pursuit. Previous studies have shown that chemical entities containing *N*-

methylpyrrolidinol or *N*-methylpiperidinol moiety readily enter the brain (Kikuchi et al., 2004; Kuhl et al., 2006; Roivainen et al., 2004); however, an increase in radioligand uptake in regions typically associated with cholinesterase AD plaques was not clearly established. For example, *in vivo* testing of 1-¹¹C-methyl-4-piperidinyl *n*-butyrate (Kuhl et al., 2006), a BChE-specific ester substrate, demonstrated rapid clearance (Roivainen et al., 2004) and overall decreased uptake in AD brain, contrary to the known histochemical and enzymatic distribution studies of BChE (Mesulam & Geula, 1994).

A recent *in vitro* study comparing radioligand uptake in AD brain tissue from a cognitively normal brain with A β plaques using autoradiography revealed that an A β imaging agent, [¹²³I]-2-(4'-dimethylaminophenyl)-6-iodoimidazo[1,2-a]pyridine ([¹²³I]IMPY, did not distinguish between the two tissue types, while a cholinesterase imaging agent, 4-[¹²³I]iodophenylcarbamate ([¹²³I]-PIP), selectively labelled plaques in the cortex of the AD brain (Macdonald et al., 2016). This demonstrates that cholinesterase imaging is a viable approach for the specific detection of AD pathology.

Other prospective ¹²³I SPECT radioligands have been generated also containing the *N*-methylpiperidinol moiety, which, again, rely on enzyme (BChE) trapping of the radiolabel (Darvesh, 2013) in an attempt to prolong ligand-enzyme latencies (Macdonald et al., 2011; Macdonald et al., 2016). To prevent early loss of radiolabel from the BChE–substrate complex, incorporation of a radioactive marker on the acyl moiety instead of the alcohol portion (first leaving group) of the ester, gives the radioactive marker longer time to remain associated with the enzyme. Specificity of BChE over AChE was achieved by increasing the size of the acyl group from the natural AChE substrate, ACh. The aromatic ring bearing an iodine atom is amenable to exchange with [¹²³I] via tributyl tin

intermediate (Macdonald et al., 2011). Earlier autoradiographic evidence was generated showing that one such iodobenzoate derivative, 1-methylpiperidin-4-yl 4-iodobenzoate, when injected into a rat, enters rodent brain and labels areas known to exhibit BChE activity in histochemical studies (Macdonald et al., 2011). Therefore, imaging of BChE in the cerebral cortex represents a promising diagnostic marker for AD that has the potential for early disease detection in the living brain, not yet realized by current A β or NFT imaging efforts.

BChE activity in the CSF has been evaluated in AD and compared in relation to AD neuropathology and cognitive assessments. BChE activity in CSF has been observed to decrease in AD (Darreh-Shori et al., 2006) in contrast to the well-established increase of BChE-associated plaques in the cerebral cortex in AD. BChE CSF levels have also been shown to be 40-60% lower in carriers of one or two *APOE4* (AD genetic risk factor) alleles and directly correlate with brain metabolism (¹⁸FDG-PET) and cognitive function (MMSE scores) (Darreh-Shori et al., 2006). This reciprocal relationship between decreased BChE in the CSF and increased BChE in the cortex in AD has been suggested to mark the incorporation of BChE into A β plaques in the brain and as such may be a predictive biomarker for AD.

1.5.5 The Functional Role of BChE in AD

The exact role of BChE in AD remains unclear. A putative role of BChE, which emanates from glia (Wright et al., 1993), is in the maturation of A β plaques (Mesulam & Geula, 1994). Higher levels of BChE in the brain could promote increased hydrolysis of AChE, further impairing cholinergic neurotransmission. In addition, in a genome-wide

association study, BChE, in conjunction with AD risk factor *APOE4* was found to be a chief determinant of A β deposition in the AD brain (Ramanan et al., 2014).

Additionally, among the over 60 known genetic variants of BChE, certain genetic variants cause reduction of BChE activity, providing an opportunity to evaluate the association of altered BChE expression to AD progression. However, the influence of BChE genetic polymorphism in AD remains controversial. The most common *BCHE-K* variant is attendant with a BChE reduction of 30% (Lockridge, 2015). While some studies have reported a protective effect of *BCHE-K* or no effect, others have suggested increased AD risk, particularly when associated with genetic risk factor *APOE4* (Wang et al., 2015).

As in human AD, mouse models of AD (5XFAD) also accumulate BChE-associated A β plaques (Darvesh & Reid, 2016). BChE knockout mice have been generated (5XFAD/BChE-KO) and interestingly, these mice see a significant reduction in fibrillar A β plaque deposition compared to the 5XFAD mice, especially in males (Figure 1.5) (Darvesh & Reid, 2016). Taken together, these data suggest that BChE may have mechanistic significance in the pathogenesis of AD. Regardless of whether BChE plays a causal role in AD development, this does not preclude its utility as a highly sensitive and specific biomarker of the disease.

The cholinergic system is a critical aspect of the proper functioning of the CNS and cholinergic deficits have been shown to be inextricably linked with cognitive impairment and A β and tau deposition in AD. BChE is an important diagnostic target in AD and could be adopted into the AD biomarker armamentarium.

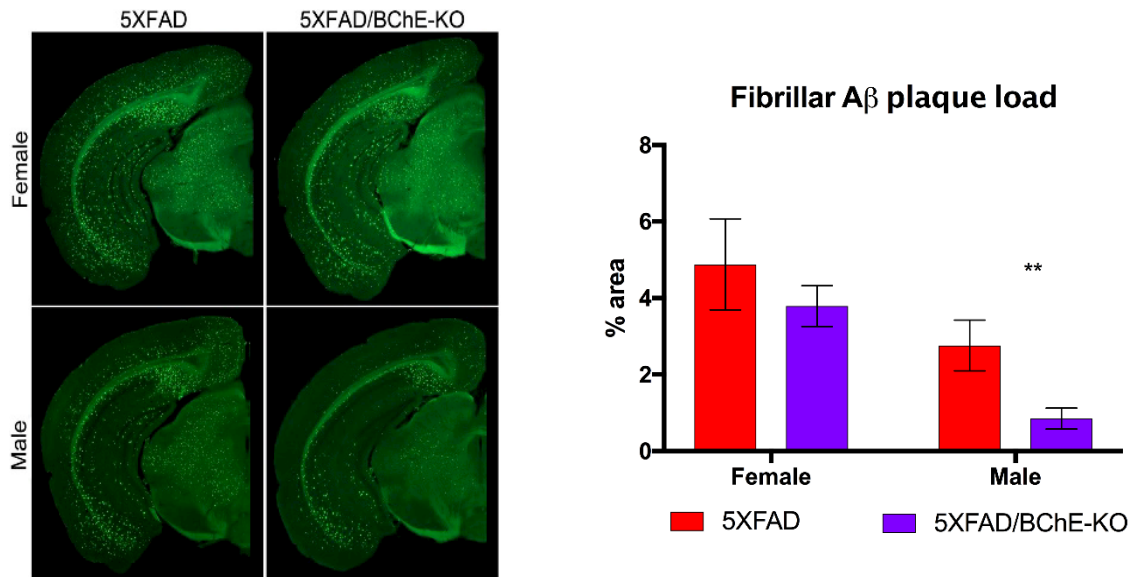


Figure 1.5 Images (left) showing thioflavin-S staining of fibrillar A β in female and male 5XFAD and 5XFAD/BChE-KO mice at 6 months. Bar graphs (right) indicate percentage of cerebral cortex area covered with fibrillar A β pathology in female and male mice, aged 6 months, presented as mean \pm SD. (**, $p < 0.01$). Data adapted from (Reid and Darvesh, 2015).

1.6 Neuroimaging Techniques

Over the last half century, the field of neuroimaging has revolutionized the way we understand the structural and functional organization of the living brain in health and disease. Non-invasive brain imaging techniques have allowed us to visualize neuroanatomy in exquisite detail *in vivo*, evaluate biochemical processes and functionally map cognitive and behavioural processes of the brain. In this way, neuroimaging has been instrumental in clinical diagnostic imaging improving the diagnosis, management and treatment of neurological disorders.

The various brain imaging techniques are described in the following sections.

1.6.1 Nuclear Medicine Imaging

The field of nuclear medicine relies on emission imaging modalities including positron emission tomography (PET) and single photon emission computed tomography (SPECT). Molecular probes specifically designed to target various biochemical processes *in vivo* are labelled with radionuclides (radioactive isotopes), which can be detected and localized by these imaging techniques (Bushberg, 2002). PET and SPECT imaging facilitates quantitative evaluation of not only the spatial distribution of the probe, but also its temporal association within target regions of a living subject, making these very powerful functional imaging techniques.

1.6.1.1 Radioactive Decay

Isotopes used in nuclear medicine undergo a spontaneous transformation of their atomic nuclei to reach more stable states. This is known as radioactive decay, upon which, radiation is emitted (Bushberg, 2002). Regardless of the mode, radioactive decay

is governed by the fundamental decay equation (Equation 1.1), which describes the quantity of radioactive material for a given radionuclide as a function of time:

$$A_t = A_0 e^{-\lambda t} \quad (\text{Equation 1.1})$$

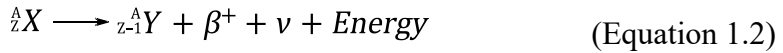
where A_t is the radioactivity at time t , A_0 is the initial activity, λ is the decay constant and t is time (Bushberg, 2002). A table of common radionuclides use in nuclear medicine and associated physical characteristics is seen in Table 1.2.

Radionuclide	Symbol	$t_{1/2}$	Energy keV (% abundance)	Decay Mode (%)	Nuclear Reaction	Production	Modality
18-Fluorine	^{18}F	110 min	511 (AR)	β^+ (97) / EC (3)	$^{18}\text{O}(\text{p,n})^{18}\text{F}$	cyclotron	PET
11-Carbon	^{11}C	20.4 min	511 (AR)	β^+ (100)	$^{10}\text{B}(\text{d,n})^{11}\text{C}$	cyclotron	PET
15-Oxygen	^{15}O	2.04 min	511 (AR)	β^+ (100)	$^{14}\text{N}(\text{d,n})^{15}\text{O}$ or $\text{N15}(\text{p,n})^{15}\text{O}$	cyclotron	PET
13-Nitrogen	^{13}N	9.97 min	511 (AR)	β^+ (100)	$^{12}\text{C}(\text{d,n})^{13}\text{N}$	cyclotron	PET
99m-Technetium	$^{99\text{m}}\text{Tc}$	6.02 hr	140 (88)	IT (100)	IT	generator	SPECT
123-Iodine	^{123}I	13.2 hr	159 (83)	EC (100)	$^{124}\text{Xe}(\text{p},2\text{n})^{123}\text{Cs}$	cyclotron	SPECT

Table 1.2 Common radionuclides used in nuclear medicine. AR, annihilation radiation; β^+ (positron) decay; d, deuterium; EC, electron capture; IT, isomeric transition (gamma ray); n, neutron; PET, positron emission tomography; p, proton; SPECT, single photon emission computed tomography; $t_{1/2}$, physical half-life. Table adapted from (Bushberg, 2002).

1.6.1.2 Principles of Positron Emission Tomography (PET)

Positron emission tomography (PET) is an emission imaging modality that measures the radioactive decay processes of unstable, positron emitting isotopes such as ^{18}F , ^{11}C , ^{15}O and ^{13}N (Bushberg, 2002). Positron emission is a form of radioactive decay known as beta-plus (β^+) decay (Equation 1.2).



In this decay scheme, a daughter nucleus (Y) is formed upon conversion of a proton to a neutron in the parent nucleus (X) which results in the ejection of a positron (positively charged anti-matter electrons of equivalent mass but opposite charge) and a neutrino, ν . This results in a new daughter nucleus (Y) with a decrease in atomic number and conserved mass number between parent and daughter (Bushberg, 2002). A common example is shown for [^{18}F] (Equation 1.3).



Subsequently, the positron travels a short distance, known as the positron range (e.g. $\sim 0.6\text{mm}$ for ^{18}F) at which point it elastically scatters with neighboring atoms and electrons, loses energy and slows down at which point it can collide with an electron at rest and the pair annihilates, generating two coincident 511 keV photons that are emitted simultaneously in opposite directions at approximately 180° apart from each other (Bushberg, 2002). It is the detection of this positron annihilation that forms the basis of the PET signal.

1.6.1.3 PET Scanners

Modern day PET scanner configurations consist of concentric rings of contiguous detector elements (scintillator crystals) which detect annihilation coincidence events originating from a subject within the scanner (James & Gambhir, 2012). Coincidence detection is the basis of PET image formation. The linear path traversed following the simultaneous propagation of two 511 keV photons in opposite directions is known as the line of response (LOR). The PET instrumentation registers the arrival of annihilation photon pairs originating along the LOR within a narrow time window (\sim ns time scale), and reject erroneous signal outside of temporal resolution (James & Gambhir, 2012). This is often termed electronic collimation. During a PET scan, the number of coincidences that occur between detector element pairs is recorded and indicates the amount of radioactivity present along each particular LOR. Projections of all possible LOR over 180° of rotation are converted into sinograms which are ultimately reconstructed into tomographic images, representing the 3D distribution of a radiotracer (James & Gambhir, 2012). Conventional tomographic reconstruction methods use analytical approaches such as the filtered back projection technique that directly computes an inverse transformation converting the measured detector signals to an image (Levin, 2005). Improvements in reconstruction algorithms have led to iterative statistical methods being employed for image reconstruction, where an initial prediction for 3D radiotracer distribution is estimated and then successively modified and reprojected to compare with the measured data in order converge on an appropriate solution (Levin, 2005). Iterative reconstruction methods offer improved spatial resolution and noise reduction compared to analytical methods.

Various factors influence PET image quality. Three types of coincidence events are possible in PET. True coincidences represent authentic events in which the LOR accurately depicts the point of origin of photon emission pair (Mittra & Quon, 2009). Scatter coincidences are the result of one or both photons experiencing the Compton scatter phenomenon where interaction with outer shell electrons of neighboring atoms causes a deviation in the registered LOR and a decrease in photon energy (Mittra & Quon, 2009). Random coincidences occur when two separate radionuclides contribute a detected photon within the time resolution of the scanner, generating a false LOR (Mittra & Quon, 2009). Scatter and random coincidences are undesirable, contributing to elevated background noise and loss of contrast and quantitative accuracy in the image.

In general, the spatial resolution of PET is limited (~1mm preclinical, 5mm clinical). PET spatial resolution is determined by a number of factors including the effect of *positron range* which is dependent on the energies of the radionuclide and thus the pathlength of positron trajectories and *photon non-collinearity* which occurs when positron annihilation does not occur from rest, resulting in coincident photons that are not emitted at 180°, thus causing a LOR mis-registration that is particularly problematic for larger scanner diameters (Levin, 2005). The PET detector element size also plays a crucial role in how precisely it can resolve the photons it detects and localizes with current scanners having detector resolutions (pixel sizes) of 4-6mm for clinical scanners and 1-2mm detectors for pre-clinical systems (Levin, 2005).

The types of detector array elements (scintillator crystals) also play a direct role in the performance of a PET scanner. Scintillator crystals absorb highly penetrant 511 keV photons and generate a pulse of light, which can be measured via highly sensitive

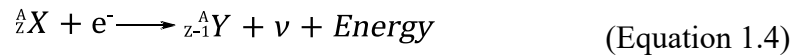
photodetectors that are coupled to the crystals. Desirable properties of a scintillator crystal include being made of high atomic number, high density material to have effective photon stopping power, and they must be narrow (for precision in photon localization). Scintillator crystals must also have high detection efficiency with bright and fast scintillation light yield to limit the dead time of the detector, thus improving the detection efficiency (Levin, 2005).

Certain corrections and calibrations have been developed to address some of the above-mentioned performance-degrading characteristics inherent to PET imaging, in particular loss of signal uniformity and quantitative accuracy. *Attenuation correction* is a method that can be applied to improve 511 keV photon signal attenuation (overall loss of counts) seen in more susceptible deeper structures. A measured correction factor can be determined via an external radiation source reference scan or by using a CT-based method to establish a set of scaled attenuation coefficients that can be applied to the a subject's PET scan (Levin, 2005).

1.6.1.4 Principles of Single Photon Emission Computed Tomography (SPECT)

Single photon emission computed tomography (SPECT) is an emission imaging modality that measures the decay of radionuclides that emit gamma ray (or high energy X-ray) photons (Bushberg, 2002). In SPECT, individual photons are ejected directly from a parent nucleus, at the speed of light, due to the relaxation of protons and neutrons that are in an excited energy state (Bushberg, 2002). Several decay modes are possible for the various SPECT radionuclides, each producing gamma photons of differing energies.

Electron capture decay occurs in neutron deficient isotopes, where the parent nucleus absorbs an electron (typically a K- or L-shell electron) which in turn causes conversion of a proton to a neutron with a simultaneous ejection of a neutrino (Equation 1.4).



Electron capture decay decreases the atomic number of the daughter nucleus, while the mass number is conserved. ${}^{123}\text{I}$ is a radiopharmaceutical that undergoes electron capture decay, releasing a characteristic 159keV photon (Bushberg, 2002) (Equation 1.5).



Isomeric transition is another form of radioactive decay that produces gamma radiation when a daughter nucleus transitions from an excited (unstable) state, to a lower-energy state through internal rearrangement, as is seen with ${}^{99m}\text{Tc}$ (Equation 1.6).



1.6.1.5 SPECT Scanners

SPECT imaging is accomplished through the use of one or more gamma cameras (detector heads) that rotate around a subject and detect incident photons originating from the administered radionuclide. Unlike PET, *physical collimation* is required to precisely determine the direction and location of an incident photon's LOR. This is accomplished through the use of high density, high atomic number collimators (typically tungsten or lead) with precise configurations of holes that allow photons to enter and strike the

detector target (Levin, 2005). Collimators of various geometries have been developed, some of the most common being parallel-hole, single pinhole and multi-pinhole (relevant for pre-clinical imaging) configurations.

There are a few scenarios in which photon events are registered with SPECT imaging. Authentic events occur when photons follow the actual LOR from the point of emission, through the collimator hole and are accurately registered at the detector. Compton scattering through photon interaction with electrons and nuclei in atoms of surrounding tissue can produce positioning errors that deviate from the photon's LOR, causing increased background noise and loss of contrast resolution. Photons can pass through undetected, or photoelectric absorption by surrounding tissue or at the level of the collimator, or crystal is also possible resulting in decreased signal collection.

As in PET, detector elements in SPECT are comprised of scintillator crystals that generate pulses of light whose signal is registered by photodetectors. The majority of SPECT systems use NaI(Tl) scintillator crystals (Levin, 2005). The total signal intensity from each individual LOR is what forms the basis of the SPECT signal measurement.

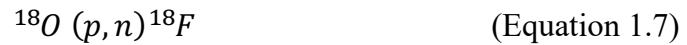
1.6.1.6 Radionuclide Production

The vast majority of radionuclides used in nuclear medicine are artificially produced using either charged particle accelerators such as a cyclotron, nuclear reactors or radionuclide generators. Many isotopes for PET and SPECT imaging are generated with a cyclotron by bombarding a variety of nuclei with high-energy charged particles. A beam of charged particles (typically ^1H , ^2H , ^3H or ^4He) are accelerated by imposing a rapidly-varying electromagnetic (RF) field between electrodes placed in a static magnetic

field (Bushberg, 2002). This sends the particles introduced into an ion chamber in the cyclotron in a spiral trajectory which then irradiate a “target” starting material at energies on the order of millions of electron-volts (MeV) (Bushberg, 2002). This provides sufficient kinetic energy to penetrate and overcome the target nuclei’s repulsive forces permitting the nucleons within the target to interact and form new isotopes.

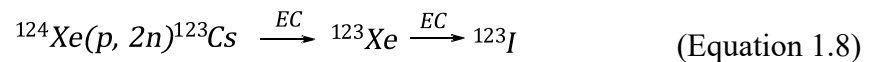
The following examples of [¹⁸F], [¹²³I] and [^{99m}Tc] radionuclide production are relevant to the current work described in this thesis.

For [¹⁸F] production, an enriched [¹⁸O]H₂O target is irradiated with ¹H protons at approximately 15-20 MeV and produces [¹⁸F]F⁻ per the following production reaction:



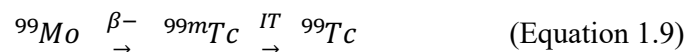
where ¹⁸O is the target material, p indicates a bombarding proton and 1 neutron, n, is emitted and [¹⁸F] is the product radionuclide (Bushberg, 2002).

For SPECT imaging, [¹²³I] is also produced via cyclotron using a ¹²⁴Xe target that proceeds via a 3-step reaction which generates a ¹²³Cs daughter radionuclide that subsequently decays via electron capture to generate ¹²³I following the production reaction:



where ¹²⁴Xe is the target material that is bombarded with a proton (p) emitting 2 neutrons, (2n) to produce ¹²³Cs (t_{1/2} = 1s) that subsequently undergoes electron capture (EC) decay to ¹²³Xe (t_{1/2} = 2hrs) and finally to [¹²³I] (Bushberg, 2002).

Technetium-99m ($[^{99m}\text{Tc}]$) is the most widely used radionuclide in nuclear medicine and is produced using a radionuclide “moly” generator, typically on site at most major hospitals. ^{99m}Tc -pertechnetate ($^{99m}\text{TcO}_4^-$) is formed using a molybdenum-99 (^{99}Mo) parent ($t_{1/2}=67\text{hrs}$), produced by nuclear fission of uranium-235 (^{235}U), which undergoes β^- decay to produce ^{99m}Tc (Equation 1.9). Ammonium molybdenate ($\text{NH}_4^+(\text{MoO}_4^-)$) is loaded into the generator on a column containing an alumina (Al_2O_3) resin. $\text{NH}_4^+(\text{MoO}_4^-)$ undergoes adsorption with the resin and the daughter isotope in the form of sodium pertechnetate $\text{Na}+(\text{MoO}_4^-)$ is eluted by running saline through the column (Bushberg, 2002).



A detailed outline of physical properties of these radionuclides are seen in Table 1.2.

1.6.2 Computed Tomography (CT)

Computed tomography (CT) is a transmission imaging technique that was first developed by Sir Godfrey Hounsfield in the early 1970’s based on principles of radiographic X-ray imaging, the seminal discovery of Wilhelm Roentgen that created the field of modern radiology. X-ray CT uses high energy X-ray beams to pulse highly collimated, homogenous X-ray photons through the body to a detector target (Bushberg, 2002). The differential X-ray attenuation properties of various tissues (e.g. bone, soft tissue and air) result in a heterogeneous distribution of X-rays that emerge from the subject, thus generating different grayscale intensities (contrast) at the level of the detector (Bushberg, 2002). Many X-ray projections are acquired at different angles while

the CT gantry is rotated around a subject. Tomographic image slices are generated from these projections through mathematical reconstruction methods (Bushberg, 2002).

CT provides high-contrast sensitivity for bone and soft tissue and is a clinical mainstay in neurology for brain imaging. CT is a complimentary imaging modality that provides anatomical reference to modalities such as PET and SPECT functional imaging.

1.6.3 Principles of Magnetic Resonance Imaging (MRI)

Based on the principles of nuclear magnetic resonance (NMR), magnetic resonance imaging (MRI) is a transmission imaging modality that relies on the response of tissues to a complex orchestration of applied magnetic fields (Bushberg, 2002). MRI exploits the magnetic properties of certain atomic nuclei, most often proton-rich hydrogen atoms (H^+), which are vastly abundant in biological tissues in the form of water and fat (McRobbie, 2004).

In the classical description of MRI, protons have both charge and spin, fundamental physical properties that produce a magnetic dipole, which in H^+ atoms create a net magnetic moment, owed to an odd number of protons. When placed in a large static magnetic field (B_0), spins that are otherwise randomly oriented, become aligned either parallel or anti-parallel to B_0 (McRobbie, 2004). A slight majority of spins (3 spins per million at 1.0T) align in parallel (a lower energy state), thus creating a net longitudinal magnetization in the direction of B_0 (z-axis) within a subject. In a magnetic field, spins precess at a characteristic resonance frequency, ω_0 , governed by the Larmour equation:

$$\omega_0 = \gamma B_0 \quad (\text{Equation 1.10})$$

where ω_0 is the precessional (Larmour) frequency, γ is the gyromagnetic ratio and B_0 is the external magnetic field strength (Bushberg, 2002). The introduction of a secondary perpendicular electromagnetic field (B_1), produced by an oscillating radiofrequency (RF) excitation pulse driven at the resonant frequency ω_0 , translates the proton net magnetization 90° into the transverse plane (x-y plane) at which point the phase of all protons are aligned, precess about the B_0 axis and subsequently undergo relaxation phenomenon as the absorbed electromagnetic energy is emitted. This induces a signal known as free induction decay (FID) which can be measured by a surrounding RF coil, specifically tuned to ω_0 (Bushberg, 2002). Superimposed magnetic field gradients (supplied by a gradient coil) permit spatial localization of this signal by imposing linear variations in field strength to B_0 and thus commensurate variation in resonant frequency ω_0 . These gradients can be applied in combination across orthogonal x,y and z planes to isolate and excite protons in a cross-sectional slice and to spatially encode the resulting signal in 3D space (Bushberg, 2002). MRI acquisitions are carried out using a pulse sequence, which is the precise orchestration of multiple RF pulses and magnetic field gradients to collect signal-averaged FID (time-domain) information that can be mathematically resolved and assigned to a location in space using what is known as a Fourier transformation (Bushberg, 2002). This is the basis of MRI image formation.

Differing MRI signal intensities are observed in various tissues, permitting delineation of the structural boundaries between tissue types (e.g. cerebral spinal fluid (CSF), grey and white matter, muscle, fat). Contrast in MRI is achieved based on the application of various pulse sequences that are weighted towards a particular signal relaxation mechanism (Bushberg, 2002). T_1 - and T_2 -weighed contrast are the most

common in MRI, corresponding to time constants of the longitudinal and transverse relaxations of spins, respectively. T_1 (spin-lattice relaxation) is a measure of the rate at which H^+ spins realign from the transverse magnetization state back to equilibrium (longitudinal magnetization) after RF excitation. T_1 is dependent on the interaction of H^+ and its dissipation of energy within its surrounding environment. *Spin Echo* or magnetization prepared gradient echo are typical T_1 -weighted pulse sequences, whose contrast can be manipulated by changing the repetition time (TR) of the RF pulse. In general, a T_1 sequence has short TR, short TE and water and CSF have long T_1 values (>2000 ms) and appear dark on T_1 -weighted images, while fat has a shorter T_1 value (260 ms), appearing bright (Bushberg, 2002; Grover et al., 2015).

T_2 (spin-spin relaxation) is a measure of the rate at which H^+ spins move out of phase with each other in the transverse plane. After a 90° RF excitation pulse, spins are in phase and precess at ω_0 . T_2 relaxation causes phase incoherence and spins de-phase at different rates as a result of local field inhomogeneities generated by the molecular interactions between H^+ atoms. In general, T_2 contrast is given by long TR and long TE. T_2 relaxation values are smaller than T_1 in structures of the brain (CSF>300, GM 64-71, WM 64-70) and water and CSF appear bright, while GM and WM appear darker.

Of particular relevance to the research conducted for this thesis, Balanced steady-state free precession (BSSFP) is another pulse sequence that provides high SNR images (Park et al., 2015). This method uses a combination of T_2/T_1 weighting.

This chapter outlined the very basics of MRI, however, there are a wealth of pulse sequences that generate various types of contrast. Other burgeoning applications of MRI

include functional MRI (fMRI), which measures the hemodynamic response to brain activity using blood oxygen level dependent (BOLD) contrast, magnetic resonance spectroscopy (MRS) and arterial spin labelling (ASL).

1.6.4 Strengths and Weaknesses of Neuroimaging Modalities

A summary of the strengths and weaknesses of the various brain imaging modalities are shown in Table 1.3.

Modality	Spatial Resolution	Temporal Resolution	Sensitivity	Safety Profile
	1-2mm (PC)			
PET	5-7mm (C)	seconds-minutes	$10^{-11} - 10^{-12}$ M	Ionizing radiation
	1-2mm (PC)			
SPECT	8-10mm (C)	minutes	$10^{-10} - 10^{-12}$ M	Ionizing radiation
	25-100 μ m (PC)			
MRI	~1mm (C)	minutes-hours	$10^{-3} - 10^{-5}$ M	No Ionizing radiation
	50-200 μ m (PC)			
CT	0.5-1mm (C)	minutes	ND	Ionizing radiation

Table 1.3 Medical imaging techniques and associated performance characteristics. PET, positron emission tomography; SPECT, single photon emission computed tomography; MRI, magnetic resonance imaging; C, clinical; PC, pre-clinical; ND, not determined. Table adapted from (Gambhir et al., 2012).

1.7 Analysis Techniques in Nuclear Medicine

This section reviews a variety of analytical approaches used for PET and SPECT image analysis, including basic quantification methods of static images, followed by dynamic PET (or SPECT) imaging and the pharmacokinetic analyses used in radiotracer development. Some of the more common compartmental modelling and graphical analysis techniques used to estimate the *in vivo* kinetic parameters of radioligands will be reviewed.

1.7.1 Quantitation of Static Images in PET and SPECT

The evaluation of PET or SPECT scans ranges from purely qualitative approaches to more advanced quantification metrics. For example, the application of validated visual rating scales (Mosconi et al., 2006) describing the distribution of established radiotracers such as [¹⁸F]FDG, remains the diagnostic mainstay in the clinical realm. Semi-quantitative and quantitative approaches including volume of interest (VOI) and voxel-wise analysis are most often used in research-based settings, requiring more computationally-involved analysis pipelines. PET and SPECT scans collect sequential radiotracer signal over time, which when corrected for scatter, attenuation and tracer decay, ultimately represent a radiotracer concentration such as activity per unit volume of tissue (e.g. kBq/mL). In general, quantification of absolute tracer concentrations is prone to several methodological challenges causing considerable inter- and intra-subject variability as well as variability between scanners. Various methods have been developed in an attempt to overcome such issues, including the standardized uptake value (SUV) (Boellaard, 2009; Thie, 2004). SUV (Equation 1.11), is a widely used semi-

quantitative measure that expresses tracer concentration at time t for a particular volume of interest ($C_{VOI}(t)$) normalized to the injected dose (ID) per body weight (BW):

$$SUV = \frac{C_{VOI}(t)}{ID/BW} \quad (\text{Equation 1.11})$$

where $C_{VOI}(t)$ is in K_{bq}/mL, ID is in (MBq) and BW is in (Kg). Other normalization factors have also been used to characterize the body volume in which a tracer is distributed, including total surface area, and lean body mass of the subject (Stahl et al., 2004). Inherent variability also exists with the SUV metric (Boellaard, 2009). To overcome this unwanted variability, an extension of the SUV method has been applied using a relative standardized uptake value (SUV_r). Radioligand uptake in a VOI is normalized to a reference region (SUV_{REF}) that, ideally, has a stable PET signal and is unaffected in the particular disease being studied. The SUV_r (Equation 1.12) is determined by the following:

$$SUV_r = \frac{SUV_{VOI}}{SUV_{REF}} \quad (\text{Equation 1.12})$$

Common SUV_{REF} regions of normalization in neuroimaging include the cerebellum, pons and whole brain. Careful selection of a suitable reference region is critical and is dependent on the targeted disease process and the tracer being evaluated. Use of a cerebellar reference region is ubiquitously applied in neuroimaging, often without cause or consideration of confounding neuroanatomical deficits that may be present including the phenomenon of crossed-cerebellar diaschisis (Tien & Ashdown, 1992). Over the last decade, a surge of research has been dedicated to computationally

deriving stable and reliable reference regions that minimize variation in large study cohorts (e.g. Rasmussen et al. (Rasmussen et al., 2012)). Nevertheless, SUV_r metrics have been successfully applied in a variety of applications. For example, in AD, SUV_r metrics have shown to be effective in establishing reliable cutoffs dichotomizing A β positivity/negativity using PiB and Florbetapir amyloid imaging agents (Landau et al., 2013). SUV_r methods have also been used regularly as A β imaging endpoints in AD clinical trials (Cash et al., 2014).

1.7.2 Dynamic Imaging Evaluation in PET and SPECT

Whereas a single static PET or SPECT image can inform one of the amount and spatial distribution of a radiotracer, dynamic PET imaging provides additional insight into the temporal association of a tracer molecule with its target, i.e. the *in vivo* kinetics of the radiotracer. The basis of dynamic PET or SPECT evaluation is the time-activity curve (TAC), which describes the concentration of radioactivity as a function of time in a given voxel or average voxel value within a volume of interest (VOI). TACs can be expressed in a variety of different ways, including absolute values of quantification (e.g. kBq/mL vs. time), as a percent of the injected dose per volume of tissue (e.g. %ID/mL vs. time) or as a scaled value relative to the peak concentration (C_{\max}) reached in a VOI (e.g. %C_{max} vs. time). In radiotracer development, %ID/mL over time is a common method to evaluate the *in vivo* behaviour of a particular radioligand (Van de Bittner et al., 2014).

1.7.3 PET Kinetic Modelling

A PET image, expressing the concentration of radiotracer over time, $C_{PET}(t)$, ultimately represents a composite of superimposed signal originating from different “states” of the tracer molecule (Equation 1.13),

$$C_{PET}(t) = \sum_{i=0}^n C_i(t) = C_a(t) + C_f(t) + C_s(t) + C_{ns}(t), \quad (\text{Equation 1.13})$$

which includes detected tracer contributions from arterial, $C_a(t)$, freely circulating, $C_f(t)$, specifically bound, $C_s(t)$, and non-specifically bound, $C_{ns}(t)$, tracer. The sum of these contributions add up to the net signal measured with PET. The accurate interpretation of PET data requires isolation of the appropriate component of interest within the overall PET image. To this end, various mathematical methods have been developed to analyze time sequences of PET images to estimate the appropriate pharmacokinetic properties of the radiotracer (Watabe et al., 2006; Wernick & Aarsvold, 2004).

Compartmental modelling is an established framework that remains the “gold standard” in estimating a radioligand’s pharmacokinetic parameters, offering insight into the overall state of a tracer within a physiological system over time. In this approach, a tracer within a physiological system is characterized by interacting subsystems which are represented as individual compartments. Each compartment reflects the concentration of a tracer over time and the change in radiotracer concentration in each compartment can be described as a linear function of the concentrations in the other compartments, which can be represented as a series of ordinary differential equations (Watabe et al., 2006) (see

section 1.7.3.2). The driving force of these interactions is the initial input of tracer present in the arterial blood after intravenous (IV) injection.

1.7.3.1 Arterial Input Function (AIF)

The arterial input function (AIF) is an essential component to characterize, as this is the direct input of radiotracer that is presented to the brain during a PET scan.

Accurate measurement of the input function is critical in order to precisely quantify the subsequent tissue response represented by the PET image. Measuring an AIF is an invasive and extremely challenging endeavour from a technical standpoint and often a significant barrier for full kinetic analysis. During a PET scan, simultaneous serial sampling and dosimetry of radioligand concentration over time is required to determine the concentration of radioactivity in the blood over the scan duration. In humans, this is typically done by cannulating and collecting blood from a radial artery every ~10 sec during the initial phase of tracer uptake. Further blood analytics are often performed to determine the fraction of radioligand in the plasma (vs. those associated with red blood cells) and metabolite correction of the AIF such that the curve represents authentic radioligand and not radiolabelled metabolites that may be circulating in the blood. Given the technically demanding nature of these pursuits, alternative approaches have been proposed including the use of image-derived AIFs (IDAIF), which leverages quantification of cardiovascular blood pools (ideally heart or a large artery, but often small vessels such as the carotid artery is used) that are in the PET image field of view (FOV). A variety of IDAIF methods have been validated, however few have been adopted for widespread use largely owed to partial volume artifacts due to the limited spatial resolution achieved by PET (Zanotti-Fregonara et al., 2011).

1.7.3.2 Generalized Three Tissue Compartment Model (3TCM)

Compartment models with differing levels of complexity have been employed to describe the various CNS radiotracers, the appropriateness depending on the chemical properties of the radiotracer and the biological properties of the target. The three tissue compartment model (3TCM) is a generalized model that describes the time-dependent exchange of tracer concentration between the *arterial blood* compartment $C_a(t)$, and three separate tissue compartments namely, the unbound *free compartment* $C_f(t)$, which exchanges with a *specific binding compartment* $C_s(t)$ (signal of interest) as well as the *non-specific binding compartment* $C_{ns}(t)$ (Figure 1.6). The net flux of tracer over time between each of these compartments can be described by the following differential equations (Equation 1.14a – Equation 1.14c).

$$\frac{dC_{ns}(t)}{dt} = k_5 C_f(t) - k_6 C_n(t) \quad (\text{Equation 1.14a})$$

$$\frac{dC_s(t)}{dt} = k_3 C_f(t) - k_4 C_s(t) \quad (\text{Equation 1.14b})$$

$$\frac{dC_f(t)}{dt} = K_1 C_a(t) + k_6 C_{ns}(t) + k_4 C_s(t) - (k_2 + k_3 + k_5) C_f(t) \quad (\text{Equation 1.14c})$$

The transfer coefficients (K_1, k_2-k_6) are the kinetic parameters of interest that establish the behaviour the radiotracer *in vivo*. For a given arterial input function $C_a(t)$ and tissue response functions ($C_f(t)$, $C_s(t)$ and $C_{ns}(t)$), these rate constants can be estimated. Compartment modelling requires certain assumptions, namely that the quantity of injected radiotracer has no pharmacological effect and causes no changes to physiology *in vivo*, that effects of the isotope does not alter the properties of the tracer

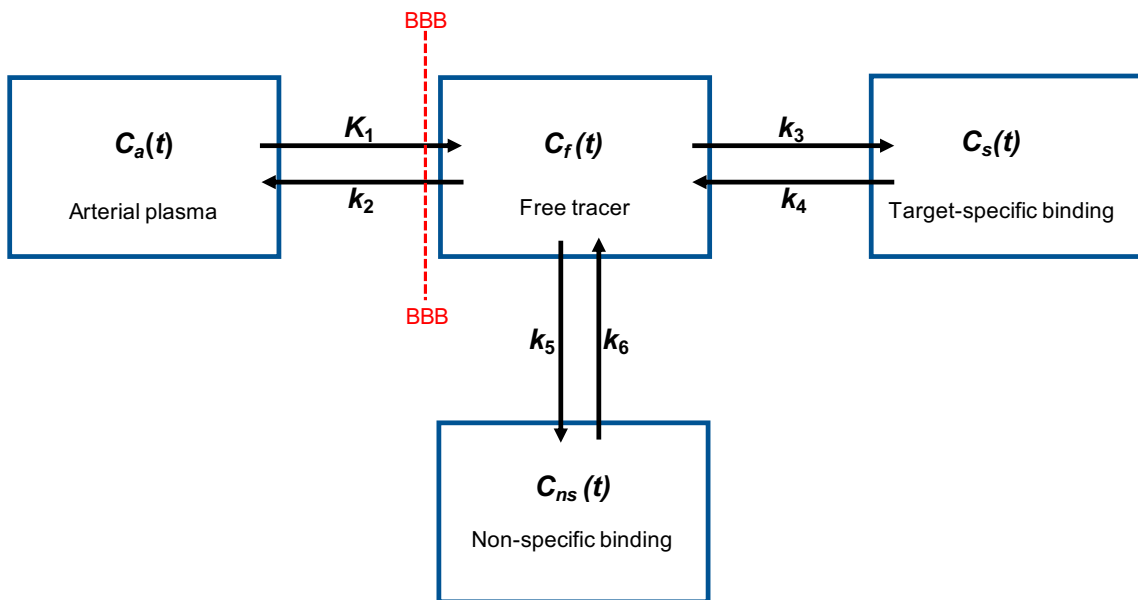


Figure 1.6 Generalized three-tissue compartment model (3TCM), reflecting transfer of radioligand concentration between four compartments, namely arterial plasma ($C_a(t)$), free tracer ($C_f(t)$), target-specific ($C_s(t)$) and non-specific ($C_{ns}(t)$) binding compartments of the brain. K_1 represents tracer perfusion transfer coefficient (rate of influx) ($\text{mL} \cdot \text{cm}^{-3} \cdot \text{min}^{-1}$) and $k_2 - k_6$ (min^{-1}) represent exchange rates of radioligand between respective compartments. BBB, blood-brain barrier.

and that the tracer is freely diffusible and in a steady state with target and can interact with the target wherever it is located. In the 3TCM, a favourable radioligand would have greater target-specific binding, thus larger $C_s(t)$ and smaller contributions from $C_{ns}(t)$ and $C_f(t)$ compartments. Greater $C_s(t)$ of a radiotracer is favoured when a larger proportion of k_3/k_4 is observed.

In practice, the fidelity of PET data generally limits the feasibility of accurately fitting a 6 parameter 3TCM model, owed to the statistical variability of the PET method. Most often, model simplifications are required to decrease the number of compartments (thus estimated parameters) and reduce the statistical variance in the data. One- and two-tissue compartment models (1TCM and 2TCM) (Watabe et al., 2006) are frequently used along with other reference tissue models (Lammertsma & Hume, 1996) and graphical analyses methods (Logan et al., 1990; Patlak et al., 1983). Selected methods, relevant to the current thesis research, are described below.

1.7.3.3 One Tissue Compartmental Model (1TCM)

The one tissue compartmental model (Figure 1.7), describes the bidirectional exchange of tracer between arterial blood and a single tissue compartment. Here, specifically and non-specifically bound as well as free tracer components are lumped together and cannot be distinguished kinetically. In this simplified model, the time-dependent tracer concentration in the tissue, $C_t(t)$, is given by the difference of the tracer flux entering the tissue from arterial blood $C_a(t)$, and the flux exiting the tissue. (Equation 1.15).

$$\frac{dC_t(t)}{dt} = K_1 C_a(t) - k_2 C_t(t) \quad (\text{Equation 1.15})$$

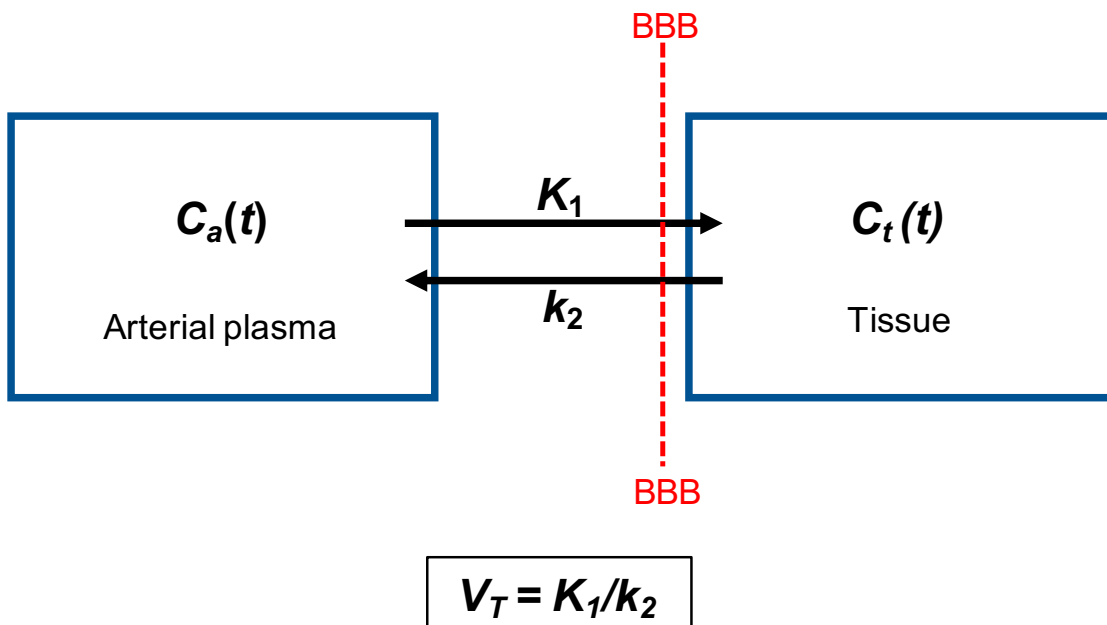


Figure 1.7 One tissue compartment model (1TCM), reflecting transfer of radioligand concentration between two compartments, namely arterial plasma ($C_a(t)$) and a tissue ($C_t(t)$) compartment. K_1 represents tracer perfusion transfer coefficient ($\text{mL}\cdot\text{cm}^{-3}\cdot\text{min}^{-1}$) and k_2 represents the exchange rate of radioligand from tissue compartment to arterial plasma. The volume of distribution, V_T , is given by the ratio K_1/k_2 . BBB, blood-brain barrier.

In equation 1.15, $C_t(t)$ is the tracer concentration in tissue, $C_a(t)$ is the tracer concentration in arterial blood, and K_1 (flux into tissue) and k_2 (efflux from tissue) are first-order transfer coefficients (rate constants) (Figure 1.7). K_1 , the rate constant for tracer transfer from arterial plasma, is expressed as mL of plasma per cm³ of tissue per min (mL•cm⁻³•min⁻¹), whereas k_2 is expressed as the fraction of mass transferred per unit time (min⁻¹).

The differential equation describing tissue tracer concentration, $C_t(t)$, and arterial input function, $C_a(t)$, in a 1TCM (Equation 1.15) can be solved giving:

$$C_t(t) = K_1 C_a(t) \otimes e^{-k_2 t} = K_1 \int_0^t C_a(\tau) e^{-k_2(\tau-t)} d\tau \quad (\text{Equation 1.16})$$

where K_1 and k_2 are the perfusion and efflux rate constants and \otimes indicates a one-dimensional time-domain convolution, derived from a Laplace transform solution of Equation 1.15 (Wiebusch et al., 1999). Non-linear least squares methods can be used to iteratively fit the resulting time-activity curve data and provide estimates of K_1 and k_2 and thus the derived volume of distribution, V_T (Equation 1.17):

$$V_T = K_1/k_2 \quad (\text{Equation 1.17})$$

In a 1TCM, a larger radioligand tissue concentration, $C_t(t)$, is favoured, governed by a larger volume of distribution, V_T , thus greater proportion of K_1/k_2 .

1.7.3.4 Simplified Reference Tissue Model (SRTM)

Reference tissue kinetic models have also been developed which obviate the need for invasive arterial blood sampling to directly measure the arterial input function. The simplified reference tissue model (SRTM) (Figure 1.8) is one such example that has been applied for neuroreceptor radioligands (Lammertsma & Hume, 1996). In this approach, a time-activity curve of tracer concentration in a reference region (devoid of receptors) serves as a proxy for the input function. The assumptions of the model are that all brain regions share a common input function, that the distribution volume is the same between tissues of interest (V_T) and the reference tissue ($V_{T'}$) (Equation 1.18) and that tissue time-activity curves (both reference and tissues of interest) can be characterized by a 1TCM model. In the latter assumption, the ratio of K_1/K_1' is expressed as a relative tracer delivery constant, R_1 (Equation 1.19), and the free and specific-binding compartments of a 2TCM are combined, giving rise to an apparent rate constant K_{2a} , describing the overall rate of transfer from specific binding compartment to arterial plasma.

$$V_T = V_{T'} ; \quad \frac{K_1}{k_2} = \frac{K_1'}{k_2'} \quad (\text{Equation 1.18})$$

$$R_1 = \frac{K_1}{K_1'} \quad (\text{Equation 1.19})$$

In addition, in the SRTM, the tracer binding potential, BP_{ND} (defined as k_3/k_4 in a 2TCM) is expressed as seen in (Equation 1.20).

$$BP_{ND} = \frac{k_2}{k_{2a}} - 1 \quad (\text{Equation 1.20})$$

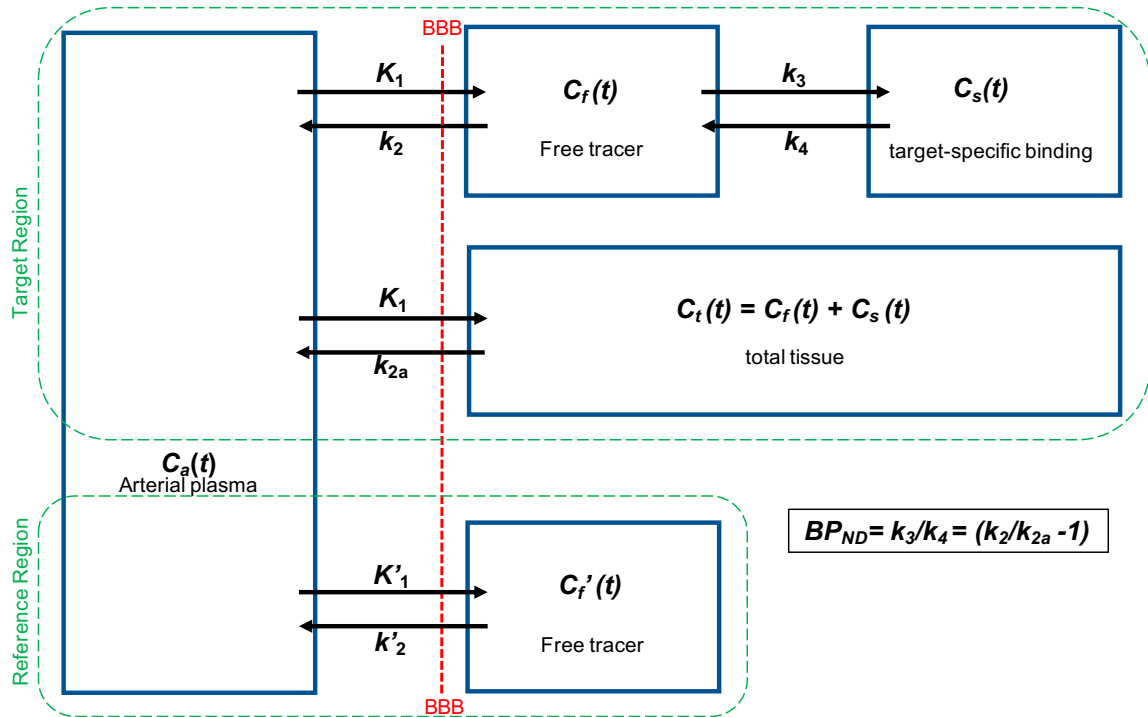


Figure 1.8 A simplified reference tissue model (SRTM) combines parameters of a two-tissue compartment model (2TCM) describing the transfer of radioligand concentration between arterial plasma ($C_a(t)$), free tracer ($C_f(t)$) and target-specific ($C_s(t)$) binding compartments, yielding a one-tissue compartment model (1TCM) with arterial plasma ($C_a(t)$) and total tissue ($C_t(t)$) compartments. A suitable reference region is selected to represent the tracer input function, also described by a 1TCM with ($C_a(t)$) and free tracer ($C_f'(t)$) compartments. K_1 and K_1' represent tracer perfusion transfer coefficient ($\text{mL} \cdot \text{cm}^{-3} \cdot \text{min}^{-1}$) in the target and reference region, respectively, while R_1 is the relative tracer delivery constant, $k_2 - k_4$ (min^{-1}) represent exchange rates of radioligand between respective 2TCM compartments, k_{2a} represents the apparent rate constant in the SRTM and k_2' the rate constant for the reference region. The binding potential BP_{ND} is expressed as $k_3/k_4 = (k_2/k_{2a} - 1)$. BBB, blood-brain barrier.

With these model simplifications, the SRTM can be described by the following differential equation (Equation 1.21),

$$\frac{dC_t(t)}{dt} = K_1 C_p(t) - k_{2a} C_t(t) \quad (\text{Equation 1.21})$$

where $C_t(t)$, is the concentration of tracer in the total tissue compartment, $C_p(t)$ is the concentration of tissue in arterial plasma, K_1 is the perfusion rate constant and k_{2a} is the apparent rate constant of overall transfer from tissue to arterial plasma.

From this, the following operational equation can be derived for a SRTM (Equation 1.22):

$$C_t(t) = R_1 C'_t(t) + \left[k_2 - \frac{R_1 k_2}{1 + BP_{ND}} \right] C'_t(t) \otimes e^{-\frac{k_2 t}{1 + BP_{ND}}} \quad (\text{Equation 1.22})$$

The result of this provides three estimated parameters, namely R_1 , k_2 and BP_{ND} and derived parameters k_2 and k_{2a} . Above is a summary of the full theoretical treatment of the model by Lammertsma et al. (Lammertsma & Hume, 1996). In the SRTM, a larger radioligand total tissue concentration, $C_t(t)$, is favoured, governed by a larger binding potential, BP_{ND} , thus greater proportion of k_3/k_4 , which is expressed as $(k_2/k_{2a} - 1)$ in the model.

1.7.3.5 Logan Graphical Analysis

Graphical analysis techniques have also been developed to simplify kinetic parameter estimates, removing the need for computationally demanding iterative fitting methods or *a priori* assumptions of a particular compartment model that a given tracer adheres to. Patlak (Patlak et al., 1983) and Logan (Logan et al., 1990) plots are common examples that have been implemented in the evaluation of irreversible and reversible

tracer binding, respectively. With the Logan analysis technique (Figure 1.9), a mathematical transformation is applied to a measured time-activity curve that expresses tissue concentration as a function of time $C_t(\tau)$ (Logan et al., 1990). The tissue activity integrated from the time of tracer injection is divided by the instantaneous tissue concentration $C_t(t)$ and is then plotted as a function of “normalized” time, expressed as the integral of the input curve $C_a(\tau)$ divided by the instantaneous tissue concentration (Equation 1.23). For reversibly binding tracers, this results in a linear relationship after equilibration time t^* (Figure 1.9).

$$\frac{\int_0^t C_t(\tau) d\tau}{C_t(t)} = m \frac{\int_0^t C_a(\tau) d\tau}{C_t(t)} + b \quad (\text{Equation 1.23})$$

The slope of this straight line, m , provides an estimate of the distribution volume V_T (Equation 1.24) analogous to what is estimated in a 1TCM.

$$\text{slope} = m \cong V_T = \frac{K_1}{k_2} \quad (\text{Equation 1.24})$$

Here K_1 is perfusion rate constant and k_2 the rate constant from tissue to arterial plasma in a 1TCM. As in a 1TCM, a radioligand with a larger volume of distribution, V_T , is favoured.

The preceding sections on the theory behind PET kinetic modeling tie into the PET imaging study carried out in Chapter 4.

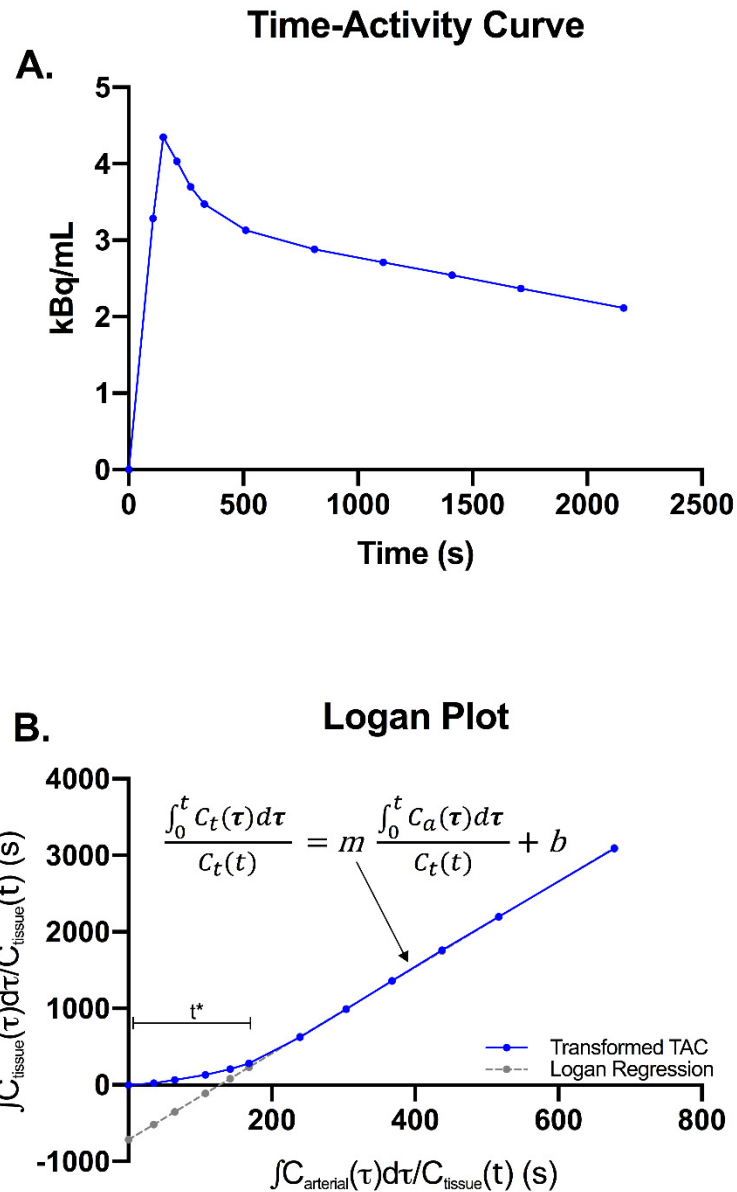


Figure 1.9 Logan graphical analysis technique applied to **A.** a time-activity curve (TAC) depicting radiotracer concentration in a volume of interest over time (blue). **B.** A TAC is mathematically transformed (in blue), integrated from the time of tracer injection and divided by the instantaneous tissue concentration $C_t(t)$ and is then plotted as a function of “normalized” time, expressed as the integral of the input curve $C_a(\tau)$ divided by the instantaneous tissue concentration. The slope, m , of this curve (grey) is linear for reversibly binding radiotracer after equilibration time t^* and is an estimate of the non-displaceable binding potential (BP_{ND}).

1.8 Central Nervous System (CNS) Radiotracer Development

Nuclear medicine (PET or SPECT) imaging has become an essential tool for visualizing neurochemical processes in the living human brain, achieving high molecular sensitivity and target specificity. Despite the plethora of protein targets available to evaluate in the central nervous system (CNS), only a small fraction of these can be effectively imaged at present. A total of 39 CNS radioligands have been successfully advanced for use in humans (National Institute of Mental Health, April, 2019), targeting various aggregate proteins (e.g. A β plaques, tau NFTs), neuroreceptors (e.g. nicotinic, mGlu r 1), enzymes (e.g. acetylcholinesterase (AChE), monoamine oxidase -A/B (MAO-A/B)), channels (e.g. translocator protein (TSPO)), and transporters (e.g. dopamine transporter (DAT)). Regardless of the type of radioligand, these tracers must satisfy a variety of stringent design criteria to be a successful molecular imaging agent. This section reviews some of these essential design criteria, the favourable physicochemical properties and the general classification of receptor- and hydrolytic enzyme-based radiotracers as well as the corresponding *in vitro* kinetic properties that make up a prospective radioligand's product profile. This ties in with the preceding Section 1.7, Analysis Techniques in Nuclear Medicine which outlines the *in vivo* kinetic profile typically assessed using various PET and SPECT image analysis techniques.

1.8.1 Radioligand Design Criteria

In general, an effective CNS radioligand must achieve a number of rather challenging tasks in order to generate a meaningful molecular image (Figure 1.10). A radiotracer (the parent) when introduced into the bloodstream, must readily penetrate the blood-brain barrier (BBB) and reach a specific target in the brain while remaining intact,

Design Criteria of Putative PET or SPECT Radioligands

- Effective blood-brain barrier (BBB) penetrance
- High affinity and selectivity for target
- Low non-specific/off-target binding
- Lack of interfering radiometabolite production
- Pharmacokinetics (uptake/clearance) suitable for a given $t_{1/2}$
- Not cleared by efflux transporters
- No toxicity

Figure 1.10 Positron Emission Tomography (PET) and Single Photon Emission Computed Tomography (SPECT) radioligand design criteria.

with negligible production or interference from radiometabolite species (Pike, 2009; Van de Bittner et al., 2014). The tracer should have high affinity for the target *in vivo* and be highly selective for that target, demonstrating a high ratio of specific binding to non-specific or off-target binding and thus good clearance properties to minimize noise contributions from background (Pike, 2009; Van de Bittner et al., 2014). If successful, a radioligand ultimately generates a resultant PET or SPECT scan that conveys image contrast specific to the molecular target of interest.

1.8.2 Physicochemical Profile

Certain fundamental physicochemical properties of molecules have been shown to govern optimal attributes that provide successful CNS penetration. Evaluation of such drugs has led to the development of a prospective multiparameter optimization (MPO) approach in drug discovery to help predict the desirability performance of a given molecule (Wager et al., 2010, 2016). An MPO score based on six evenly weighted parameters has been implemented, which include a) lipophilicity index calculated via partition coefficient (ClogP), b) calculated distribution coefficient at pH 7.4 (ClogD), c) molecular weight (MW), d) topological polar surface area (TPSA), e) number of hydrogen bond donors (HBD) and f) most basic center (pK_a). Each of these parameters are given a continuous score between 0-1 and collectively summed to provide a total MPO desirability score between 0-6. An MPO score ≥ 3.0 predicts a high likelihood of a molecule crossing the blood-brain barrier (BBB) with favourable pharmacokinetic permeability (Wager et al., 2010, 2016). A summary of MPO parameters is seen in Table 1.4.

physicochemical property	desirability function, T_0	more desirable Range ($T_0 = 1$)	less desirable range ($T_0 = 0$)
MW	monotonic decreasing	≤ 360	> 500
ClogP	monotonic decreasing	≤ 3	> 5
ClogD	monotonic decreasing	≤ 2	> 4
TPSA	hump function	$40 < \text{TPSA} \leq 90$	$\text{TPSA} \leq 20$; $\text{TPSA} > 120$
HBD	monotonic decreasing	≤ 0.5	> 3.5
pK _a	monotonic decreasing	≤ 8	> 10

Table 1.4 Multiparameter optimization (MPO) properties of CNS drugs. 6 evenly weighted physicochemical properties are assigned desirability functions (T_0) that are scored between 0-1. Those parameters in the most desirable range, receive a score of 1 and in the less desirable range receive a score of 0. Those that lie between are scored according to their respective T_0 function. The composite score of all six parameters makes up the MPO score. In general, a molecule with $\text{MPO} \geq 3$ has a high probability of possessing favourable drug-like pharmacokinetic properties. MW, molecular weight; TPSA, topological polar surface area; pK_a, most basic center; clogP, calculated partition coefficient; clogD, calculated distribution coefficient at pH 7.4. Table adapted from (Wager et al., 2010).

In practical terms, in order to cross the BBB, a radioligand needs to have a relatively small MW (< 400 Da) and the molecule should be moderately lipophilic to improve permeability of the BBB lipid bilayer (Davis & American College of Neuropsychopharmacology., 2002). However, a trade-off exists regarding lipophilicity, as once in brain, a tracer needs to have relatively low lipophilicity (to avoid unwanted plasma protein binding) yet high affinity in order achieve high specific binding to non-specific binding (Davis & American College of Neuropsychopharmacology., 2002; Pike, 2009, 2016).

1.8.3 Radioligand Classification

Radioligands can be classified in distinct categories based on their particular target and consequently, their corresponding mechanism of action and kinetics. Here we focus attention on radioligands that act through passive transport, which comprise the majority of current radiotracers, as opposed to actively transported endogenous analogues such as [¹⁸F]FDG. Reversibly binding receptor-based radioligands (Innis et al., 2007; Pike, 2016) are the most common tracers in use today and their kinetic evaluation is largely generalizable to other classes of radioligands. Of particular relevance to the current work, however, are radioligands that target hydrolytic enzymes of which three general classes exist, including substrate-based radioligands, reversible inhibitors and irreversible inhibitors (Rempel et al., 2017).

1.8.3.1 Receptor Radioligands

Reversibly-binding receptor radioligands (Innis et al., 2007) follow the *in vitro* equilibrium binding reaction (Equation 1.25):



R = receptor

F = free ligand

B = bound receptor-ligand complex

k_{on} = association rate constant

k_{off} = dissociation rate constant

From this reaction equation, one can determine a radioligand's binding potential (BP), the ratio of bound (B) to free (F) radioligand, defined by the receptor density (more generally, target protein concentration), B_{max} , and ligand binding affinity (defined as the inverse of the radioligand equilibrium dissociation constant, K_D (Equation 1.26):

$$BP = \frac{B}{F} = B_{max} \cdot \text{affinity} = \frac{B_{max}}{K_D} \quad (\text{Equation 1.26})$$

Here, the radioligand equilibrium dissociation constant, K_D is the ratio of dissociation rate constant (k_{off}) to association rate constant (k_{on}) (Equation 1.27):

$$K_D = \frac{k_{off}}{k_{on}} \quad (\text{Equation 1.27})$$

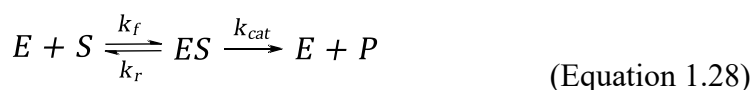
In general, greater BP makes for a more efficient tracer and is directly proportional to the target concentration and the affinity of the ligand for the target (Pike, 2016). A summary of radioligand *in vitro* kinetic parameters is seen in Table 1.5.

1.8.3.2 Hydrolytic Enzyme Radioligands: Substrate, Reversible and Irreversible Inhibitors

Hydrolase enzymes are a family of enzymes that break down a variety of biological molecules and are important in the proper functioning of the body and in various disease states. Three general classes of enzyme radioligands exist, including substrate-based radioligands, reversible inhibitors and irreversible inhibitors.

Substrate Radioligands: Substrate-based radioligands act as a substrate for enzymatic action and subsequently become fragmented into two, with one of the radiolabel-retaining products becoming trapped in nearby cells or tissues. The accumulation of radiotracer signal from substrate radioligands correlates with areas of high enzymatic activity (as opposed to reflecting total enzyme concentration) (Rempel et al., 2017). Substrate radioligands have the distinct advantage of signal amplification, whereby catalytically active enzymes can turn over multiple radioligand molecules generating large radioactive signal accumulation in regions of high enzyme activity. In designing a substrate-based radioligand, the proper selection of the labelled hydrolytic product and the selectivity of the tracer for the target enzyme are among the more challenging features to overcome as related enzymes could also interact with the substrate.

Hydrolytic enzyme substrates follow Michaelis-Menten kinetics (Rempel et al., 2017), where a given substrate rapidly binds to an enzyme and is irreversibly transformed to product in a one-step reaction (Equation 1.28):



E = free enzyme

S = free substrate

ES = enzyme-substrate complex

P = product

k_{cat} = rate of first committed chemical step

k_f = forward reaction rate

k_r = reverse reaction rate

The reaction rate or velocity (V) of this process is described by the following equation (Equation 1.29):

$$V = \frac{V_{max} [S]}{K_m + [S]} \quad (\text{Equation 1.29})$$

V = velocity of reaction

$[S]$ = concentration of substrate (tracer)

V_{max} = maximal rate of reaction

K_m = affinity of substrate to form enzyme-substrate complex (ES), defined by the substrate concentration needed to reach $\frac{1}{2} V_{max}$

The rate of first committed chemical step, k_{cat} , is defined as the ratio of V_{max} to the total enzyme concentration:

$$k_{cat} = \frac{V_{max}}{[E_{total}]} \quad (\text{Equation 1.30})$$

V_{max} = maximal rate of reaction

$[E_{total}]$ = total concentration of enzyme

K_m can be described by the following equation (Equation 1.31):

$$K_m = (k_{cat} + K_D) \quad (\text{Equation 1.31})$$

where K_D is defined as the ratio of k_{off}/k_{on} . The enzymatic efficiency of hydrolysing a substrate is a metric that is defined by the ratio of k_{cat} to K_m (Equation 1.32):

$$\text{Enzymatic Efficiency} = \frac{k_{cat}}{K_m} \quad (\text{Equation 1.32})$$

The key kinetic parameters for substrate-based radioligands are V_{max} , K_m and enzymatic efficiency (k_{cat}/K_m). At low K_m , the enzyme has high affinity for the substrate (tracer) thus even at low substrate concentrations, enough levels of hydrolysis will occur. At high K_m , the enzyme requires a high concentration of tracer to reach high levels of substrate turnover. Ideally, a substrate-based ligand would have higher k_{cat} values (efficient enzyme processing of substrate) and lower K_m (low concentration of substrate needed for efficient processing). The enzymatic efficiency metric reflects both of these parameters, representing a second order rate constant describing the reaction of free enzyme and free product and accounts for the binding affinity of the substrate and catalytic efficiency of the enzyme for the substrate (Rempel et al., 2017). High enzymatic efficiency values indicate that a substrate will be efficiently processed by the enzyme at physiological concentrations and tracer levels of radioligand, taking account of substrate binding and turnover rates.

Reversible Inhibitors: Reversible inhibitors act by forming non-covalent bonds with the target enzyme with very high affinity, causing large accumulation of tracer in regions of

elevated enzyme concentration and relatively low signal in background areas with little enzyme. Unlike substrate radioligands, reversible inhibitors directly reflect enzyme expression in a 1:1 manner, regardless of whether enzymatic activity is present (Rempel et al., 2017). Generally speaking, reversible inhibitors can proceed via competitive, non-competitive or mixed inhibition. Most radioligands are competitive inhibitors and an increase in apparent K_m is observed in these tracers, to compete with substrate. Non-competitive inhibition comes at the expense of decreased efficiency of substrate processing (decrease in apparent k_{cat}), while mixed inhibition is attendant with changes in both K_m and k_{cat} .

In competitive inhibition, a radioligand binds to the enzyme's active site and blocks further substrate binding and catalysis. The most common kinetic parameters for reversible inhibitors are $K_{i\ reversible}$ and IC_{50} metrics. $K_{i\ reversible}$ represents the inhibition equilibrium constant, a metric of inhibitor binding determined by ratio of enzyme-inhibitor dissociation (k_{off}) to association (k_{on}) (Equation 1.33):

$$K_{i\ reversible} = \frac{k_{off}}{k_{on}} \quad (\text{Equation 1.33})$$

IC_{50} is a relatively easy way to measure relative inhibitor potency and is defined as the substrate concentration at which enzyme activity is reduced by 50%.

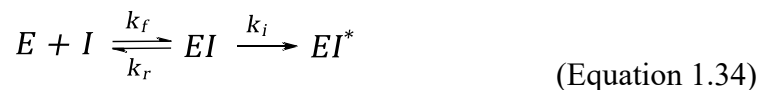
In general, low $K_{i\ reversible}$ (and IC_{50}) values are favourable for reversibly inhibiting radioligands, deriving their potency by reducing k_{off} , given that k_{on} is limited by rate of diffusion ($\sim 10^8\ \text{M}^{-1}\text{s}^{-1}$). However, a lower limit of $K_{i\ reversible}$ exists for reversible inhibitors ($\sim 10\text{nM}$), at which point anything lower are considered tight-binding

inhibitors (they don't rapidly equilibrate with target enzyme and thus behave more like irreversible inhibitors).

Irreversible Inhibitors: Irreversible inhibitors are analogous to substrate radioligands; however once they interface with the enzyme, an intermediate is generated that covalently attaches to the active site of the enzyme (typically a nucleophilic amino acid residue). This causes inhibition of the enzyme either by blocking its active site or because a catalytic residue of the enzyme ceases to function as required (Rempel et al., 2017). Irreversible inhibitors reflect enzymatic inactivation; however, given the irreversible nature of inhibition, where a stable tracer-enzyme intermediate is formed, a 1:1 tracer to enzyme ratio is displayed and signal amplification (as seen with substrate-based radioligands) is not possible (Rempel et al., 2017).

Enzymatic activity is reduced by irreversible inhibitors by formation of stable covalent bonds between inhibitor and enzyme. Covalent modification of an essential catalytic residue or physical blockage of an active site can cause irreversible inhibition.

Irreversible inhibitors follow the kinetic scheme (Equation 1.34):



E = free enzyme

I = inhibitor

EI = enzyme-inhibitor complex

EI^* = inactivated form of enzyme

k_i = reaction rate constant generating EI^*

k_f = forward reaction rate

k_r = reverse reaction rate

A reaction rate, analogous to that of a substrate-based ligand is described by the following equation (Equation 1.35):

$$V = \frac{V_{max} [I]}{k_i + [I]} \quad (\text{Equation 1.35})$$

where k_i (analogous to k_{cat} for substrates), is the reaction rate constant generating EI^* , the inactivated form of the enzyme and is similarly described by (equation 1.36):

$$k_i = \frac{V_{max}}{[E_{total}]} \quad (\text{Equation 1.36})$$

Here, V_{max} is the maximum enzymatic rate and $[E_{total}]$ is the total concentration of enzyme. $K_{i\text{ irreversible}}$ is a parameter analogous to K_m for a substrate-based radioligand and is defined as the concentration at which inactivation of the enzyme proceeds at $\frac{1}{2} V_{max}$. In general, irreversible inhibitors have high k_i values (indicating rapid formation of inhibitor-enzyme complex) and low $K_{i\text{ irreversible}}$ values (reflecting low concentration of inhibitor required for efficient processing) (Rempel et al., 2017).

A summary of all *in vitro* kinetic parameters reviewed in the current section among each class of radioligands is seen in Table 1.5.

Kinetic Parameter	Units	Definition	Class of radiotracer	Favourable
B_{max}	(pM•mg ⁻¹)	protein target density	receptors, enzymes	↑
BP	-	binding potential BP = B_{max}/K_D	receptors, enzymes	↑
k_{on}	(min ⁻¹)	association rate constant: Substrate binding rate to active site of enzyme	receptors, enzymes	↑
k_{off}	(nM L ⁻¹ min ⁻¹)	dissociation rate constant	receptors, enzymes	↓
K_D	(nM•L ⁻¹)	equilibrium dissociation constant $K_D = k_{off}/k_{on}$	receptors, enzymes	↓
V_{max}	(M•min ⁻¹)	maximum enzymatic reaction rate	enzymes	↑
K_m	(M)	Michaelis constant: [Substrate] required to reach 1/2 V_{max} $K_m = (k_{cat} + K_D)$	enzymes:substrate	↓
k_{cat}	(min ⁻¹)	rate of 1 st chemical step $k_{cat} = V_{max}/[Enzyme]_{total}$	Enzymes:substrate	↑
EE	(M ⁻¹ •min ⁻¹)	enzymatic efficiency EE = k_{cat}/K_m	Enzymes:substrate	↑
K_i reversible	(M)	inhibition equilibrium constant $K_i = k_{off}/k_{on}$	Enzymes:inhibitors	↓
K_i irreversible	(M)	[Inhibitor] required to reach 1/2 V_{max}	Enzymes:inhibitors	↓
k_i	(min ⁻¹)	Rate constant of reaction generating inactive form of enzyme EI* (analogous to k_{cat} for substrate)	Enzymes:inhibitors	↑
IC ₅₀	(M)	[Substrate] at which enzyme activity reduced by 50%	Enzymes:inhibitors	↓

Table 1.5 Summary of *in vitro* radioligand kinetic parameters. Adapted from (Innis et al., 2007; Pike, 2009; Rempel et al., 2017; Van de Bittner et al., 2014).

1.9 Thesis Objective & Hypothesis

The Darvesh group has developed several lead candidate ^{18}F and ^{123}I radioligands that target the BChE enzyme for PET and SPECT imaging, respectively. These radioligands possess favourable physicochemical and *in vitro* enzyme kinetics attributes which may be well suited to effectively target and label BChE for brain imaging of the enzyme. However, until now, the *in vivo* performance of these radioligands using PET and SPECT imaging has not yet been evaluated.

The objective of this PhD thesis was to develop and implement a multimodal neuroimaging analysis framework for the *in vivo* evaluation of these lead candidate radioligands. In order to accomplish this, PET or SPECT imaging, with additional CT and MRI anatomical imaging was carried out in established mouse models of AD. Evaluation of the biodistribution and retention characteristics of these radiotracers offered the first direct *in vivo* assessment of these attributes which feed forward to the product profile of each radioligand. Ultimately, this rigorous preclinical evaluation of candidate radioligands provides an essential step towards reaching exploratory investigational new drug (IND) status for imaging of BChE in the human brain.

We hypothesized that [^{18}F] and [^{123}I] radioligands that are substrates for BChE can be effectively utilized to visualize brain BChE *in vivo*. Upon IV injection into the bloodstream, these BChE-specific radioligands would cross the BBB, reach the brain and exhibit patterns of regional retention that recapitulate the known distribution of BChE in the AD brain, effectively distinguishing an AD brain from that of control groups that lack appreciable BChE expression.

1.10 Chapter Overviews

The following chapters outline work dedicated to addressing the aforementioned objective of this thesis, in the *in vivo* evaluation of candidate BChE radioligands.

Chapter 2 describes the synthesis and preliminary evaluation of lead SPECT radiotracer candidate *N*-Methylpiperidin-4-yl 4- ^{123}I iodobenzoate (TRV6001) which was carried out to determine its *in vivo* biodistribution and to evaluate patterns of regional brain retention in the 5XFAD mouse model of AD and wild-type (WT) controls.

Building on this work, Chapter 3 focused on the development and implementation of a 2D dynamic planar scintigraphy imaging approach, offering improved temporal resolution for the *in vivo* screening of putative BChE radioligands for SPECT imaging. Six ^{123}I radioligands among three classes of radiotracers (pyridone, pyridine and carbamate ligands) were evaluated to establish their biodistribution, and tracer clearance kinetics in relevant mouse models that exhibit differential expression of brain BChE. Kinetic summary measures for each radioligand were compared between the mouse models evaluated. Additional comparisons were made between the radioligands studied to elucidate potential differences in clearance characteristics among the different classes of radiotracers evaluated.

In Chapter 4, a previously developed cholinesterase radioligand 1-methyl-4-piperidinyl- *p* ^{18}F fluorobenzoate (TRV6501), demonstrating high affinity as a BChE substrate, was evaluated with *in vivo* PET imaging. Pharmacokinetic modeling approaches were employed to evaluate TRV6501 retention in 5XFAD and WT/BChE-KO mice, models exhibiting brain BChE abundance and absence, respectively. A single tissue compartment model (1TCM), simplified reference tissue model (SRTM) and

Logan graphical analysis techniques were applied to evaluate TRV6501 retention. Chapters 5 and 6 focused on the further neuroimaging characterization of the mouse models regularly used in the current AD diagnostics program. Chapter 5 describes the exploratory use of ^{99m}Tc -Examatazime SPECT to establish baseline brain perfusion patterns in 5XFAD and WT mouse models to determine whether the hypoperfusion signatures of human AD are maintained in the 5XFAD model. Characterizing brain perfusion in these models is essential in order to establish the effects of disease progression on physiological parameters such as cerebral blood flow (CBF). CBF is directly relevant parameter to monitor in the delivery of radiotracer to the brain, hence an important aspect to reconcile in our BChE radioligand diagnostics development program.

Chapter 6 describes the evaluation of brain function in a BChE knockout mouse model of AD (5XFAD/BChE-KO) using [^{18}F]FDG PET imaging. The study sought to determine whether a BChE-induced reduction of fibrillar $\text{A}\beta$ seen in these knockout mice, conferred an improvement in brain function compared to BChE-expressing 5XFAD mice. Determining the precise interplay between BChE, fibrillar $\text{A}\beta$ and brain function in AD will help aid in the understanding of the pathogenesis of AD and the role of these established AD biomarkers.

Chapter 7 consolidates the overall findings and conclusions drawn from each of the preceding thesis chapters and offers insight into the current state and future of BChE brain imaging, outlining the future directions and hurdles to overcome on the road to clinical translation. The significance of the current body of work and more broadly the significance of BChE imaging in AD will be discussed.

Chapter 2 Preliminary *In Vivo* Neuroimaging Evaluation of Lead Candidate Radioligand *N*-Methylpiperidin-4-yl 4-[¹²³I]iodobenzoate: A Butyrylcholinesterase (BChE)-Specific Radiotracer for Alzheimer's Disease (AD)

2.1 Publication Status

Published manuscript presented with permission.

DeBay DR, Reid GA, Pottie IR, Martin E, Bowen CV, Darvesh S. *Targeting butyrylcholinesterase for preclinical single photon emission computed tomography (SPECT) imaging of Alzheimer's disease.* *Alzheimer's Dement* (N Y). 2017 Feb 24; 3(2):166-177. DOI: 10.1016/j.trci.2017.01.005. PMID:29067326 (DeBay, Reid, Pottie, et al., 2017).

2.2 Overview

The current chapter describes the preliminary *in vivo* evaluation of lead candidate radioligand *N*-Methylpiperidin-4-yl 4-[¹²³I]iodobenzoate (TRV6001). The imaging of TRV6001 represents the first images acquired on a dedicated pre-clinical scanner and some of the first *in vivo* images acquired on a SPARK SRT-50TM SPECT scanner (Cubresa Inc., Winnipeg, MB). This research was published as a feature article in *Alzheimer's & Dementia: Translational Research and Clinical Interventions* (DeBay, Reid, Pottie, et al., 2017) and appears in this chapter in its original published form.

2.3 Abstract

Diagnosis of Alzheimer's disease (AD) *in vivo*, by molecular imaging of amyloid or tau, is constrained because similar changes can be found in brains of cognitively normal individuals. Butyrylcholinesterase (BChE), which becomes associated with these structures in AD, could elevate the accuracy of AD diagnosis by focusing on BChE pathology in the cerebral cortex, a region of scant BChE activity in healthy brain.

Methods: *N*-Methylpiperidin-4-yl 4-¹²³I]iodobenzoate, a BChE radiotracer, was injected intravenously into B6SJL-Tg(APP^{Sw}FLon,PSEN1*^{M146L}*^{L286V})6799Vas/Mmjax (5XFAD) mice and their wild-type (WT) counterparts for comparative single photon emission computed tomography (SPECT) studies. SPECT, computed tomography (CT) and magnetic resonance imaging (MRI) enabled comparison of whole brain and regional retention of the BChE radiotracer in both mouse strains.

Results: Retention of the BChE radiotracer was consistently higher in the 5XFAD mouse than in WT and differences were particularly evident in the cerebral cortex.

Discussion: Cerebral cortical BChE imaging with SPECT can distinguish 5XFAD mouse model from the WT counterpart.

2.4 Introduction

Alzheimer's disease (AD) is a common cause of dementia (Scheltens et al., 2016). Presently, AD diagnosis is definitively confirmed at autopsy by detecting cerebral pathology including β -amyloid (A β) plaques and tau neurofibrillary tangles (NFTs) (Hyman & Trojanowski, 1997). To improve clinical diagnosis, Positron Emission

Tomography (PET) molecular imaging has been used to visualize A β and NFT in living brain (Bloudek et al., 2011; McKhann et al., 2011). These agents represent a leap forward in detecting the presence of A β and tau pathology (Johnson, Minoshima, Bohnen, Donohoe, Foster, Herscovitch, Karlawish, Rowe, Carrillo, Hartley, Hedrick, Pappas, & Thies, 2013). However, the presence of A β in cognitively normal individuals (10% at 50 years to 44% at 90 years) and NFTs in non-AD tauopathies limits the predictive value of these methods for AD diagnosis (Johnson, Minoshima, Bohnen, Donohoe, Foster, Herscovitch, Karlawish, Rowe, Carrillo, Hartley, Hedrick, Pappas, & Thies, 2013; Noble & Scarmeas, 2009). Although cognitively normal individuals with PET amyloid positivity may represent pre-clinical stages of AD, conversion to AD has not yet been shown (Dubois et al., 2016; Grimmer et al., 2016). Therefore, the need is great for biomarkers to enhance existing armamentarium for AD diagnosis.

Neuronal loss, particularly cholinergic, contributes to cognitive and behavioural symptoms of AD (Bartus et al., 1982; Coyle et al., 1983; Davies & Maloney, 1976). With this, there is decrease in levels of acetylcholinesterase (AChE) and an increase in the levels of the related enzyme butyrylcholinesterase (BChE), that accumulate in plaques and tangles in the brain (Mesulam & Geula, 1994). This accumulation of BChE in plaques and tangles enables differentiation of AD from old age (Mesulam & Geula, 1994). The observation that there is scant BChE detected histochemically in the normal cerebral cortex, but accumulates there in association with AD pathology, suggests an opportunity to detect this pathology during life by imaging BChE (Darvesh, 2016).

Pioneering work in cholinesterase imaging provided PET probes targeting AChE (Irie et al., 1996; Kuhl et al., 2006; Namba et al., 2002; Ota et al., 2004; Pappata et

al., 1996; Snyder et al., 1998) and BChE (Kikuchi et al., 2004; Kuhl et al., 2006; Snyder et al., 2001). For example, *N*-[¹¹C] methylpiperidin-4-yl acetate ([¹¹C]MP4A) could monitor AChE activity *in vivo* in the AD brain (Ota et al., 2010). Imaging BChE met less success using the butyrate ester of *N*-[¹¹C]methylpiperidinol, which entered the brain, but without increased radioligand uptake in regions that typically accumulate BChE-associated AD plaques (Kikuchi et al., 2004; Kuhl et al., 2006; Roivainen et al., 2004). Moreover, decreased uptake in AD brain compared to normal brain was observed, in contrast to histochemical and isolation studies of this enzyme (Darvesh et al., 2010; Geula & Mesulam, 1989, 1995; Guillozet et al., 1997; Mesulam & Geula, 1994).

A recent autoradiographic study (Macdonald et al., 2016), using a cholinesterase radioligand, phenyl 4-[¹²³I]iodophenylcarbamate, was able to distinguish AD amyloid plaques from those found in the cerebral cortex of cognitively normal brains. However, in further *in vivo* studies, this radiotracer did not provide satisfactory brain retention. Prospective substrate-type ¹²³I SPECT radioligands containing the *N*-methylpiperidinol moiety were designed to prolong ligand-enzyme latencies preventing loss of [¹²³I] on the initial leaving group (Macdonald et al., 2011; Macdonald et al., 2016). *Ex vivo* autoradiographic evidence was earlier reported for *N*-methylpiperidin-4-yl 4-[¹²³I]iodobenzoate, which, injected intravenously into a rat, entered the brain and labeled areas known to exhibit BChE activity in histochemical studies (Macdonald et al., 2011). In the current study we extend this work by employing dynamic SPECT images to evaluate BChE engagement and compare uptake, retention and brain distribution of *N*-methylpiperidin-4-yl 4-[¹²³I]iodobenzoate radiotracer in the 5XFAD mouse model compared to that in its wild-type (WT) counterpart (Oakley et al., 2006). The 5XFAD

model accumulates A β plaques and is associated BChE activity, as in human AD (Darvesh & Reid, 2016; Reid & Darvesh, 2015). This animal model has significant BChE pathology over an aggressive course of amyloidosis (Reid & Darvesh, 2015). The increased activity of this enzyme in the brain, compared to the WT counterpart, makes this model well suited for examining the preclinical potential of BChE imaging agents as a proof of principle. Significantly higher radiolabel retention in the 5XFAD brain, particularly in the cerebral cortex, holds promise for such agents as imaging biomarkers for AD diagnosis.

2.5 Materials and Methods

Formal approval to conduct these experiments was obtained from the Dalhousie University Radiation Safety Committee and Canadian Nuclear Safety Commission.

2.5.1 Synthesis/Biochemical Materials

Na¹²³I in 0.1N NaOH was obtained from MDS Nordion. Other chemicals and solvents were from Sigma Aldrich (Canada). Isofluorane gas mixtures were diluted with oxygen. UV analysis was on Ultrospec 2100 pro UV/Visible Spectrophotometer (Biochrom) with Swift II software (Amersham). HPLC purifications were on an Agilent 1260 Infinity HPLC with ZORBAX Eclipse XDB-C18, 4.6 \times 250mm, 5 μ m column (Agilent Technologies), and a RediFrac fraction collector (Amersham Biosciences).

2.5.2 Enzyme Specificity

To determine murine BChE specificity for *N*-methylpiperidin-4-yl 4-iodobenzoate (Macdonald et al., 2011), repetitive scans for change in absorbance used mouse serum as

enzyme source. Briefly, in a quartz cuvette, to a reaction mixture of 0.1M phosphate buffer (2mL, pH 7.4) containing 0.1% gelatin, 5XFAD serum (200 μ L) and either: i) 50%_(aq) acetonitrile (60 μ L, no inhibitor), ii) 1mM ethopropazine (60 μ L, BChE inhibitor) or iii) 1mM BW 284C51 (60 μ L, AChE inhibitor) in 50%_(aq) acetonitrile, and mixed (Mikalsen et al., 1986). Reaction was initiated with 1mM *N*-methylpiperidin-4-yl 4-iodobenzoate in 50%_(aq) acetonitrile (30 μ L). The UV absorbance of each mixture was scanned from 200–300nm every 30min for a total of 3.5h.

2.5.3 Synthesis and Labelling of Radiotracer

Synthesis of *N*-methylpiperidinol-4-yl 4-[¹²³I]iodobenzoate was performed with modification of the procedure described previously (Macdonald et al., 2011). Briefly, in a plastic microtube (250 μ L), Na¹²³I (~157MBq) in 0.1M NaOH_(aq) (17 μ L) was diluted with 0.1M NaOH_(aq) (10 μ L), then acidified with 0.1M HCl_(aq) (32 μ L), followed by addition of *N*-methylpiperidin-4-yl 4-(tributylstannyl) benzoate in acetonitrile (50 μ L, 4.6mM). The reaction was initiated by adding *N*-chlorosuccinimide in acetonitrile (50 μ L, 3mM). After vortexing (7.5min) the mixture at room temperature, 0.1M NaOH_(aq) was added (13 μ L). Precursor and non-radioactive iodobenzoate established HPLC retention times. Radiolabelled product was purified using HPLC with 80% methanol_(aq) at 2mL/min as eluent. Fractions were collected every 30s for 10min. Collected fractions containing pure *N*-methylpiperidinol-4-yl 4-[¹²³I]iodobenzoate were combined and solvent evaporated at 40°C under a stream of argon. The radiochemical yield, on average, was 83%, based on HPLC radiograms and was consistent with radioscanned TLC experiments that determined radiochemical purity to be >98%. Radiotracer was re-dissolved in 0.9% saline (0.4mL) for animal administration.

2.5.4 Animals

Mice were cared for according to guidelines set by the Canadian Council on Animal Care; research approved by Dalhousie University Committee on Laboratory Animals. Pairs of female wild-type (C57BL/6J x SJL/J F1, Stock Number: 100012-JAX) and male transgenic hemizygous 5XFAD mice (B6SJL-Tg(APPswFILon,PSEN1*M146L*L286V)6799Vas/Mmjax, Stock Number: 006554-JAX) were obtained from Jackson Laboratory (Bar Harbor, ME), and cared for as described previously (Reid & Darvesh, 2015). Imaging was performed during light phase of the light-dark cycle. A total of 5 female mice (5XFAD n=3, WT n=2) and 7 male mice (5XFAD n=4, WT n=3) were imaged; average age was 11.1±1.1 months. This age group was chosen to ensure robust deposition of pathology to increase the likelihood of detecting differences in BChE activity between WT and 5XFAD mice.

2.5.5 SPECT-CT Imaging

Mice were weighed immediately prior to imaging, anaesthetized with 3% isoflurane in an induction chamber, restrained in a TailVeiner Restrainer (Braintree Scientific) while under a continuous stream of 1.5% isoflurane. Mice were secured in prone position in a Magnetic Resonance (MR)-compatible animal bed. *N*-Methylpiperidin-4-yl 4-[¹²³I]iodobenzoate (17.65-44.77MBq in 0.9% saline (140-200µL)) was administered through the lateral tail vein catheter line and subsequently flushed with saline. Mice were wrapped in a blanket on a heated bed, maintained under continuous stream of 1.5-2% isoflurane and respiration rate monitored for the duration of scan (SA Instruments Inc. Stony Brook, NY). The mouse head region was centered on a 14mm axial field of view (FOV); sequential SPECT frames (4 projections per frame)

were acquired in super list mode (SLM) over three 5min windows followed by six 10min windows with a SPARK™ SRT-50 (Cubresa Inc.) single head standalone tabletop SPECT scanner integrated with a Triumph XO LabPET pre-clinical computed tomography (CT) scanner (Trifoil Imaging, CA). After initial scanner setup and homing cycle of the SPECT gantry, frame 1 commenced 3.5min post injection with subsequent frames acquired on average at 3.5, 9.75, 16.0, 22.5, 33.75, 45.0 and 56.75min. Following SPECT scanning, a CT scan was acquired for anatomical reference and subsequently co-registered with anatomical magnetic resonance imaging (MRI) acquired in a separate scan (see below). CT images were collected in fly mode with a 70 kVp x-ray beam energy (160μA beam current), 512 projections, 4 summed frames/projection, with 2×2 binning and magnification of 2.26X, providing complete whole brain coverage in a 56mm FOV. CT scan duration was 8.5min.

2.5.6 MR Imaging

MRI scans were performed in a separate session prior to SPECT/CT imaging to facilitate regional analyses of radiotracer retention in the brain. MR imaging was carried out as described in a MRI protocol (Macdonald et al., 2014). Images ((142μm)³, full brain coverage) were acquired at 3.0T over 61min using a 3D balanced Steady-State Free Precession, (b-SSFP) imaging sequence (T₂/T₁-weighting).

2.5.7 Image Processing

Sequential SPECT images were reconstructed over each of seven frames acquired (three 5min frames and four 10min frames) as follows: SPECT super list mode (SLM) data were converted to list mode data using built-in Cubresa SPARK™ preprocessing

routine at 160keV with a 20% energy window applied. List mode data was reconstructed using an iterative 3D Maximum-Likelihood Expectation Maximization (MLEM) algorithm (9 iterations) using HiSPECT software (SciVis GmbH, Göttingen, Germany). Resultant SPECT images yielded an effective in-plane resolution of 0.7mm. Dark image and quantitative calibrations were performed weekly for the duration of the study and applied to each image acquired.

CT images were reconstructed with a 512×512×512 image matrix over a 56 mm FOV using built-in optimum noise reconstruction procedures with the Triumph XO CT acquisition software, yielding images with (102µm)³ isotropic resolution. Fusion of SPECT and CT images was achieved using established coordinate transformations between two modalities, whose common coordinate frames were applied in AMIDE Imaging Analysis software (Loening & Gambhir, 2003). Images were assessed by visual inspection to ensure accurate fusion results. MRI images underwent 3D maximum intensity projection (MIP) processing of 4 phase cycle frequencies and resulting reconstructed images were zero-padded (interpolated to higher resolution grid to increase the effective resolution and image quality) in ImageJ (NIH, USA).

2.5.8 SPECT/CT/MRI Coregistration and Dynamic SPECT Regional Analysis

Inter-modality registration performed between SPECT/CT/MRI and a MR-based 3D digital mouse atlas permitted parcellation of the brain for regional analyses as described previously (Macdonald et al., 2014). A 6-parameter rigid body registration was performed between mouse MR and a standard brain from which the digital atlas was derived using Automated Image Registration 5.3.0 (Woods et al., 1998). Higher spatial transformations (warping) were applied to standard brain and corresponding warped MR

atlas. MRI and warped MR atlas, along with SPECT/CT fused images were imported into AMIDE, where affine registration between modalities was carried out (Loening & Gambhir, 2003).

SPECT ROI statistics were generated to determine *N*-methylpiperidin-4-yl 4-[¹²³I]iodobenzoate retention for six regions of interest (ROI) defined by the MR atlas: i) whole brain, ii) cerebral cortex, iii) hippocampal formation, iv) amygdala, v) thalamus and vi) basal ganglia. Composite ROIs were derived using *fslmaths* scripts employing threshold and subtraction commands carried out in FSL (Oxford, UK). Whole brain ROIs contained all atlas brain structures excluding the cerebellum and brainstem. “Rest of brain” masks were also generated for each brain structure investigated, comprised of whole brain excluding the ROI of interest. *N*-Methylpiperidin-4-yl 4-[¹²³I]iodobenzoate retention values in raw time activity curves are reported as the average (mean voxel value) percent injected dose per mL of brain tissue (%ID/mL). Retention indices were computed for each ROI, expressed as relative standardized uptake values (SUVRs) with each rest of brain internal reference tissue (represented as $SUVR_{ROI} = SUV_{ROI}/SUV_{(whole\ brain-ROI)}$). This metric was used to limit any possible inter-subject or inter-scan variability.

2.5.9 BChE Histochemistry

Brain tissue processing and BChE histochemistry were carried out as described previously to generate photomicrographs of BChE distributions in 5XFAD and WT mouse brains (Darvesh & Reid, 2016).

2.5.10 Statistical Analysis

Unpaired t-tests (single tailed, assuming unequal variances) of group means (5XFAD vs WT) were carried out at each time-activity curve interval for both %ID/mL and SUVR metrics. Differences were concluded at a significance level of 5% ($p < 0.05$, *), 1% ($p < 0.01$, **) and trends were identified at ($p < 0.1$, †). All data are presented as group means \pm standard error of the mean (SEM). All statistical tests were performed in Excel[®] (Microsoft Office, v.15.13.1).

2.6 Results

2.6.1 Synthesis of *N*-Methylpiperidin-4-yl 4-[¹²³I]iodobenzoate

The radiotracer was prepared and purified using modifications to an earlier procedure (Macdonald et al., 2011). Here, acetonitrile replaced methanol as reaction solvent to prevent ester methanolysis. Reaction time was reduced (15min to 7.5min) by continuous vortexing once reactants were combined. Better separation and purification of product by HPLC was effected by making the reaction mixture slightly alkaline with 0.1M NaOH_(aq) instead of NaHCO_{3(aq)}. These modifications provided radiochemical yields >80%, radiochemical purity >98% and calculated specific activity of approximately 4500 GBq/ μ mol.

2.6.2 Cholinesterase Specificity for 1-Methylpiperidin-4-yl 4-Iodobenzoate

The non-radioactive iodobenzoate was examined using mouse serum containing both AChE and BChE. As indicated in repetitive scans (Figure 2.1A), the ester underwent slow hydrolysis at pH 7.4 over 210min. When mouse serum was first treated

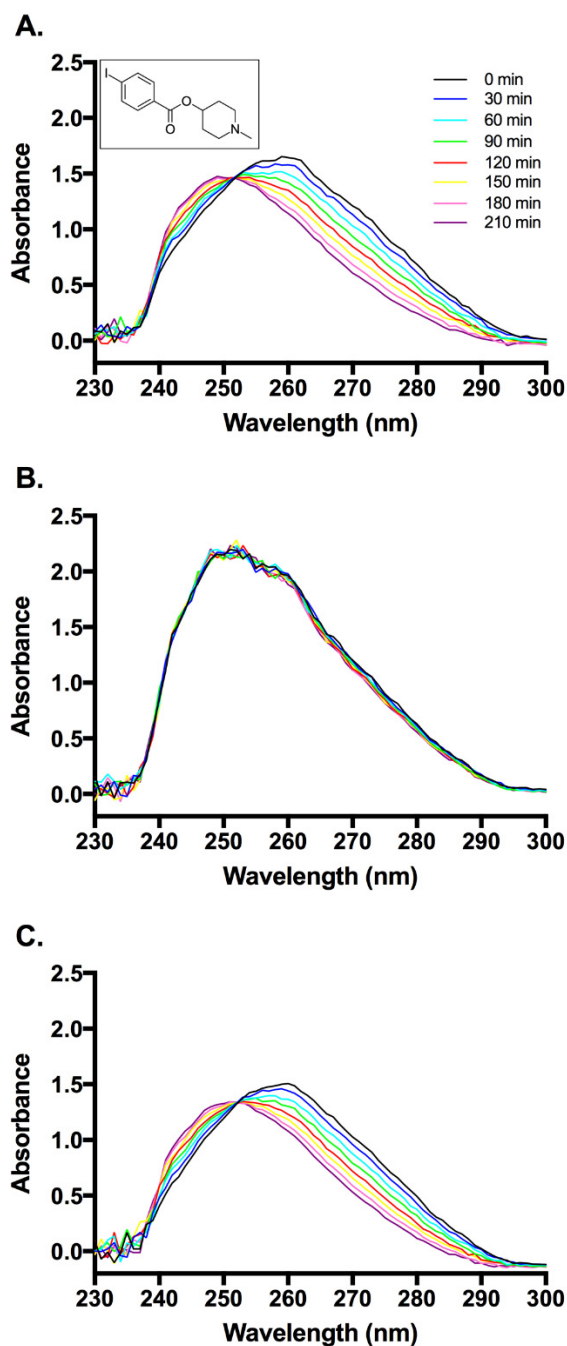


Figure 2.1 5XFAD mouse serum hydrolysis of *N*-methylpiperidin-4-yl 4-iodobenzoate demonstrated by repetitive UV scans at 30min intervals over 3.5h in 0.1M phosphate buffer (pH 7.4) **A.** Without inhibitor added (inlay shows probe chemical structure). **B.** In the presence of BChE inhibitor ethopropazine. **C.** In the presence of AChE inhibitor, BW 284C51. No effect on hydrolysis in the presence of BW 284C51. Abbreviations: AChE, acetylcholinesterase; BChE, butyrylcholinesterase; 5XFAD, B6SJL-Tg(APP^{Sw}FILon, PSEN1^{*M146L}*L286V)6799Vas/Mmjax mouse strain; UV, ultraviolet.

with BChE inhibitor ethopropazine, under the same conditions, no hydrolysis occurred (Figure 2.1B) (Mikalsen et al., 1986). In contrast, AChE inhibitor, BW 184C51, showed no effect on ester hydrolysis (Figure 2.1C), indicating the iodobenzoate interacts with BChE over AChE (Mikalsen et al., 1986).

2.6.3 Sequential SPECT Imaging

Following injection of *N*-methylpiperidin-4-yl 4-^[123I]iodobenzoate, sequential SPECT scans of mouse brain were acquired over 60 min, divided into 5 and 10min frames. Sequential SPECT frames generated 472,846 to 1,044,089 counts for 5min frames and 671,233 to 1,901,199 counts for 10min frames. These count levels provided sufficient signal-to-noise ratio (SNR) and reconstructed image quality for assessment of brain uptake and retention of radiotracer. SPECT, CT and MRI image registration provided robust and reproducible affine and non-linear registration of these modalities with corresponding MR-based digital atlas (Macdonald et al., 2014). From this, comparisons of brain retention of radiotracer could be assessed in 5XFAD and compared to WT mice.

2.6.4 Whole Brain Retention of Radioligand

Time-activity curves, reflecting retention of radiolabel (Figure 2.2 B), were generated from dynamic SPECT images (Figure 2.2 A) at each time point over whole brain SPECT scans in 5XFAD and WT brains. This enabled semi-quantitative comparison of radiotracer retention between 5XFAD and WT groups. Results described represent pooled male and female data since no sex differences were observed (separate analysis, not shown).

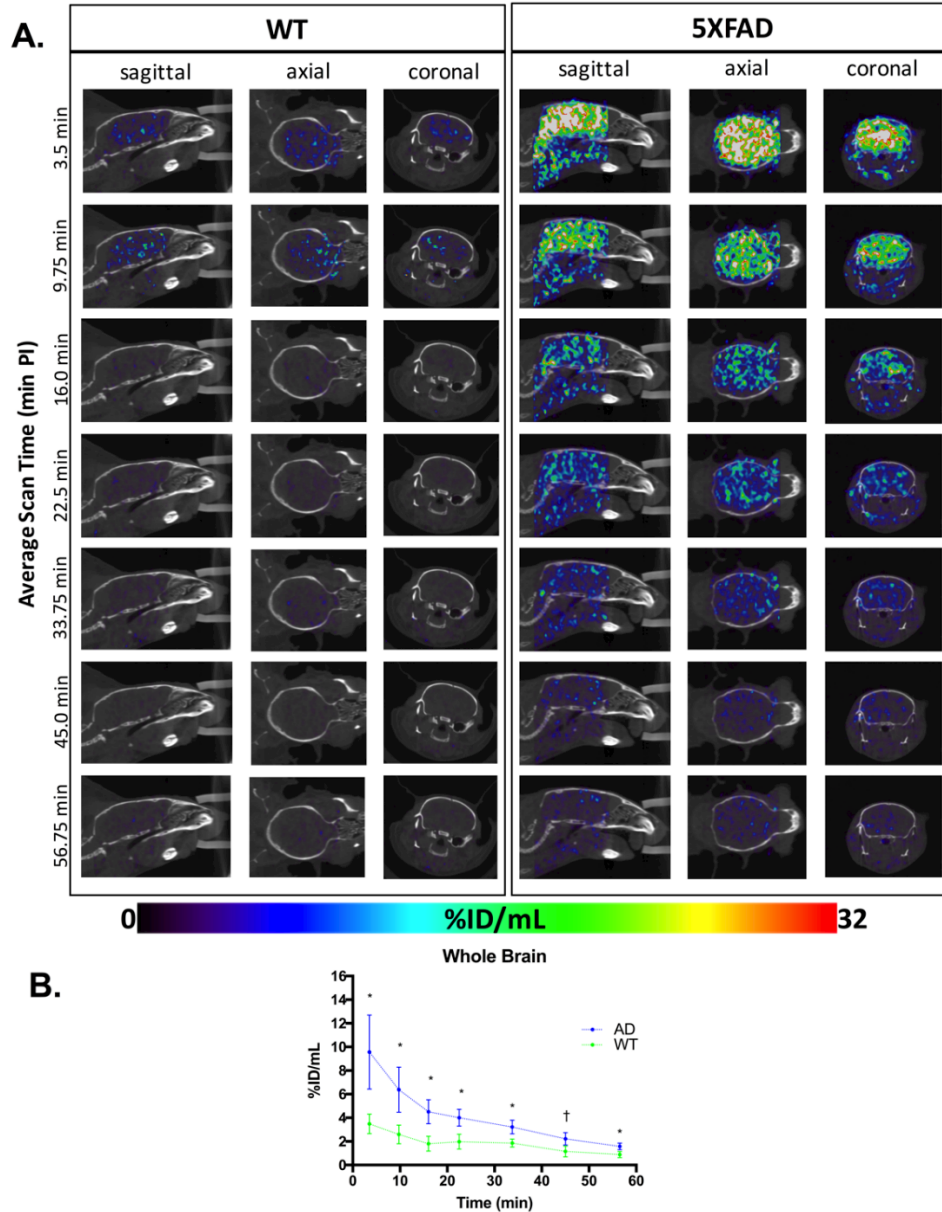


Figure 2.2 A. Representative WT (left) and 5XFAD (right) sequential SPECT/CT brain images in sagittal, axial and coronal planes. SPECT activity source maps indicate initial uptake and blood-brain barrier penetrance of radiotracer by 3.5min post-injection (PI) in both WT and 5XFAD brains, with greater radiotracer retention in the 5XFAD brain compared to WT. Image intensities expressed as percent injected dose per mL (%ID/mL) are set to a common color scale of 0-32%ID/mL. **B.** Corresponding whole brain radiotracer SPECT time-activity curves for 5XFAD (blue) and WT (green) mice (Mean \pm SEM). Significantly greater cerebral retention is evident in 5XFAD compared to WT. * denotes statistically significant differences ($p < 0.05$); † indicates a statistical trend ($p < 0.10$).

Both WT and 5XFAD strains showed rapid uptake of radiotracer into the brain (Figure 2.2 A,B), indicating it readily crossed the blood-brain barrier. Shown in the time-activity curves (Figure 2.2 B), by 3.5min after ligand injection, radioactivity is clearly visible in both 5XFAD and WT mouse brains (Figure 2.2 A). Time-activity curves (Figure 2.2 B) indicate subsequent washout of radiotracer in 5XFAD and WT brains within 15-20min post-injection. In each time frame up to 60min, there was greater (up to 2.3-fold) retention of label in 5XFAD brains relative to WT. Heterogeneous distribution of radiolabel throughout the whole brain (Figure 2.2 A) was evident. Distribution differences of radiolabel in WT and 5XFAD brains could reflect areas of high BChE-associated AD pathology. Radiotracer assessment of the regional distribution demonstrated specific patterns of retention that distinguish 5XFAD brains from WT controls.

2.6.5 Comparative Histochemical- and SPECT-Visualized Regional Butyrylcholinesterase Activity

Histological analysis represents the “gold standard” for detection of BChE activity in brain tissue and indicates a heterogeneous distribution of the enzyme throughout the brain. For example, as observed in the normal human brain, WT mouse brain (Figure 2.3, top) exhibits very little BChE histochemical staining in the cerebral cortex (Darvesh et al., 2010; Mesulam & Geula, 1994). However, the cerebral cortex of 5XFAD shows marked BChE accumulation (Darvesh & Reid, 2016; Reid & Darvesh, 2015) (Figure 2.3, bottom). Since both the cerebral cortex and subcortical regions, such as the hippocampal formation and thalamus develop BChE-associated AD pathology, it may be assumed that a region such as the cerebral cortex, that normally has little BChE activity, may provide the greatest contrast for detecting BChE-associated AD

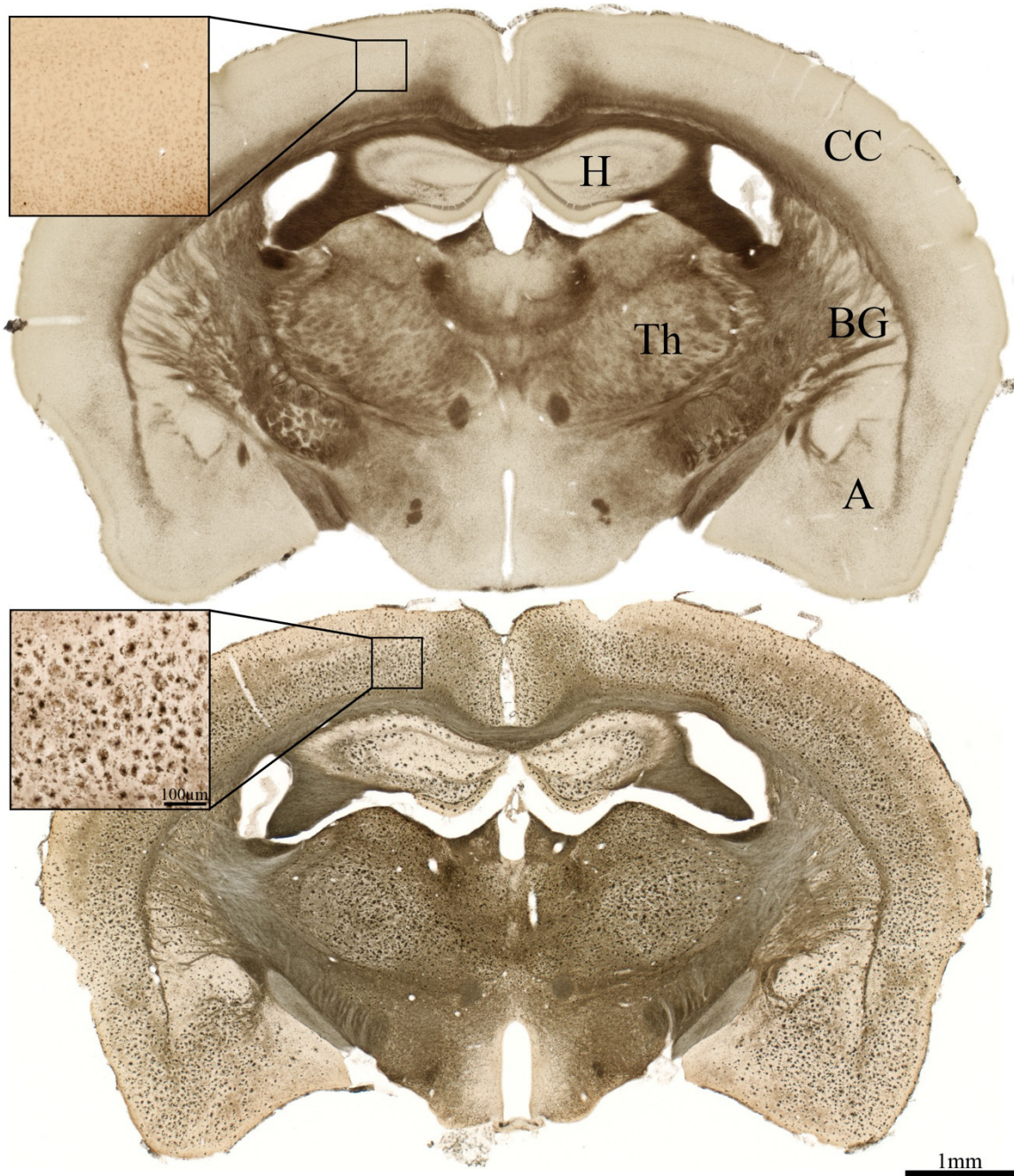


Figure 2.3 Photomicrographs showing representative BChE histochemical staining at mid-coronal level in WT (top) and 5XFAD (bottom) brains. Note little BChE staining in cerebral cortex of WT mice and marked elevation of BChE in cerebral cortex of 5XFAD mice. Significant accumulation of BChE in subcortical regions is also apparent, beyond that observed in the WT brain. CC=cerebral cortex, H=hippocampal formation, BG=basal ganglia, Th=thalamus, A=amygdala. Scale bar = 1mm and 100µm (inlay).

pathology (Figure 2.3) than would subcortical regions that express BChE in the absence of AD pathology. This notion is supported by semi-quantitative analyses of SPECT radiolabel retention (Figure 2.4). To compare potential differences in radiotracer retention between 5XFAD and WT brains, several different regional metrics were tested to generate time-activity curves. ROIs examined included the cerebral cortex, basal ganglia, hippocampal formation, amygdala and thalamus (Figures 2.3, Figure 2.4).

2.6.6 Cortical and Subcortical Retention Comparisons

Time-activity curves for regional comparisons (Figure 2.5) of 5XFAD and WT images (expressed as %ID/mL) showed similar trends in each ROI to observed for whole brain evaluation (Figure 2.2 B). This was true for the cerebral cortex (Figure 2.5A) as well as some subcortical structures (Figure 2.5B-E). It is evident that it depends on the ROI examined as to whether significant differences in retention of radiotracer could identify AD pathology through BChE association. For example, comparing robust retention in the cerebral cortex of 5XFAD relative to WT (Figure 2.5A) with that in the amygdala (Figure 2.5E), where there is no significant difference detected for the retention in the two strains. A summary graph of fold difference in radiotracer retention between 5XFAD and WT time-activity curves is presented for the cerebral cortex and subcortical areas in Figure 5F. All ROIs show the same trend of greater radiotracer retention in 5XFAD brain relative to WT. However, the greatest difference in radiotracer retention over time (~3-fold) is seen for the cerebral cortex. Since increased BChE accumulation

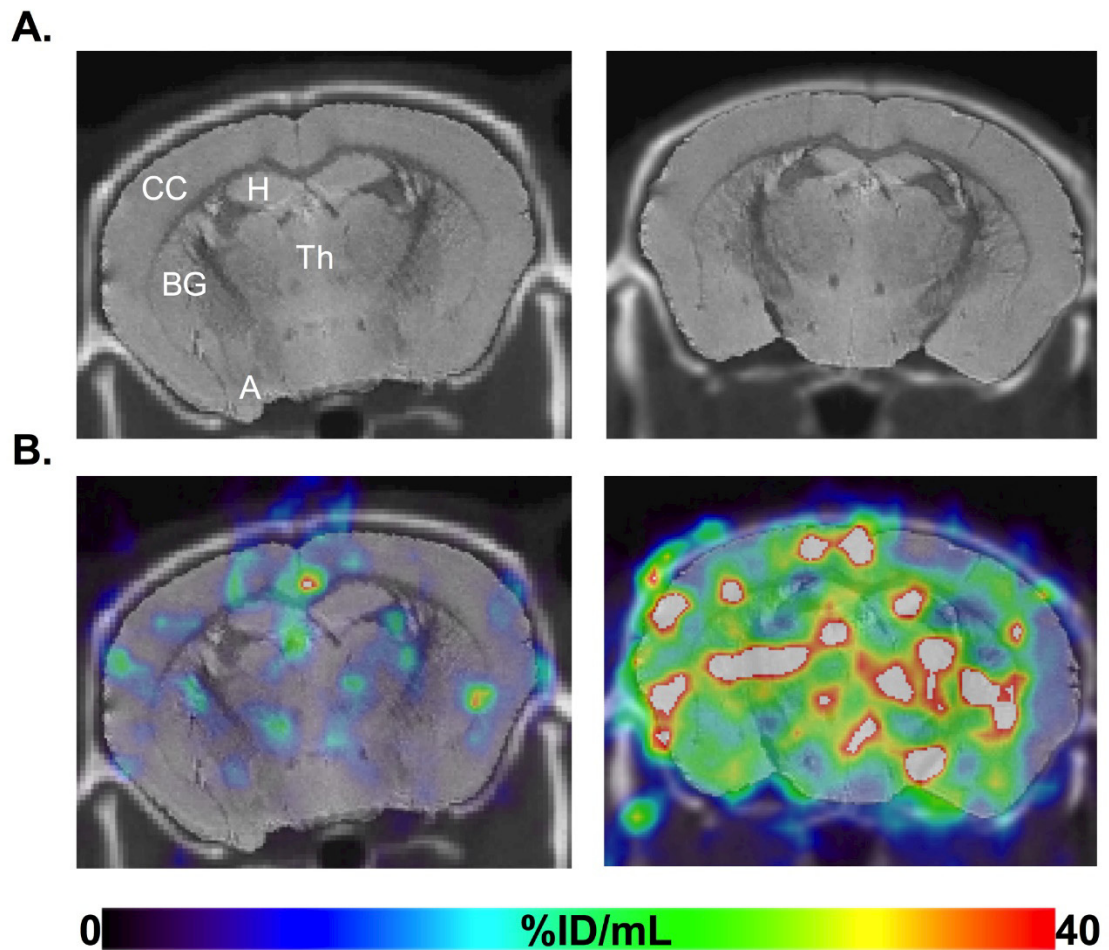


Figure 2.4 Comparison of BChE activity at mid-coronal level (as in Figure 2.3) in specific brain regions of WT (left) and 5XFAD (right) mice detected with radiotracer SPECT analysis. **A.** CT with co-registered MR. CC=cerebral cortex, H=hippocampal formation, BG=basal ganglia, Th=thalamus, A=amygdala. **B.** SPECT images acquired at 4min post-injection with co-registered CT/MR and ROIs. Marked retention in the 5XFAD cerebral cortex is evident in the 5XFAD brain compared to WT with less difference in retention evident in amygdala, hippocampus, basal ganglia and thalamus. Image intensities expressed as %ID/mL and set to a common scale of 0-40%ID/mL.

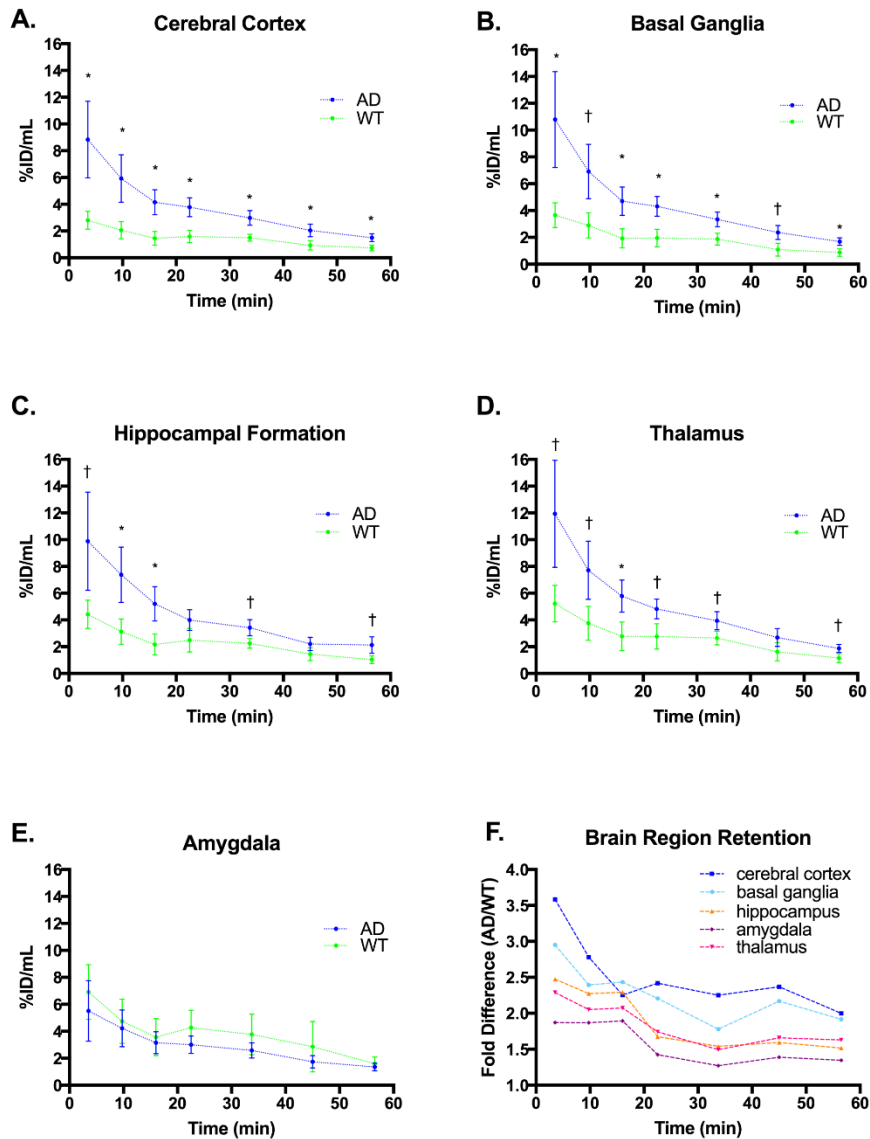


Figure 2.5 Corresponding N-methylpiperidin-4-yl 4- 123 I]iodobenzoate time activity curves for 5XFAD (blue) and WT (green) mice. Mean \pm SEM. * denotes statistically significant differences ($p < 0.05$), † indicates a statistical trend ($p < 0.10$). **A.** Sustained retention in the cerebral cortex over each dynamic frame was observed in 5XFAD compared to WT up to 60min. **B.** A similar trend of sustained retention was observed in basal ganglia up to 60min. **C.** Early retention in hippocampus was greater in the 5XFAD brain up to 30min, **D.** A similar trend of early retention was seen in the thalamus up to 30min. **E.** No differences were observed in amygdala retention between 5XFAD and WT over the entire time course. **F.** Ratio of 5XFAD to WT time activity curve means indicating the fold difference (increase) in radiotracer retention in the cerebral cortex (blue), basal ganglia (light blue), hippocampus (orange), thalamus (pink) and amygdala (purple) relative to WT controls. Cerebral cortex retention was approximately 3.5 fold greater at 4min post-injection and was maintained at approximately 2.5 fold up to 60min post-injection.

in cerebral cortex is a prominent feature of AD progression, it is of value to assess the relative proportion of radiotracer in the brain that can be attributed to the cortex (Darvesh et al., 2010; Mesulam & Geula, 1994; Perry, Perry, et al., 1978). The cortical retention index, a relative SUV ($SUVR_{c.cortex/(whole\ brain-c.cortex)}$) metric that expresses tracer retention in the cortex normalized to radiotracer uptake in the rest of the brain, serves as a means to assess cortical retention while limiting inter-scan and inter-subject variability between scans. With this metric, the cortical retention index was found to be significantly greater (18-31%) in 5XFAD brain than in WT controls (Figure 2.6A), which was sustained over the 60min of study. This is indicated by the ratio of label retention in 5XFAD cerebral cortex over that of WT controls is consistently on the order of 1.2 to 1.3 over each time point examined (Figure 2.6B).

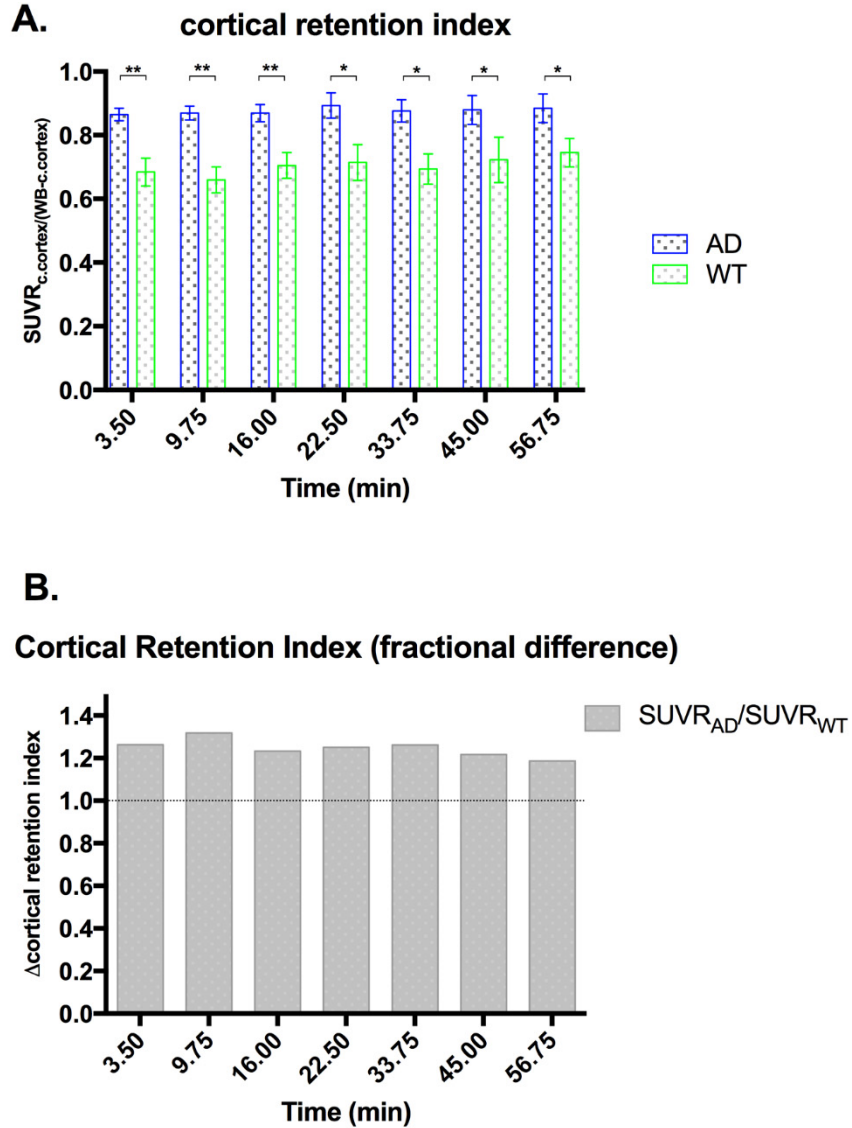


Figure 2.6 A. *N*-Methylpiperidin-4-yl 4-[¹²³I]iodobenzoate retention indices for 5XFAD (blue) and WT (green) mice. Mean ± SEM. **A.** Cortical retention index (SUVr_{c.cortex/whole brain}: cortical retention normalized to whole brain) was 18-31% greater in 5XFAD brains vs WT over the 60 min imaging window. * and ** denote statistically significant differences (p<0.05, p<0.01, respectively). **B.** Fractional difference in cortical retention index between 5XFAD and WT indicating between 1.18-1.31X greater retention in the cerebral cortex of 5XFAD mice compared to WT.

2.7 Discussion

A number of approaches have been undertaken to develop biomarkers for definitive diagnosis of AD, including PET brain imaging of amyloid and tau. Several amyloid imaging agents have been approved as ancillary agents to test for AD and tau imaging agents are being developed (Villemagne et al., 2015). However, since amyloid plaques and tau neurofibrillary tangles can also be found in cognitively normal individuals, development of additional biomarker targets seems imperative to improve the diagnosis of AD during life (Hou et al., 2004; Johnson, Minoshima, Bohnen, Donohoe, Foster, Herscovitch, Karlawish, Rowe, Carrillo, Hartley, Hedrick, Pappas, & Thies, 2013). Changes in components of the cholinergic system, such as the appearance of BChE associated with AD pathology in the cerebral cortex, provides an opportunity to image this pathology without registering similar anomalies that may also be present in the brains of many cognitively normal individuals. Thus, BChE may represent a viable diagnostic imaging target which must be carefully considered. In other dementias, such as dementia with Lewy bodies and vascular dementia, there are no reported increases in levels of BChE (Perry et al., 2003; Xiao et al., 2012). However, for tauopathies, BChE radiotracers will need to be evaluated in appropriate mouse models to determine their specificity.

The radiotracer *N*-methylpiperidin-4-yl 4-¹²³I]iodobenzoate, selectively engages with BChE and undergoes slow hydrolysis (Figure 2.1). This radiotracer crosses the blood-brain barrier and there is greater retention in brains of the 5XFAD mouse model than WT counterparts (Figure 2.2). Sequential SPECT imaging analysis measuring differential retention of radioactivity in the cerebral cortex and various subcortical

regions (Figure 2.4) revealed known histochemical BChE activity (Figure 2.3). Time-activity curves derived from sequential SPECT analysis consistently indicate elevated retention of radioactivity in brains of 5XFAD mice compared to WT counterparts (Figures 2.2 and 2.5), that is particularly evident in the cerebral cortex (Figures 2.5 and 2.6).

In previous attempts, *N*-methylpiperidiny acetate and propionate could image AChE in the human brain while *N*-methylpiperidiny butyrate, a specific substrate for BChE, entered the brain and accumulated in certain regions (Roivainen et al., 2004), but it was unable to distinguish AD from normal brain (Kuhl et al., 2006). It is not clear why *N*-methylpiperidiny butyrate could not recapitulate what is known from post-mortem brain histochemistry. There are several possibilities that include nonspecific or off-target binding of the tracer, or that the radioactive atom (^{11}C) is located on the side of the ester molecule that is the first leaving group during the BChE-catalyzed hydrolysis. This could cause the radioactive atom being rapidly dispersed away from the target. To test this possibility, a radiotracer with a larger acyl group bearing the radioactive atom was employed. The placement of the radioactive atom (^{123}I) on the acyl portion of the ester ensures a longer lived enzyme-acyl intermediate than the earlier ligands. Altering the placement of the radioactive atom appeared to improve the imaging outcomes in this study. More importantly, these findings are in keeping with earlier observations in human AD that BChE associates with AD pathology (Geula et al., 1994; Geula & Mesulam, 1995; Guillozet et al., 1997; Ota et al., 2004). Evidence that BChE radiotracers can distinguish between AD pathology and that in cognitively normal brains with pathology bodes well for increased diagnostic performance with the development of

selective BChE targeted imaging agents for comparative studies focused on the cerebral cortex (Macdonald et al., 2016).

2.8 Conclusions

These preliminary findings provide *in vivo* evidence of *N*-methylpiperidin-4-yl 4-[¹²³I]iodobenzoate crossing the blood-brain barrier and are suggestive of target engagement of this radioligand with BChE-associated pathology in the cerebral cortex of the 5XFAD brain. The current study demonstrates that BChE-specific radiotracers can be developed as AD diagnostic agents. This work opens avenues for further investigations to determine the temporal association of BChE accumulation in pathology using SPECT BChE radiotracers in this and other pre-clinical models and, ultimately, in human AD.

2.9 Acknowledgements

D.R. DeBay contributed aspects of SPARK SRT-50 SPECT design, development, integration and testing in collaboration with Cubresa Inc. as well as conceptualization of study, research design, image acquisition and processing, statistical analysis and interpretation, manuscript preparation and revisions. Radiosynthesis was performed by G.A. Reid and I.R. Pottie. The authors would like to thank Christa Davis, Dr. Erin Mazerolle and Selena Maxwell for their technical support, S Burrell and C.V. Bowen for imaging discussions and S Darvesh for conceptualization and study design. This research was supported by the Canadian Institutes of Health Research (MOP-82798, RNS-117795, MOP-119343), Capital Health Research Fund, Nova Scotia Health Research Foundation (Scotia ScholarTM, MED-MAT-2011-7512), Faculty and Department of

Medicine of Dalhousie University, Innovacorp, Mount Saint Vincent University
Committee on Research and Publication, Dalhousie Medical Research Foundation Gunn
Family Research Prize, DeWolfe Graduate Studentship, Mrs. Sadie MacLeod through the
Dalhousie Medical Research Foundation Adopt-a-Researcher program and the Dalhousie
Medical Research Foundation Irene MacDonald Sobey Endowed Chair in Curative
Approaches to Alzheimer's Disease.

Chapter 3 *In Vivo* Screening of BChE Radioligands using 2D Dynamic Planar Scintigraphy

3.1 Publication Status

Manuscript in preparation.

D.R. DeBay, I.R. Pottie, G.A. Reid, K. Kanayama, E. Martin, S. Burrell, C.V. Bowen, S. Darvesh. *2D Dynamic Planar Scintigraphy evaluation of putative BChE AD Diagnostic Radioligands.*

3.2 Overview

This chapter builds on the pre-clinical Single Photon Emission Computed Tomography (SPECT) imaging and analysis framework developed in Chapter 2 which permitted a preliminary *in vivo* evaluation of lead candidate radioligand *N*-methylpiperidinyl-4-¹²³Iiodobenzoate (TRV6001) targeting butyrylcholinesterase (BChE) for AD diagnostics (DeBay, Reid, Pottie, et al., 2017). This imaging scheme utilized sequential three-dimensional (3D) SPECT images acquired over one hour with subsequent co-registration of computed tomography (CT) and magnetic resonance imaging (MRI) for anatomical localization of tracer uptake. The strength of this method lied in the ability to determine the regional distribution of TRV6001 in the brain, albeit at the expense of temporal resolution and with images of relatively low signal to noise ratio (SNR). SPECT acquisition using a single head gamma camera required the acquisition of four separate projections to generate a single SPECT image frame ultimately provided an imaging timepoint every ~4 minutes. Radiotracer kinetics, particularly in the early uptake (perfusion) phase after intravenous (IV) administration typically occur at a much more rapid timescale on the order of seconds (Kang et al., 2016).

The work in the current chapter focuses on developing and implementing two-dimensional (2D) dynamic planar scintigraphy capabilities with the Cubresa SPARK™ SRT-50 tabletop SPECT scanner (Cubresa Inc., Winnipeg, MB). This approach offered greatly increased temporal resolution, through the continuous acquisition of 2D lateral projections of the mouse brain. Proof-of-concept evaluation of BChE radioligand clearance characteristics provided insight into the kinetic profile of six candidate [¹²³I] radioligands and ultimately validated the use of 2D dynamic planar scintigraphy as a rapid screening tool to evaluate candidate [¹²³I] BChE radioligands.

3.3 Abstract

In central nervous system (CNS) radioligand development, rapid screening of lead radiotracer candidates in animal models is an essential component in establishing a radioligand's product profile, putting the most promising candidates forward for evaluation in human clinical trials. In Alzheimer's disease (AD), a number of molecular imaging agents have been developed and evaluated in humans including those that target A β and tau. However, in general, these agents lack specificity for AD as up to 30% of cognitively normal individuals have evidence of this pathology. As such, a definitive diagnosis of AD during life remains elusive. The enzyme butyrylcholinesterase (BChE) is a highly sensitive and specific AD biomarker and a promising candidate for brain imaging diagnostics. To this end, we have developed several classes of radioligands for brain imaging that target BChE. The synthesis and *in vivo* evaluation of six such BChE radioligands is described here.

Methods: A series of lead [^{123}I] BChE-targeting radioligand candidates in three classes of molecules were synthesized, including pyridones: i) (*p*-[^{123}I]iodophenyl)methyl 6-oxo-1*H*-pyridine-2-carboxylate (TRV7005), ii) (*p*-[^{123}I]iodophenyl)methyl 1-methyl-6-oxo-1*H*-pyridine-2-carboxylate (TRV7006), iii) (*p*-[^{123}I]iodophenyl)methyl 6-methoxy-2-pyridinecarboxylate (TRV7019), iv) benzyl 6-[(*p*-[^{123}I]iodophenyl)methoxy]-2-pyridinecarboxylate TRV7040); diphenyl carbamates: *p*-[^{123}I]iodophenylamino benzoate (TRV5001) and piperidines: *N*-Methylpiperidin-4-yl 4-[^{123}I]iodobenzoate (TRV6001). The product profile of each radioligand was characterized based on their physicochemical attributes (using multiparametric optimization (MPO) scoring) and *in vitro* kinetic profile (evaluating standard enzyme kinetics parameters, including the maximum enzymatic reaction rate (V_{max}), rate of first chemical step (K_{cat}), Michaelis constant (K_m), enzymatic efficiency (k_{cat}/K_m) and inhibition equilibrium constant (K_i)). Radioligands were then imaged *in vivo* over one hour using two-dimensional (2D) dynamic planar scintigraphy in four strains of mice exhibiting differential expression of BChE. These mice included a familial AD mouse model (5XFAD) and corresponding wild-type (WT) counterparts in addition to BCHE-knockout BCHE-KO mice and a derived 5XFAD-BCHE-KO strain both of which lack a BChE-expressing phenotype. Scintigraphy imaging permitted determination of each radiotracer's ability to cross the blood-brain barrier (BBB) in addition to their biodistribution in the brain over time. Whole brain time-activity curves, generated from dynamic scintigraphy acquisitions binned into 60x 1-minute frames, were fit with a mono-exponential decay function from which the rate of tracer clearance, $k_{clearance}$ (min^{-1}), the half-life of tracer clearance, $t_{1/2clearance}$ (min) and asymptotic radiotracer concentration (i.e. tracer concentration remaining in the brain), C_A ($\%C_{max}$)

could be derived and evaluated. For each radioligand, these kinetic summary measures were then compared between the groups of mice imaged. Pooled data of mouse strains within each radioligand permitted an overall comparison of tracer kinetics between radioligands using an analysis of variance (ANOVA) statistical design.

Results: [^{123}I] radioligands were successfully synthesized with all radioligands achieving sufficiently good radiochemical yields (56.5-87%) and radiochemical purity (95.2-95.9%). In general, most radioligands possessed favourable physicochemical characteristics, registering MPO scores ranging between 3.43-4.74 for TRV7005, TRV7006, TRV7019, TRV5001 and TRV6001, while TRV7040 had a lower MPO score 2.41. *In vitro* enzyme kinetics identified the radioligands as having high specificity for BChE. 2D dynamic planar scintigraphy provided sufficient image quality to evaluate the biodistribution of the radioligands evaluated. With the exception of TRV7040, all pyridone radioligands, including TRV7005, TRV7006 and TRV7019, crossed the BBB and were taken up in the brain. Diphenyl carbamate radioligand TRV5001 and piperidine radioligand TRV6001 also crossed the BBB and were taken up in the brain. Whole brain time-activity curves were generated from which kinetic summary measures of tracer clearance were successfully evaluated. In general, no significant differences in $k_{clearance}$, $t_{1/2clearance}$ and C_A were observed between mouse strains for each radioligand evaluated, save TRV7019, where a 58% decrease in $k_{clearance}$ (5XFAD = $0.23 \pm 0.4 \text{ min}^{-1}$; WT = $0.4 \pm 0.04 \text{ min}^{-1}$; $p=0.041$) and commensurate increase of 82% in $t_{1/2clearance}$ (5XFAD = $3.22 \pm 0.55 \text{ min}$; WT = $1.77 \pm 0.15 \text{ min}$ $p=0.065$ (statistical trend)) were demonstrated. However, no significant difference in asymptotic tracer concentration, C_A (5XFAD = 56.2

$\pm 5.0\%$; WT = $55.9 \pm 6.1\%$, $p = 0.964$) was apparent between 5XFAD and WT groups. Comparison of kinetic summary measures between radioligands revealed significantly greater $t_{1/2 \text{ clearance}}$ (thus faster $k_{\text{clearance}}$) for TRV5001 and TRV6001 compared to all other radioligands. The asymptotic tracer concentration, C_A was also significantly greater for TRV5001 and TRV6001 compared to all other radioligands suggesting greater brain retention of these radioligands.

Discussion: In general, the BChE radioligands evaluated in the current study possessed favourable physicochemical characteristics, with all but one radioligand (TRV7040) crossing the BBB which was accurately predicted by MPO score. 2D dynamic planar scintigraphy proved to be a robust technique with sufficient sensitivity to evaluate radioligand kinetics clearance and was able to distinguish different rates of clearance between radioligands. Even within the same class of radioligands, different clearance behaviour was apparent. 2D dynamic planar scintigraphy imaging can be combined with *in vitro* kinetics and MPO scores as part of the tracer product profile and provide valuable information that can be incorporated into a “go/no go” paradigm for further characterization and development of candidate BChE radioligands.

3.4 Introduction

Alzheimer’s disease (AD) is the most common cause of dementia (Scheltens et al., 2016) and a definitive diagnosis of AD during life remains elusive. Brain imaging biomarkers that measure β -amyloid plaques ($A\beta$), tau neurofibrillary tangles (NFT) and neurodegeneration (Jack et al., 2018), though informative, generally lack the diagnostic

specificity required for a definitive diagnosis. There is a great need for improved brain imaging biomarkers to enhance the accuracy of an AD diagnosis during life.

AD is a state of cholinergic dysfunction, which significantly contributes to the cognitive decline associated with AD (Coyle et al., 1983). The cholinergic enzyme butyrylcholinesterase (BChE) associates with A β and tau pathology in AD. We have recently shown in human brains at autopsy that BChE is a highly sensitive and specific biomarker of AD, has strong predictive value and could therefore elevate the accuracy of an AD diagnosis.

To this end, we have developed several classes of radioligands for brain imaging that target BChE. The synthesis and *in vivo* evaluation of six such BChE radioligands are described here, which include pyridones: i) (*p*-[¹²³I]iodophenyl)methyl 6-oxo-1*H*-pyridine-2-carboxylate (TRV7005), ii) (*p*-[¹²³I]iodophenyl)methyl 1-methyl-6-oxo-1*H*-pyridine-2-carboxylate (TRV7006), iii) (*p*-[¹²³I]iodophenyl)methyl 6-methoxy-2-pyridinecarboxylate (TRV7019), iv) benzyl 6-[(*p*-[¹²³I]iodophenyl)methoxy]-2-pyridinecarboxylate (TRV7040); a diphenyl carbamate: *p*-[¹²³I]iodophenylamino benzoate (TRV5001) and a piperidine: *N*-Methylpiperidin-4-yl 4-[¹²³I]iodobenzoate (TRV6001).

3.5 Materials and Methods

Formal approval to conduct the current experiments was obtained from the Dalhousie University Radiation Safety Committee and the Canadian Nuclear Safety Commission (license 07154-2-17.10). Mice were cared for according to the guidelines set by the Canadian Council on Animal Care (Dalhousie University Committee on Laboratory Animals Protocol 15-070).

3.5.1 Physicochemical Evaluation of [¹²³I] Radioligands

Multiparametric optimization (MPO) scores were determined as outlined by Wager et al. (Wager et al., 2010). Six physicochemical properties of each radioligand including molecular weight (MW), topological polar surface area (TPSA) most basic center (pK_a), calculated partition coefficient (clogP), calculated distribution coefficient at pH 7.4 (clogD) and hydrogen bond donors (HBD) were determined. These properties were evenly weighted and scored between 0-1 to give a composite MPO score. Typically, an MPO \geq 3.0 is predictive of a radioligand's ability to cross the blood-brain barrier (BBB) and reach the brain.

3.5.2 *In Vitro* Enzyme Kinetics

In vitro enzyme kinetics were carried out using standard methods that have been described previously (Darvesh, Walsh, et al., 2003). Enzyme kinetic parameters included the maximum enzymatic reaction rate (V_{max} (M•min⁻¹)), rate of first chemical step (K_{cat} (min⁻¹)), Michaelis constant (K_m), enzymatic efficiency (k_{cat}/K_m) and inhibition equilibrium constant (K_i (min⁻¹)).

3.5.3 Radiosynthesis

3.5.3.1 (*p*-[¹²³I]iodophenyl)methyl 6-oxo-1H-pyridine-2-carboxylate (TRV7005)

Synthesis of (*p*-[¹²³I]iodophenyl)methyl 6-oxo-1H-pyridine-2-carboxylate was performed with modifications of a procedure described previously (DeBay, Reid, Pottie, et al., 2017). Briefly, in a plastic microtube (250 μ L), Na¹²³I (~185 MBq) in 0.1 M NaOH_(aq) (20 μ L) was diluted with 1 M NaOH_(aq) (20 μ L), then acidified with 1 M HCl_(aq) (25.5 μ L). The solution was vortexed, centrifuged and checked to ensure the pH

was acidic. To this was added acetonitrile (50 μ l) followed by (*p*-(tributylstannyl)phenyl)methyl 6-oxo-1H-pyridine-2-carboxylate in acetonitrile (50 μ l, 4.64mM). The reaction was initiated by adding *N*-chlorosuccinimide in acetonitrile (50 μ l, 3mM). After vortexing (7.5 minutes) at room temperature, the reaction mixture was centrifuged and injected in an Agilent Infinity 1260 HPLC with a 250mm zorbax xdb eclipse C18 column with an eluent of 80% methanol and 20% water run at 1ml per minute. After 6 minutes, the eluent was switched to 100% acetonitrile at 3 ml per minute to remove any unreacted precursor. Fractions were collected every 30 seconds. Using a retention time established with (*p*-Iodophenyl)methyl 6-oxo-1H-pyridine-2-carboxylate, the appropriate fractions containing the radioligand were collected and combined in a glass v-vial. The combined solution, with 5 μ l of 1M HCl added, was dried at 55°C under a light stream of argon. Radiotracer was re-dissolved in 5% ethanol and 0.9% saline (0.25 mL) for animal administration.

3.5.3.2 (*p*-[¹²³I]Iodophenyl)methyl 1-methyl-6-oxo-1H-pyridine-2-carboxylate (TRV7006)

Synthesis of (*p*-[¹²³I]Iodophenyl)methyl 1-methyl-6-oxo-1H-pyridine-2-carboxylate was performed with modifications of a procedure described previously (DeBay, Reid, Pottie, et al., 2017). Briefly, in a plastic microtube (250 μ L), Na¹²³I (~185 MBq) in 0.1 M NaOH_(aq) (20 μ L) was diluted with 1 M NaOH_(aq) (15 μ L), then acidified with 1 M HCl_(aq) (20 μ L). The solution was vortexed, centrifuged and checked to ensure the pH was acidic. The precursor, (*p*-(tributylstannyl)phenyl)methyl 1-methyl-6-oxo-1H-pyridine-2-carboxylate in acetonitrile (20 μ l, 3mM), was added and the reaction was initiated by adding *N*-chlorosuccinimide in acetonitrile (20 μ l, 3mM). After vortexing (7.5 minutes) at room temperature, the reaction mixture was centrifuged and

injected in an Agilent Infinity 1260 HPLC with a 250mm zorbax xdb eclipse C18 column with an eluent of 100% acetonitrile at 0.7ml per minute. Fractions were collected every 30 seconds. Using a retention time established with (*p*-Iodophenyl)methyl 1-methyl-6-oxo-1H-pyridine-2-carboxylate, the appropriate fractions containing the radioligand were collected and combined in a glass v-vial. The combined solution, with 5µl of 1M HCl added, was dried at 55°C under a light stream of argon. Radiotracer was re-dissolved in 5% ethanol and 0.9% saline (0.25 mL) for animal administration.

3.5.3.3 (*p*-[¹²³I]Iodophenyl)methyl 6-methoxy-2-pyridinecarboxylate (TRV7019)

Synthesis of (*p*-[¹²³I]Iodophenyl)methyl 6-methoxy-2-pyridinecarboxylate was performed with modifications of a procedure described previously (DeBay, Reid, Pottie, et al., 2017). Briefly, in a plastic microtube (250 µL), Na¹²³I (~185 MBq) in 0.1 M NaOH_(aq) (20 µL) was diluted with 1 M NaOH_(aq) (15 µL), then acidified with 1 M HCl_(aq) (19.5 µL). The solution was vortexed, centrifuged and checked to ensure the pH was acidic. To this was added acetonitrile (50 µl) followed by (*p*-(tributylstannyl)phenyl)methyl 6-methoxy-2-pyridinecarboxylate in acetonitrile (50 µl, 3mM). The reaction was initiated by adding *N*-chlorosuccinimide in acetonitrile (50 µl, 3mM). After vortexing (7.5 minutes) at room temperature, the reaction mixture was centrifuged and injected in an Agilent Infinity 1260 HPLC with a 250mm zorbax xdb eclipse C18 column with an eluent of 90% acetonitrile and 10% water run at 1ml per minute. Fractions were collected every 30 seconds. Using a retention time established with (*p*-Iodophenyl)methyl 6-methoxy-2-pyridinecarboxylate, the appropriate fractions containing the radioligand were collected and combined in a glass v-vial. The combined solution, with 5µl of 1M HCl added, was dried at 55°C under a light stream of argon.

Radiotracer was re-dissolved in 5% ethanol and 0.9% saline (0.25 mL) for animal administration.

3.5.3.4 benzyl 6-[(*p*-[¹²³I]iodophenyl)methoxy]-2-pyridinecarboxylate (TRV7040)

Synthesis of benzyl 6-[(*p*-[¹²³I]iodophenyl)methoxy]-2-pyridinecarboxylate was performed with modifications of a procedure described previously (DeBay, Reid, Pottie, et al., 2017). Briefly, in a plastic microtube (250 µL), Na¹²³I (~185 MBq) in 0.1 M NaOH_(aq) (20 µL) was diluted with 1 M NaOH_(aq) (10 µL), then acidified with 1 M HCl_(aq) (17 µL). The solution was vortexed, centrifuged and checked to ensure the pH was acidic. To this was added acetonitrile (50 µl) followed by benzyl 6-[(*p*-(tributylstannyl) phenyl)methoxy]-2-pyridinecarboxylate in acetonitrile (25 µl, 3mM). The reaction was initiated by adding N-chlorosuccinimide in acetonitrile (25 µl, 3mM). After vortexing (7.5 minutes) at room temperature, the reaction mixture was centrifuged and injected in an Agilent Infinity 1260 HPLC with a 250mm zorbax xdb eclipse C18 column with an eluent of 90% acetonitrile and 10% water run at 1ml per minute. Fractions were collected every 30 seconds. Using a retention time established with Benzyl 6-[(*p*-iodophenyl)methoxy]-2-pyridinecarboxylate, the appropriate fractions containing the radioligand were collected and combined in a glass v-vial. The combined solution was dried at 55°C under a light stream of argon. Radiotracer was re-dissolved in 5% ethanol and 0.9% saline (0.25 mL) for animal administration.

3.5.3.5 *p*-[¹²³I]iodophenylamino benzoate (TRV5001)

The synthesis of TRV5001 followed methods that have been described previously (Macdonald et al., 2016).

3.5.3.6 *N*-Methylpiperidin-4-yl 4-[¹²³I]iodobenzoate (TRV6001)

The synthesis of TRV6001 followed methods described previously (DeBay, Reid, Pottie, et al., 2017).

3.5.4 Animals

In the current study, four strains of mice were utilized to evaluate candidate radioligands, namely 5XFAD and wild-type (WT) mice with additional BChE-KO and 5XFAD-BChE-KO mice evaluated in some instances and are detailed below. The 5XFAD mouse model (Oakley et al., 2006) is based on familial AD mutations and the model overexpresses human amyloid precursor protein (*APP*) and presenilin 1 (*PS1*) mutations. 5XFAD is a model of aggressive amyloidosis exhibiting A β deposition as early as ~2 months of age (Oakley et al., 2006). In addition, a number of similarities between this AD animal model and human AD have been documented, including loss of synaptic markers, cognitive impairment (Eimer & Vassar, 2013; Oakley et al., 2006) and importantly, association of BChE with AD pathology (Darvesh & Reid, 2016; Reid & Darvesh, 2015). 5XFAD, WT, BChE-KO and 5XFAD/BChE-KO mice were produced and strains maintained as outlined previously (DeBay, Reid, Macdonald, et al., 2017).

A summary of mice demographics including age, sex, sample size (n) and average injected dose for each radioligand is seen in Table 3.1.

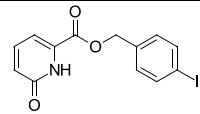
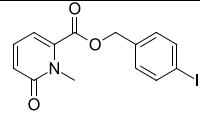
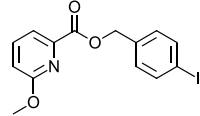
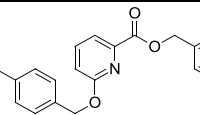
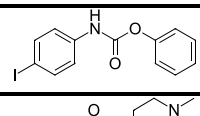
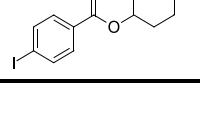
TRV #	Structure	IUPAC Name	Modality	5XFAD n (M,F)	WT n (M,F)	BCHE-KO n (M,F)	Age (months)	ID (mCi) Total Cts (x10 ⁶)
TRV7005		(<i>p</i> -Iodophenyl)methyl 6-oxo-1H-pyridine-2-carboxylate	2D dynamic planar scintigraphy	4 (4M,0F)	4 (4M,0F)	1 (5X-BCHE-KO) (1M,0F)	(11.2 ± 0.2)	(1.45 ± 0.114) mCi (9.08 ± 1.12)
TRV7006		(<i>p</i> -Iodophenyl)methyl 1-methyl-6-oxo-1H-pyridine-2-carboxylate	2D dynamic planar scintigraphy	n/a	3 (0M,3F)	1 (BCHE-KO) (0M,1F)	(12.3 ± 0.0)	(0.959 ± 0.029) mCi (6.56 ± 0.15)
TRV7019		(<i>p</i> -Iodophenyl)methyl 6-methoxy-2-pyridinecarboxylate	2D dynamic planar scintigraphy	3 (0M,3F)	3 (0M,3F)	n/a	(12.7 ± 0.3)	(1.398 ± 0.200) mCi (9.21 ± 1.38)
TRV7040		Benzyl 6-[(<i>p</i> -iodophenyl)methoxy]-2-pyridinecarboxylate	2D dynamic planar scintigraphy/ 3D SPECT	2 (2M,0F)	2 (1M,1F)	n/a	(8.4 ± 1.1)	(1.175 ± 0.130) mCi (7.15 ± 0.86)
TRV5001		<i>p</i> -Iodophenylamino benzoate	2D dynamic planar scintigraphy	2 (0M,2F)	1 (0M,1F)	n/a	(5.1 ± 0.8)	(0.871 ± 0.062) mCi (6.19 ± 0.36)
TRV6001		<i>N</i> -Methylpiperidin-4-yl 4-iodobenzoate	2D dynamic planar scintigraphy	n/a	1 (1M,0F)	1 (5X-BCHE-KO) (1M,0F)	(10.1 ± 0.0)	(0.864 ± 0.110) mCi (3.20 ± 0.75)

Table 3.1 2D dynamic planar scintigraphy subject demographics, grouped by butyrylcholinesterase (BChE) [¹²³I] radioligand. IUPAC = International Unit of Pure and Applied Chemistry nomenclature; n = number of subjects; M = male; F = female; ID = injected dose in millicuries (mCi); Total cts = total counts of radioactive decay acquired over scan. Mean ± SEM.

3.5.5 2D dynamic Planar Scintigraphy

3.5.5.1 Dynamic Scintigraphy Acquisition

At least two hours prior to imaging, mice were weighed and given an intraperitoneal (IP) injection of Lugol's solution (potassium iodide (KI)), dosed at 8.63uL/g to block potential accumulation (albeit a small proportion) of free [^{123}I] in the thyroid, a gland that avidly uptakes [^{123}I] in the form of Na[^{123}I]. Mice were then placed in an induction chamber, anaesthetized with 3% isoflurane (in 97% oxygen) and restrained in a TailVeiner Restrainer (Braintree Scientific Inc., Braintree MA, USA) while under a continuous stream of 1.5% isoflurane gas. A custom built, in-house catheter line (30-gauge, 0.5 inch needle; 0.025/0.012 inch polyethylene tubing, Braintree Scientific Inc., Braintree MA, USA) was placed in the lateral tail vein. Mice were then secured in prone position, wrapped in a blanket on a heated animal bed and maintained under continuous stream of 1.5-2% isoflurane while the respiration rate monitored for the duration of the imaging procedure (SA Instruments Inc. Stony Brook, NY). Scans were acquired with a SPARKTM SRT-50 tabletop SPECT scanner (Cubresa Inc., MB, CA) equipped with a 1mm diameter single pinhole tungsten collimator (SciVis GmbH, Göttingen, Germany) with a transaxial aperture field of view (FOV) of 30mm and inherent sensitivity of 50 cps/MBq. The mouse head region was centered on the scanner's FOV and demarked with fiducial markers incubated with [^{123}I] and integrated within the imaging bed. A 2D planar scintigraphy acquisition was initiated, acquired as a continuous lateral projection over 60 minutes. Two minutes after the start of the scan, each radioligand was administered through the tail vein catheter line over ~15sec and

subsequently flushed with ~20 μ L saline. A summary of the average injected doses of each radioligand is seen in Table 3.1.

2D planar scintigraphy projections were converted to list mode data using built-in Cubresa SPARKTM preprocessing routine at 159 keV with a 20% energy window applied. Images were reconstructed to a 208X208 matrix, yielding a resolution of 0.8mm. List mode data of the 60 minute scan were then re-binned into 60 second frames giving an effective temporal resolution of 60 sec for each projection image.

3.5.5.2 3D SPECT/CT Imaging of TRV7040

For radioligand TRV7040, corroboration with three-dimensional (3D) SPECT was performed to more closely evaluate the regional distribution of tracer in the brain. Animal preparation for SPECT imaging followed a similar procedure outlined in section 3.5.5.1 with the following modifications. Mice received an IV injection of TRV7040 (1.27mCi in 210 μ L), followed by a saline flush of ~10 μ L. Tracer uptake occurred in conscious mice over 10 minutes. The mouse head region was centered on a 14mm axial field of view (FOV) and a 3D static SPECT scan was acquired in super list mode (SLM) over 40 minutes (4 projections) on the SPARKTM SRT-50 single head standalone tabletop SPECT scanner (Cubresa Inc., Winnipeg, MB) integrated with a Triumph XO LabPET pre-clinical computed tomography (CT) scanner (Trifoil Imaging, CA). Following SPECT imaging, a CT scan was acquired for anatomical reference. CT images were collected in fly mode with a 70 kVp x-ray beam energy (160 μ A beam current), 512 projections, 4 summed frames/projection, with 2 \times 2 binning and magnification of 2.26X, providing complete whole brain coverage in a 56mm FOV. CT scan duration was 8.5min.

3.5.5.3 2D Dynamic Planar Scintigraphy Imaging and Statistical Analyses

At the frame of peak tracer concentration in the brain (C_{\max}), a 5mmx15mm rectangular ROI was manually placed over the lateral whole brain projection (aligned with the fiducial markers) and then propagated over each of the remaining 59 frames for analysis in VivoQuant® (Invicro, Boston, MA). Mean whole brain projection ROI values of each frame were extracted and used to generate time-activity curves of the 60-minute scintigraphy acquisition. Time-activity curves were expressed as a percentage relative to the peak concentration (i.e. $\%C_{\max}$) of tracer that reached the brain.

The brain retention characteristics of each radioligand were evaluated by fitting a single mono-exponential decay function (Figure 4.1), via iterative least squares method to the respective radioligand's time-activity curves depicting $\%C_{\max}$ in the brain.

Exponential fits were constrained to start at a peak brain concentration, C_{\max} , of 100%.

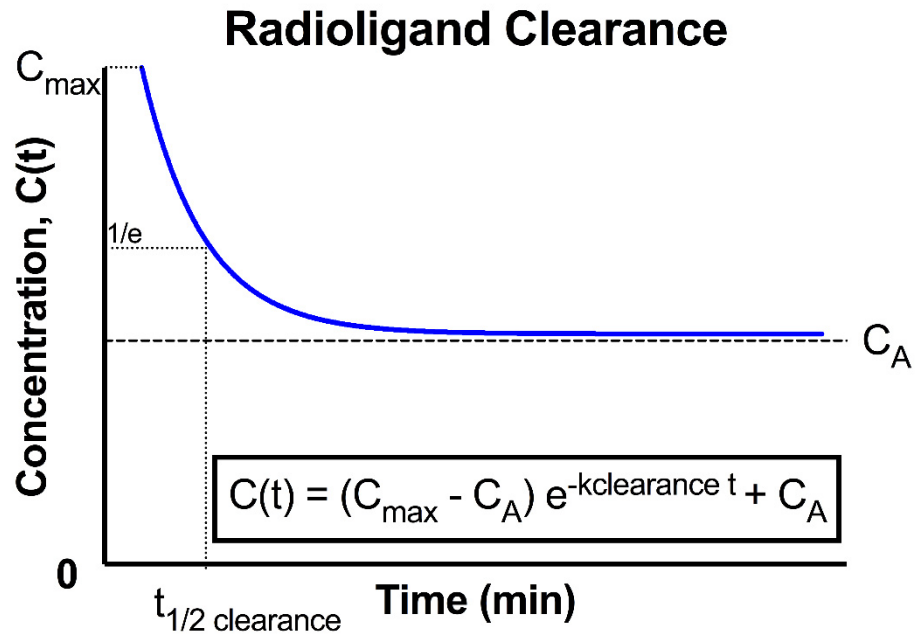


Figure 3.1 Radioligand concentration in the brain as a function of time, $C(t)$, depicting the single-phase clearance of a radiotracer from the brain with an initial peak concentration, C_{\max} . Clearance is expressed as a decreasing monoexponential function with associated kinetic parameters $t_{1/2 \text{ clearance}}$ (the half-life of tracer clearance (min)), $k_{\text{clearance}}$ (the rate of tracer clearance (min^{-1})), and C_A (the asymptotic tracer concentration, expressed as $\%C_{\max}$).

Goodness of fit of the resultant exponential curves was evaluated using R^2 and standard deviation of the residuals ($S_{y,x}$) metrics, with higher R^2 and lower $S_{y,x}$ values indicating fits that better-describe the overall data. Exponential fitting was performed in PRISM 8.0 (GraphPad, San Diego, CA). Three derived parameters of the exponential fits were evaluated, providing summary measures of radiotracer clearance, namely, the rate constant of tracer clearance, $k_{clearance}$ (min^{-1}), the half-life of tracer clearance, $t_{1/2\ clearance}$ (min), and the asymptotic concentration of tracer, C_A ($\%C_{\text{max}}$).

For each radioligand, group means of these derived summary measures were compared between mouse strains imaged using independent samples student t-tests at a significance level of 5% ($p < 0.05$), assuming equal variances (to permit statistical comparison among even those groups with only single mice represented).

A separate analysis of these summary measures was performed to evaluate the inter-tracer differences in kinetic summary measures using an analysis of variance (ANOVA) statistical design. If significant, post-hoc analyses were subsequently carried out to compare groups using least significant difference (LSD) comparisons. All statistical tests were performed in SPSS (IBM, Armonk, NY).

3.6 Results

3.6.1 Physicochemical Profile of [^{123}I] Radioligands

In general, radioligands possessed favourable physicochemical characteristics, registering MPO scores that ranged between 3.43-4.74 for TRV7005, TRV7006, TRV7019, TRV5001 and TRV6001, while TRV7040 had a lower MPO score of 2.41. A

summary of all six physicochemical properties that comprise the MPO score for a given radioligand is seen in Table 3.2. A central nervous system (CNS) radioligand with MPO ≥ 3 has a high probability of crossing the blood brain barrier. A desirable CNS radioligand typically possesses a lower MW (≤ 360 g/mol), possess a TPSA between 40-90, have fewer HBD (≤ 0.5), and favours smaller ClogP (≤ 3), ClogD (≤ 2) and pKa (≤ 8) values.

3.6.2 *In Vitro* Enzyme Kinetic Profile of [¹²³I] Radioligands

Evaluation of enzyme kinetic revealed that [¹²³I] radioligands in the current study had favourable *in vitro* kinetic profiles, suggesting suitable specificity for BChE. A complete summary of *in vitro* enzyme kinetic parameters is seen in Table 3.3.

3.6.3 Radiosynthesis

[¹²³I] radioligands were successfully synthesized with all radioligands achieving sufficiently good radiochemical yields, with a range between 56.5-87% and high radiochemical purity, with a range between 95.2-99.9% among the radioligands evaluated. A full summary of these radiosynthesis results is seen in Table 3.3.

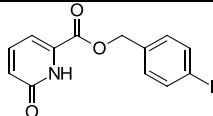
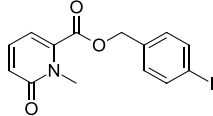
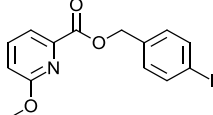
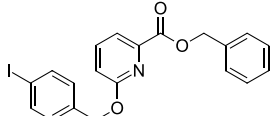
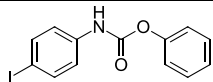
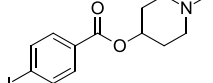
TRV #	Structure	Name	MW (g/mol)	TPSA	pKa	clogP/clogD	HBD	MPO
TRV7005		(<i>p</i> -Iodophenyl)methyl 6-oxo-1H-pyridine-2- carboxylate	355.13	55.4	9.51	2.68 / 2.67	1	4.74
TRV7006		(<i>p</i> -Iodophenyl)methyl 1-methyl-6-oxo-1H- pyridine-2- carboxylate	369.15	48.33	20	2.9 / 2.9	0	4.50
TRV7019		(<i>p</i> -Iodophenyl)methyl 6-methoxy-2- pyridinecarboxylate	369.15	48.42	20	4.04 / 4.04	0	3.43
TRV7040		Benzyl 6-[(<i>p</i> - iodophenyl)methoxy]- 2-pyridinecarboxylate	445.26	48.42	20	5.76 / 5.76	0	2.41
TRV5001		<i>p</i> -Iodophenylamino benzoate	339.13	38.33	12.3	3.44 / 3.45	1	3.80
TRV6001		<i>N</i> -Methylpiperidin-4- yl 4-iodobenzoate	345.18	29.54	7.72	3.05 / 3.45	0	4.73

Table 3.2 Physicochemical profile of lead butyrylcholinesterase (BChE) [¹²³I] radioligands, evaluated from six physicochemical properties including MW, molecular weight; TPSA, topological polar surface area; pKa, most basic center ; clogP, calculated partition coefficient; clogD, calculated distribution coefficient at pH 7.4 and HBD, hydrogen bond donors. These properties are evenly weighted and scored between 0-1 to give a composite Multiparametric Optimization (MPO) score (Wager et al., 2010). In general, a central nervous system (CNS) radioligand with MPO ≥4 has a high probability of crossing the blood brain barrier. A desirable CNS radioligand typically possesses a lower MW (≤360g/mol), possess a TPSA between 40-90, have fewer HBD (≤0.5), and favours smaller ClogP (≤3), ClogD (≤2) and pKa (≤8) values.

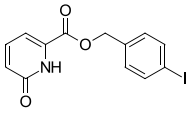
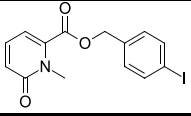
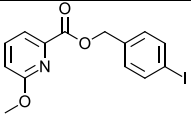
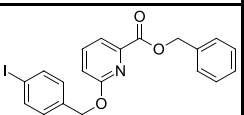
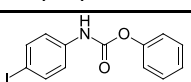
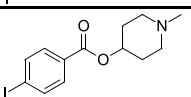
TRV #	Structure	Name	Enzyme Kinetics					Radiosynthesis	
			V_{max} (M•min ⁻¹)	k_{cat} (min ⁻¹)	K_m	K_{cat} / K_m	K_i (min ⁻¹)	RCY (%)	RCP (%)
TRV7005		(<i>p</i> -Iodophenyl)methyl 1-methyl-6-oxo-1 <i>H</i> -pyridine-2-carboxylate	n/a	4900	1.5x10 ⁻⁵	3.3x10 ⁸	4.38x10 ⁻⁵	68	96.3
TRV7006		(<i>p</i> -Iodophenyl)methyl 6-methoxy-2-pyridinecarboxylate	n/a	3000	2.1x10 ⁻⁵	1.5x10 ⁸	3.1x10 ⁻⁵	56.5	95.2
TRV7019		Benzyl 6-[(<i>p</i> -iodophenyl)methoxy]-2-pyridinecarboxylate	n/a	80000	1.1x10 ⁻⁴	7.6x10 ⁸	8.8x10 ⁻⁶	74.2	99.9
TRV7040		<i>p</i> -Iodophenylamino benzoate	not substrate or inhibitor	not substrate or inhibitor	not substrate or inhibitor	not substrate or inhibitor	not substrate or inhibitor	78.7	98.8
TRV5001		<i>p</i> -Iodophenylamino benzoate	n/a	n/a	n/a	n/a	n/a	87	96
TRV6001		<i>N</i> -Methylpiperidin-4-yl 4-iodobenzoate	21.0x10 ⁻⁶	328	123x10 ⁻⁶	2.7x10 ⁶	n/a	83	98

Table 3.3 *In vitro* enzyme kinetic parameters and radiosynthesis results of candidate butyrylcholinesterase (BChE) [¹²³I] radioligands. For *in vitro* kinetics, the maximal enzymatic reaction rate, V_{max} (M•min⁻¹), k_{cat} (min⁻¹) rate of the first committed chemical step, K_m Michaelis constant, enzymatic efficiency (K_{cat}/K_m) and K_i , inhibition equilibrium constant were evaluated. In general, an effective BChE radioligand possesses a higher value of V_{max} , k_{cat} , k_{cat}/K_m and K_i and a lower K_m value. The radiosynthesis of these tracers resulted in a radiochemical yield (RCY) between (56.5 – 87)% and a radiochemical purity (RCP) between (95.2 – 99.9)%.

3.6.4 2D Dynamic Planar Scintigraphy

The following results describe the 2D dynamic planar scintigraphy imaging findings of six BChE radioligands that were administered through IV tail vein injections into mice two minutes after the start of a 60-minute scintigraphy scan that was acquired in the lateral plane. Whole brain time-activity curves were generated from which a single exponential function was fitted to determine kinetic parameters of tracer clearance from the brain. Goodness of fit metrics for each radioligand are seen in Table 3.4 and in general, indicate a strong correspondence of the fitted curves with the measured scintigraphy time-activity curve data suggesting that this approach adequately describes the clearance characteristics for each radiotracer.

In the subsequent sections, time-activity curves for each radioligand are shown in sequence following the scintigraphy image series and are also shown in a combined summary panel at the end of the current section (Figure 3.21).

In general, scintigraphy projections of the mouse brain showed sufficient image quality, generating between (3.20 ± 0.75) – (9.21 ± 1.38) million counts across radioligands (Table 3.1). Scintigraphy images could delineate whole brain from other extracranial structures in close proximity. Differential patterns of distribution were observed over time between the various radioligands evaluated, as detailed in subsequent sections.

¹²³ I Radioligand	Goodness of fit		
	mean ± SEM (range)		
	R ²	SS	Sy.x
TRV7005	0.93 ± 0.02 (0.76 – 0.98)	446 ± 59 (122 - 684)	2.87 ± 0.17 (2.05 – 3.56)
TRV7006	0.92 ± 0.02 (0.88 - 0.97)	392 ± 52 (271 - 494)	2.68 ± 0.18 (2.24 - 3.03)
TRV7019	0.95 ± 0.01 (0.93 – 0.98)	159 ± 13 (132 - 202)	1.71 ± 0.07 (1.57 – 1.93)
TRV7040			
TRV5001	0.91 ± 0.04 (0.84 – 0.97)	446 ± 59 (137 - 303)	2.13 ± 0.26 (1.62 – 2.39)
TRV6001	0.94 ± 0.02 (0.92 – 0.96)	219 ± 68 (151 – 287)	2.04 ± 0.33 (1.71 – 2.37)

Table 3.4 Goodness of fit metrics for each [¹²³I] radioligand modeled by a single decreasing exponential function. R², Sum of squares (SS), and standard deviation of residuals (Sy.x) were evaluated for the brain clearance curves for each radioligand. Mean ± SEM shown in addition to the range of values in parentheses. Smaller SS, Sy.x values and R² values closer to 1.0 indicating better overall fits. In general, these goodness of fit metrics indicated a strong correspondence with the measured scintigraphy time-activity curve data, suggesting that this approach adequately describe the radioligand clearance kinetics for each radiotracer. TRV 7040 was not evaluated as it did not cross the blood-brain barrier.

3.6.4.1 TRV7005

2D dynamic planar scintigraphy scans revealed significant whole brain uptake of TRV7005, confirming the ability of TRV7005 to cross the blood-brain barrier (BBB). Representative images series for 5XFAD and WT mice are seen in Figure 3.2 and Figure 3.3, respectively. Peak radioligand uptake occurred in the 5XFAD and WT brain at frame 4 (2 minutes post-injection) in all but one WT mouse (frame 5), with uptake largely restricted to the brain and subsequent washout of TRV7005 from the brain in both 5XFAD and WT mice was apparent by visual inspection over the scan duration (Figure 3.2, Figure 3.3). A diffusely distributed background signal was also seen in extracranial regions within the animal as the scan progressed. Whole brain time-activity curves are seen in Figure 3.4, presented as mean time activity curves for 5XFAD and WT groups (Figure 3.4A, Figure 3.20A), as individual subject data with corresponding fits (Figure 3.4B, Figure 3.20B) and as fitted curves alone (Figure 3.4C, Figure 3.20C). Mean time-activity curves for 5XFAD and WT were similar, with considerable overlap apparent between the time-activity curves of the two groups (Figure 3.4A), save a subtle divergence of the curves observed between 5-15 minutes suggesting a short period of latent clearance in the 5XFAD brain, that subsequently reaches values similar to that of WT. Nevertheless, no significant differences were observed in the overall rate of tracer clearance, $k_{clearance}$ (5XFAD = $0.12 \pm 0.03 \text{ min}^{-1}$; WT = $0.12 \pm 0.02 \text{ min}^{-1}$; $p = 0.971$) the half-life of clearance, $t_{1/2clearance}$ (5XFAD = $6.51 \pm 1.19 \text{ min}$; WT = $7.21 \pm 1.75 \text{ min}$; $p = 0.756$) or asymptotic tracer concentration, C_A (5XFAD = $49.2 \pm 5.10\%$; WT = $42.5 \pm 1.03\%$; $p = 0.281$) between 5XFAD and WT groups (Figure 3.21A-C, Table 3.5).

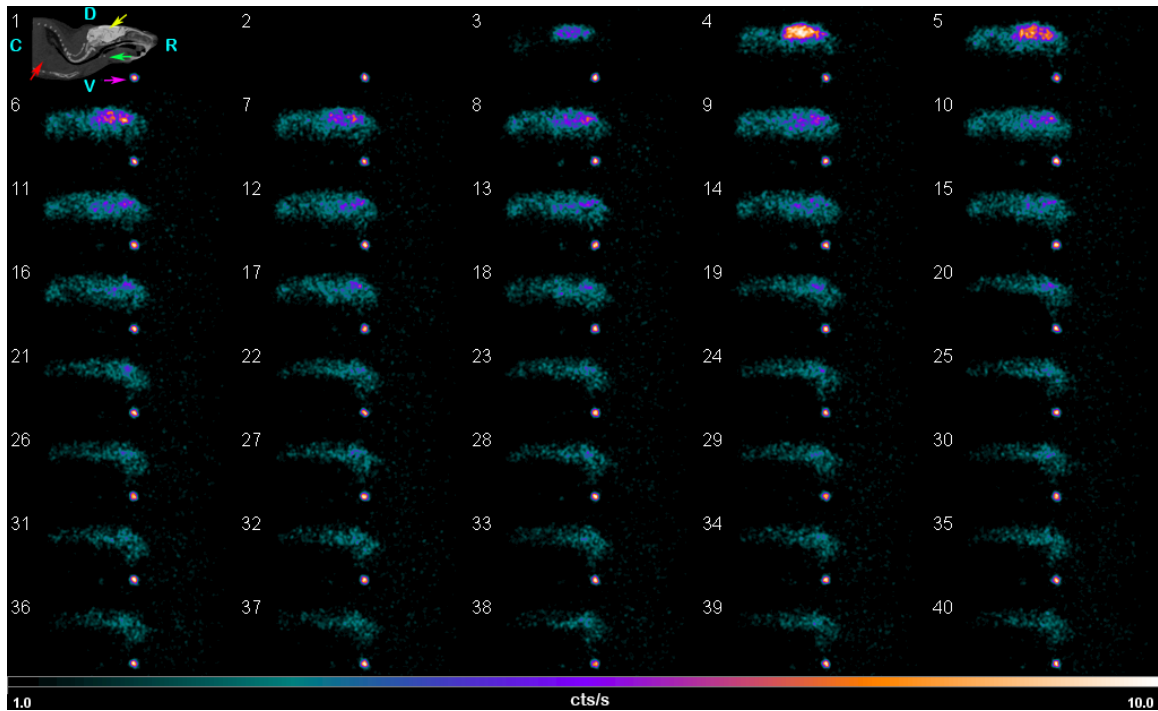


Figure 3.2 TRV7005 dynamic planar scintigraphy scans for a representative 5XFAD mouse. Lateral projections were acquired dynamically over 60 minutes with radioligand administration occurring 2 minutes after the start of the scan. Images were binned into 60X 1-minute frames for analysis (frames 1-40 displayed in the figure, denoted numerically in white at the top left of each image). A fused CT/MRI overlay serves as an anatomical reference in frame 1 indicating brain (yellow arrow), heart (red arrow), thyroid/salivary gland region (green arrow) and integrated fiducial marker placed at the most rostral extent of the olfactory bulb (purple arrow). D=dorsal; V=ventral, R= rostral; C = caudal. TRV7005 crossed the blood-brain barrier (BBB) and was taken up in the brain with peak radiotracer accumulation occurring at 2 minutes post-injection (frame 4) in 5XFAD mice. Radiotracer uptake was largely restricted to the brain with subsequent washout of TRV7005 apparent over the course of the scan. A diffuse distribution of background signal is also seen extracranially within the animal over the course of the scan. Corresponding whole brain time-activity curves are seen in Figure 3.4, Figure 3.20 and associated kinetic summary measures of tracer clearance are seen in Figure 3.21, Table 3.5. Colour scale represents average counts per second (cts/s) in a given image pixel.

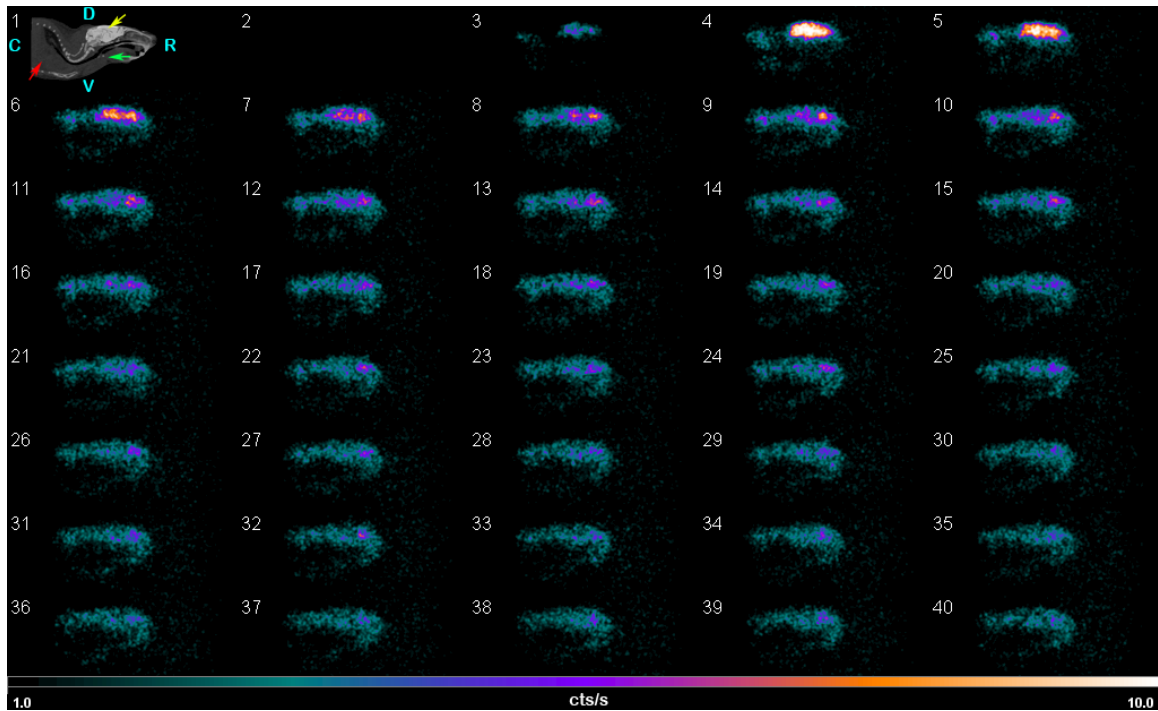


Figure 3.3 TRV7005 dynamic planar scintigraphy scans for a representative WT mouse. Lateral projections were acquired dynamically over 60 minutes with radioligand administration occurring 2 minutes after the start of the scan. Images were binned into 60X 1-minute frames for analysis (frames 1-40 displayed in the figure, denoted numerically in white at the top left of each image). A fused CT/MRI overlay serves as an anatomical reference in frame 1 indicating brain (yellow arrow), heart (red arrow), thyroid/salivary gland region (green arrow). D=dorsal; V=ventral, R= rostral; C = caudal. TRV7005 crosses the blood-brain barrier (BBB) and is taken up in the brain with peak tracer concentration (C_{max}) occurring at 2 minutes post-injection (frame 4) in all but one WT mouse (C_{max} reached at 3 minutes post-injection). As in 5XFAD, radiotracer uptake was largely restricted to the brain with subsequent washout of TRV7005 apparent over the course of the scan. A diffuse distribution of background signal is also seen extracranially within the animal over the course of the scan. Corresponding whole brain time-activity curves are seen in Figure 3.4, Figure 3.20 and associated kinetic summary measures of tracer clearance are seen in Figure 3.21, Table 3.5. Colour scale represents average counts per second (cts/s) in a given image pixel.

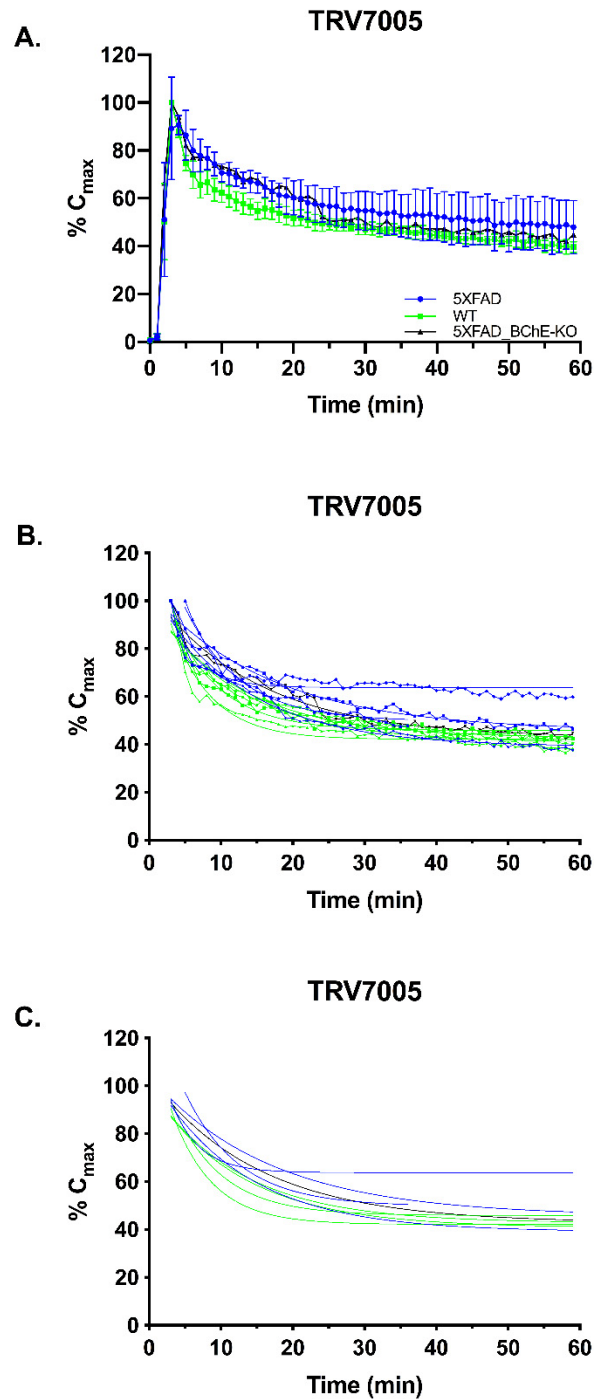


Figure 3.4 Whole brain time-activity curves for TRV7005 expressed as percent of peak concentration (%C_{max}) in brain. **A.** Mean time-activity curves (mean ± SEM) are shown for WT (green), 5XFAD (blue) and 5XFAD-BChE-KO (black). **B.** Time-activity curves of individual mice and corresponding fitted exponential function (solid line). **C.** Fitted exponential functions alone for individual mice from which kinetic summary measures were derived and compared (Table 3.5, Figure 3.21).

3.6.4.2 TRV7006

TRV7006, a structurally similar radioligand to TRV7005, also readily crosses the BBB and is taken up in the brain. Representative image series for WT and BChE-KO mice are seen in Figure 3.5 and Figure 3.6, respectively. Peak radioligand uptake reliably occurred at frame 4 (2 minutes post-injection) in the WT and BChE-KO mice. A similar pattern of brain uptake was observed to that of TRV7005 (Figure 3.5, Figure 3.6).

Washout of TRV7006 also occurred in both WT and BChE-KO mice. Whole brain time-activity curves are seen in Figure 3.7, presented as mean time activity curves for WT and BChE-KO mice (Figure 3.7A), as individual subject data with fitted functions (Figure 3.7B) and as fitted curves alone (Figure 3.7C). Mean time-activity curves for WT and BChE-KO demonstrated considerable overlap apparent between the time-activity curves of the two groups (Figure 3.7A). No significant differences were observed in the rate of clearance $k_{clearance}$ (WT = $0.16 \pm 0.06 \text{ min}^{-1}$; BChE-KO = $0.21 \pm 0.03 \text{ min}^{-1}$; $p = 0.525$) $t_{1/2clearance}$ (WT = $4.72 \pm 0.93 \text{ min}$; BChE-KO = $3.27 \pm 0.93 \text{ min}$; $p = 0.517$) or asymptotic tracer concentration, C_A (WT = $52.3 \pm 4.6\%$; BChE-KO = 49.3 ± 4.6 , $p = 0.770$) between WT and BChE-KO mice (Figure 3.21D-F, Table 3.5).

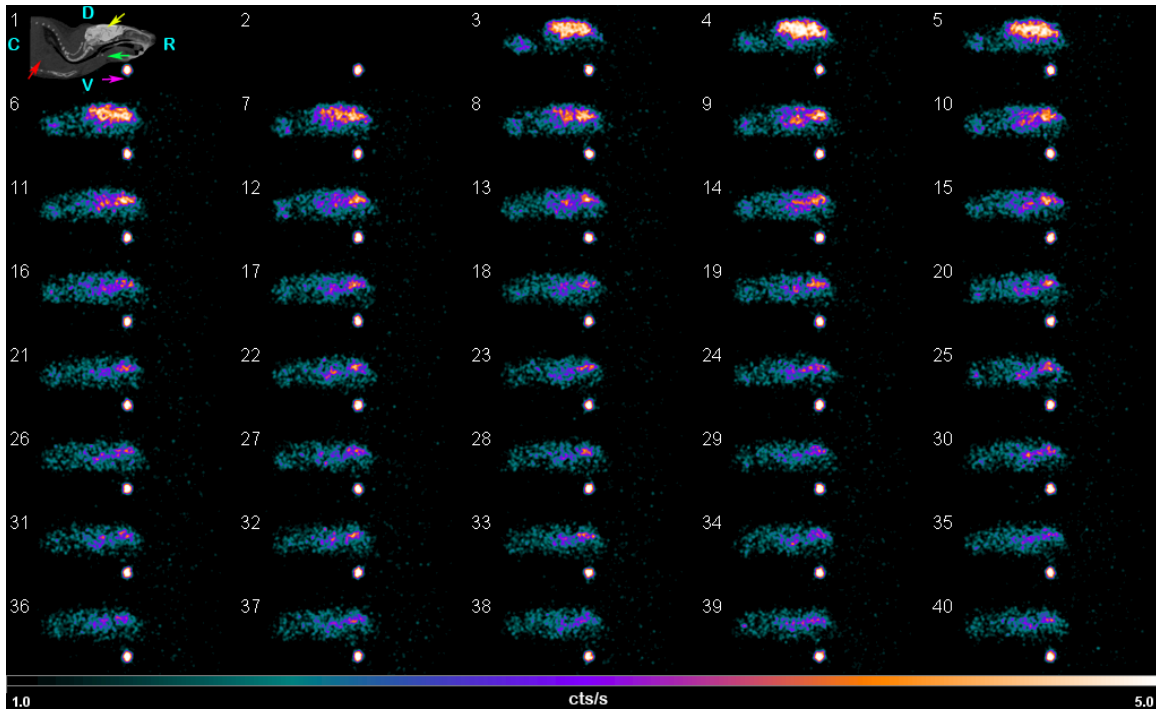


Figure 3.5 TRV7006 dynamic planar scintigraphy scans for a representative WT mouse. Lateral projections were acquired dynamically over 60 minutes with radioligand administration occurring 2 minutes after the start of the scan. Images were binned into 60X 1-minute frames for analysis (frames 1-40 displayed in the figure, denoted numerically in white at the top left of each image). A fused CT/MRI overlay serves as an anatomical reference in frame 1 indicating brain (yellow arrow), heart (red arrow), thyroid/salivary gland region (green arrow) and integrated fiducial marker placed at the most rostral extent of the olfactory bulb (purple arrow). D=dorsal; V=ventral, R= rostral; C = caudal. TRV7006 crosses the blood-brain barrier (BBB) and is taken up in the brain with peak tracer accumulation reliably occurring at 2 minutes post-injection (frame 4) in the WT mouse. A similar pattern of uptake was observed as with TRV7005, with subsequent washout apparent over the course of the scan. A diffuse distribution of background signal is also seen extracranially within the animal over the course of the scan with additional cardiac signal accumulation at early timepoints. Corresponding whole brain time-activity curves are seen in Figure 3.7, Figure 3.20 and associated kinetic summary measures of tracer clearance are seen in Figure 3.21, Table 3.5. Colour scale represents average counts per second (cts/s) in a given image pixel.

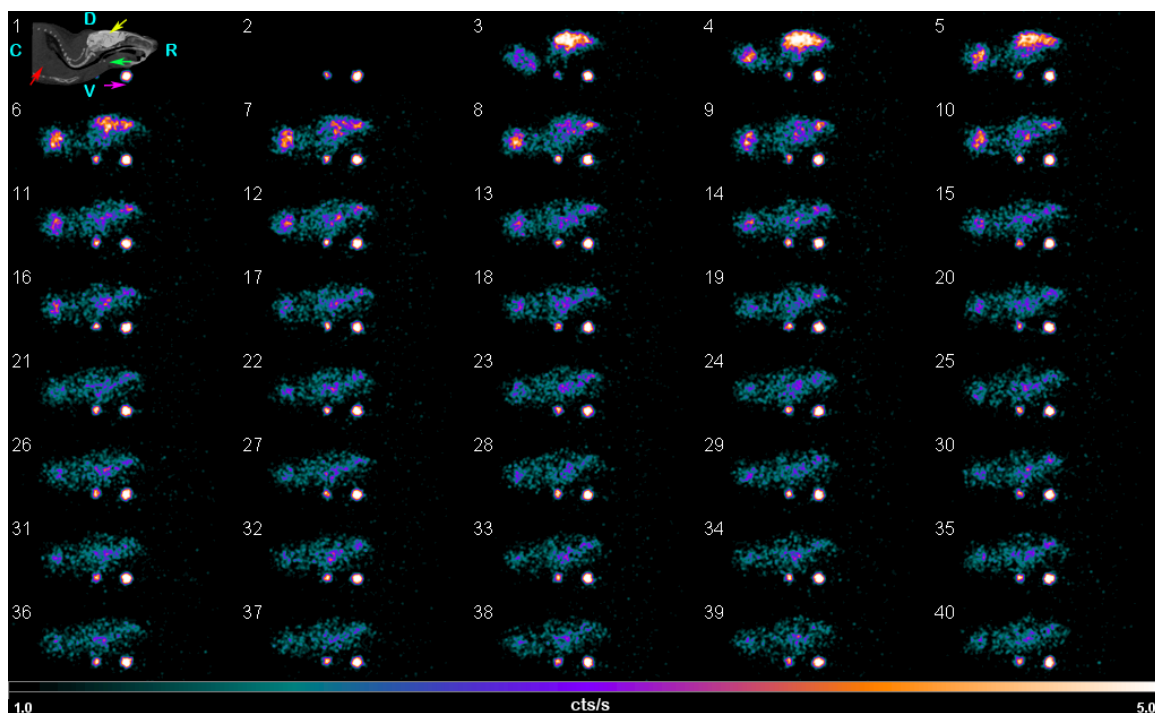


Figure 3.6 TRV7006 dynamic planar scintigraphy scans for a representative BCHE-KO mouse. Lateral projections were acquired dynamically over 60 minutes with radioligand administration occurring 2 minutes after the start of the scan. Images were binned into 60X 1-minute frames for analysis (frames 1-40 displayed in the figure, denoted numerically in white at the top left of each image). A fused CT/MRI overlay serves as an anatomical reference in frame 1 indicating brain (yellow arrow), heart (red arrow), thyroid/salivary gland region (green arrow) and integrated fiducial marker placed at the most rostral extent of the olfactory bulb (purple arrow). D=dorsal; V=ventral, R= rostral; C = caudal. TRV7006 crosses the blood-brain barrier (BBB) and is taken up in the brain with peak tracer accumulation reliably occurring at 2 minutes post-injection (frame 4) in the BCHE-KO mouse. A similar pattern of uptake was observed to WT, with subsequent washout apparent over the course of the scan. A diffuse distribution of background signal is also seen extracranially within the animal over the course of the scan with prominent cardiac signal accumulation at early timepoints. Corresponding whole brain time-activity curves are seen in Figure 3.7, Figure 3.20 and associated kinetic summary measures of tracer clearance are seen in Figure 3.21, Table 3.5. Colour scale represents average counts per second (cts/s) in a given image pixel.

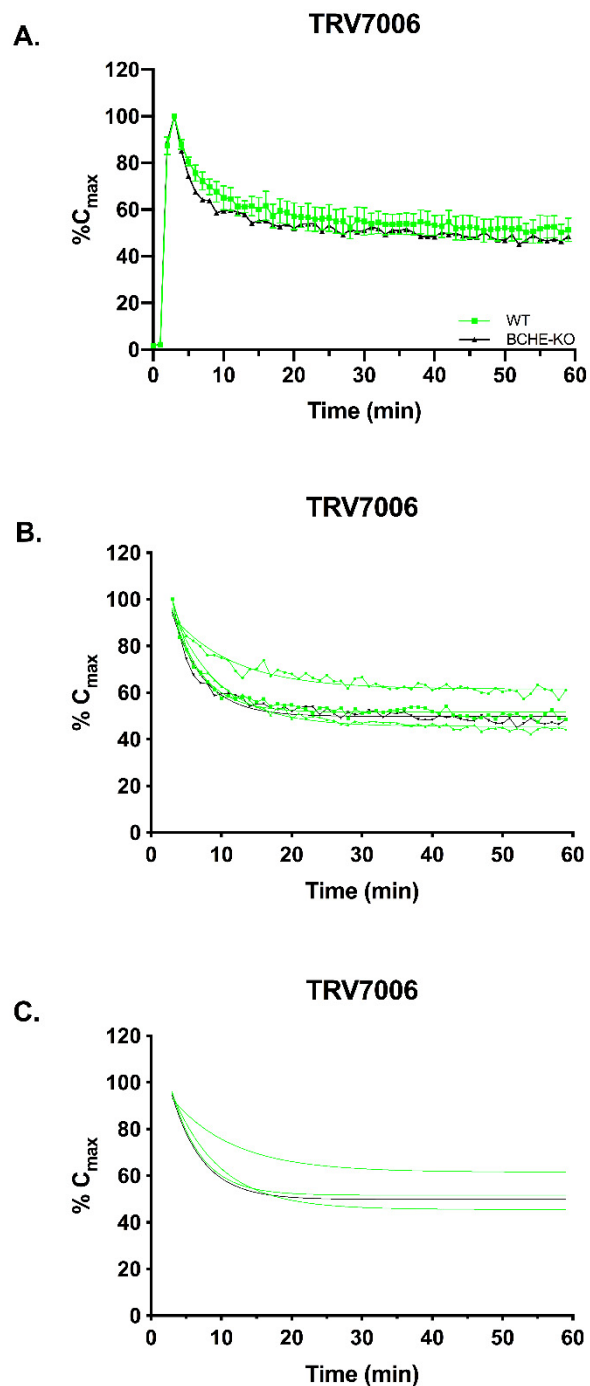


Figure 3.7 Whole brain time-activity curves for TRV7006 expressed as percent of peak concentration (%C_{max}) in brain. **A.** Mean time-activity curves (mean ± SEM) are shown for WT (green) and BChE-KO (black). **B.** Time-activity curves of individual mice and corresponding fitted exponential function (solid line). **C.** Fitted exponential functions alone for individual mice from which kinetic summary measures were derived and compared (Table 3.5, Figure 3.21).

3.6.4.3 TRV7019

TRV7019 also readily crosses the BBB and is taken up in the brain.

Representative image series for 5XFAD and WT mice are seen in Figure 3.8 and Figure 3.9, respectively. Peak brain perfusion reliably occurred at frame 3 (1-minute post-injection) in the 5XFAD and WT mice investigated, with prominent tracer uptake in the brain and notably, unlike TRV7005 and TRV7006, sustained cardiac tracer signal accumulation was a notable feature (Figure 3.8 and Figure 3.9) in addition to diffusely distributed background signal throughout the body. Washout of TRV7019 also occurred in both 5XFAD and WT mice. Whole brain time-activity curves are seen in Figure 3.10, presented as mean time activity curves for WT and BChE-KO mice (Figure 3.10A), as individual subject data with fitted functions (Figure 3.10B) and as fitted curves (Figure 3.10 C).

Mean time-activity curves for 5XFAD and WT (Figure 3.10A), showed a divergence of the curves observed between 5-15 minutes, similar to what was observed with TRV7005. Significant differences were observed in kinetic summary measures between 5XFAD and WT, where a 58% decrease in $k_{clearance}$ (5XFAD = $0.23 \pm 0.4 \text{ min}^{-1}$; WT = $0.4 \pm 0.04 \text{ min}^{-1}$; $p = 0.041$) (Figure 3.21G) and commensurate increase in $t_{1/2clearance}$ (5XFAD = $3.22 \pm 0.55 \text{ min}$; WT = $1.77 \pm 0.15 \text{ min}$ $p = 0.065$ (statistical trend)) (Figure 3.21H) were demonstrated in the 5XFAD brain. However, no significant difference in asymptotic tracer concentration, C_A (5XFAD = $56.2 \pm 5.0\%$; WT = $55.9 \pm 6.1\%$, $p = 0.964$) was apparent between 5XFAD and WT groups (Figure 3.21I). A summary of these tracer clearance metrics is seen in Figure 3.21G-I and Table 3.5.

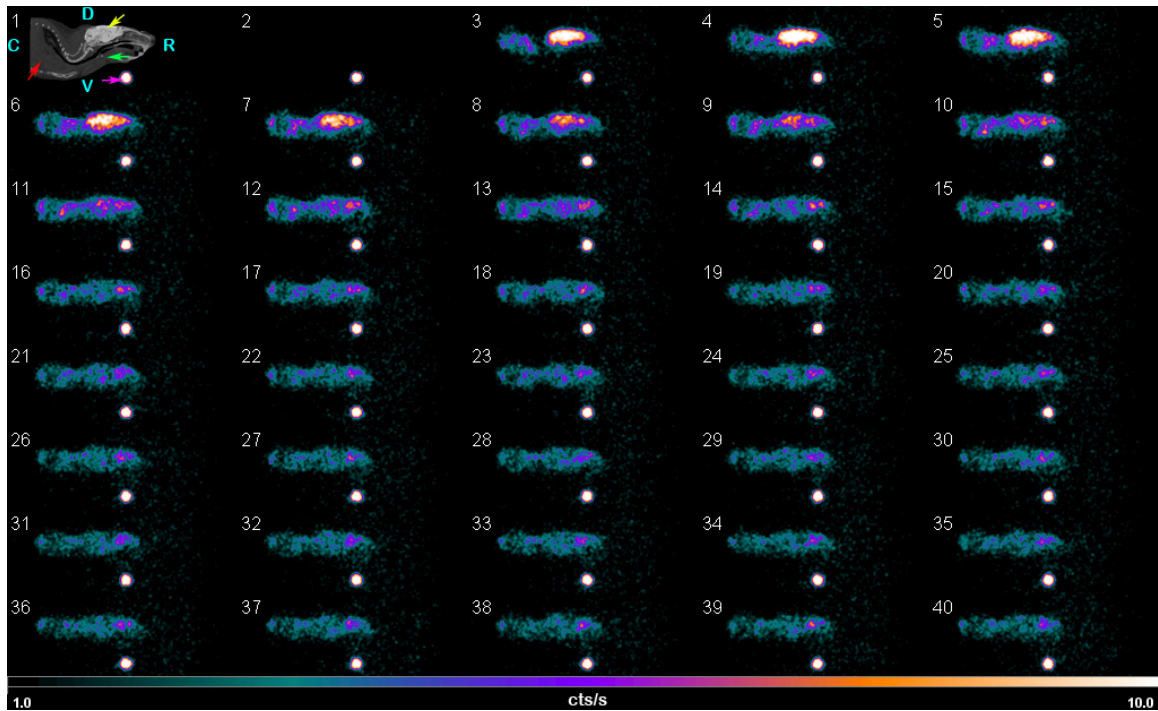


Figure 3.8 TRV7019 dynamic planar scintigraphy scans for a representative 5XFAD mouse. Lateral projections were acquired dynamically over 60 minutes with radioligand administration occurring 2 minutes after the start of the scan. Images were binned into 60X 1-minute frames for analysis (frames 1-40 displayed in the figure, denoted numerically in white at the top left of each image). A fused CT/MRI overlay serves as an anatomical reference in frame 1 indicating brain (yellow arrow), heart (red arrow), thyroid/salivary gland region (green arrow) and integrated fiducial marker placed at the most rostral extent of the olfactory bulb (purple arrow). D=dorsal; V=ventral, R= rostral; C = caudal. TRV7019 crosses the blood-brain barrier (BBB) and is taken up in the brain with peak tracer accumulation reliably occurring at 1-minute post-injection (frame 3) in 5XFAD mice. Prominent brain uptake is observed (in a similar pattern to that of TRV7005 and TRV7006) with subsequent washout of TRV7019 over the duration of the scan. A diffuse distribution of background signal is also seen extracranially within the animal over the course of the scan. Corresponding whole brain time-activity curves are seen in Figure 3.10, Figure 3.20 and associated kinetic summary measures of tracer clearance are seen in Figure 3.21, Table 3.5. Colour scale represents average counts per second (cts/s) in a given image pixel.

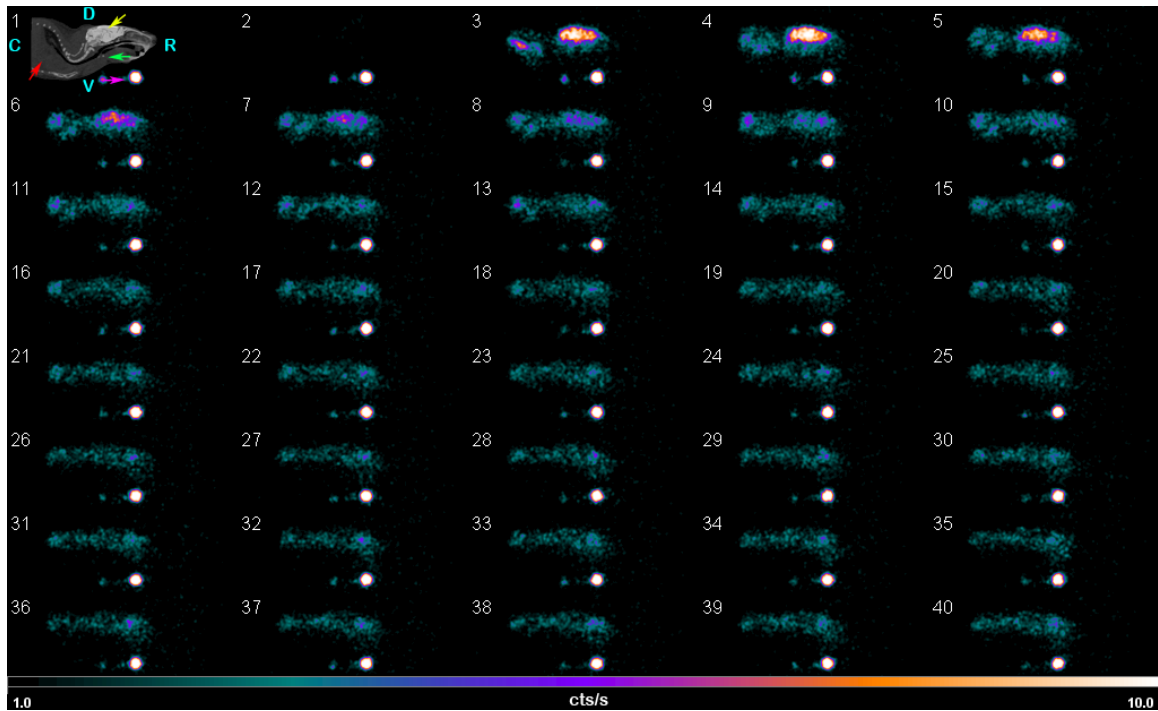


Figure 3.9 TRV7019 dynamic planar scintigraphy scans for a representative WT mouse. Lateral projections were acquired dynamically over 60 minutes with radioligand administration occurring 2 minutes after the start of the scan. Images were binned into 60X 1-minute frames for analysis (frames 1-40 displayed in the figure, denoted numerically in white at the top left of each image). A fused CT/MRI overlay serves as an anatomical reference in frame 1 indicating brain (yellow arrow), heart (red arrow), thyroid/salivary gland region (green arrow) and integrated fiducial marker placed at the most rostral extent of the olfactory bulb (purple arrow). D=dorsal; V=ventral, R= rostral; C = caudal. TRV7019 crosses the blood-brain barrier (BBB) and is taken up in the brain with peak tracer accumulation reliably occurring at 1-minute post-injection (frame 3) in WT mice. Prominent brain uptake is observed (as was observed in 5XFAD) with subsequent washout of TRV7019 over the duration of the scan. A diffuse distribution of background signal is also seen extracranially within the animal over the course of the scan. Corresponding whole brain time-activity curves are seen in Figure 3.10, Figure 3.20 and associated kinetic summary measures of tracer clearance are seen in Figure 3.21, Table 3.5. Colour scale represents average counts per second (cts/s) in a given image pixel.

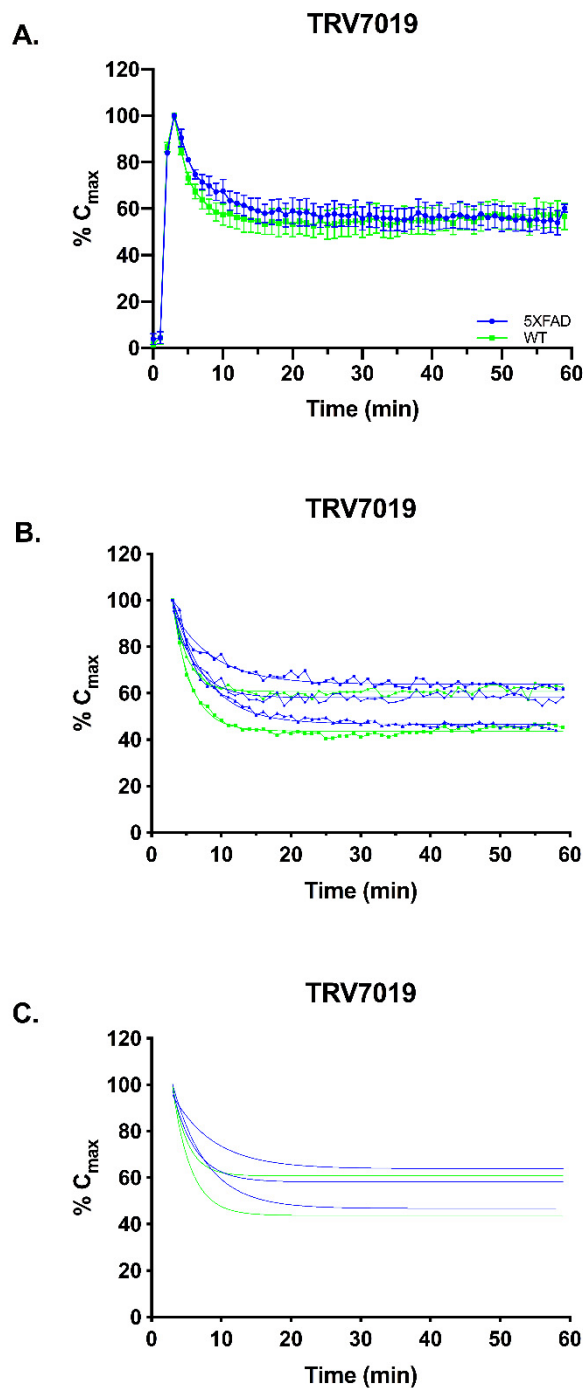


Figure 3.10 Whole brain time-activity curves for TRV7019 expressed as percent of peak concentration ($\%C_{max}$) in brain. **A.** Mean time-activity curves (mean \pm SEM) are shown for WT (green) and 5XFAD (blue). **B.** Time-activity curves of individual mice and corresponding fitted exponential function (solid line). **C.** Fitted exponential functions alone for individual mice from which kinetic summary measures were derived and compared (Table 3.5, Figure 3.21).

3.6.4.4 TRV7040

Scintigraphy imaging of TRV7040 revealed an apparent inability of the radioligand to cross the BBB in appreciable amounts. Representative images series of TRV7040 for 5XFAD and WT mice are seen in Figure 3.11 and Figure 3.12, respectively. Within 1 minute after TRV7040 injection (frame 3), signal accumulation is apparent in the heart and avid uptake of tracer in the ocular region and proximal arteries that serve this area is observed. Sustained retention in this region occurs over the duration of the 1-hour scan. Tracer accumulation in thyroid and salivary gland regions gradually emerges by 8 minutes post-injection (Frame 10), and is maintained over the duration of the scan.

Where no clear uptake in the brain was apparent, further tracer kinetic analyses were not carried out. However, 3D SPECT imaging was investigated to evaluate the precise distribution of the tracer *in vivo*. A 5XFAD mouse received 1.27mCi of radiotracer and after 10 minutes of uptake, underwent a 40min static SPECT/CT scan. Results confirm the planar scintigraphy findings, with negligible radioligand reaching the brain however, avid uptake of TRV7040 is seen in the eye and hardarian glands with a focal distribution of radiotracer seen in these regions (Figure 3.13). This is consistent with the 2D dynamic planar scintigraphy scans acquired (Figure 3.11 and Figure 3.12).

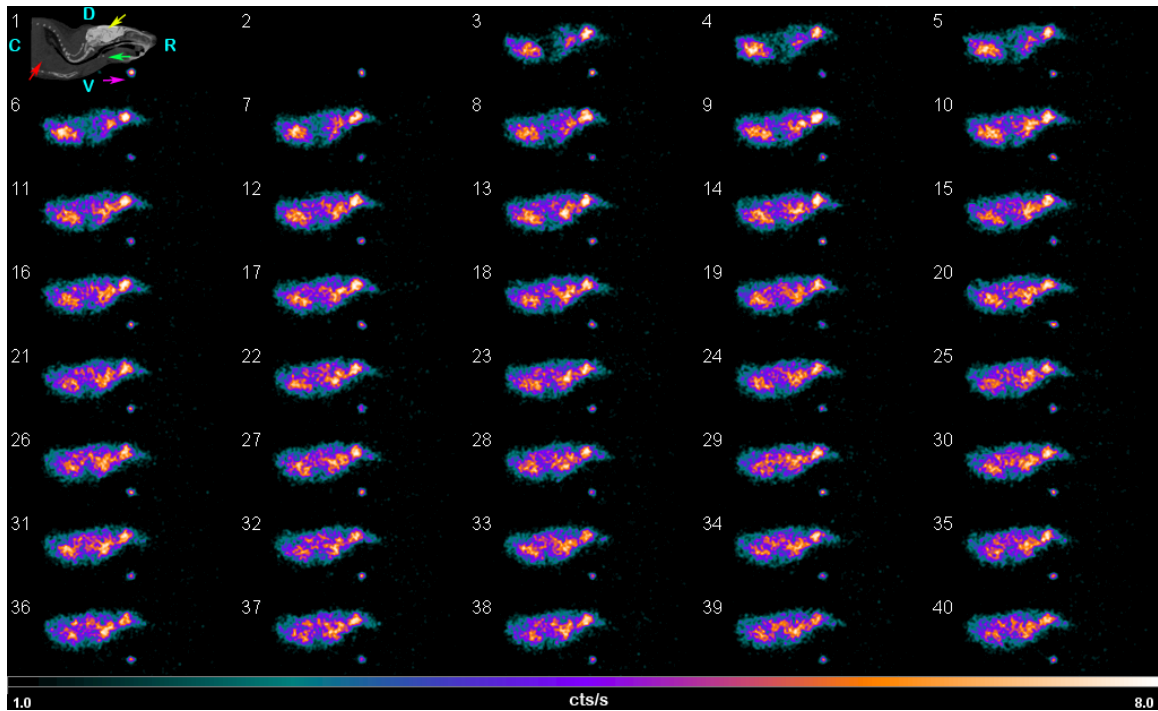


Figure 3.11 TRV7040 dynamic planar scintigraphy scans for a representative 5XFAD mouse. Lateral projections were acquired dynamically over 60 minutes with radioligand administration occurring 2 minutes after the start of the scan. Images were binned into 60X 1-minute frames for analysis (frames 1-40 displayed in the figure, denoted numerically in white at the top left of each image). A fused CT/MRI overlay serves as an anatomical reference in frame 1 indicating brain (yellow arrow), heart (red arrow), thyroid/salivary gland region (green arrow) and integrated fiducial marker placed at the most rostral extent of the olfactory bulb (purple arrow). D=dorsal; V=ventral, R= rostral; C = caudal. TRV7040 fails to cross the blood-brain barrier (BBB); however, avid uptake and sustained retention of radiotracer in the ocular region is a prominent feature with gradual accumulation of TRV7040 ventrally over time in the thyroid and salivary gland region. Strong cardiac signal accumulation is a feature of this particular TRV7040 scan. Colour scale represents average counts per second (cts/s) in a given image pixel.

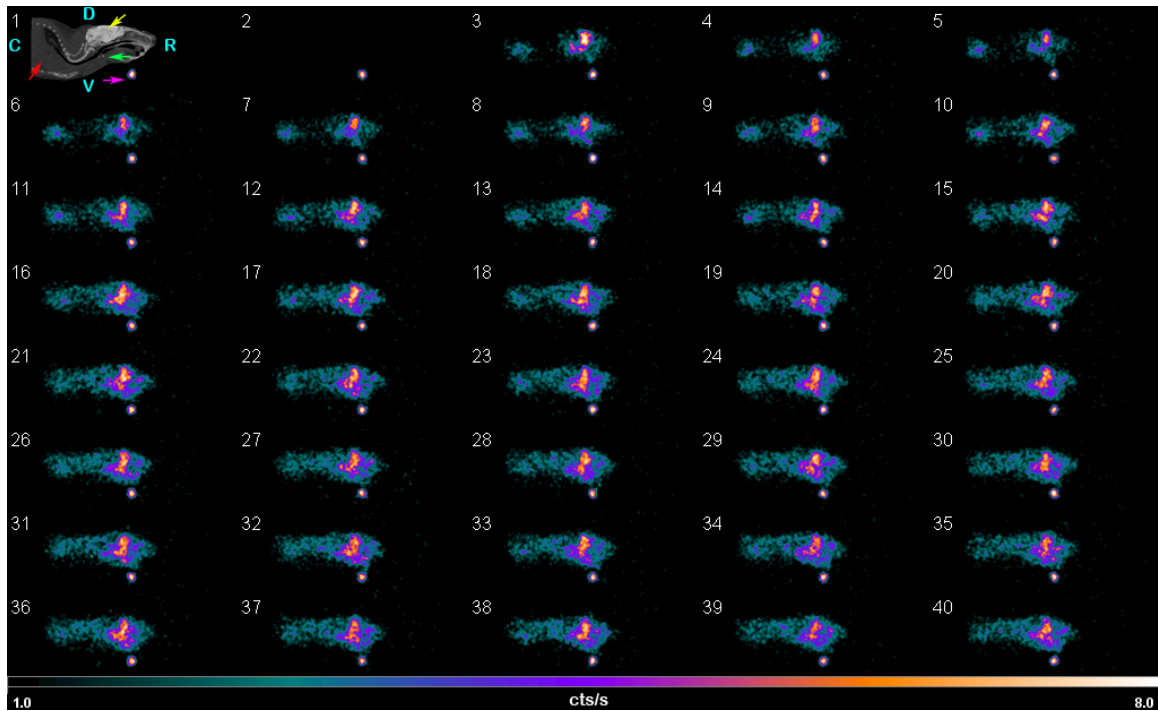


Figure 3.12 TRV7040 dynamic planar scintigraphy scans for a representative WT mouse. Lateral projections were acquired dynamically over 60 minutes with radioligand administration occurring 2 minutes after the start of the scan. Images were binned into 60X 1-minute frames for analysis (frames 1-40 displayed in the figure, denoted numerically in white at the top left of each image). A fused CT/MRI overlay serves as an anatomical reference in frame 1 indicating brain (yellow arrow), heart (red arrow), thyroid/salivary gland region (green arrow) and integrated fiducial marker placed at the most rostral extent of the olfactory bulb (purple arrow). D=dorsal; V=ventral, R=rostral; C = caudal. As in 5XFAD mice, TRV7040 fails to cross the blood-brain barrier (BBB) in WT; however, avid uptake and sustained retention of radiotracer in the ocular region is a prominent feature with gradual accumulation of TRV7040 ventrally over time in the thyroid and salivary gland region. Colour scale represents average counts per second (cts/s) in a given image pixel.

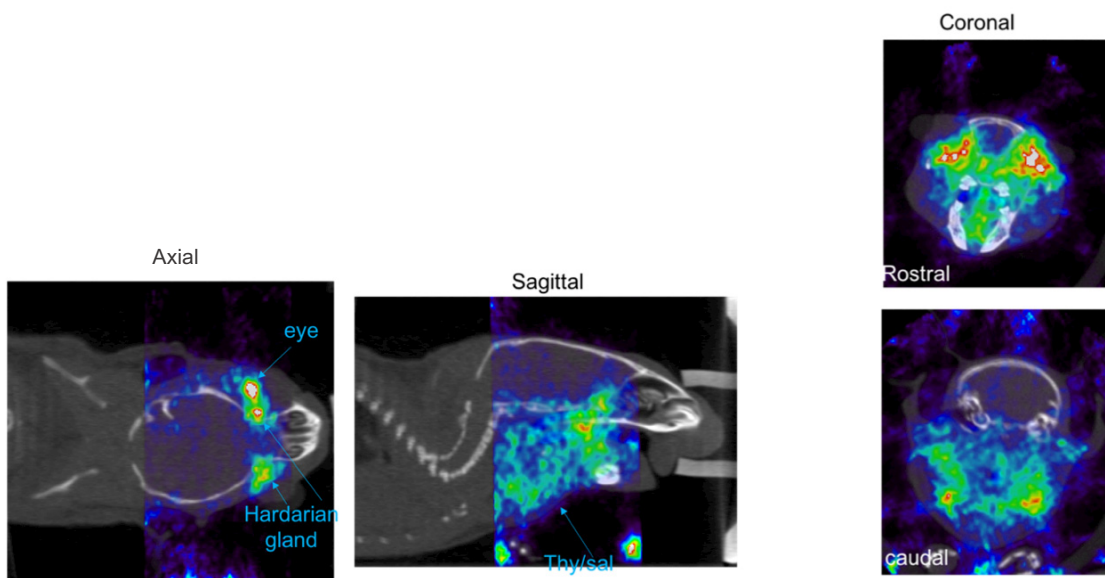


Figure 3.13 TRV7040 3D single photon emission computed tomography (SPECT) scan of a 5XFAD mouse that received 1.27mCi of radiotracer and after 10 minutes of uptake, underwent a 40 min static SPECT/CT scan. Negligible radioligand reached the brain however, avid uptake of TRV7040 is seen in the eye and Hardarian glands with a focal distribution of radiotracer seen in these regions. This is consistent with the 2D dynamic planar scintigraphy scans acquired (Figure 3.11 and Figure 3.12).

3.6.4.5 TRV5001

Dynamic scintigraphy images revealed that TRV5001 readily crosses the BBB and is taken up in the brain. Representative images series for 5XFAD and WT mice are seen in Figure 3.14 and Figure 3.15, respectively. Peak brain uptake occurred between frames 4-6 (6-8 minutes PI). Uptake was largely restricted to the brain, with elevated extracranial background signal observed within the animal (Figure 3.14 and Figure 3.15). Washout of TRV5001 was apparent by visual inspection in both 5XFAD and WT brains, albeit over a prolonged period compared to TRV7005, TRV7006 or TRV7019. Whole brain time-activity curves are seen in Figure 3.16, presented as mean time activity curves for 5XFAD and WT groups (Figure 3.16A), as individual subject data with corresponding fits (Figure 3.16B) and as fitted curves alone (Figure 3.16C).

No significant differences were observed in the overall rate of tracer clearance, $k_{clearance}$ (5XFAD = $0.12 \pm 0.03 \text{ min}^{-1}$; WT = $0.12 \pm 0.02 \text{ min}^{-1}$; $p = 0.971$) the half-life of clearance, $t_{1/2clearance}$ (5XFAD $6.51 \pm 1.19 \text{ min}$; WT = $7.21 \pm 1.75 \text{ min}$; $p = 0.756$) or asymptotic tracer concentration, C_A (5XFAD = $49.2 \pm 5.10\%$; WT = $42.5 \pm 1.03\%$; $p = 0.281$) between 5XFAD and WT groups (Figure 3.21J-L, Table 3.5).

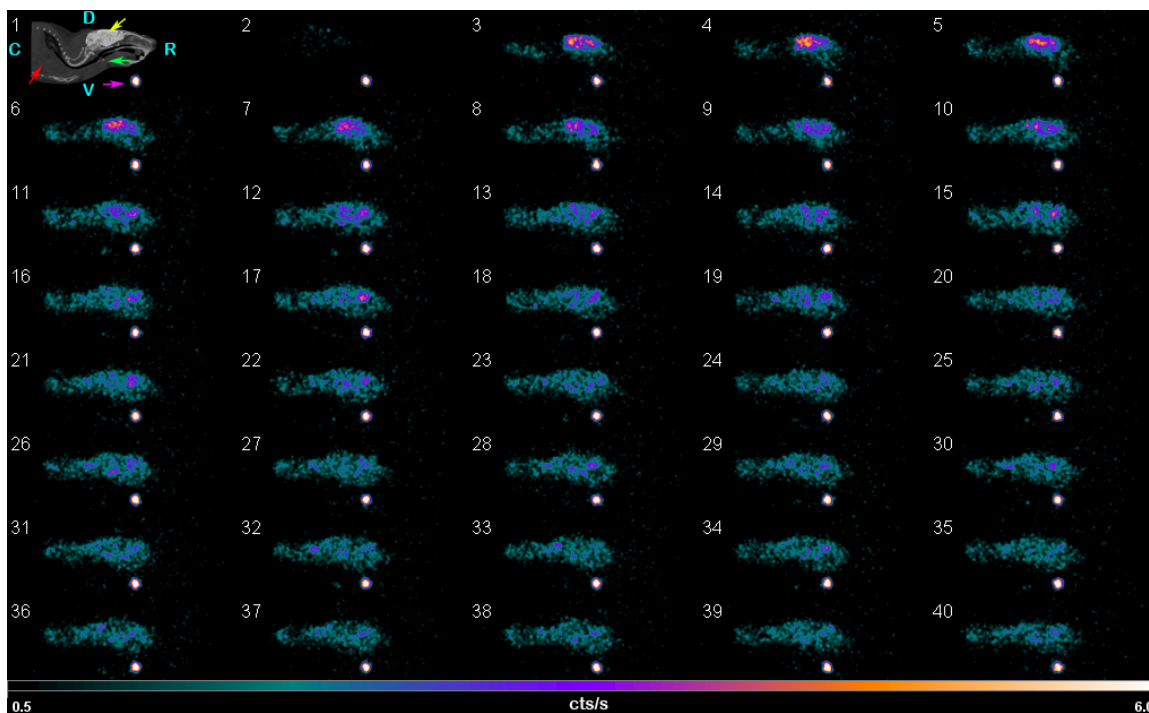


Figure 3.14 TRV5001 dynamic planar scintigraphy scans for a representative 5XFAD mouse. Lateral projections were acquired dynamically over 60 minutes with radioligand administration occurring 2 minutes after the start of the scan. Images were binned into 60X 1-minute frames for analysis (frames 1-40 displayed in the figure, denoted numerically in white at the top left of each image). A fused CT/MRI overlay serves as an anatomical reference in frame 1 indicating brain (yellow arrow), heart (red arrow), thyroid/salivary gland region (green arrow) and integrated fiducial marker placed at the most rostral extent of the olfactory bulb (purple arrow). D=dorsal; V=ventral, R=rostral; C = caudal. TRV5001 crosses the blood-brain barrier (BBB) and is taken up in the brain with peak tracer accumulation reliably occurring at 1-minute post-injection (frame 3) in 5XFAD mice. Washout of TRV5001 also occurred in the 5XFAD brain; however, longer periods of brain retention are apparent vs. other pyridones such as TRV7005, TRV7006 and TRV7019. Corresponding whole brain time-activity curves are seen in Figure 3.16, Figure 3.20 and associated kinetic summary measures of tracer clearance are seen in Figure 3.21, Table 3.5. Colour scale represents average counts per second (cts/s) in a given image pixel.

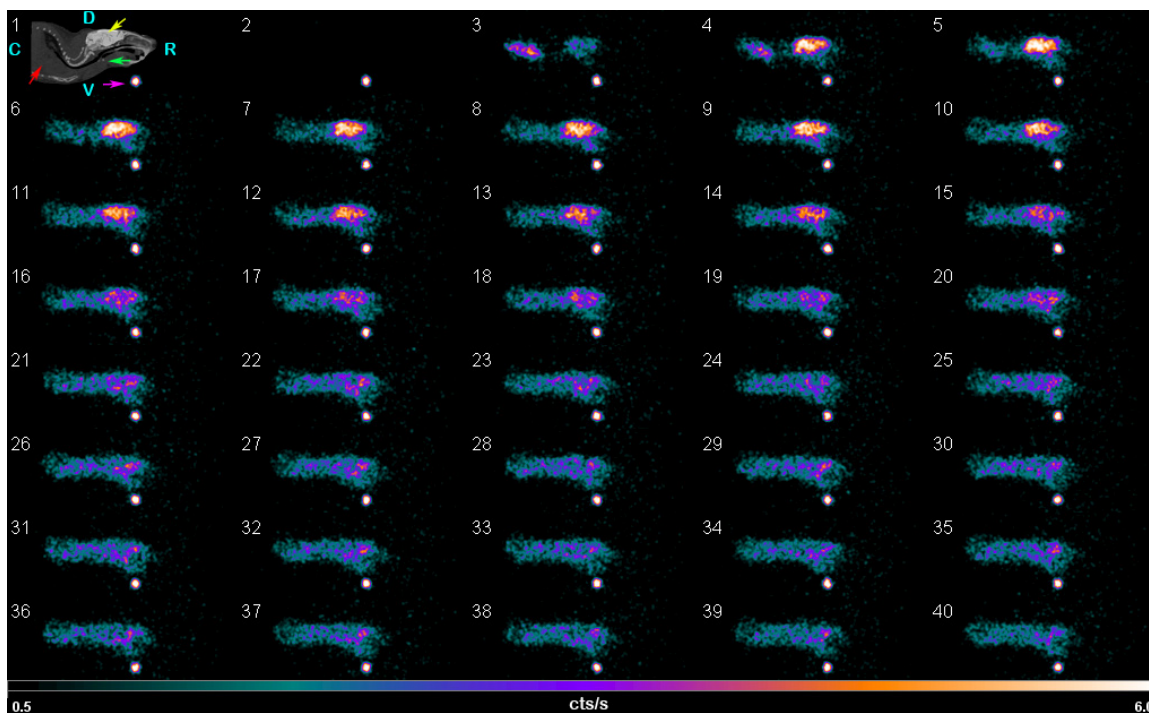


Figure 3.15 TRV5001 dynamic planar scintigraphy scans for a representative WT mouse. Lateral projections were acquired dynamically over 60 minutes with radioligand administration occurring 2 minutes after the start of the scan. Images were binned into 60X 1-minute frames for analysis (frames 1-40 displayed in the figure, denoted numerically in white at the top left of each image). A fused CT/MRI overlay serves as an anatomical reference in frame 1 indicating brain (yellow arrow), heart (red arrow), thyroid/salivary gland region (green arrow) and integrated fiducial marker placed at the most rostral extent of the olfactory bulb (purple arrow). D=dorsal; V=ventral, R= rostral; C = caudal. TRV5001 crosses the blood-brain barrier (BBB) and is taken up in the brain. Peak brain uptake reliably occurred at frame 3 (1-minute post-injection) in the WT mice investigated. Prominent tracer uptake and sustained retention is observed in the brain, exhibiting longer periods of retention prior to radiotracer washout in WT mice. Corresponding whole brain time-activity curves are seen in Figure 3.16, Figure 3.20 and associated kinetic summary measures of tracer clearance are seen in Figure 3.21, Table 3.5. Colour scale represents average counts per second (cts/s) in a given image pixel.

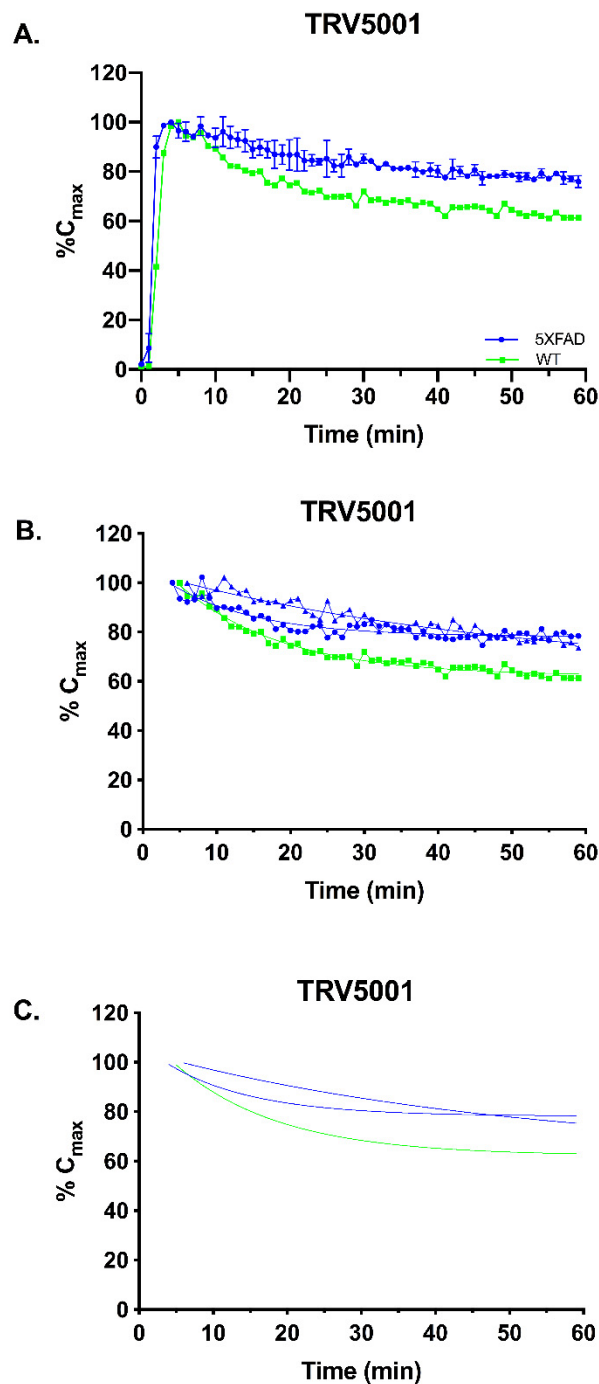


Figure 3.16 Whole brain time-activity curves for TRV5001 expressed as percent of peak concentration (%C_{max}) in brain. **A.** Mean time-activity curves (mean ± SEM) are shown for WT (green) and 5XFAD (blue). **B.** Time-activity curves of individual mice and corresponding fitted exponential function (solid line). **C.** Fitted exponential functions alone for individual mice from which kinetic summary measures were derived and compared (Table 3.5, Figure 3.21).

3.6.4.6 TRV6001

Dynamic scintigraphy images revealed that TRV6001 readily crosses the BBB and is taken up in the brain. Representative images series for WT and 5XFAD/BChE-KO mice are seen in Figure 3.17 and Figure 3.18, respectively. Peak brain uptake occurred between frames 4-6 (6-8 minutes PI). Uptake was largely restricted to the brain, with elevated extracranial background signal observed within the animal (Figure 3.17 and Figure 3.18). Washout of TRV6001 was apparent by visual inspection in both 5XFAD and WT brains. Whole brain time-activity curves are seen in Figure 3.19, presented as mean time activity curves for WT and 5XFAD/BChE-KO groups (Figure 3.19A), as individual subject data with corresponding fits (Figure 3.19B) and as fitted curves alone (Figure 3.19C). Statistical comparisons of $k_{clearance}$, $t_{1/2clearance}$ or C_A were not possible, as only one mouse per group was evaluated.

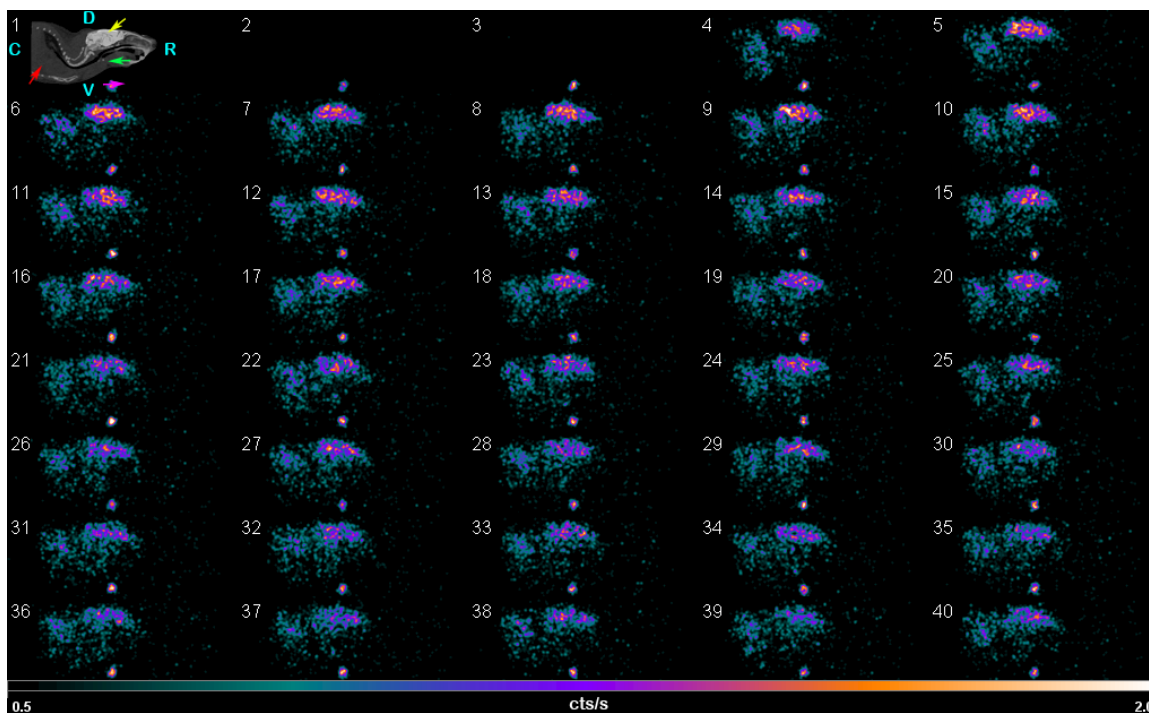


Figure 3.17 TRV6001 dynamic planar scintigraphy scans for a representative WT mouse. Lateral projections were acquired dynamically over 60 minutes with radioligand administration occurring 2 minutes after the start of the scan. Images were binned into 60X 1-minute frames for analysis (frames 1-40 displayed in the figure, denoted numerically in white at the top left of each image). A fused CT/MRI overlay serves as an anatomical reference in frame 1 indicating brain (yellow arrow), heart (red arrow), thyroid/salivary gland region (green arrow) and integrated fiducial marker placed at the most rostral extent of the olfactory bulb (purple arrow). D=dorsal; V=ventral, R= rostral; C = caudal. TRV6001 crosses the blood-brain barrier (BBB) and is taken up in the brain. Peak brain uptake reliably occurred at frame 6 (4 minutes post-injection) in the WT mouse and a more sustained distribution of radiotracer is seen in the brain over time compared to pyridone radioligands such as TRV7005, TRV7006 and TRV7019. Corresponding whole brain time-activity curves are seen in Figure 3.19, Figure 3.20 and associated kinetic summary measures of tracer clearance are seen in Figure 3.21, Table 3.4. Colour scale represents average counts per second (cts/s) in a given image pixel.

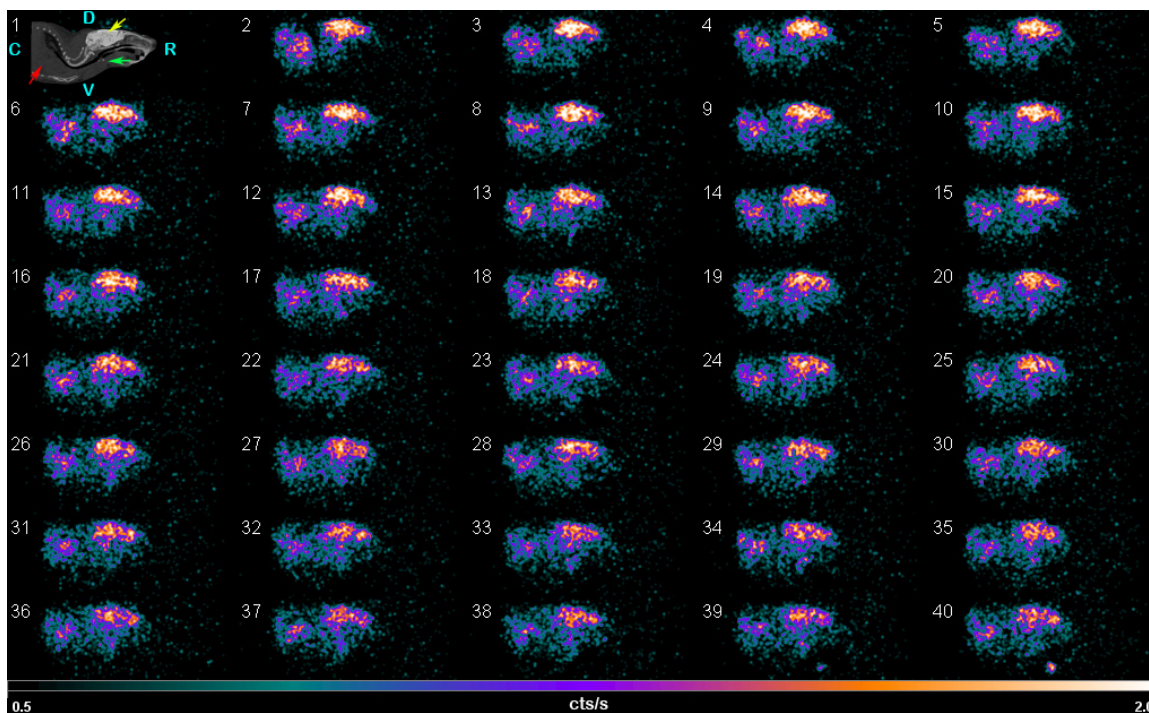


Figure 3.18 TRV6001 dynamic planar scintigraphy scans for a representative 5X-BChE-KO mouse. Lateral projections were acquired dynamically over 60 minutes with radioligand administration occurring 2 minutes after the start of the scan. Images were binned into 60X 1 minute frames for analysis (frames 1-40 displayed in the figure, denoted numerically in white at the top left of each image). A fused CT/MRI overlay serves as an anatomical reference in frame 1 indicating brain (yellow arrow), heart (red arrow), thyroid/salivary gland region (green arrow). D=dorsal; V=ventral, R= rostral; C = caudal. TRV6001 crosses the blood-brain barrier (BBB) and is taken up in the brain. Peak brain perfusion occurred at frame 5 (3 minute post-injection) in the 5XFAD-BChE-KO brain a more sustained distribution of radiotracer is seen in the brain over time compared to pyridone radioligands such as TRV7005, TRV7006 and TRV7019. Corresponding whole brain time-activity curves are seen in Figure 3.19, Figure 3.20 and associated kinetic summary measures of tracer clearance are seen in Figure 3.21, Table 3.5. Colour scale represents average counts per second (cts/s) in a given image pixel.

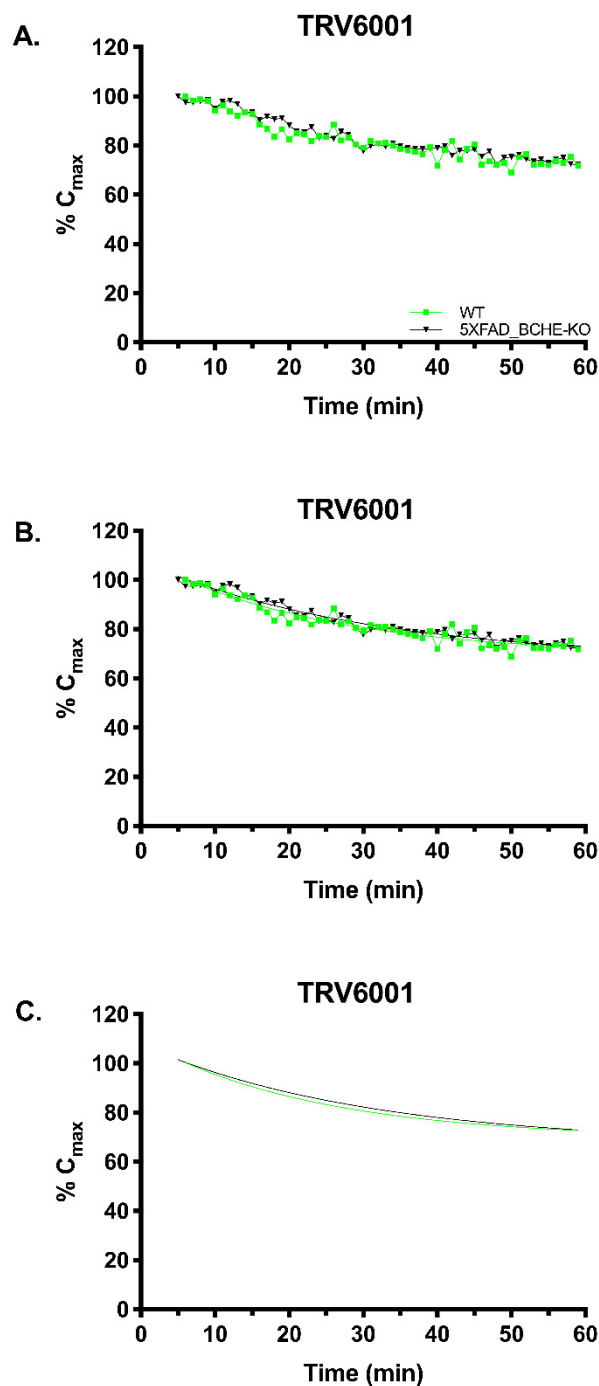


Figure 3.19 Whole brain time-activity curves for TRV6001 expressed as percent of peak concentration (%C_{max}) in brain. **A.** Time-activity curves are shown for WT (green), 5XFAD-BCHE-KO (black). **B.** Time-activity curves of individual mice and corresponding fitted exponential function (solid line). **C.** Fitted exponential functions alone for individual mice from which kinetic summary measures were derived and compared (Table 3.5, Figure 3.21).

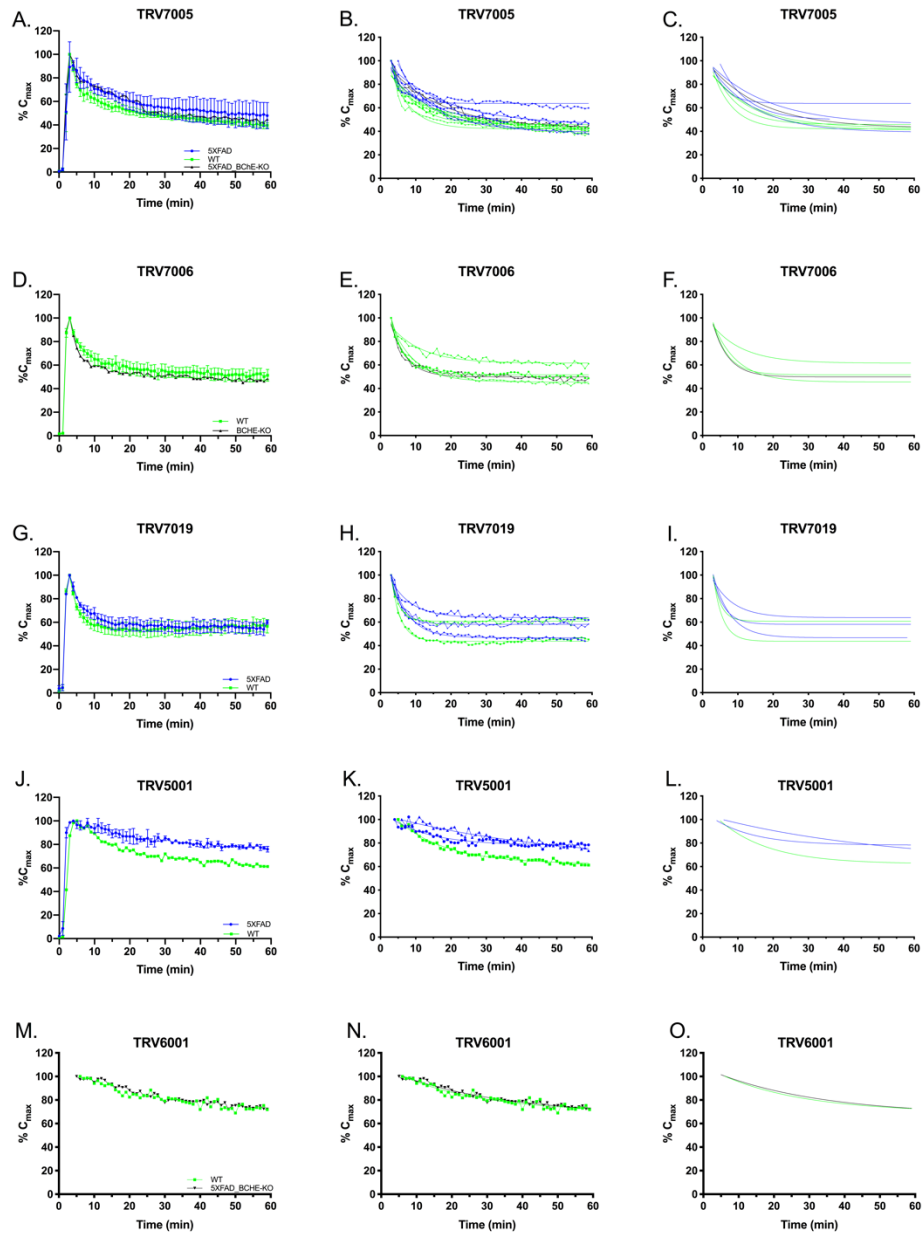


Figure 3.20 Whole brain time-activity curves for TRV7005 (A,B,C), TRV7006 (D,E,F), TRV7019 (G,H,I), TRV5001 (J,K,L) and TRV6001 (M,N,O) radiotracers, expressed as % of peak concentration ($\%C_{max}$) in brain. Mean time-activity curves (mean \pm SEM) are shown in the left column (A,D,G,J,M) across the strains evaluated for each respective radioligand (blue = 5XFAD; green = WT; black = BChE-KO or 5XFAD-BChE-KO). Time-activity curves of individual mice within a strain are shown in the middle column (B,E,H,K,N) with corresponding exponential fit (solid line). Exponential fits alone are seen in the right column (C,F,I,L,O) for each radioligand, from which kinetic summary measures were derived and compared (Figure 3.21, Table 3.5).

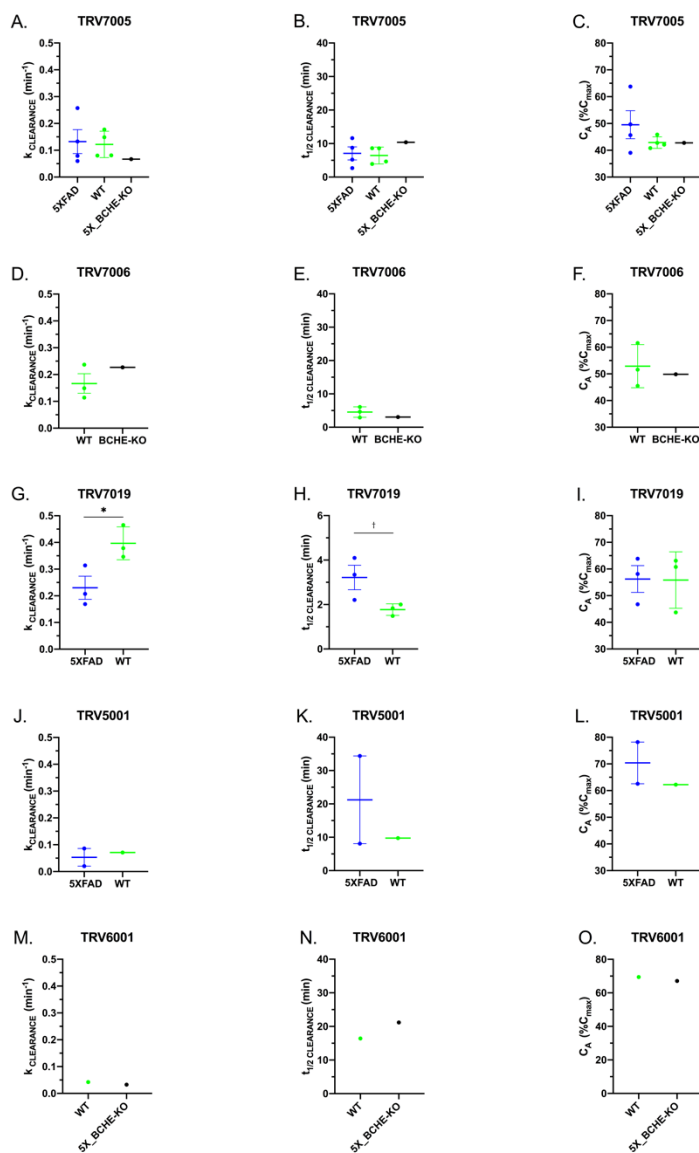


Figure 3.21 Kinetic summary measures of tracer clearance from the brain for TRV7005 (A,B,C), TRV7006 (D,E,F), TRV7019 (G,H,I), TRV5001 (J,K,L) and TRV6001 (M,N,O) radioligands. For each radioligand, the rate of tracer clearance, $k_{clearance}$ (min^{-1}), shown in the left column (A,D,G,J,M), half-life of tracer clearance $t_{1/2clearance}$ (min), shown in center column, (B,E,H,K,N) and asymptotic tracer concentration, C_A ($\%C_{max}$), shown in right column (C,F,I,L,O) were compared between 5XFAD (blue), WT (green) and in some instances BChE-KO (black) and 5XFAD-BChE-KO (black) mice. Mean (\pm SEM). No significant differences between mouse strains were observed in $k_{clearance}$, $t_{1/2clearance}$ or C_A for TRV7005, TRV7006 or TRV5001 ($p \geq 0.281$); statistical comparison not possible for TRV6001. A 58% decrease in $k_{clearance}$ (5XFAD = 0.23 ± 0.04 ; WT = 0.40 ± 0.04 ; $p = 0.041$) and a commensurate increase in $t_{1/2clearance}$ (5XFAD = 3.22 ± 0.55 ; WT = 1.77 ± 0.15 ; $p = 0.065$ (statistical trend)) was observed with TRV7019; however, C_A was not significantly different between 5XFAD and WT with TRV7019. *, $p < 0.05$; †, $p < 0.10$ (statistical trend).

TRV#	$k_{clearance}$ (min ⁻¹)				$t_{1/2}$ clearance (min)				C_A (% C_{max})			
	5XFAD	WT	BCHE-KO 5XBCHE-KO	p value	5XFAD	WT	BCHE-KO 5XBCHE-KO	p value	5XFAD	WT	BCHE-KO 5XBCHE-KO	p value
TRV7005	0.12 ± 0.03	0.12 ± 0.02	0.07	0.971	6.51 ± 1.19	7.21 ± 1.75	10.38	0.756	49.2 ± 5.1	42.5 ± 1.0	42.8	0.281
TRV7006	n/a	0.16 ± 0.03	0.21 ± 0.03	0.525	n/a	4.72 ± 0.93	3.27 ± 0.93	0.517	n/a	52.4 ± 4.6	49.3 ± 4.6	0.334
TRV7019	0.23 ± 0.04	0.40 ± 0.04	n/a	0.041*	3.22 ± 0.55	1.77 ± 0.15	n/a	0.065†	56.2 ± 5.0	55.9 ± 6.1	n/a	0.964
TRV7040												
TRV5001	0.05 ± 0.03	0.07 ± 0.03	n/a	0.803	21.2 ± 13.2	9.74 ± 13.2	n/a	0.703	70.4 ± 7.8	62.2 ± 7.8	n/a	0.654
TRV6001	n/a	0.04	0.03	n/a	n/a	16.4	21.2	n/a	n/a	69.5	67.1	n/a

Table 3.5 Dynamic planar scintigraphy kinetic summary measures of radioligand clearance for each of the radiotracers evaluated in 5XFAD, WT, BCHE-KO and 5XFAD-BCHE-KO mice (mean ± SEM). The rate of tracer clearance ($k_{clearance}$), half-life of tracer clearance ($t_{1/2clearance}$) and asymptotic tracer concentration (C_A) were compared (where possible) between mouse groups using an independent samples student's t-test, assuming equal variances. For TRV7019, $k_{clearance}$ was significantly (58%) lower and a commensurate increase in $t_{1/2clearance}$ in the 5XFAD brain was observed compared to WT; however, the final asymptotic radiotracer concentration in the brain, C_A was not significantly different between 5XFAD and WT mice. No other significant differences were observed between mouse strains in each of the other radioligands evaluated. * denotes statistical significance ($p < 0.05$) and † denotes a statistical trend ($p < 0.10$). Entries with "n/a" indicate that no data was available and the greyed-out entry for TRV7040 is owed to the lack of blood-brain barrier penetration required to evaluate brain radioligand kinetics.

3.7 Comparison of Kinetics Between Radioligands

To compare the clearance behaviour between radioligands, data were pooled across each radiotracer (combining available 5XFAD, WT, BChE-KO and 5XFAD-BChE-KO mice) to generate mean time-activity curves. Given that no differences were observed between mouse strains (save subtle differences in TRV7019 analysis), this approach was justifiable to provide a overall picture of radioligand behaviour. In the ANOVA statistical design, if significant interaction was present ($p < 0.05$), post-hoc comparisons were made using least significant difference (LSD) comparisons.

Overall mean time-activity curves for each radioligand are shown in Figure 3.22A. Differing clearance characteristics are apparent by qualitative inspection of these curves, suggesting differential brain retention among the radioligands evaluated. Pooled kinetic summary measures between radioligands were compared using ANOVA. Main effects of tracer clearance rate, $k_{clearance}$ ($p = 0.0001$), half-life of clearance, $t_{1/2clearance}$ ($p = 0.0015$), and asymptotic tracer concentration C_A ($p = 0.0011$) were significant. TRV5001 and TRV6001 both had significantly greater $t_{1/2clearance}$ (TRV5001 = 17.4 ± 8.5 min; TRV6001 = 18.8 ± 2.4 min) compared all other radioligands ($p \leq 0.065$) representing retention in the brain that was 2.6-7.5x longer than TRV7005, TRV7006 and TRV7019 (Figure 3.22 B). Owing to the inverse relationship between $t_{1/2clearance}$ and $k_{clearance}$ an identical but opposite trend of increased $k_{clearance}$ was also observed (data not shown). The asymptotic tracer concentration, C_A , of TRV5001 ($67.7 \pm 5.3\%C_{max}$) and TRV6001 ($68.3 \pm 1.2\%C_{max}$) was also significantly greater (1.2-1.5X greater) than the other radioligands evaluated ($p \leq 0.04$) indicating that more radioligand remains at the end of the 60-minute scan duration (Figure 3.22C).

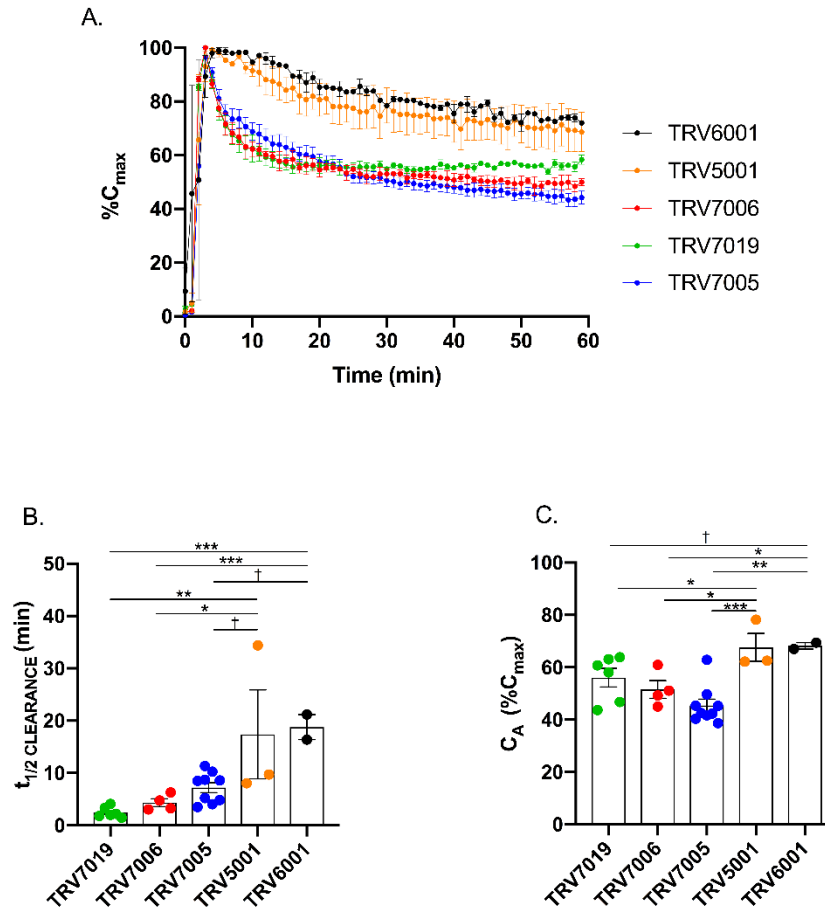


Figure 3.22 Average time-activity curves (A) and kinetic summary measures (B-C) including (B) half-life of tracer clearance, $t_{1/2\text{clearance}}$ (min) and (C) asymptotic tracer concentration, C_A ($\%C_{\text{max}}$) for BChE radioligand candidates derived from pooled data across each radiotracer. Mean \pm SEM. In general, TRV5001 and TRV6001 both had significantly greater $t_{1/2\text{clearance}}$ (TRV5001 = 17.4 ± 8.5 min; TRV6001 = 18.8 ± 2.4 min) compared all other radioligands ($p \leq 0.065$). A similar trend was seen for rate of tracer clearance ($k_{\text{clearance}}$). The average C_A of TRV5001 ($67.7 \pm 5.3\%C_{\text{max}}$) and TRV6001 ($68.3 \pm 1.2\%C_{\text{max}}$) was also significantly greater (1.2-1.5X greater) than the other radioligands evaluated ($p \leq 0.04$) indicating that more radioligand remains at the end of the 60-minute scan duration. Shown are radiotracers that readily cross the blood-brain barrier. TRV7005, blue; TRV7006, red; TRV7019, green; TRV5001, orange; TRV6001, black. †, $p < 0.10$; *, $p < 0.05$; **, $p < 0.01$; ***, $p < 0.001$.

TRV#	<i>in vivo</i> kinetic Summary Metrics (pooled)			
	n	$k_{clearance}$ (min^{-1})	$t_{1/2\ clearance}$ (min)	C_A ($\%C_{\text{max}}$)
TRV7005	9	0.11 ± 0.02	7.23 ± 0.95	45.4 ± 2.4
TRV7006	4	0.17 ± 0.03	4.36 ± 0.75	51.6 ± 3.4
TRV7019	6	0.31 ± 0.05	2.50 ± 0.41	56.1 ± 3.5
TRV7040				
TRV5001	3	0.06 ± 0.02	17.4 ± 8.5	67.7 ± 5.3
TRV6001	2	0.04 ± 0.01	18.8 ± 2.4	68.3 ± 1.2

Table 3.6 Pooled *in vivo* kinetic summary measures for lead BChE radioligands. The rate of tracer clearance, $k_{clearance}$ (min^{-1}), half-life of tracer clearance $t_{1/2\ clearance}$ (min) and asymptotic tracer concentration, C_A ($\%C_{\text{max}}$) were compared using an ANOVA statistical design (see Figure 3.22). TRV7040 was not taken up by the brain and thus not included for the current analysis.

3.8 Discussion

This proof-of-concept study was aimed at developing and implementing a 2D dynamic planar scintigraphy method to evaluate *in vivo* kinetic characteristics of candidate BChE radioligands using the Cubresa SPARK™ SRT-50 tabletop SPECT scanner. It was our expectation that this method could be implemented as a rapid screening tool to help evaluate the radioligands in development by characterizing the kinetics of tracer brain clearance and retention, which is valuable information that feeds forward into the product profile of each radiotracer.

The radiosynthesis of six radiotracers was performed in the current work including molecules in the pyridone class (TRV7005, TRV7006, TRV7019 and TRV7040), a diphenyl carbamate (TRV5001) and a piperidine radioligand (TRV6001). Each were successfully synthesized producing high radiochemical yields (56.5-87%) and radiochemical purity (95.2-95.9%). In general, most radioligands possessed favourable physicochemical characteristics, registering MPO scores ranging between 3.43-4.74 for TRV7005, TRV7006, TRV7019, TRV5001 and TRV6001, while TRV7040 had a lower MPO score 2.41. *In vitro* enzyme kinetics identified the radioligands of each class as having favourable kinetic properties that indicate good selectivity for the BChE enzyme.

The first question we sought to determine was whether a particular radiotracer has the ability to cross the BBB and be taken up in the brain. 2D planar scintigraphy image quality was sufficient to generate sagittal projections garnering between 3.2-9.2 million counts that were able to depict the biodistribution of radioligands at the whole brain level as a stand-alone method, without the use of CT for anatomical reference. Differing

patterns of radioligand distribution were revealed with this technique. Other anatomical features were discernable including uptake in regions such as salivary glands and thyroid as well as ocular regions in some instances. In general, for those radioligands that crossed the BBB, the distribution of tracer in the perfusion phase was similar, with tracer signal predominantly in the brain, followed by washout of the tracer over time.

Dynamic scintigraphy was able to distinguish those tracers that reached the brain versus those that did not. TRV7005, TRV7006, TRV7019, TRV5001 and TRV6001 were all taken up by the brain while TRV7040 did not reach the brain in appreciable amounts. The MPO score served as a good predictor of BBB penetrance. The MPO of TRV7040 (MPO = 2.41) was the only tracer lower than the suggested MPO threshold (≤ 3) and scintigraphy confirmed the inability of TRV7040 to cross the BBB and reach the brain. This is an interesting finding given that TRV7040, which is structurally similar to other radioligands in the same class of molecules, exhibits drastically different biodistribution behaviour *in vivo*.

Whole brain time-activity curves depicting radioligand concentration over time expressed relative to the peak concentration reached in the brain ($\%C_{\max}$) were generated from which a single exponential function was fitted to data. Goodness of fit metrics, in general, indicate a strong correspondence of the fitted curves with the measured scintigraphy time-activity curve data suggesting that this approach adequately describes the clearance characteristics for each radiotracer. Direct quantification was not possible in the current study, however raw time activity curves expressed as cps/cc and cps/ID were also generated (data not shown). Exponential fits were also carried out on these

data, producing near-identical results in estimates of $k_{clearance}$ and $t_{1/2clearance}$ to that obtained by time-activity curves expressed as $\%C_{max}$.

The 2D dynamic planar scintigraphy approach provided sufficient sensitivity to monitor the clearance of radioligands over time and was able to detect different tracer clearance behaviour *in vivo*. In comparisons of pooled data between radiotracers, TRV5001 and TRV6001 both had significantly longer half-lives ($t_{1/2clearance}$) and greater residual concentration (C_A) in the brain compared all other radioligands evaluated. This indicated greater retention of these radioligands in the brain that is sustained even at 1 hour after radioligand administration.

For radioligand TRV7019, comparisons of 5XFAD and WT mice revealed significant differences in $k_{clearance}$ and $t_{1/2clearance}$ between the two strains, with more rapid clearance of tracer in WT mice compared to 5XFAD, reaching similar overall concentrations at the end of the 60 minute scan. No other significant differences between mouse strains were detected in the radioligands evaluated. Interestingly, TRV7019 had the highest *in vitro* enzymatic efficiency (k_{cat}/k_m) of the radioligands studied yet clears the fastest whereas TRV6001 with the lowest enzymatic efficiency clears the slowest in the brain. This is perhaps counterintuitive as one might expect the opposite with a highly selective BChE radioligand engaging with the BChE target in the brain. The relationship between *in vitro* enzyme kinetics and *in vivo* imaging evaluation of these radioligands warrants further investigation.

There are a number of limitations in the current study. The statistical power is limited owed to relatively low sample size and given that data is comprised of a number

of different strains of mice. Pooled data were used for comparisons of tracer clearance between radioligands, a justifiable choice to strengthen statistical comparisons, particularly given the minimal differences in tracer clearances observed between strains evaluated within each radioligand. Adding additional numbers within each strain to strengthen the statistical power of these inter-strain comparisons is recommended.

In general the current results represent a temporal resolution (60 seconds) that is somewhat coarse, as tracer kinetics occur much more rapidly (on the order of seconds) (Kang et al., 2016), particularly in the early perfusion phase of brain uptake. This likely means that capturing the true peak radiotracer concentration, C_{\max} is not possible owed to a lower sampling rate. The net result is likely an underestimation of C_{\max} and thus an underestimation of C_A , $k_{clearance}$ and $t_{1/2\ clearance}$ from the fitted curves.

In the future, a modification to the study design would be to immediately sacrifice mice and excise the brain to determine the remaining radioactivity left in the brain after a scintigraphy scan for the various radioligands being evaluated. Back-correction to the time of peak concentration would provide a proper estimate of %ID/cc which could be compared with other radioligands, as has been described previously (Apostolova et al., 2012).

In conclusion, the results from this study reveal important in vivo kinetic characteristics of putative BChE radioligands that, until this point have not been evaluated. 2D dynamic planar scintigraphy is an effective pre-clinical imaging technique to evaluate the biodistribution of putative BChE radioligands and has the sensitivity to detect differences in radioligand clearance kinetics in the mouse brain. This method can

be combined with *in vitro* kinetics and MPO scores as part of the tracer product profile and provide valuable information that can be incorporated into a “go/no go” paradigm for further characterization and development of the candidate radioligand.

3.9 Acknowledgements

D.R. DeBay was responsible for the implementation and preliminary testing of 2D planar scintigraphy capabilities, study conceptualization, data acquisition and processing, analysis pipeline development, statistical design and interpretation and manuscript preparation. Development and implementation of these methods on the Cubresa SPARK SRT-50 were performed in collaboration with Cubresa software engineers Geoff Chen and Ryan Sparks. Radiosynthesis and *in vitro* kinetic analyses were performed jointly by Dr. Ian Pottie, Andrew Reid and Kosuke Kanayama in addition to current manuscript contributions. Manuscript support and assistance with image preparation provided by David Luke. Valuable guidance was provided by E. Martin and S.Darvesh (Chemistry) and by S. Burrell and C.V. Bowen (nuclear medicine imaging). The authors would like to thank Christa Davis for her technical support. This research was supported by the Canadian Institutes of Health Research (MOP-82798, RNS- 117795, MOP-119343), Capital Health Research Fund, Nova Scotia Health Research Foundation (Scotia Scholar^{OM}, MED-MAT-2011-7512), Faculty and Department of Medicine of Dalhousie University, Innovacorp, Mount Saint Vincent University Committee on Research and Publication, Dalhousie Medical Research Foundation (DMRF) Gunn Family Research Prize, DeWolfe Graduate Studentship, Mrs. Sadie MacLeod (DMRF Adopt-a-Researcher program) and the DMRF Irene MacDonald Sobey Endowed Chair in Curative Approaches to Alzheimer's Disease.

Chapter 4 Synthesis and *In Vivo* Evaluation of 1-methyl-4-piperidinyl- *p* [¹⁸F]fluorobenzoate: A Butyrylcholinesterase Radioligand for PET Imaging of the Brain in Alzheimer's Disease

4.1 Publication Status

Manuscript in preparation.

D.R. DeBay, I.R. Pottie, G.A. Reid, E. Martin, S. Burrell, A. Bou Laouz, C.V. Bowen, S. Darvesh. *Synthesis and in vivo evaluation of 1-methyl-4-piperidinyl- p [¹⁸F]fluorobenzoate: A butyrylcholinesterase radioligand for PET imaging of the brain in Alzheimer's disease.*

4.2 Overview

The current chapter focuses on the synthesis and *in vivo* positron emission tomography (PET) evaluation of a previously developed cholinesterase radioligand 1-methyl-4-piperidinyl *p*-¹⁸[F]fluorobenzoate (TRV6501). Originally developed as a potential acetylcholinesterase (AChE) imaging agent (Bormans et al., 1996) this molecule was largely abandoned owed to initial evidence suggesting rapid washout from AChE-rich structures in the brain, casting suspicion about its suitability as a substrate for AChE. Nevertheless, its role as a BChE imaging agent has not been fully explored. Given the structural similarities of TRV6501 to other radioligands in development that are selective for BChE, further *in vivo* evaluation of TRV6501 is warranted. The current work represents initial progress in [¹⁸F] radiochemistry in our group and serves as an exemplar to establish a PET pharmacokinetic modelling analysis framework, ultimately expanding

the analytical toolkit that is essential in order to rigorously characterize putative BChE radioligands for AD diagnostic development.

4.3 Abstract

There are currently no effective means to definitively diagnose Alzheimer's disease (AD) during life. Molecular imaging of amyloid or tau pathology in the AD brain, though informative, has limited diagnostic value because similar changes are found in brains of ~30% of cognitively normal individuals. We have recently shown that the enzyme butyrylcholinesterase (BChE), typically present in high levels in the AD cerebral cortex (yet largely absent in normal brain), is a highly sensitive and specific biomarker for the disease and could therefore provide enhanced accuracy as an AD diagnostic. The synthesis and *in vivo* evaluation of one such positron emission tomography (PET) BChE radiotracer, 1-methyl-4-piperidinyl *p*-¹⁸[F]fluorobenzoate (TRV6501) is described here.

Methods: The physicochemical and *in vitro* kinetic profile of TRV6501 were evaluated using multiparametric optimization (MPO) scoring and standard enzyme kinetics techniques. TRV6501 was synthesized and injected into 5XFAD mice (n=3) and WT/BChE-KO counterparts (n=3), chosen due to their abundance and absence of BChE expression in the brain, respectively. Dynamic PET acquisitions were acquired over 42 min, followed by computed tomography (CT) scans for anatomical reference. Regional PET time-activity curves were generated from a magnetic resonance (MR)-based template mouse brain atlas coregistered to the PET/CT images. Relevant structures to the cholinergic system and AD were evaluated, including whole brain, neocortex, hippocampus, globus pallidus, caudate/putamen, and cerebellum. To establish the *in vivo* pharmacokinetic behaviour of TRV6501, kinetic modelling was employed using

three approaches, namely, a one tissue compartment model (1TCM) with an image-derived arterial input function (IDAIF) derived from the proximal common carotid artery (CCA), a simplified reference tissue model (SRTM) with cerebellar gray matter reference region and finally, through Logan graphical analyses techniques. Estimates of brain distribution volume (V_T), binding potential (BP_{ND}) and associated kinetic parameters including influx rate constants K_I (1TCM), R_I (SRTM) and efflux rate constant k_2 were compared between 5XFAD and WT/BChE-KO strains. The suitability of the selected models in describing the kinetics of TRV6501 was evaluated with various goodness of fit metrics including sum of squares (SS), R^2 , and standard deviation of residuals ($Sy.x$) methods.

Results: TRV6501 demonstrated a favourable physicochemical profile, with an overall MPO score of 4.69 and in vitro enzyme kinetic profile indicating high specificity for BChE. Cerebral uptake of TRV6501 indicated that this radiotracer readily crossed the blood-brain barrier (BBB) reaching the brain. Marked tracer accumulation was observed at early timepoints in both the 5XFAD and WT/BChE-KO brain, with a regionalized distribution evident in cortical and subcortical regions. Subsequent washout of TRV6501 was observed over the duration of the scan in both 5XFAD and WT/BChE-KO mice.

Using a 1TCM, whole brain estimates of K_I (5XFAD, $0.43 \pm 0.13 \text{ mL}\cdot\text{cm}^{-3}\cdot\text{min}^{-1}$; WT/BChE-KO, $1.79 \pm 0.77 \text{ mL}\cdot\text{cm}^{-3}\cdot\text{min}^{-1}$), k_2 (5XFAD, $0.14 \pm 0.02 \text{ min}^{-1}$; WT/BChE-KO, $0.42 \pm 0.13 \text{ min}^{-1}$) and V_T (5XFAD, $3.05 \pm 1.11 \text{ mL}\cdot\text{cm}^{-3}$; WT/BChE-KO, $3.73 \pm 0.91 \text{ mL}\cdot\text{cm}^{-3}$) were not significantly different between 5XFAD and WT/BChE-KO mice

($p \geq 0.178$). Similarly, regional estimates of K_I (5XFAD, $(0.21 \pm 0.10 - 0.76 \pm 0.18)$ $\text{mL}\cdot\text{cm}^{-3}\cdot\text{min}^{-1}$; WT/BChE-KO, $(0.71 \pm 0.24 - 3.18 \pm 1.40)$ $\text{mL}\cdot\text{cm}^{-3}\cdot\text{min}^{-1}$), k_2 (5XFAD, $(0.01 \pm 0.01 - 0.18 \pm 0.02)\text{min}^{-1}$; WT/BChE-KO, $(0.16 \pm 0.02 - 0.55 \pm 0.19)\text{min}^{-1}$) and V_T (5XFAD, $(2.24 \pm 1.10 - 4.71 \pm 0.51)\text{mL}\cdot\text{cm}^{-3}$; WT/BChE-KO, $(2.95 \pm 0.60 - 5.46 \pm 1.49)\text{mL}\cdot\text{cm}^{-3}$) were not significantly different between 5XFAD and WT/BChE-KO in the brain structures investigated ($p \geq 0.382$).

Using a SRTM with cerebellar gray matter reference region, whole brain estimates of R_I (5XFAD, 0.81 ± 0.21 $\text{mL}\cdot\text{cm}^{-3}\cdot\text{min}^{-1}$; WT/BChE-KO, 0.92 ± 0.07 $\text{mL}\cdot\text{cm}^{-3}\cdot\text{min}^{-1}$), k_2 (5XFAD, $0.68 \pm 0.32\text{min}^{-1}$; WT/BChE-KO, 0.05 ± 0.05 min^{-1}) and BP_{ND} (5XFAD, 0.08 ± 0.07 $\text{mL}\cdot\text{cm}^{-3}$; WT/BChE-KO, 6.61 ± 6.60 $\text{mL}\cdot\text{cm}^{-3}$) were not significantly different between 5XFAD and WT/BChE-KO mice ($p \geq 0.188$). Similarly, regional estimates of R_I (5XFAD, $(0.96 \pm 0.44 - 4.21 \pm 2.93)$ $\text{mL}\cdot\text{cm}^{-3}\cdot\text{min}^{-1}$; WT/BChE-KO, $(1.10 \pm 0.85 - 4.10 \pm 2.95)\text{mL}\cdot\text{cm}^{-3}\cdot\text{min}^{-1}$), k_2 (5XFAD, $(0.07 \pm 0.06 - 0.68 \pm 0.32)\text{min}^{-1}$; WT/BChE-KO, $(0.13 \pm 0.06 - 0.35 \pm 0.17)\text{min}^{-1}$) and BP_{ND} (5XFAD, $(0.03 \pm 0.02 - 6.75 \pm 6.63)\text{min}^{-1}$; WT/BChE-KO, $(0.01 \pm 0.01 - 6.98 \pm 6.52)\text{min}^{-1}$) were not significantly different between 5XFAD and WT/BChE-KO in the brain structures investigated ($p \geq 0.274$).

Using Logan graphical analyses techniques, whole brain estimates of V_T (5XFAD, $2.93 \pm 1.35\text{mL}\cdot\text{cm}^{-3}$; WT/BChE-KO, 3.27 ± 1.18 $\text{mL}\cdot\text{cm}^{-3}$) were not significantly different between 5XFAD and WT/BChE-KO ($p = 0.861$). In a similar manner, regional estimates of V_T (5XFAD, $(2.28 \pm 1.25 - 5.77 \pm 1.20)$ $\text{mL}\cdot\text{cm}^{-3}$;

WT/BChE-KO, $(2.45 \pm 0.38 - 4.28 \pm 1.83)\text{mL}\cdot\text{cm}^{-3}$) were not significantly different between 5XFAD and WT/BChE-KO in the brain structures investigated ($p \geq 0.136$).

Goodness of fit metrics of 1TCM, SRTM and Logan graphical analyses indicated a strong correspondence with the empirical data (SS: 0.002-3.77; R^2 : 0.61-1.00; Sy.x: 0.01-0.44) suggesting that the various models evaluated describe the estimated TRV6501 pharmacokinetic parameters well.

Conclusions: These preliminary findings indicate that TRV6501 readily crosses the blood brain barrier and perfuses the brain. There is washout of TRV6501 and in the various models evaluated, no significant differences in rates of influx (K_I , R_I), efflux (k_2) or corresponding retention metrics V_T or BP_{ND} were seen between 5XFAD and WT/BChE-KO mice. Further evaluation with greater sample size will minimize variance and strengthen the statistical power of these analysis. Validation of the proposed IDAIF method using a metabolite-corrected plasma input function generated through direct arterial blood sampling will refine the precision of these analyses and may help to further elucidate the *in vivo* kinetics of TRV6501.

4.4 Introduction

Alzheimer's disease (AD) is the most common cause of dementia (Scheltens et al., 2016). A definitive diagnosis of AD during life remains elusive, owed largely to the lack of suitable biomarkers that can distinguish individuals with AD from those who are cognitively normal or those with non-AD dementias (Morris et al., 2016). Brain imaging biomarkers that measure β -amyloid plaques ($A\beta$), tau neurofibrillary tangles (NFT) and

neurodegeneration (the so-called AT(N) framework (Jack et al., 2018)), though informative, generally lack the diagnostic specificity required for a definitive diagnosis. Therefore, the need is great for improved biomarkers to enhance existing armamentarium for AD diagnosis.

The cholinergic system is one of the first neuronal networks affected in AD (Davies & Maloney, 1976), which has led to the formulation of the cholinergic hypothesis of AD, whereby the loss of cholinergic function significantly contributes to the cognitive decline associated with AD (Coyle et al., 1983). With this, there is decrease in levels of acetylcholinesterase (AChE) and an increase in the levels of the related enzyme butyrylcholinesterase (BChE), that associate with plaques and tangles in the brain (Mesulam & Geula, 1994; Perry, Perry, et al., 1978). We have recently shown in human brains at autopsy that BChE is a highly sensitive and specific biomarker of AD, has strong predictive value and could therefore elevate the accuracy of an AD diagnosis (Macdonald et al., 2017).

A number of cholinergic radioligands have been developed, with particular attention focused on acetylcholinesterase (AChE) imaging agents (Irie et al., 1996; Namba et al., 2002; Ota et al., 2004; Pappata et al., 1996; Snyder et al., 1998), including *N*-[¹¹C] methylpiperidin-4-yl acetate ([¹¹C]MP4A), which has shown to successfully map AChE activity *in vivo* in the AD brain (Ota et al., 2010; Ota et al., 2004). However, less success has been met in developing radioligands for imaging of BChE, where putative radiotracers have failed to demonstrate labelling of BChE that represents the known histochemical distribution of the enzyme in humans (Kuhl et al., 2006; Roivainen et al., 2004).

1-methyl-4-piperidinyl *p*-¹⁸[F]fluorobenzoate (TRV6501) is a piperidine radioligand that was originally developed as a potential AChE imaging agent (Bormans et al., 1996). *Ex vivo* biodistribution studies in mice demonstrated that though this molecule readily entered the brain, rapid washout occurred with no significant retention of the radioligand in regions of AChE enzymatic activity (Bormans et al., 1996). It was concluded that this radioligand was not a suitable AChE imaging agent. Nevertheless, its role as a putative BChE imaging agent has not been fully explored. Given the structural similarities of TRV6501 to other selective BChE radioligands we have developed, including [¹²³I] SPECT analogue of *N*-methylpiperidin-4-yl 4-¹²³Iodobenzoate (TRV6001) (DeBay, Reid, Pottie, et al., 2017; Macdonald et al., 2011) further *in vivo* evaluation of TRV6501 is warranted.

The purpose of the current study was to perform an *in vivo* evaluation of TRV6501 using PET imaging in a familial (5XFAD) mouse model of AD (Oakley et al., 2006) and in wild-type BCHE-knockout (WT/BCHE-KO) counterparts, who lack BCHE expression. The 5XFAD model is an AD model of aggressive amyloidosis based on the overexpression of the human amyloid precursor protein (*APP*) and presenilin 1 (PS1) mutations. Aβ deposition as early as ~2 months of age (Oakley et al., 2006). Importantly, as in human AD, BChE associates with plaques in the 5XFAD mice (Darvesh & Reid, 2016; Reid & Darvesh, 2015), making it a suitable model to evaluate putative BChE diagnostic radioligands. We hypothesized that the *in vivo* pharmacokinetic behaviour of TRV6501 could be described as a reversibly binding radioligand and, as such, suitable kinetic models including a single tissue compartment model (1TCM), a simplified reference tissue model (SRTM) (Lammertsma & Hume,

1996) and Logan graphical analyses (Logan et al., 1990) were employed to evaluate TRV6501 pharmacokinetics *in vivo*.

4.5 Materials and Methods

Formal approval to conduct the current experiments was obtained from the Dalhousie University Radiation Safety Committee and the Canadian Nuclear Safety Commission (license 07154-2-17.10). Mice were cared for in accordance with the guidelines set by the Canadian Council on Animal Care (Dalhousie University Committee on Laboratory Animals Protocol 15-070).

4.5.1 Synthesis, Enzyme Kinetics and Labelling of Radiotracer

Unless otherwise stated, reagents and solvents were commercially available and used without further purification. Water was removed from CH₃CN by distillation from CaH₂ under an atmosphere of anhydrous argon. [¹⁸F]KF in 98% H₂¹⁸O and 2% (H₂¹⁶O + H₂¹⁷O) was obtained from the Department of Diagnostic Imaging, Nova Scotia Health Authority. QMA light Sep-Pak were preconditioned by running 0.5 M K₂CO₃ (5 mL), distilled water (10 mL) and then air (10 mL) through the Sep-Pak. After the preconditioning, the Sep-Paks were immediately used. Infrared Spectra were recorded on a Bruker Alpha Infrared Spectrometer that was fitted with an attenuated total reflectance (ATR) module. Nuclear magnetic resonance spectra were recorded at the NMR facility at Mount Saint Vincent University on a Bruker Avance Neo spectrometer operating at 400.1 MHz for proton and 100.1 MHz for carbon-13. Chemical Shifts are reported in ppm relative to TMS (0 ppm) in ¹H NMR experiments while ¹³C NMR experiments are relative to the CDCl₃ chemical shift (77.16 ppm). The purity of the compounds was

determined using an Agilent Technologies 1200 series HPLC system that was equipped with a Zorbax Eclipse XDB-C18 analytical column (4.6 x 250 mm; 5 micron, PN 990967-902) and compounds were identified using a photodiode array detector operating at the wavelength indicated. The eluent for each compound is identified. UV-Visible experiments were performed on a VWR 1600-PC UV-Visible Spectrophotometer operating with M.Wave 1.0 software. Physicochemical properties (pka, clogP, clogD, total polar surface area, and molecular weight) were calculated using MarvinSketch 19.1 (ChemAxon Ltd.) to generate a Multiparametric Optimization (MPO) score (Wager et al., 2016).

4.5.2 Synthesis of *N*-methylpiperidin-4-yl *p*-fluorobenzoate

Under an argon atmosphere, triethylamine (4.2997 g, 42.49 mmol) was added to a mixture of *N*-methyl-4-piperidinol (3.8194 g, 33.16 mmol) and 4-fluorobenzoyl chloride (5.5210 g, 34.82 mmol) dichloromethane (40 mL). The resulting mixture was stirred for 24 h at room temperature. The reaction was extracted with water (3 × 25 mL) and the organic layer dried over Na₂SO₄ (15 min). The drying agent was removed by gravity filtration and the solvent was removed *in vacuo* to yield a pale yellow solid. This solid was purified using flash chromatography (5% methanol in CH₂Cl₂) to afford a white solid (6.761 g, 86%): IR (ATR) 2937(w), 2774(w), 2757(w), 1709(s), 1591(w), 1453(w), 1402(w), 1323(w), 1277(s), 1143(m), 1116(m), 1088(w), 1032(m), 1013(m), 954(w), 852(m), 758(s), 685(m), 530(w), 476(w); ¹H NMR (400.1 MHz, CDCl₃) δ 8.09-8.04 (m, 2H), 7.14-7.09 (m, 2H), 5.07-5.02 (m, 1H), 2.74-2.68 (m, 2H), 2.40-2.35 (m, 2H), 2.33 (s, 3H), 2.07-2.00 (m, 2H), 1.92-1.83 (m, 2H); ¹³C NMR (100.6 MHz, CDCl₃) δ 165.9 (d, ¹J_{CF} = 253.8 Hz), 165.1, 132.2 (d, ³J_{CF} = 9.5 Hz), 127.0 (d, ⁴J_{CF} = 2.7 Hz), 115.6 (d, ²J_{CF}

= 22.0 Hz), 70.4, 53.0, 46.3, 31.0; HPLC retention time: 2.88 minutes, purity: 96.8%.

This data agrees with previously published data (Bormans et al., 1996).

4.5.3 Synthesis of *N*-methylpiperidin-4-yl *p*-nitrobenzoate

This molecule was synthesized as previously described (Bormans et al., 1996) and analytical data below was consistent with the structure of the molecule.

¹H NMR (400.1 MHz, CDCl₃) δ 8.31-8.28 (m, 2H), 8.23-8.20 (m, 2H), 5.12-5.11 (m, 1H), 2.71 (app br s, 2H), 2.36 (app br s, 2H), 2.34 (s, 3H), 2.10-2.03 (m, 2H), 1.94-1.86 (m, 2H); ¹³C NMR (100.6 MHz, CDCl₃) δ 164.2, 150.6, 136.1, 130.8, 123.6, 71.6, 52.9, 46.3, 31.0.

4.5.4 *In Vitro* Evaluation of *N*-methylpiperidin-4-yl *p*-fluorobenzoate as a Cholinesterase Substrate

The specificity, affinity, and rate of hydrolysis of each synthetic compound were determined spectrophotometrically, making use of differences in the aryl chromophores of substrates and products. Briefly, 30 μL of AChE (66.7 U / mL) or BChE (66.7 U / mL) dissolved in 0.1% gelatin (aq), containing 0.01% sodium azide, and 1.52 mL of 0.1 M phosphate buffer (pH 7.4) were placed in a quartz cuvette of 1 cm path length. The reaction was commenced with the addition of 50 μL of 1.7 mM *N*-methylpiperidin-4-yl *p*-fluorobenzoate in 50% acetonitrile(aq). The absorbance was scanned from 200–850 nm every 2 min for a total of 18 min using a VWR 1600-PC UV-Vis spectrophotometer. The wavelength corresponding to the maximum absorbance change for the compound during hydrolysis was used for the subsequent determination of affinity constant (K_M), turnover number (k_{cat}) and catalytic efficiency (k_{cat}/K_M), using Lineweaver-Burk double reciprocal

plots. This was accomplished by measuring the change in absorbance per min ($\Delta A/\text{min}$) at 249nm, using a fixed amount of BChE (1.25 U) and varying amounts of *N*-methylpiperidin-4-yl *p*-fluorobenzoate ($5.3 \times 10^{-5} - 1.8 \times 10^{-5}$ M), using a VWR 1600-PC UV-Vis spectrophotometer. The plot of $1/v$ against $1/s$ gave K_M as the negative reciprocal of the intercept on the $1/s$ -axis and V_{max} as the reciprocal of the $1/v$ -axis intercept.

4.5.5 Synthesis of *N*-methylpiperidin-4-yl *p*-[^{18}F]fluorobenzoate

487 MBq of [^{18}F]KF in 2.5 mL of 98% H_2^{18}O and 2% ($\text{H}_2^{16}\text{O} + \text{H}_2^{17}\text{O}$) was run through a preconditioned QMA light Sep-Pak. Most of the radioactivity (98%) was retained in the Sep-Pak. A mixture of 83% CH_3CN :17% 5 mM K_2CO_3 was pushed through the radioactive Sep-Pak into a glass V-vial containing kryptofix [2.2.2] (5.5 mg, 1.5×10^{-5} mol). The resulting mixture, containing 427 MBq of [^{18}F]KF, was evaporated under a continuous stream of argon at 95 °C for 10 min. Anhydrous CH_3CN (3 x 600 μL) was added, and the mixture was again evaporated at 95 °C under argon flow.

N-Methylpiperidin-4-yl *p*-nitrobenzoate (1.2 mgs, 4.5×10^{-6} mol) solid and anhydrous DMSO (300 μL) was placed directly in the V-vial containing the radioactivity. The V-vial was sealed with an atmosphere of argon and heated at 130 °C for 45 min. After this heating time, the reaction vial was removed from the heating block and let stand for 10 minutes at room temperature. Water (4.5 mL) was added and the resulting mixture was extracted with CH_2Cl_2 (500 μL). The combined organic layers (160 MBq) were placed in a new glass vial and concentrated under a stream of argon at 45 °C. The remaining water layer contained 68 MBq of radioactivity. The concentrate from the organic layer was taken up in a mixture of CH_3CN (125 μL) : distilled H_2O (86 μL) and

0.1M NaOH (10 μ L) and injected directly onto an HPLC. Fractions were collected from the HPLC. Fractions that contained the radioactive *N*-methylpiperidin-4-yl [18 F] *p*-fluorobenzoate peak were combined and concentrated under stream of argon at 55 $^{\circ}$ C. This peak has a retention time corresponding to authentic *N*-methylpiperidin-4-yl *p*-fluorobenzoate. The concentrate was taken up in 5% ethanol in saline for injection into an appropriate mouse. The total radiochemical synthesis takes approximately 120 minutes and *N*-methylpiperidin-4-yl [18 F] *p*-fluorobenzoate was generated with 17 % radiochemical yield and a radiochemical purity: of 97%.

4.5.6 Animals

Female wild-type (C57BL/ 6J x SJL/J F1; The Jackson Laboratories, Stock # 100012), male transgenic hemizygous 5XFAD (B6SJL- Tg (APPS^{wFILon},PSEN1*^{M146L}*^{L286V}) 6799Vas/Mmjax; Mutant Mouse Regional Resource Center, 034840-JAX) (Oakley et al., 2006) and heterozygous butyrylcholinesterase (B6.129S1- Bchetm1^{Loc}/J; The Jackson Laboratories, Stock # 008087), referred to here as BChE-het mice, were obtained from Jackson Laboratory (Bar Harbor, ME). Mice were housed in same-sex groups of 1– 5, within polyethylene cages (30x19x13cm), containing a wood-chip bedding and covered by a metal cage top and micro-isolator filter. Food (Purina rodent chow, #5001) and tap water were available *ad libitum*. Animals were kept in normal light/dark cycle. Homozygous BChE-knockout (WT/BChE-KO) mice were produced from BChE-het males and females to maintain the strain and produce mice for subsequent study.

A total of 6 mice (5XFAD n=3 (2M,1F); WT/BChE-KO n=3 (3M)) aged 12.2 ± 0.4 months were imaged in the current study. At this age, robust BChE accumulation is present in distinct areas of the 5XFAD brain, and importantly, is notably absent in WT/BChE-KO mouse.

4.5.7 PET/CT Imaging

Mice were weighed and placed in an induction chamber, anaesthetized with 3% isoflurane (in 100% oxygen) and restrained in a TailVeiner Restrainer (Baintree Scientific) while under a continuous stream of 1.5% isoflurane in 100% oxygen. A custom, in-house catheter line was placed in the lateral tail vein. Mice were then secured in prone position, wrapped in a blanket on a heated animal bed and maintained under continuous stream of 1.5-2% isoflurane while the respiration rate monitored for the duration of the imaging procedure (SA Instruments Inc. Stony Brook, NY). The mouse head region was centered on the scanner's 37 mm axial field of view (FOV). A dynamic acquisition was initiated with PET coincidence events being acquired in list mode over a 42 minute scan period, on a LabPET4 TriumphXO pre-clinical PET/CT scanner (Trifoil Imaging, CA). Two minutes after the start of the scan, *N*-Methylpiperidin-4-yl *p*-[¹⁸F]Fluorobenzoate (17.65-44.77MBq) in 0.9% saline (140-200μL)) was administered through the tail vein catheter line and subsequently flushed with ~20μL saline.

Immediately following PET scanning, a computed tomography (CT) image was performed in fly mode with a 70 kVp x-ray beam energy (160 μA beam current), 512 projections, 4 summed frames/projection, with 2X2 binning and a magnification of 2.26X, providing complete whole brain coverage in a 56 mm FOV. CT scan duration was approximately 8.5 min.

4.5.8 PET Image Processing and Analysis

Dynamic PET images for each subject were generated yielding a series of twelve frames over the 42min scan (one x 2 min, five x 1 min, five x 5 min and one x 10 min frames) as follows: PET list-mode data were temporally histogrammed according to the above scheme and binned according to their line of response. Coincidence events were rebinned over a maximum span field of 31 oblique planes using a single slice rebinning algorithm. An iterative reconstruction approach was employed via a 3D Maximum-Likelihood Expectation Maximization (MLEM) algorithm, which was performed 100 times and constrained to a 46 mm radial FOV. The resultant PET images yielded an effective isotropic resolution of 1.2 mm. Normalization correction (to account for variable count-rate sensitivity of sensors), decay correction, scatter and CT-based attenuation corrections were applied to the reconstructed data sets. Quantitative calibrations were performed each imaging session and applied to generate PET radioactivity source maps scaled to kBq/cc. CT images were reconstructed with a 512×512×512 image matrix over a 56 mm FOV using built-in optimum noise reconstruction procedures with the Triumph XO CT acquisition software, yielding images with 102µm isotropic resolution.

Dynamic PET and CT images were fused to a common coordinate frame using established coordinate transformations between the modalities. Both PET and CT images were then interpolated, resolution-matched at 100µm and subsequently underwent affine (6-parameter, rigid body) registration to a standard 3D MR-based mouse brain atlas template (Ma et al., 2005; Ma et al., 2008). This permitted parcellation of the brain for volume of interest (VOI) analysis over time, ultimately enabling the generation of

dynamic PET time-activity curves (TACs), which permitted evaluation of TRV6501 retention in 5XFAD and WT/BChE-KO brains. The mean voxel value of TRV6501 concentration (kBq/cc) for seven relevant brain structures were evaluated: i) whole brain (all but olfactory bulb, brain stem and cerebellum), ii) neocortex, iii) hippocampus, iv) globus pallidus, v) amygdala, vi) caudate/putamen and vii) cerebellum. An imaged-derived arterial input function (IDAIF) was also employed using PET-based localization and quantification of the proximal common carotid artery (CCA) to estimate the average concentration (kBq/cc) of radiotracer in the blood over time. Separate penumbral VOIs were delineated from left and right proximal CCAs in sagittal, axial and coronal planes, and propagated from frame 2 to all other frames in the acquisition series. VOIs consisted of an outer bounding spherical VOI (VOI_{out} , 2.5mm radius), from which the maximal average peak cluster of voxels (kBq/cc) within a smaller (VOI_{in} , 0.5mm radius) sphere was determined. The difference between the inner and outer VOIs ($VOI_{in} - VOI_{out}$) were determined for left and right CCAs, the average of which was taken as the mean IDAIF concentration (kBq/cc) for each mouse. All image registration and VOI processing was performed using PMOD (PMOD Technologies, Zurich, Switzerland).

4.5.9 Kinetic Modeling and Statistical Analysis

Time-activity curves were generated from the radioactivity source maps for each acquisition frame of each subject and were expressed in kBq/cc and %ID/mL representing the average activity per unit volume and percent injected dose per unit volume, respectively, in each of the seven brain structures evaluated.

Three kinetic models were evaluated including a one tissue compartment model (1TCM) a simplified reference tissue model (SRTM) (Lammertsma & Hume, 1996) and by Logan graphical analysis (Logan et al., 1990).

The 1TCM describes the exchange (uptake and washout) of tracer between blood plasma and a single tissue compartment (as reviewed in Chapter 1). In this model, the whole blood CCA IDAIF was used as the input function, fitted using a sum of two exponential functions, optimized using a Marquardt-Levenberg algorithm over 200 iterations. From the operational model curve, fitted kinetic parameters included K_1 ($\text{mL}\cdot\text{cm}^{-3}\cdot\text{min}^{-1}$), k_2 (min^{-1}) with a fixed physiological blood volume fraction, v_B set to 5%. From these parameters, the volume of distribution, V_T , was determined, where $V_T = K_1/k_2$ ($\text{mL}\cdot\text{cm}^{-3}$).

For the SRTM (as reviewed in Chapter 1) cerebellar gray matter was used as a reference region owed to the relatively low BChE accumulation in this region of the brain. Estimates of the relative influx rate constant R_1 ($\text{mL}\cdot\text{cm}^{-3}\cdot\text{min}^{-1}$), efflux rate constant k_2 (min^{-1}) and BP_{ND} ($\text{mL}\cdot\text{cm}^{-3}$) were obtained.

A Logan graphical analysis was also performed (as reviewed in Chapter 1) where average TRV6501 time-activity curves (kBq/cc) underwent a mathematical transformation, expressed as the integral of tissue concentration as a function of time, $C_T(\boldsymbol{\tau})$ divided by instantaneous tissue concentration, $C_T(t)$, plotted against a “normalized time”, represented by the integral of plasma concentration $C_p(\boldsymbol{\tau})$ divided by instantaneous tissue concentration, the slope, K , of which represents an estimate of distribution volume V_T (Equation 4.1).

$$\frac{\int_0^t c_T(\tau) d\tau}{c_T(t)} = K \frac{\int_0^t c_p(\tau) d\tau}{c_T(t)} + b \quad (\text{Equation 4.1})$$

A linear regression was fitted to the resulting Logan plot, using a maximum error criterion of 10%, whereby early data points outside a 10% deviation of the fit were excluded from the regression. The slope of this curve provides an estimate of total distribution volume V_T ($\text{mL} \cdot \text{cm}^{-3}$).

The suitability of the selected models in describing the kinetics of TRV6501 was evaluated with goodness of fit metrics including sum of squares (SS), R^2 and standard deviations of residuals (Sy.x) methods. All kinetic modelling was performed in the PKIN module of PMOD (Zurich, Switzerland). The average kinetic parameters in each brain region, expressed as group means \pm standard error of the mean (SEM), were compared between 5XFAD and WT/BCKE-KO mice using unpaired t-tests (two-tailed, assuming unequal variances) in SPSS (IBM Inc., Armonk, NY).

A retrospective power analysis (Vroman Battle et al., 2000) was also performed for post-hoc evaluation of the power of the statistical comparisons of this preliminary study. Estimates of V_T (1TCM and Logan graphical analysis) and BP_{ND} (SRTM) were evaluated in the neocortex and reported based on the observed Cohn's D effect size between 5XFAD and WT/BChE-KO for each of these metrics. The neocortex was chosen due to the preferential increase of BChE in this region of the 5XFAD brain, where retention of BChE-targeting TRV6501, in theory, would be elevated. Subsequent *a priori* sample size calculations were performed based on the observed effect size between 5XFAD and WT/BChE-KO, a power (1- β) of 0.80 and an alpha error probability, α , of

0.05. Power calculations were performed in GPower statistical analysis software (GPower 3.1, Dusseldorf, Germany).

4.6 Results

4.6.1 Physicochemical and *In Vitro* Kinetic Profile of *N*-Methylpiperidin-4-yl *p*-fluorobenzoate

The physicochemical and *in vitro* kinetic properties of TRV6501 are described in Table 4.1. In general, TRV6501 possesses a favourable physicochemical profile, with an MPO score of 4.69, owed to a relatively low molecular weight, topological surface area. An MPO score of ≥ 3 indicates a high likelihood of the radioligand crossing the BBB.

The nonradioactive fluorobenzoate was examined using purified human plasma BChE and purified recombinant human AChE. As indicated in repetitive scans, the ester underwent hydrolysis at pH 7.4 over 18 minutes with BChE. No hydrolysis occurred with AChE under the same conditions. From a Lineweaver-Burk plot, K_M , k_{cat} and k_{cat}/K_M were calculated. K_M was determined to be $6.65 \pm 1.23 \times 10^{-5}$ M, k_{cat} was determined to be $650 \pm 84 \text{ min}^{-1}$ and the enzymatic efficiency, k_{cat}/K_M was calculated to be $1.30 \pm 0.64 \times 10^6 \text{ M}^{-1}\text{min}^{-1}$. Taken together, these results indicate high selectivity of TRV6501 for BChE.

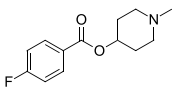
TRV #	Structure	Name	Physicochemical Profile					
			MW (g/mol)	TPSA (Å)	pKa	clogP / clogD	HBD	MPO
TRV6501		1-methyl-4-piperidinyl <i>p</i> - ¹⁸ [F]fluorobenzoate	237.27	30.74	9.69	2.15 / 0.84	0	4.69
			<i>In vitro</i> Kinetic Profile					
			V_{max} (M•min ⁻¹)	k_{cat} (min ⁻¹)	K_m	K_{cat} / K_m		
			24.7x10 ⁻⁶	385	284x10 ⁻⁶	1.30x10 ⁶		

Table 4.1 Radioligand characteristics that make up the product profile of BChE radioligand 1-methyl-4-piperidinyl *p*-¹⁸[F]fluorobenzoate (TRV6501) for positron emission tomography (PET) imaging. TRV6501 has a favourable physicochemical profile with a Multiparametric Optimization (MPO) score of 4.69 (≥ 3.0), indicating a high likelihood of crossing the BBB and being taken up in the brain. The *in vitro* kinetic profile also indicates high enzymatic selectivity for BChE, suggesting a greater probability of *in vivo* target engagement with BChE in the brain. MW, molecular weight; TPSA, topological polar surface area; pKa = $-\log_{10}K_a$, acid dissociation constant; clogP / clogD = partition coefficient / dissociation coefficient, measure of lipophilicity; HBD, hydrogen bond donors, MPO, Multiparametric Optimization Score (Wager et al. 2016); V_{max} , maximum enzymatic reaction rate; k_{cat} , turnover number; K_m , Michaelis constant.

4.6.2 Radiochemical Synthesis of *N*-Methylpiperidin-4-yl *p*-¹⁸F]Fluorobenzoate

The radiosynthesis of *N*-methylpiperidin-4-yl *p*-¹⁸F]fluorobenzoate was achieved using a modified procedure published previously (Bormans et al., 1996). Modifications include purification of [¹⁸F]KF with a QMA light Sep-Pak and the incorporation of a chemically active extraction. Using this modified procedure, *N*-methylpiperidin-4-yl *p*-¹⁸F]fluorobenzoate was isolated from radio-HPLC with 17% radiochemical yield. A small amount was reinjected into the radio-HPLC to confirm the radiopurity. The radiopurity of this compound was 97%.

4.6.3 Image-derived Arterial Input Function (IDAIF)

An image-derived arterial input function (IDAIF) based on PET quantification estimates of whole blood radioligand concentration in the proximal CCA was determined over the scan duration. PET acquisitions offered reproducible localization of left and right CCA over the course of the dynamic imaging series (Figure 4.1A). The average of left and right CCA time-activity curves for each mouse are shown in Figure 4.1B and the corresponding fitted curves (Figure 4.1C) were used as the input function for subsequent kinetic modeling with 1TCM and Logan graphical analysis methods.

A.

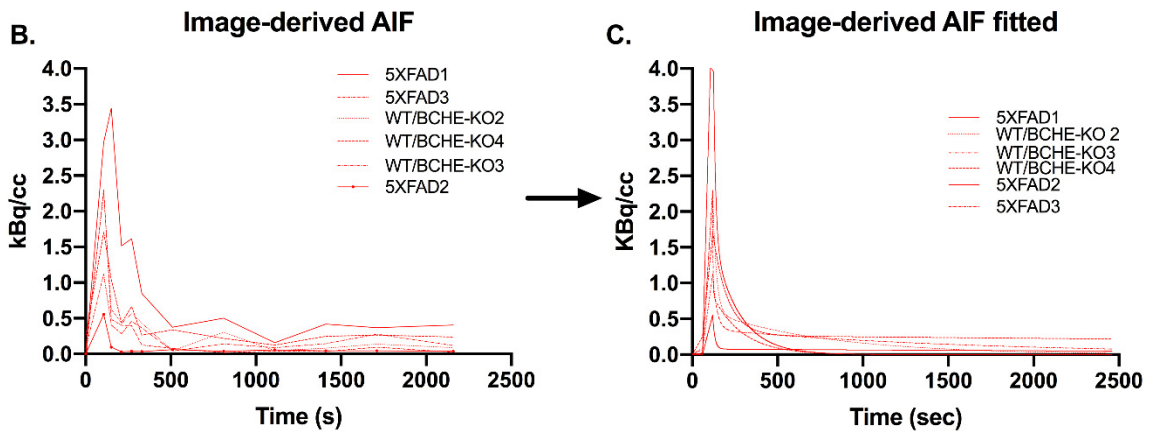
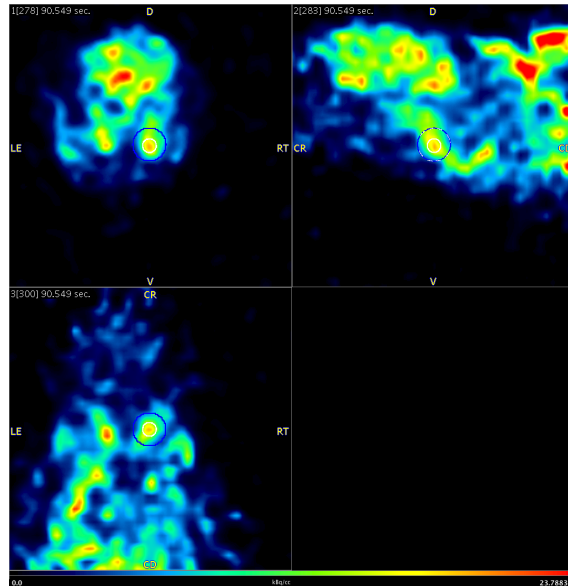


Figure 4.1 Image-derived arterial input function (IDAIF) estimates for 5XFAD and WT/BCHE-KO mice were determined via PET-based quantification of TRV6501 concentration in common carotid artery (CCA) over time. **A.** Representative coronal, sagittal and axial TRV6501 PET images showing delineation of proximal CCA. Penumbra spherical volumes of interest (VOIs) (outer bounding VOI_{out} , blue; inner maximal peak cluster VOI_{in} , white) were placed on left and right proximal CCA, with the average of VOI_{in} - VOI_{out} for both left and right CCA representing mean IDAIF. **B.** IDAIF time-activity curves (kBq/cc) for 5XFAD and WT/BCHE-KO mice. **C.** Corresponding fitted IDAIF curves were used as the input function for subsequent kinetic modelling using a single tissue compartment model (ITCM) and Logan graphical analysis.

4.6.4 Dynamic PET Imaging

PET imaging demonstrated cerebral uptake of TRV6501 in both 5XFAD and WT/BChE-KO mice, indicating that TRV6501 crossed the BBB. Marked radioligand accumulation was observed at early timepoints in both the 5XFAD (Figure 4.2) and WT/BChE-KO (Figure 4.3) brains, with a regionalized distribution evident in cortical areas and certain subcortical structures. This was followed by washout of TRV6501 over the duration of the scan as illustrated in representative time-activity curves of 5XFAD (Figure 4.4) and WT/BChE-KO (Figure 4.5) mice.

Across each of the brain structures investigated, peak concentrations (C_{\max}) of the radioligand were reached within the first minute post-injection (approximately 2.5min (150 sec) after the start of the PET scan) as evidenced in the time-activity curves expressed in both %ID/mL (Figure 4.6) and % C_{\max} (Figure 4.7). In measurements of whole brain uptake, this corresponded to an average TRV6501 concentration of (0.0043 ± 0.0022) %ID/mL in 5XFAD and (0.0102 ± 0.0038) %ID/mL in WT/BChE-KO mice, which was not significantly different ($p=0.269$).

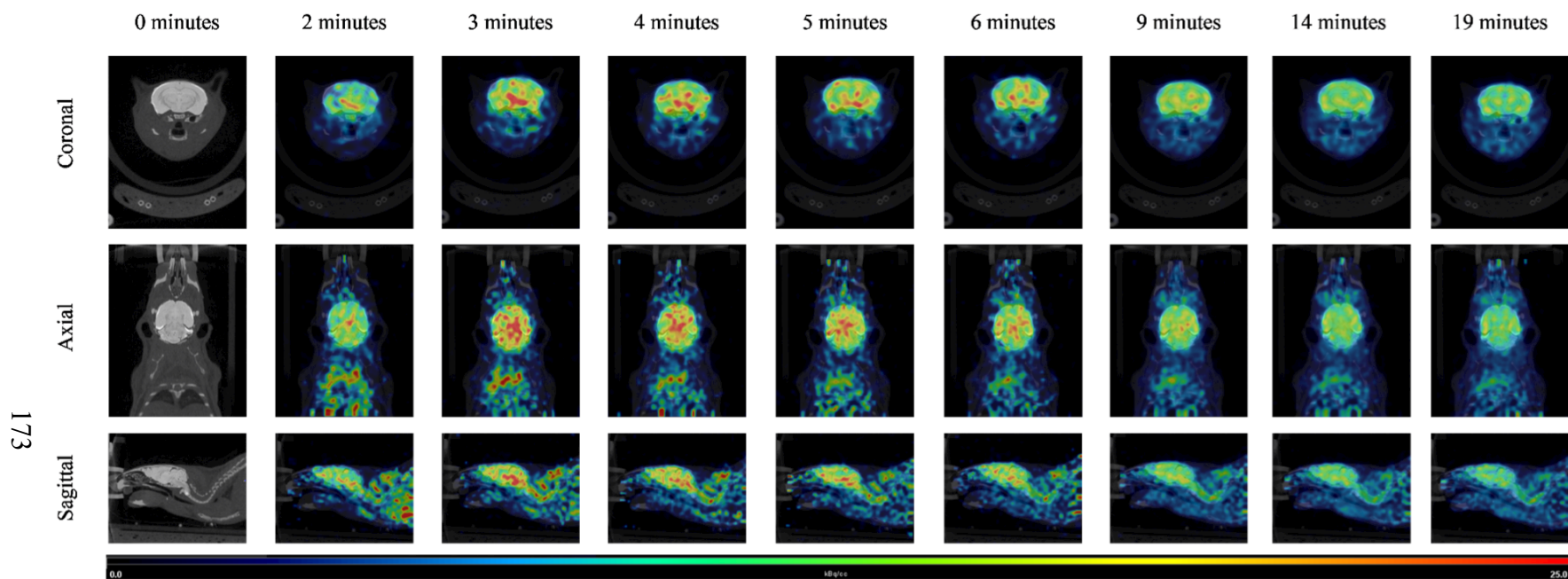


Figure 4.2 TRV6501 dynamic Positron Emission Tomography (PET) imaging series for a representative 5XFAD mouse in coronal (top), axial (middle) and sagittal (bottom) planes. PET images were co-registered with computed tomography (CT) and a magnetic resonance imaging (MRI) template brain for anatomical reference. Mice received a tail vein injection of TRV6501 2 minutes after the start of a 42-minute PET scan. 12 dynamic frames (one x 1.5 min, five x 1 min, five x 5 min and one x 10 min frame) were acquired, the first 9 are shown here. Figure timepoints indicate midpoint of each acquisition frame. TRV6501 crosses the blood brain barrier and is taken up in the brain with marked tracer accumulation in the brain followed by washout of the radioligand over the course of the scan. Color scale set from 0-25 kBq/cc.

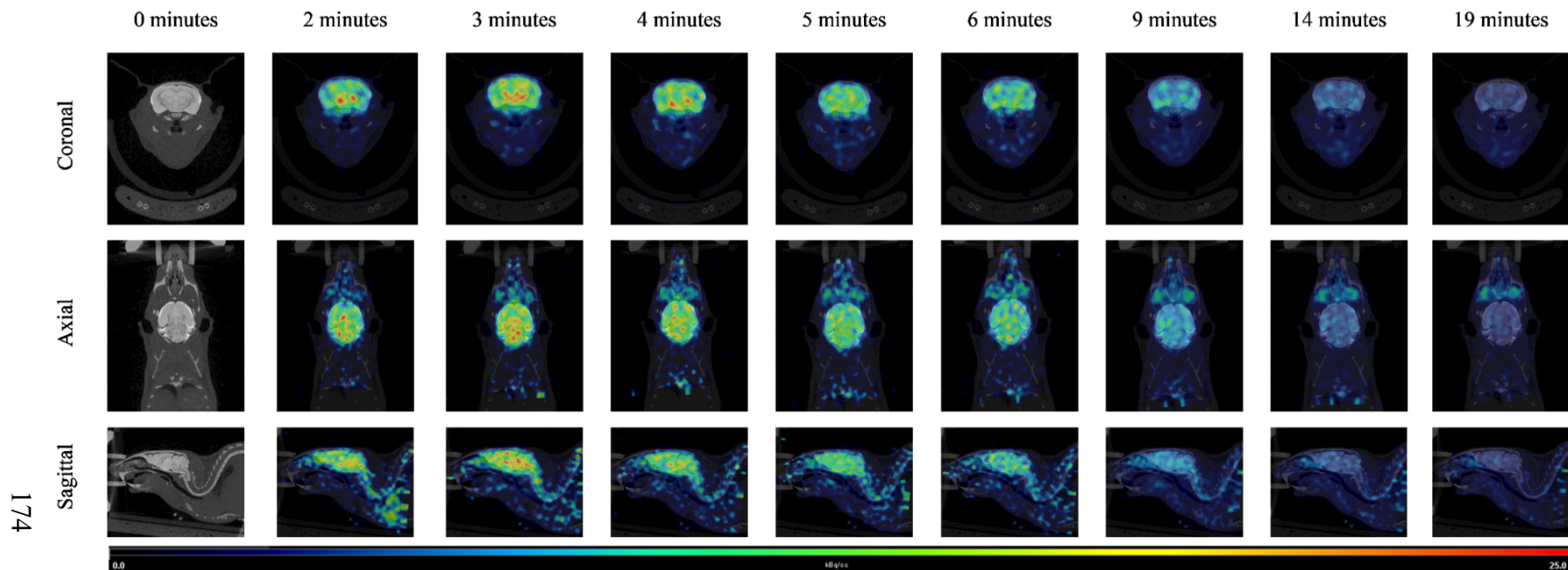


Figure 4.3 TRV6501 dynamic Positron Emission Tomography (PET) imaging series for a representative WT/BChE-KO mouse in coronal (top), axial (middle) and sagittal (bottom) planes. PET images were co-registered with computed tomography (CT) and a magnetic resonance imaging (MRI) template brain for anatomical reference. Mice received a tail vein injection of TRV6501 two minutes after the start of a 42-minute PET scan. 12 dynamic frames (one x 1.5 min, five x 1 min, five x 5 min and one x 10 min frame) were acquired, the first 9 are shown here. Figure timepoints indicate midpoint of each acquisition frame. TRV6501 crosses the blood brain barrier and is taken up in the brain with marked tracer accumulation in the brain followed by washout of the radioligand over the course of the scan. Color scale set from 0-25 kBq/cc.

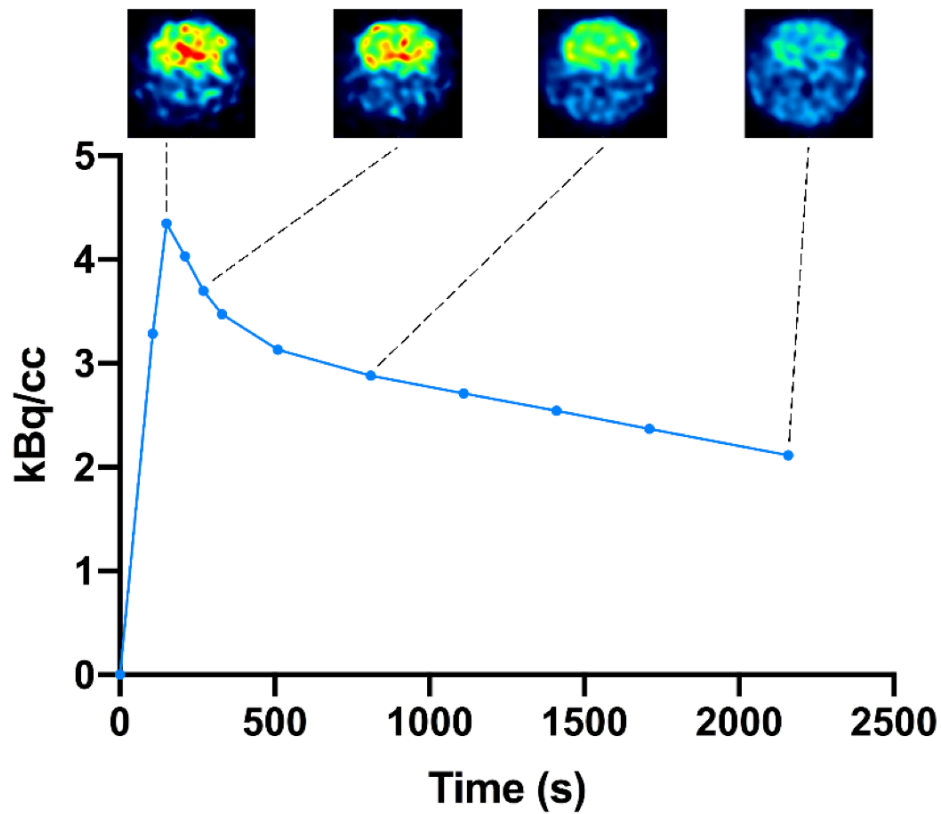


Figure 4.4 TRV6501 Positron Emission Tomography (PET) whole brain time-activity curves (kBq/cc) for a representative 5XFAD mouse. Mice received a tail vein injection of TRV6501 two minutes after the start of a 42-minute PET scan. 12 dynamic frames (one x 1.5 min, five x 1 min, five x5 min and one x 10 min frame) were acquired, with coronal TRV6501 brain images shown at 3,5, 14 and 42 minutes). Washout of TRV6501 is observable in the time-activity curve and in the associated imaging timepoints.

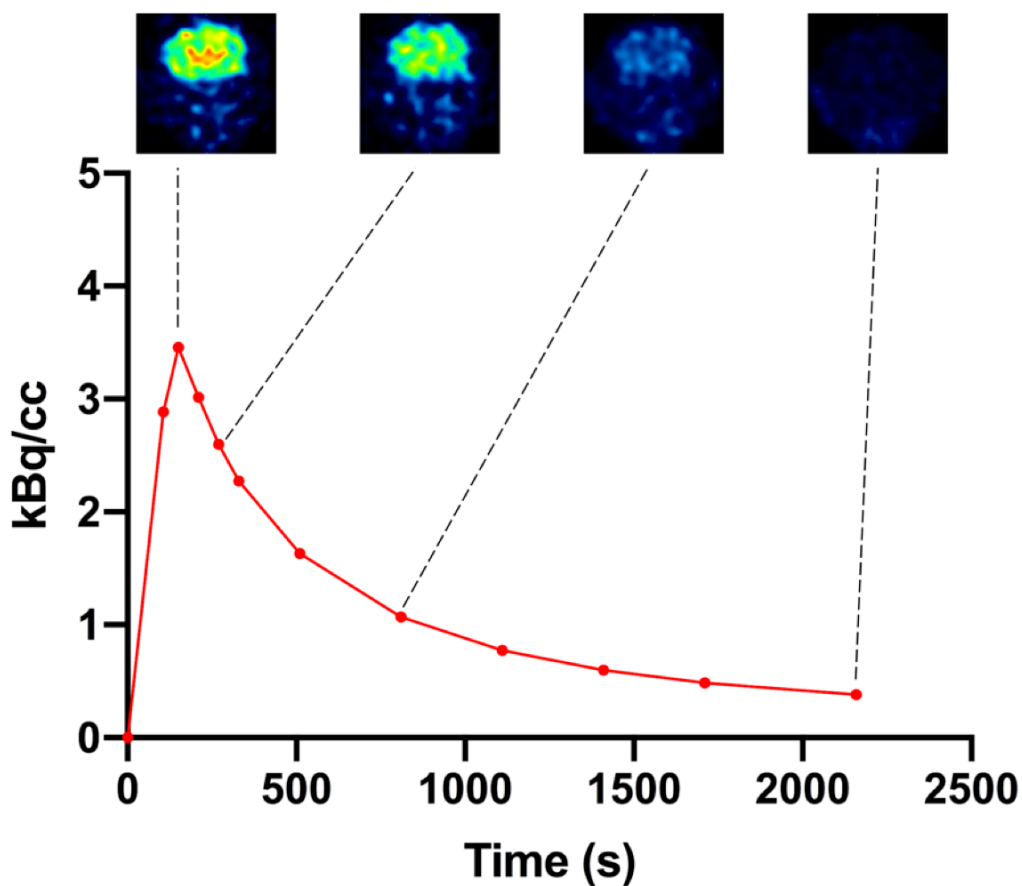


Figure 4.5 TRV6501 Positron Emission Tomography (PET) whole brain time-activity curves (kBq/cc) for a representative WT/BCHE-KO mouse. Mice received a tail vein injection of TRV6501 two minutes after the start of a 42-minute PET scan. 12 dynamic frames (one x 1.5 min, five x 1 min, five x 5 min and one x 10 min frame) were acquired, with coronal TRV6501 brain images shown at 3, 5, 14 and 42 minutes). Washout of TRV6501 is observable in the time-activity curve and in the associated imaging timepoints.

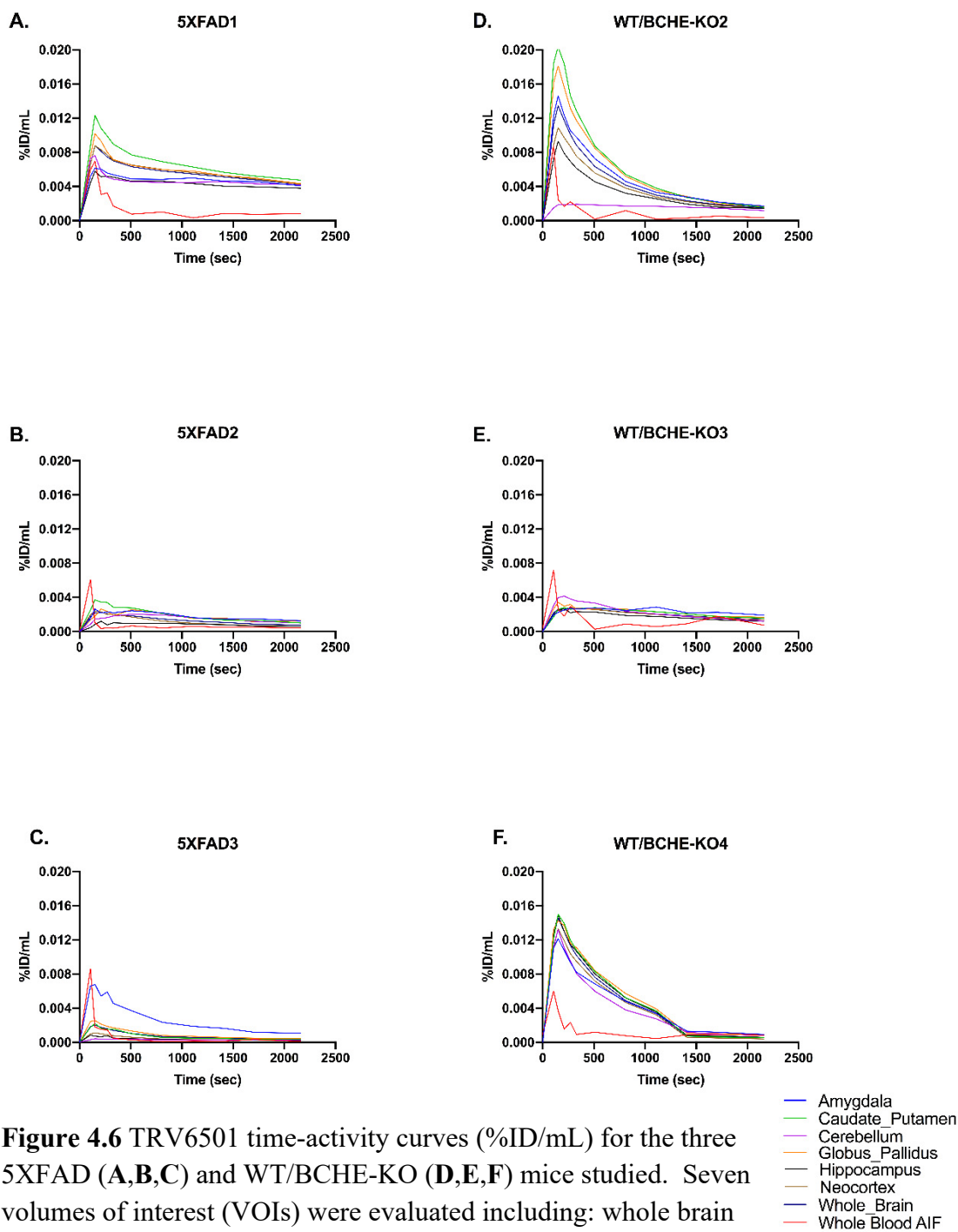


Figure 4.6 TRV6501 time-activity curves (%ID/mL) for the three 5XFAD (A,B,C) and WT/BCHE-KO (D,E,F) mice studied. Seven volumes of interest (VOIs) were evaluated including: whole brain (indigo), amygdala (blue), caudate/putamen (green), cerebellum (purple), globus pallidus (gold), hippocampus (black), neocortex (tan) and an image-derived arterial input function (red) estimated from TRV6501 concentration in the common carotid artery (CCA).

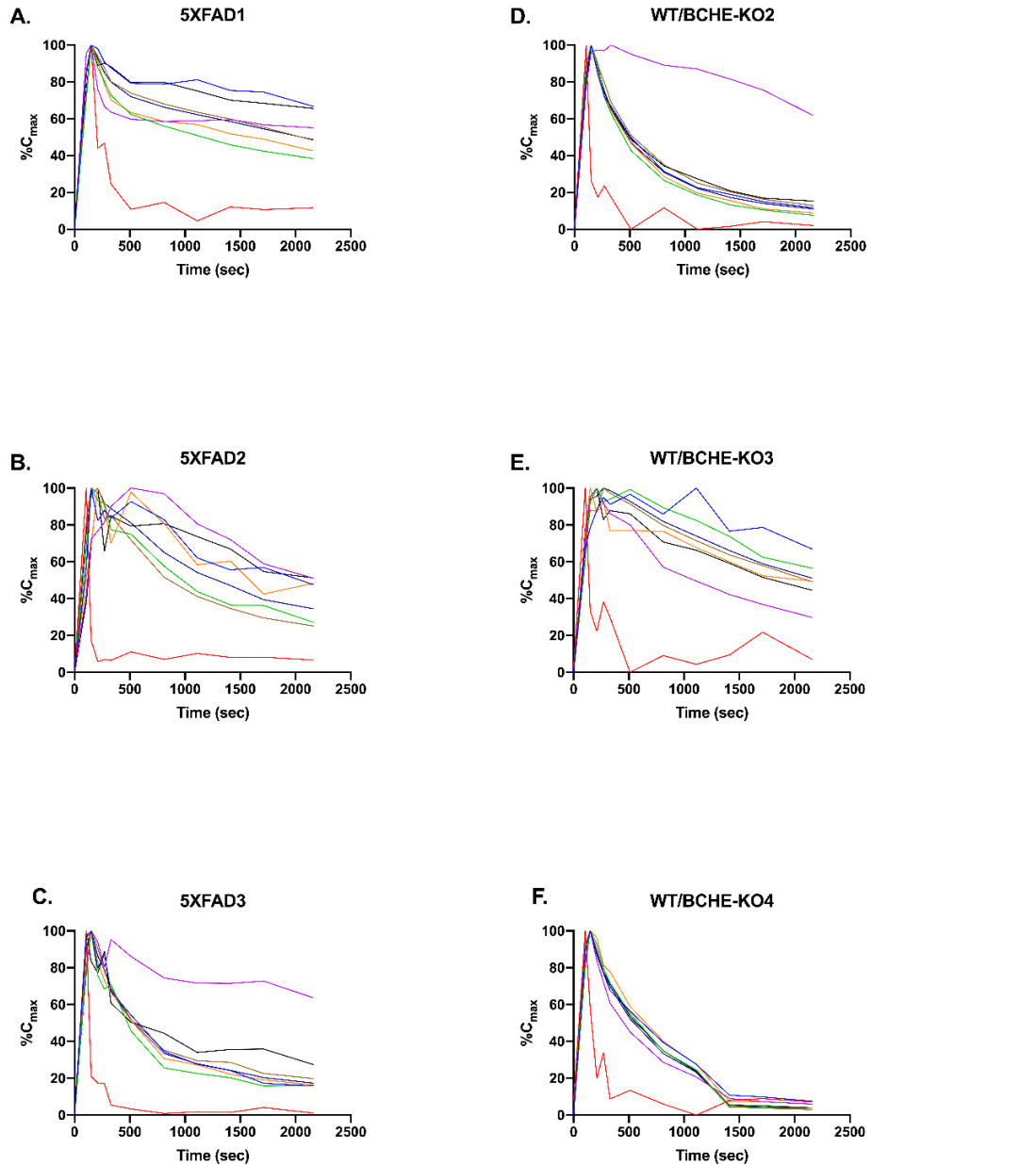


Figure 4.7 TRV6501 time-activity curves expressed as a percentage of the maximum concentration ($\%C_{\max}$) for the three 5XFAD (A,B,C) and WT/BCHE-KO (D,E,F) mice studied. Seven volumes of interest (VOIs) were evaluated including: whole brain (indigo), amygdala (blue), caudate/putamen (green), cerebellum (purple), globus pallidus (gold), hippocampus (black), neocortex (tan) and an image-derived arterial input function (red) estimated from TRV6501 concentration in the common carotid artery (CCA). In most instances, C_{\max} occurred approximately 30 seconds after TRV6501 was administered (2.5mins after scan start).

- Amygdala
- Caudate_Putamen
- Cerebellum
- Globus_Pallidus
- Hippocampus
- Neocortex
- Whole_Brain
- Whole Blood AIF

4.6.5 PET Kinetic Modeling

TRV6501 uptake and retention in the brain was evaluated using kinetic modelling approaches including 1TCM, SRTM and Logan graphical analyses.

4.6.5.1 1TCM Evaluation of TRV6501

Regional tissue time-activity curves (kBq/cc) for 5XFAD (Figure 4.8 A,D,G) and WT/BChE-KO (Figure 4.9 A,D,G) underwent a convolution with the corresponding whole blood IDAIF for each mouse. The resulting curves were fitted using non-linear regressions and are shown for 5XFAD (Figure 4.8 B, E, H) and WT/BChE-KO (Figure 4.9 B,E,H) mice in each of the brain regions investigated. K_1 and k_2 parameter estimates were determined for each region and compared between 5XFAD and WT/BChE-KO mice (Figure 4.10, Table 4.2). Whole brain estimates of K_1 (5XFAD, $0.43 \pm 0.13 \text{ mL}\cdot\text{cm}^{-3}\cdot\text{min}^{-1}$; WT/BChE-KO, $1.79 \pm 0.77 \text{ mL}\cdot\text{cm}^{-3}\cdot\text{min}^{-1}$), k_2 (5XFAD, $0.14 \pm 0.02 \text{ min}^{-1}$; WT/BChE-KO, $0.42 \pm 0.13 \text{ min}^{-1}$) and V_T (5XFAD, $3.05 \pm 1.11 \text{ mL}\cdot\text{cm}^{-3}$; WT/BChE-KO, $3.73 \pm 0.91 \text{ mL}\cdot\text{cm}^{-3}$) were not significantly different between 5XFAD and WT/BChE-KO mice ($p \geq 0.178$) (Figure 4.10, Table 4.2). Similarly, regional estimates of K_1 (5XFAD, $(0.21 \pm 0.10 - 0.76 \pm 0.18) \text{ mL}\cdot\text{cm}^{-3}\cdot\text{min}^{-1}$; WT/BChE-KO, $(0.71 \pm 0.24 - 3.18 \pm 1.40) \text{ mL}\cdot\text{cm}^{-3}\cdot\text{min}^{-1}$), k_2 (5XFAD, $(0.01 \pm 0.01 - 0.18 \pm 0.02) \text{ min}^{-1}$; WT/BChE-KO, $(0.16 \pm 0.02 - 0.55 \pm 0.19) \text{ min}^{-1}$) and V_T (5XFAD, $(2.24 \pm 1.10 - 4.71 \pm 0.51) \text{ mL}\cdot\text{cm}^{-3}$; WT/BChE-KO, $(2.95 \pm 0.60 - 5.46 \pm 1.49) \text{ mL}\cdot\text{cm}^{-3}$) were not significantly different between 5XFAD and WT/BChE-KO in the brain structures investigated ($p \geq 0.382$) (Figure 4.10, Table 4.2).

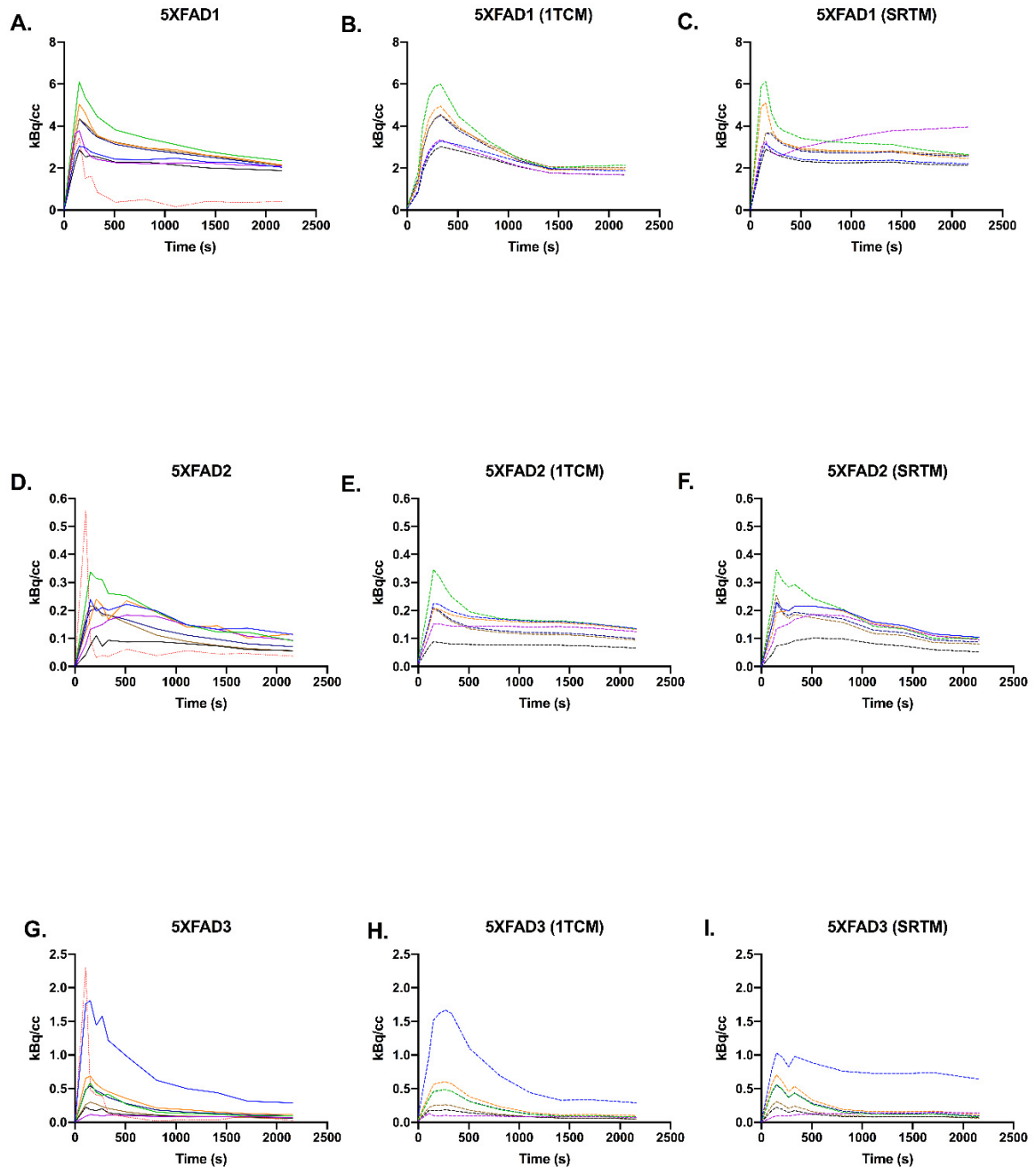


Figure 4.8 TRV6501 time-activity curves (kBq/cc) for the three 5XFAD mice evaluated (A,B,C). Corresponding single tissue compartment model (1TCM) (D,E,F) and simplified reference tissue model (SRTM) (G,H,I) curves generated from the same 5XFAD mice. 1TCM curves were fitted to estimate kinetic parameters K_1 , k_2 and V_T (Figure 4.10) and SRTM curves were used to derive kinetic BP_{ND} (Figure 4.11). Seven volumes of interest (VOIs) were evaluated including: whole brain (indigo), amygdala (blue), caudate/putamen (green), cerebellum (purple), globus pallidus (gold), hippocampus (black), neocortex (tan) and an image-derived arterial input function (red) estimated from TRV6501 concentration in the common carotid artery (CCA).

- Amygdala
- Caudate_Putamen
- Cerebellum
- Globus_Pallidus
- Hippocampus
- Neocortex
- Whole_Brain
- Whole Blood AIF

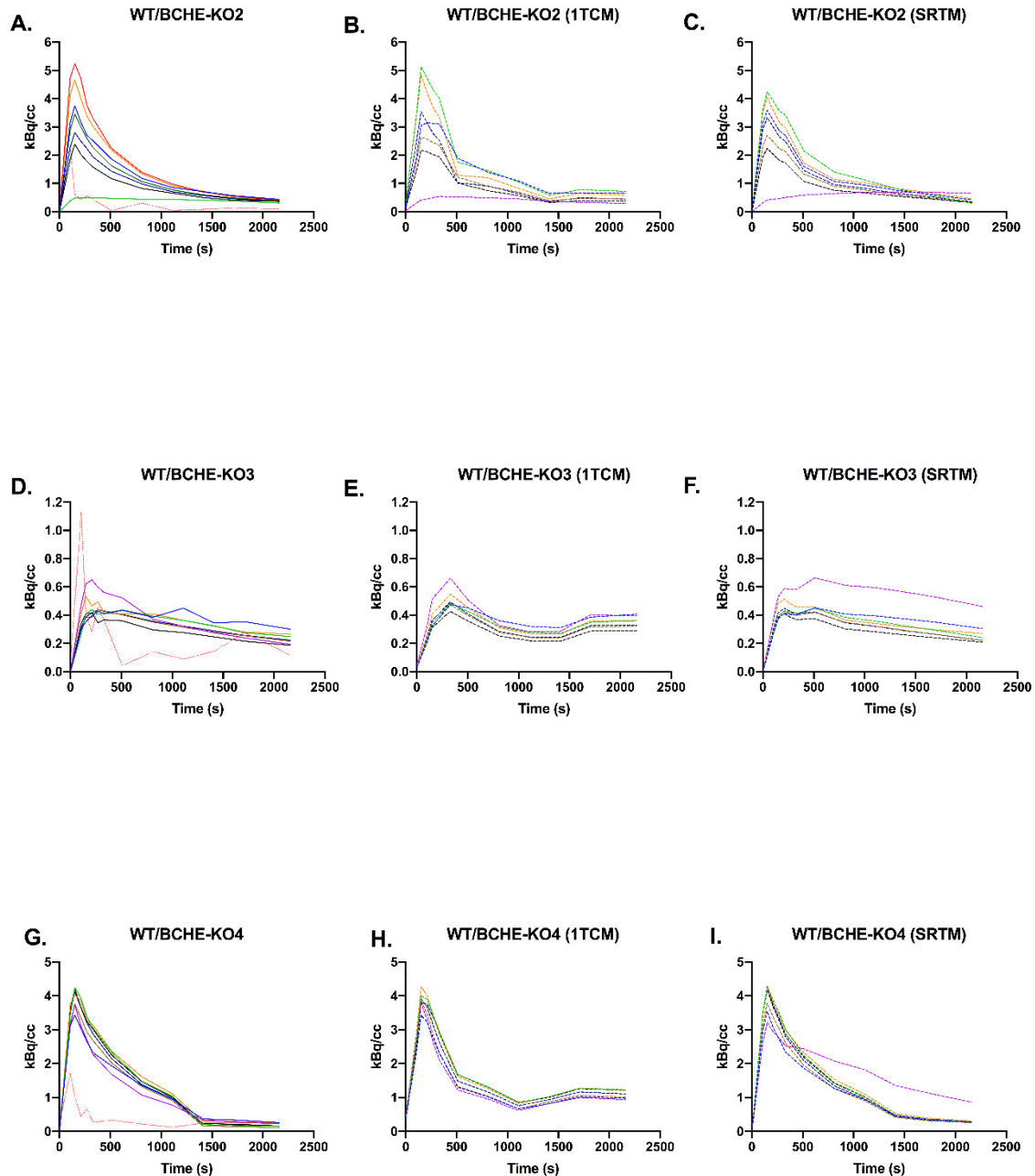


Figure 4.9 TRV6501 time-activity curves (kBq/cc) for the three WT/BCHE-KO mice evaluated (A,B,C). Corresponding single tissue compartment model (1TCM) (D,E,F) and simplified reference tissue model (SRTM) (G,H,I) curves generated from the same WT/BCHE-KO mice. 1TCM curves were fitted to estimate kinetic parameters K_1 , k_2 and V_T (Figure 4.10) and SRTM curves were used to derive kinetic BP_{ND} (Figure 4.11). Seven volumes of interest (VOIs) were evaluated including: whole brain (indigo), amygdala (blue), caudate/putamen (green), cerebellum (purple), globus pallidus (gold), hippocampus (black), neocortex (tan) and an image-derived arterial input function (red) estimated from TRV6501 concentration in the common carotid artery (CCA).

- Amygdala
- Caudate_Putamen
- Cerebellum
- Globus_Pallidus
- Hippocampus
- Neocortex
- Whole_Brain
- Whole Blood AIF

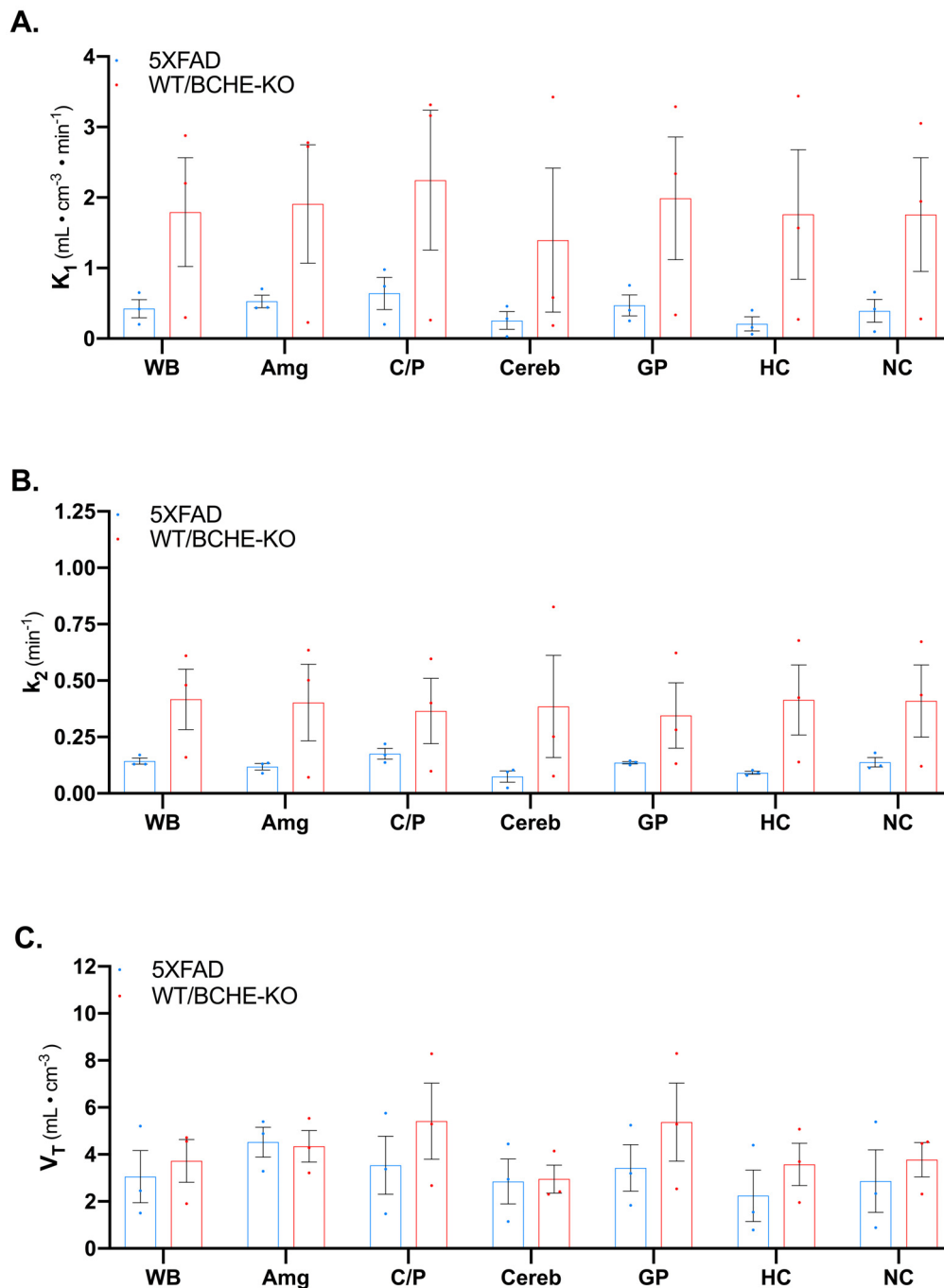


Figure 4.10 TRV6501 single tissue compartment model (1TCM) kinetic parameter estimates of **A.** influx rate constant K_1 ($\text{mL} \cdot \text{cm}^3 \cdot \text{min}^{-1}$) **B.** efflux rate constant k_2 (min^{-1}) and **C.** the volume of distribution, V_T for 5XFAD (blue) and WT/BChE-KO (red) mice. All values mean \pm SEM. No significant differences in K_1 , k_2 or V_T were observed between 5XFAD and WT/BChE-KO mice in the brain structures evaluated ($0.173 \leq p \leq 0.930$) (Table 4.2) WB=whole brain, Amg=amygdala, C/P=caudate/putamen, Cereb=cerebellum, GP= globus pallidus, HC=hippocampus, NC= neocortex.

Brain Region	K_I (mL•cm ⁻³ •min ⁻¹)			k_2 (min ⁻¹)			V_T (mL•cm ⁻³)		
	5XFAD	KO	p value	5XFAD	KO	p value	5XFAD	KO	p value
WB	0.43 ± 0.13	1.79 ± 0.77	0.215	0.14 ± 0.02	0.42 ± 0.13	0.178	3.05 ± 1.11	3.73 ± 0.91	0.663
Amg	0.53 ± 0.09	1.91 ± 0.84	0.241	0.12 ± 0.02	0.40 ± 0.17	0.236	4.52 ± 0.64	4.34 ± 0.67	0.860
C/P	0.64 ± 0.23	2.25 ± 0.99	0.244	0.18 ± 0.02	0.37 ± 0.15	0.320	3.54 ± 1.24	5.42 ± 1.62	0.412
GP	0.47 ± 0.15	1.99 ± 0.87	0.221	0.14 ± 0.01	0.35 ± 0.15	0.285	3.43 ± 0.99	5.37 ± 1.66	0.382
HC	0.21 ± 0.10	1.76 ± 0.92	0.232	0.01 ± 0.01	0.27 ± 0.16	0.173	2.24 ± 1.10	3.57 ± 0.90	0.403
NC	0.39 ± 0.16	1.76 ± 0.81	0.229	0.14 ± 0.02	0.41 ± 0.16	0.230	2.87 ± 1.33	3.77 ± 0.73	0.592
Cerebel	0.26 ± 0.13	1.40 ± 1.02	0.380	0.08 ± 0.03	0.39 ± 0.23	0.304	2.85 ± 0.96	2.95 ± 0.60	0.930

Table 4.2 TRV6501 single tissue compartment model (1TCM) kinetic parameters: influx rate constant, K_I (mL•cm⁻³•min⁻¹); efflux rate constant, k_2 (min⁻¹) and distribution volume, V_T (mL•cm⁻³) for 5XFAD and WT/BChE-KO mice (mean ± SEM). No significant differences were observed in K_I , k_2 or V_T between 5XFAD and WT/BChE-KO mice in any of the brain structures evaluated ($0.173 \leq p \leq 0.930$) with limited sample size in this preliminary study. WB, whole brain; Amg, amygdala; C/P, caudate/putamen; CC/EC, corpus callosum/external capsule; GP, globus pallidus; HC, hippocampus; hypo, hypothalamus; NC, neocortex; Thal, thalamus; BS, brainstem; Cerebel, cerebellum.

4.6.5.2 SRTM Evaluation of TRV6501

Using a simplified reference tissue model (SRTM) with cerebellar gray matter reference region, whole brain estimates of R_I (5XFAD, $0.81 \pm 0.21 \text{ mL} \cdot \text{cm}^{-3} \cdot \text{min}^{-1}$; WT/BChE-KO, $0.92 \pm 0.07 \text{ mL} \cdot \text{cm}^{-3} \cdot \text{min}^{-1}$), k_2 (5XFAD, $0.68 \pm 0.32 \text{ min}^{-1}$; WT/BChE-KO, $0.05 \pm 0.05 \text{ min}^{-1}$) and BP_{ND} (5XFAD, $0.08 \pm 0.07 \text{ mL} \cdot \text{cm}^{-3}$; WT/BChE-KO, $6.61 \pm 6.60 \text{ mL} \cdot \text{cm}^{-3}$) were not significantly different between 5XFAD and WT/BChE-KO mice ($p \geq 0.188$) (Figure 4.11, Table 4.3). Similarly, regional estimates of R_I (5XFAD, $(0.96 \pm 0.44 - 4.21 \pm 2.93) \text{ mL} \cdot \text{cm}^{-3} \cdot \text{min}^{-1}$; WT/BChE-KO, $(1.10 \pm 0.85 - 4.10 \pm 2.95) \text{ mL} \cdot \text{cm}^{-3} \cdot \text{min}^{-1}$), k_2 (5XFAD, $(0.07 \pm 0.06 - 0.68 \pm 0.32) \text{ min}^{-1}$; WT/BChE-KO, $(0.13 \pm 0.06 - 0.35 \pm 0.17) \text{ min}^{-1}$) and BP_{ND} (5XFAD, $(0.03 \pm 0.02 - 6.75 \pm 6.63) \text{ min}^{-1}$; WT/BChE-KO, $(0.01 \pm 0.01 - 6.98 \pm 6.52) \text{ min}^{-1}$) were not significantly different between 5XFAD and WT/BChE-KO in the brain structures investigated ($p \geq 0.274$) (Figure 4.11, Table 4.3).

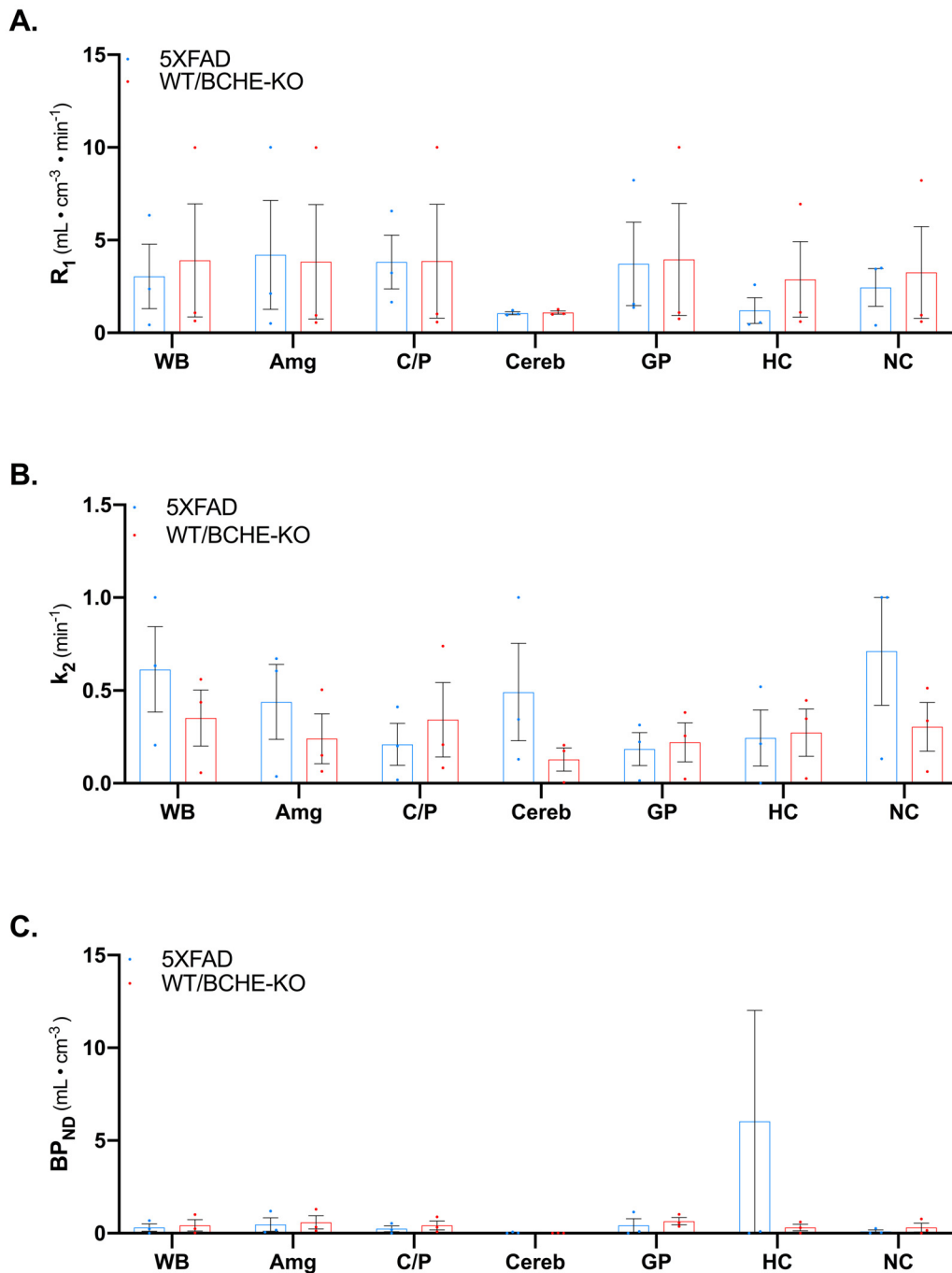


Figure 4.11 TRV6501 simplified reference tissue model (SRTM) kinetic parameter estimates of **A.** apparent influx rate constant R_1 ($\text{mL} \cdot \text{cm}^{-3} \cdot \text{min}^{-1}$) **B.** efflux rate constant k_2 (min^{-1}) and **C.** the non-displaceable binding potential BP_{ND} ($\text{mL} \cdot \text{cm}^{-3}$) for 5XFAD (blue) and WT/BChE-KO (red) mice. All values mean \pm SEM. No significant differences in R_1 , k_2 or BP_{ND} were observed between 5XFAD and WT/BChE-KO mice in the brain structures evaluated ($0.188 \leq p \leq 0.989$) (Table 4.3) WB=whole brain, Amg=amygdala, C/P=caudate/putamen, Cereb=cerebellum, GP= globus pallidus, HC=hippocampus, NC= neocortex.

Brain Region	R_I (mL·cm ⁻³ ·min ⁻¹)			k_2 (min ⁻¹)			BP _{ND} (mL·cm ⁻³)		
	5XFAD	KO	p value	5XFAD	KO	p value	5XFAD	KO	p value
WB	3.05 ± 1.74	3.91 ± 3.05	0.648	0.68 ± 0.32	0.05 ± 0.05	0.188	0.30 ± 0.07	0.42 ± 0.31	0.427
Amg	4.21 ± 2.93	3.83 ± 3.09	0.934	0.438 ± 0.20	0.24 ± 0.14	0.466	0.47 ± 0.36	0.59 ± 0.36	0.833
C/P	3.82 ± 1.45	3.87 ± 3.07	0.989	0.21 ± 0.11	0.34 ± 0.20	0.603	0.23 ± 0.16	0.42 ± 0.24	0.556
GP	3.72 ± 2.26	3.95 ± 3.03	0.954	0.18 ± 0.09	0.22 ± 0.11	0.804	0.42 ± 0.37	0.65 ± 0.19	0.612
HC	1.20 ± 0.70	2.89 ± 2.04	0.502	0.24 ± 0.15	0.27 ± 0.12	0.891	6.03 ± 5.98	0.30 ± 0.18	0.439
NC	2.45 ± 1.01	3.26 ± 2.48	0.785	0.71 ± 0.29	0.30 ± 0.13	0.297	0.10 ± 0.08	0.31 ± 0.24	0.470
Cerebel	1.06 ± 0.08	1.10 ± 0.85	0.790	0.49 ± 0.26	0.13 ± 0.06	0.299	0.03 ± 0.02	0.01 ± 0.01	0.333

Table 4.3 TRV6501 simplified reference tissue model (SRTM) kinetic parameters: apparent influx rate constant, R_I (mL·cm⁻³·min⁻¹); efflux rate constant, k_2 (min⁻¹) and distribution volume BP_{ND} (mL·cm⁻³) for TRV6501 in 5XFAD and WT/BCHE-KO (KO) mice (mean ± SEM). No significant differences were observed in R_I , k_2 or BP_{ND} between 5XFAD and WT/BCHE-KO mice in any of the brain structures evaluated ($0.188 \leq p \leq 0.989$) with limited sample size in this preliminary study. WB, whole brain; Amg, amygdala; C/P, caudate/putamen; CC/EC, corpus callosum/external capsule; GP, globus pallidus; HC, hippocampus; hypo, hypothalamus; NC, neocortex; Thal, thalamus; BS, brainstem; Cerebel, cerebellum.

4.6.5.3 Logan Graphical Analysis of TRV6501

Logan graphical analysis was also carried out to provide an estimate of the volume of distribution, V_T , of TRV6501. Whole brain Logan plots and corresponding linear regressions for 5XFAD and WT/BChE-KO are seen in Figure 4.12. The slope of the linear regression provides an estimate of V_T . Logan plot linear regression summaries for whole brain and regional analysis are provided in Figure 4.13. Whole brain and estimates of V_T (5XFAD, $2.93 \pm 1.35 \text{ mL} \cdot \text{cm}^{-3}$; WT/BChE-KO, $3.27 \pm 1.18 \text{ mL} \cdot \text{cm}^{-3}$) were not significantly different between 5XFAD and WT/BChE-KO ($p = 0.861$) (Figure 4.14). Similar to the whole brain results, regional estimates of V_T (5XFAD, $(2.28 \pm 1.25 - 5.77 \pm 1.20) \text{ mL} \cdot \text{cm}^{-3}$; WT/BChE-KO, $(2.45 \pm 0.38 - 4.28 \pm 1.83) \text{ mL} \cdot \text{cm}^{-3}$) were not significantly different between 5XFAD and WT/BChE-KO in the brain structures investigated ($p \geq 0.136$) (Figure 4.14).

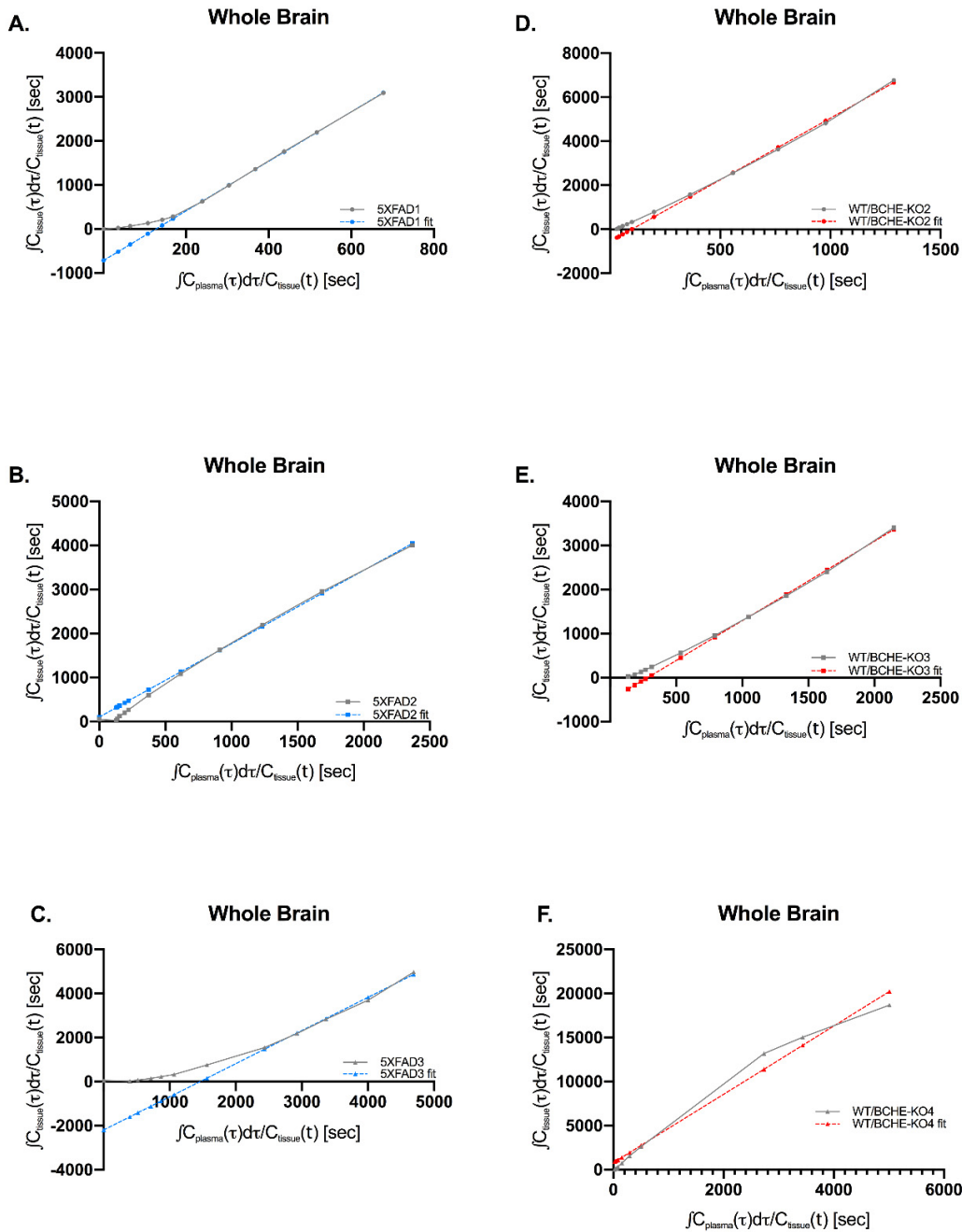


Figure 4.12 TRV6501 whole brain Logan plots for 5XFAD (A,B,C) and WT/BChE-KO (D,E,F) mice. A mathematical transformation is applied to time-activity curves, expressing tissue activity as a function of time $C_{\text{tissue}}(t)$ divided by instantaneous tissue concentration $C_i(t)$ and plotted against a normalized time (expressed as the integral of the input curve $C_a(t)$ divided by $C_{\text{tissue}}(t)$). The slope of the resulting linear relationship provides an estimate of the volume of distribution (V_T). Whole brain linear regressions shown for (5XFAD, blue), (WT/BChE-KO, red), the results of which are summarized in Figure 4.13 and Figure 4.14.

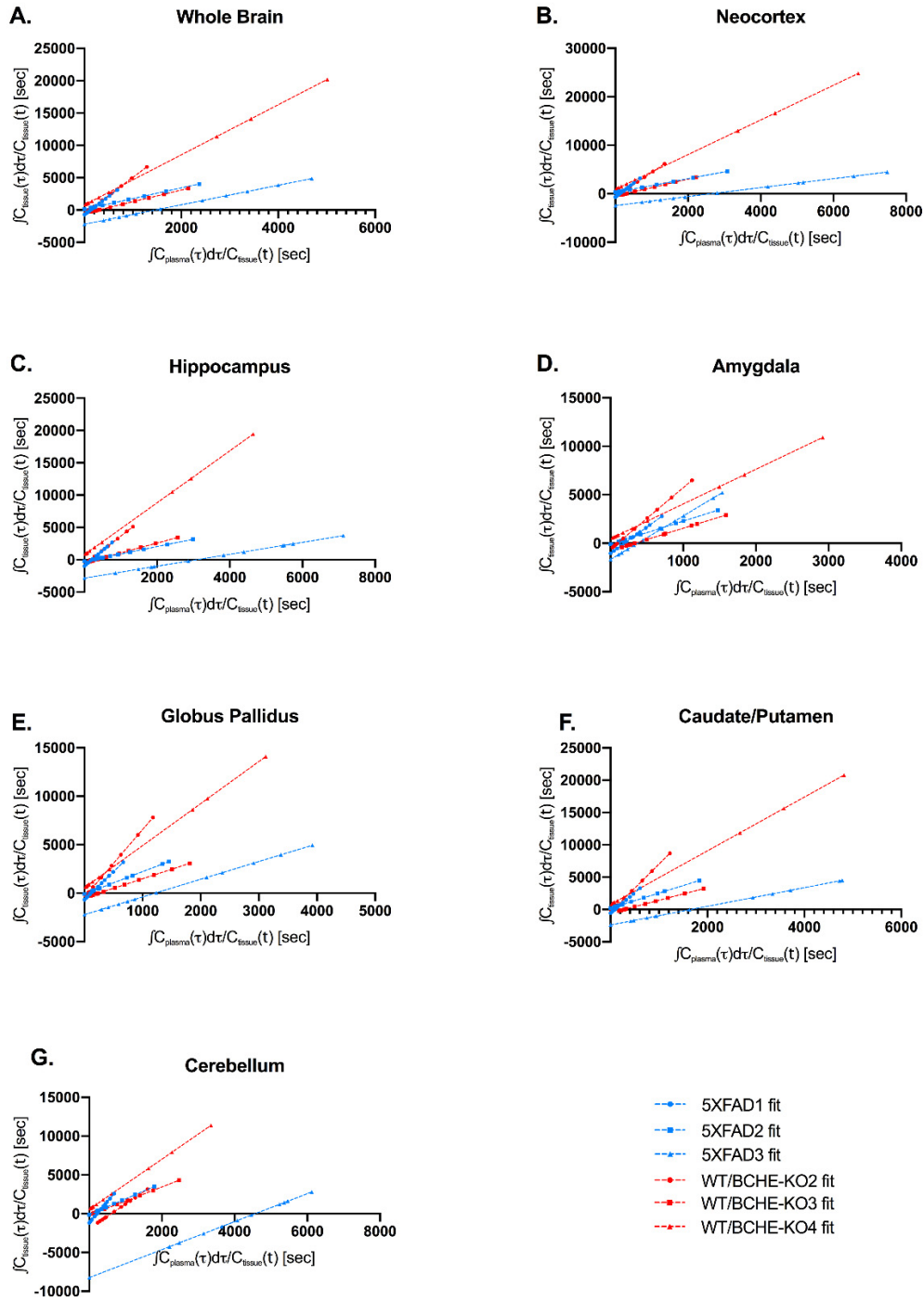
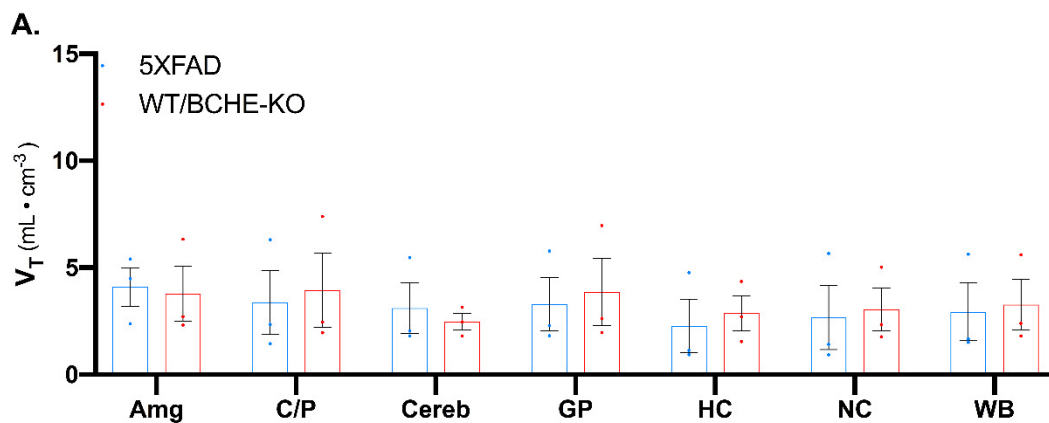


Figure 4.13 TRV6501 Logan plot linear regressions (transformed time-activity curve data not shown) for 5XFAD (blue) and WT/BChE-KO (red) mice in **A.** whole brain, **B.** neocortex, **C.** hippocampus, **D.** Amygdala, **E.** globus pallidus, **F.** caudate/putamen and **G.** cerebellum. Slopes of linear regressions provided estimate of volume of distribution (V_T). V_T results are shown in Figure 4.14.



B.

Brain Region	V_T (mL·cm ⁻³)		
	5XFAD	WT/BChE-KO	p value
WB	2.93 ± 1.35	3.27 ± 1.18	0.861
Amg	4.09 ± 0.89	3.78 ± 1.28	0.853
C/P	3.37 ± 1.49	3.94 ± 1.73	0.815
GP	3.30 ± 1.25	3.86 ± 1.57	0.795
HC	2.28 ± 1.25	2.87 ± 0.82	0.717
NC	2.67 ± 1.51	3.05 ± 1.00	0.847
Cerebel	3.10 ± 1.19	2.48 ± 0.39	0.659

Figure 4.14 (A,B) Logan plot estimates of V_T for TRV6501 in 5XFAD (blue) and WT/BChE-KO (red) mice (mean ± SEM). No significant differences were observed between 5XFAD and WT/BChE-KO mice in any of the regions evaluated ($p \geq 0.659$). WB, whole brain; Amg, amygdala; C/P, caudate/putamen; GP, globus pallidus; HC, hippocampus; NC, neocortex; Cerebel, cerebellum.

4.6.5.4 Suitability of Models to Describe TRV6501 *In Vivo* Kinetics: Goodness of Fit Metrics

To confirm the suitability of the 1TCM, SRTM and Logan graphical analysis techniques in describing the pharmacokinetic behaviour of TRV6501, various goodness of fit metrics were evaluated including sum of squares (SS), R^2 , and standard deviation of residuals (Sy.x) methods. In general, these goodness of fit metrics indicated a strong correspondence with the empirical data. For TRV6501 evaluation in a 1TCM, SS values ranged between 1.24 ± 0.72 and 3.77 ± 2.63 , R^2 values ranged from 0.61 ± 0.19 to 0.78 ± 0.09 and Sy.x values ranged from 0.25 ± 0.11 to 0.44 ± 0.18 (Table 4.4). For the SRTM, SS values ranged between 0.002 ± 0.001 and 1.20 ± 0.71 , R^2 values ranged from 0.87 ± 0.14 to 0.99 ± 0.01 and Sy.x values ranged from 0.01 ± 0.01 to 0.32 ± 0.18 (Table 4.4). Finally for the Logan graphical analysis technique, an R^2 metric was evaluated, estimating the goodness of fit in the linear region of the transformed data. R^2 values were high, ranging between 0.992 ± 0.005 to 1.000 ± 0.001 .

Brain Region	1TCM			SRTM			Logan
	SS	R ²	Sy.x	SS	R ²	Sy.x	R ²
WB	2.32 ± 1.49	0.78 ± 0.09	0.33 ± 0.15	0.28 ± 0.27	0.94 ± 0.11	0.09 ± 0.07	1.000 ± 0.001
Amg	1.53 ± 0.84	0.71 ± 0.12	0.31 ± 0.11	0.64 ± 0.47	0.87 ± 0.14	0.18 ± 0.09	1.000 ± 0.002
C/P	3.77 ± 2.63	0.78 ± 0.08	0.43 ± 0.20	2.35 ± 1.5	0.92 ± 0.04	0.32 ± 0.18	0.990 ± 0.006
GP	3.55 ± 2.10	0.66 ± 0.11	0.44 ± 0.18	1.20 ± 0.71	0.91 ± 0.03	0.26 ± 0.11	0.997 ± 0.001
HC	1.24 ± 0.72	0.72 ± 0.09	0.25 ± 0.11	0.07 ± 0.03	0.92 ± 0.04	0.07 ± 0.02	0.992 ± 0.005
NC	2.00 ± 1.45	0.77 ± 0.09	0.30 ± 0.15	0.34 ± 0.27	0.93 ± 0.03	0.12 ± 0.07	0.997 ± 0.002
Cerebel	2.42 ± 2.11	0.61 ± 0.19	0.29 ± 0.18	0.002 ± 0.001	0.99 ± 0.01	0.01 ± 0.01	0.969 ± 0.029

Table 4.4 TRV6501 goodness of fit metrics for single tissue compartment model (1TCM), simplified reference tissue model (SRTM) and Logan graphical analysis methods (mean ± SEM). Sum of squares (SS), R² and standard deviation of residuals (Sy.x) were evaluated for the three methods, with smaller SS, Sy.x values and R² values closer to 1.0 indicating better fits. In general, these goodness of fit metrics indicated a strong correspondence with the measured PET time-activity curve data, suggesting that all three models adequately describe the pharmacokinetic characteristics of TRV6501.

4.7 Discussion

This preliminary *in vivo* PET evaluation of TRV6501 has provided considerable insight into the pharmacokinetic behaviour of this putative cholinesterase radioligand, expanding upon what has been established previously (Bormans et al., 1996). Originally developed as an AChE radioligand, TRV6501 failed to recapitulate the known AChE distribution of the brain gleaned from *ex vivo* biodistribution studies in mice. That is, no significant retention of the radioligand in regions of AChE enzymatic activity was observed and it was concluded that this radioligand was not a suitable AChE imaging agent (Bormans et al., 1996). The role of TRV6501 as a putative BChE imaging agent had not been fully explored, which prompted us to carry out the current study.

Previously, we have evaluated an [^{123}I] SPECT analogue of TRV6501, *N*-methylpiperidin-4-yl 4- ^{123}I iodobenzoate (TRV6001), which showed high selectivity for BChE as opposed to AChE (DeBay, Reid, Pottie, et al., 2017; Macdonald et al., 2011). In the current study, a modified method of Borman's et al. (Bormans et al., 1996) was used to effectively incorporate [^{18}F] into *N*-methylpiperidin-4-yl *p*-nitrobenzoate to produce *N*-methylpiperidin-4-yl *p*-[^{18}F]fluorobenzoate, which improved the radiochemical yield of the radioligand. Considering the [^{18}F]KF used in the previous synthesis contained significantly less heavy water, it was decided to purify the [^{18}F]KF using a QMA light Sep-Pak. To improve the reaction time, a chemically active extraction was used instead of using another Sep-Pak in the radiochemical procedure. These two minor modifications produced the *N*-methylpiperidin-4-yl *p*-[^{18}F]fluorobenzoate in 17% radiochemical yield with a radiochemical purity of 97%.

In vitro enzyme kinetics indicated that with a relatively high V_{max} (24.7×10^{-6} M \cdot min $^{-1}$), k_{cat} (385 min $^{-1}$) and a low K_m (284×10^{-6}), the corresponding BChE enzymatic efficiency, k_{cat}/K_m , was high (1.30 ± 0.64) $\times 10^6$ M $^{-1}$ min $^{-1}$. This suggests that TRV6501 will be processed efficiently by BChE. Taken together these data indicated that TRV6501 is a selective BChE substrate.

TRV6501 PET imaging results from the current study indicate that TRV6501 crosses the blood brain barrier and is readily taken up into the brain. This is in agreement with what was previously shown by Borman's et al. (Bormans et al., 1996) and is consistent with the favourable physicochemical properties of the molecule, namely possessing an MPO score of 4.69 (≤ 3), which is predictive of blood brain barrier penetrance. This is also in agreement with what we have shown previously with SPECT imaging of *N*-methylpiperidin-4-yl 4-[123 I]iodobenzoate (DeBay, Reid, Pottie, et al., 2017). Marked accumulation of TRV6501 was observed in the brain in 5XFAD and WT/BChE-KO mice at early timepoints, showing a regional distribution that favoured cortical and some subcortical regions. Subsequent washout was observed in both the 5XFAD and WT/BChE-KO brain. Previous *ex vivo* biodistribution studies in the mouse brain revealed a decrease of radioligand concentration to $\sim 9\%$ in the cerebral cortex between 2 minutes and 30 minutes post-administration of TRV6501. By comparison, in the current study, this corresponds to a concentration decrease to $\sim 30\%$ in the cerebral cortex of a representative 5XFAD or WT/BChE-KO mouse (Figure 4.7 C and D as an example). *Ex vivo* biodistribution methodologies differ significantly from quantitative PET, which may explain the observed discrepancies that may contribute to an underestimation of TRV6501 concentration using the *ex vivo* method.

Three approaches were used to evaluate the pharmacokinetic behaviour of TRV6501 *in vivo*, namely a 1TCM, SRTM and Logan graphical analysis techniques. These data showed that the various models evaluated describe the estimated TRV6501 pharmacokinetic parameters well, with generally better fits achieved via the SRTM compared to 1TCM owed to smaller observed SS and $Sy.x$ values and larger R^2 values. This could be explained by the introduction of variance in the 1TCM from the IDAIF implemented in the current study, that to this point has not been sufficiently validated. The simplicity of the Logan graphical analysis technique and the strong correlation between the empirical and fitted data make this method an attractive approach.

No apparent differences between 5XFAD and WT/BChE-KO were observed in pharmacokinetic parameters including the rates of influx (K_I , R_I), rates of efflux k_2 , or corresponding distribution volume (V_T) and binding potential (BP_{ND}) metrics at the whole brain or regional level, though admittedly in this preliminary analysis, sample size is limited. Low statistical power notwithstanding, the similar results observed among the 1TCM, SRTM and Logan graphical analysis methods may also suggest that though TRV6501 crosses the BBB and perfuses the brain, it may not be effectively interacting with its BChE target. This could be due to various factors including hydrolysis of the parent radioligand by available BChE in the bloodstream, producing radiometabolites that though may enter the brain, do not engage with the target. If this is the case, the trend of larger K_I in WT/BChE-KO determined by a 1TCM (though not statistically significant) suggests that perhaps more intact tracer reaches the brain and is not hydrolyzed in the blood in WT/BChE-KO mice. Radiometabolite analysis of the blood is warranted and

underway to accurately reconcile the fate of TRV6501 and its metabolites *in vivo* over the course of an imaging experiment.

A number of limitations are evident in these first-pass analyses. This study suffers from relatively low statistical power and as such, a considerable amount of variability is seen in the data. No clear differences are seen in TRV6501 retention between 5XFAD and WT/BChE-KO brains and this may be attributed the small sample size of the current study. Retrospective power analyses were carried out based on the observed effect sizes between 5XFAD and WT/BChE-KO for estimates of V_T (1TCM and Logan graphical analysis) and BP_{ND} (SRTM) in the neocortex. The range of effect sizes was determined to be between 0.169-0.690 which corresponded an achieved statistical power of between 0.071-0.175. *A priori* sample size calculations were also carried out based on the observed effect sizes, a desired power ($1-\beta$) of 0.8 and $\alpha=0.05$. These results indicated that at least 27 mice (1TCM) and as many as 433 mice (Logan graphical analysis) per group would be required to glean significance between 5XFAD and WT/BChE groups in metrics of TRV6501 neocortical retention (the region most associated with accumulation of BChE in 5XAD mice). No statistically separable differences in TRV6501 retention were apparent between 5XFAD and WT/BChE-KO brains using the analytical methods employed in the current study. While larger group numbers will help strengthen the statistical power of the study and potentially uncover differences in radiotracer retention, particular attention should also be placed on the possible refinement of analysis techniques to overcome the considerable variability observed in the derived PET retention metrics that either rely on a suitable reference region or arterial input function.

The selection of an appropriate reference region is essential when using reference tissue models such as the SRTM. Selection of a cerebellar gray matter reference region appeared to be a reasonable choice in the current study, based on visual inspection of the PET images. However, the stability of such a reference region should be evaluated in larger groups in order to adopt its widespread utility for these analyses.

A critical aspect to accurate kinetic modeling lies in the ability to acquire precise measurements of the input function that drives the entire model. In this sense, the fidelity of one's PET imaging data is directly constrained by the measured precision of an arterial input function. This is typically done with simultaneous blood sampling during the imaging study to determine the concentration of tracer in the blood. This is performed at high sampling frequencies on the order of ~10 seconds in the initial several minutes of the experiment. In practice, the execution of such a study is immensely challenging, even in humans but especially in mice. We have developed a means to estimate the input function using an IDAIF evaluated at the level of the proximal CCA. This is convenient as it is very close to the brain and was present in each of our imaging FOVs. A PET-based localization of CCA was utilized, as anatomical-based segmentation of CCA was not possible using a CT image without enhancement such as CT angiography (CTA). Several pitfalls exist with a PET-based delineation of the CCA. Spill-out and spill-in artifacts arise from partial volume effects owed to the relatively small size of mouse CCA and the low resolution of PET (~1.2mm). This can cause an underestimation and overestimation, respectively, of the true radiotracer concentration (Innis et al 2011). The use of an un-validated IDAIF has the potential to introduce a significant amount of variability in the data which could confound results in the 1TCM as well as Logan

graphical analysis techniques, where the IDAIFs were applied. Considerable variability in the IDAIFs between mice was seen in the current study, which may represent limitations of the technique that could be inducing scaling errors in the quantitation and generally introducing variance to the pharmacokinetic analyses. Careful validation of such an IDAIF method is necessary to have complete confidence in this analysis. A direct metabolite-corrected plasma fraction representing true, unchanged tracer concentration is critical in order to properly evaluate and model the kinetics of a new radiotracer and should be done in conjunction with IDAIF to validate the method. Alternatively, stochastic AIFs (population averaged shape) could also be explored to maintain a more consistent AIF measurement that is applied to the PET data.

Additionally, in this preliminary analysis, the temporal resolution of the current study is relatively coarse (60 seconds or greater) owed to a trade-off between signal-to-noise ratio (SNR) and temporal resolution. This was chosen in order to produce high SNR images, for visualization of tracer behaviour at the expense, on some level, of the temporal component. The consequence of such is that the true peak concentration (i.e. $\%C_{\max}$), is likely underestimated and could plausibly contribute to less accurate fitting of the derived kinetic parameters.

Even with the accurate execution of a carefully designed PET study, PET imaging in mice ultimately suffers from the relatively low resolution afforded by PET as a modality. As such, the regional results, particularly of smaller brain structures should be interpreted with caution. Careful and precise validation of an IDAIF corroborated with direct blood sampling in mice is warranted. In the future, a reasonable approach for each new prospective radioligand would be to perform direct blood sampling in a separate

(non-imaging) cohort of mice to obtain a representative AIF for each radiotracer. Proper plasma fraction and metabolite-corrected curves could be derived to more precisely characterize the true unchanged parent input function and ultimately the kinetics of the radioligand. This is especially important for these substrate-based enzymatic radiotracers, particularly ones targeting BChE, an enzyme that is prominent in the bloodstream. Radiometabolite-correction will be an important aspect of future analyses.

The current work represents initial progress in [^{18}F] radiochemistry in our group and in the enhancement of available neuroimaging analysis techniques. The research conducted in this chapter serves as an exemplar to establish a PET pharmacokinetic modelling analysis framework, ultimately expanding the analytical toolkit that is essential in order to rigorously characterize putative BChE radioligands *in vivo* for AD diagnostic development.

4.8 Acknowledgements

D.R. DeBay was responsible for the conception of the study design, PET/CT acquisition and data processing, development and implementation of the analysis pipeline, all statistical analysis and interpretation in addition to manuscript preparation. I.R. Pottie, K Kamamana and G.A. Reid were responsible for the radiosynthesis in conjunction with A. Bou Laouz and I.R. Pottie, K Kamamana and G.A. Reid were involved with the *in vitro* enzyme kinetics studies in addition to current manuscript contributions. Valuable guidance was provided by E. Martin and S. Darvesh (Chemistry) and by S. Burrell and C.V. Bowen (nuclear medicine imaging). The authors would like to thank Christa Davis for her technical support. This research was supported by the

Canadian Institutes of Health Research (MOP-82798, RNS- 117795, MOP-119343), Capital Health Research Fund, Nova Scotia Health Research Foundation (Scotia Scholar^{OM}, MED-MAT-2011-7512), Faculty and Department of Medicine of Dalhousie University, Innovacorp, Mount Saint Vincent University Committee on Research and Publication, Dalhousie Medical Research Foundation Gunn Family Research Prize, DeWolfe Graduate Studentship, Mrs. Sadie MacLeod through the Dalhousie Medical Research Foundation Adopt-a-Researcher program and the Dalhousie Medical Research Foundation Irene MacDonald Sobey Endowed Chair in Curative Approaches to Alzheimer's Disease.

Chapter 5 Cerebral Perfusion in the 5XFAD Mouse Model of Alzheimer's Disease

5.1 Publication Status

Manuscript in preparation.

D.R. DeBay, T Phi, C.V. Bowen, S. Burrell, S. Darvesh. *Cerebral Perfusion in the 5XFAD Mouse Model of Alzheimer's Disease*.

5.2 Overview

The following chapter describes a Single Photon Emission Computed Tomography (SPECT) study aimed at implementing preclinical brain perfusion imaging methods with ^{99m}Tc -Exametazime in the 5XFAD mouse model as part of a neuroimaging validation of the Cubresa Spark tabletop SPECT scanner for our diagnostics program. An introductory section provides background on the current use of perfusion-based imaging agents in AD and is followed by the current study methods, results and discussion.

5.3 Abstract

Functional neuroimaging with ^{99m}Tc -Exametazime (^{99m}Tc -hexamethyl propyleneamine oxime (^{99m}Tc -HMPAO, CeretecTM) Single Photon Emission Computed Tomography (SPECT) has been used as an ancillary test in Alzheimer's disease (AD) to evaluate regional cerebral blood flow (rCBF). Stereotypical patterns of hypoperfusion and hypometabolism have been established in human AD using ^{99m}Tc -Exametazime-SPECT and ^{18}F FDG-PET, respectively. Hypometabolism has been observed in animal

models, including the 5XFAD mouse; however, it is unknown whether hypoperfusion signatures of AD are also present in the 5XFAD model, often used for diagnostic and therapeutic drug development. The objective of the current study was to assess baseline perfusion patterns in 5XFAD compared to wild-type (WT) mice using ^{99m}Tc -Exametazime SPECT imaging and determine whether the perfusion signatures of human AD are recapitulated in the 5XFAD model.

Methods: 5XFAD (n=9) and age-matched wild-type (WT) (n=8) mice at 11.5 ± 0.2 months underwent a 45-minute SPECT scan 20min after ^{99m}Tc -Exametazime administration and subsequently imaged using computed tomography (CT) and magnetic resonance imaging (MRI) for anatomical reference. For comparative evaluation of brain perfusion in these mice, whole brain and regional standardized uptake values (SUVs) as well as regional relative standardized uptake values (SUV_r) with a whole brain reference region were compared between 5XFAD and WT groups. Brain structures including whole brain, neocortex, amygdala, hippocampus, striatum, globus pallidus, thalamus and cerebellum were evaluated.

Results: In general, brain perfusion appears to be conserved in 5XFAD brain. Whole brain ^{99m}Tc -Exametazime retention revealed no significant differences in SUV (5XFAD, 0.372 ± 0.254 ; WT, 0.640 ± 0.338 ; $p = 0.536$). Similarly, regional analysis revealed no significant differences in ^{99m}Tc -Exametazime SUV or SUV_r metrics between 5XFAD and WT mice (SUV: $0.357 \leq p \leq 0.640$; SUV_r: $0.595 \leq p \leq 0.936$).

Discussion: These exploratory results suggest an apparent disconnect between cerebral blood flow and glucose metabolism (neurovascular decoupling) in the 5XFAD brain.

Establishing baseline perfusion patterns in the 5XFAD model is essential and identifying discrepancies from human AD should be taken under advisement in pre-clinical diagnostic and therapeutic drug discovery programs.

5.4 Introduction

Brain function is governed by the activity of neurons. The regional activation of neurons in the brain evokes a closely regulated hemodynamic response, supplying blood containing energy substrates oxygen and glucose to satisfy the local metabolic requirements of activated neurons (Catafau, 2001; Iadecola, 2017). This proportional enhancement of regional cerebral blood flow (rCBF) in activated areas of the brain reflects a so-called neurovascular coupling phenomenon, highlighting the close linkage of neural activity to brain perfusion and metabolism (Pike, 2012). The exact mechanisms governing cerebral hemodynamics are complex and in general are poorly understood. Various physiological parameters influence cerebral blood flow which include mean arterial blood pressure, intracranial blood pressure, cerebral perfusion pressure (CPP), cerebrovascular resistance, and venous outflow among others, which has been reviewed extensively elsewhere (Iadecola, 2017). In general, cerebral autoregulation orchestrates the interplay of various mediators at the molecular level to control perfusion homeostasis in the brain through vasodilation. In periods of neuronal activity, increased oxidative metabolism by neurons results in the extracellular excretion of ions and metabolites such as hydrogen ions (H^+), CO_2 and adenosine which contribute to vasodilation and the observed increase in blood flow, often termed functional hyperemia (Catafau, 2001).

This neurovascular coupling phenomenon forms the basis of various

neuroimaging techniques measuring brain perfusion and metabolism, serving as surrogate measures of brain function. A variety of neuroimaging correlates of brain perfusion and metabolism have been devised including perfusion single photon emission computed tomography (SPECT), [^{18}F] fluorodeoxyglucose ([^{18}F]FDG-PET) functional MRI (fMRI) and arterial spin labelling (ASL).

5.4.1 Brain Perfusion Agents

A number of radiotracers have been developed to evaluate rCBF in the brain. These have included SPECT imaging with ^{133}Xe gas, ^{123}I *p*-iodo-*N*-isopropylamphetamine (^{123}IMP) and ^{15}O PET imaging, among others (Catafau, 2001). Various pitfalls have hampered the widespread clinical utility of such agents, including rapid clearance, poor SNR and low resolution images, and signal attenuation in deep brain structures associated with the low γ -ray energy of ^{133}Xe , whereas with ^{123}IMP , the prolonged latency of peak brain activity and redistribution over time in conjunction with high production costs and limited availability of ^{123}IMP has limited the practical use of such an agent.

Today, $^{99\text{m}}\text{Tc}$ -based SPECT agents have become the mainstay to evaluate brain perfusion including $^{99\text{m}}\text{Tc}$ -Exametazime (CereteTM, GE Healthcare), originally developed as $^{99\text{m}}\text{Tc}$ -d,l hexamethyl propyleneamine oxime ($^{99\text{m}}\text{Tc}$ -HMPAO) (Neirinckx et al., 1987; Nowotnik et al., 1985) (Figure 5.1), and $^{99\text{m}}\text{Tc}$ -ethyl cysteinate dimer ($^{99\text{m}}\text{Tc}$ -ECD) (Catafau, 2001). $^{99\text{m}}\text{Tc}$ -Exametazime and $^{99\text{m}}\text{Tc}$ -ECD are small (<500 Daltons) lipophilic molecules of neutral charge that readily cross the BBB and are retained in cells of the brain upon conversion into hydrophilic compounds. Both radiotracers possess

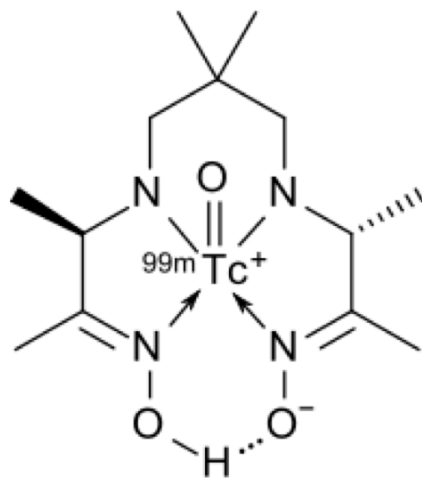


Figure 5.1 Chemical structure of ^{99m}Tc -Exametazime (^{99m}Tc -HMPAO).

similar pharmacokinetic characteristics, reaching peak activity in the brain at ~2min post injection (^{99m}Tc -Exametazime, 2-3%ID; ^{99m}Tc -ECD, 4-7%ID) and maintain a fixed flow-dependent distribution pattern in the brain (over several hours) that is proportional to rCBF at the time of injection (Neirinckx et al., 1987). Significant, prolonged brain retention is seen with both tracers (^{99m}Tc -Exametazime, 85-88% by 15 mins, 73% by 24hrs ; ^{99m}Tc -ECD, 86-88% by 1hr and subsequent 6%/hr washout) with rapid washout of background tissues providing high gray-to-white matter contrast (^{99m}Tc -Exametazime, 2-3:1; ^{99m}Tc -ECD, 4:1) and an imaging window of at least 2 hrs post injection (^{99m}Tc -Exametazime, up to 4hrs; ^{99m}Tc -ECD, up to 2 hrs). Whereas ^{99m}Tc -ECD is a relatively stable molecule, ^{99m}Tc -Exametazime is highly unstable *in vitro* and is normally incorporated with a stabilizing agent such as methylene blue or cobalt chloride for brain imaging applications (Catafau, 2001).

Despite the similarities in pharmacokinetic profile, ^{99m}Tc -Exametazime and ^{99m}Tc -ECD mechanisms of brain retention differ. The brain retention of ^{99m}Tc -Exametazime has been thought to largely reflect an intracellular interaction with glutathione, an antioxidant which comprises the majority of all free thiols in mammalian tissue. ^{99m}Tc forms a chelated lipophilic complex with Exametazime and when introduced into the blood stream, readily crosses the blood brain barrier through cell membranes where it is trapped intracellularly upon a glutathione-dependent conversion of the primary ^{99m}Tc -Exametazime complex to a non-diffusible hydrophilic form (Lassen et al., 1988; Neirinckx et al., 1988; Nowotnik et al., 1985). A competing trapping mechanism has been suggested where overall intracellular accumulation of ^{99m}Tc -Exametazime more specifically relates to reduction-oxidation (redox) activity of the

tissue (Jacquier-Sarlin et al., 1996b), thus having a certain dependence not only on cerebral perfusion but also on cellular metabolism.

On the other hand, the hydrophilic conversion of ^{99m}Tc -ECD has been shown to proceed by de-esterification via cellular esterase activity (Jacquier-Sarlin et al., 1996a) and thus cellular metabolism is considered the predominant mechanism of ECD retention in the brain. Variations in the relative proportion of cytosolic and membrane esterase activity have shown to modulate overall ^{99m}Tc -ECD retention, where cells with high membrane esterase activity inhibit the passage of ^{99m}Tc -ECD into the cell yielding a reduction in observed ^{99m}Tc -ECD signal.

In general, both ^{99m}Tc -Exametazime and ^{99m}Tc -ECD correlate well with rCBF in the healthy brain (Catafau, 2001); however, the different characteristics and retention mechanisms may serve to reconcile discrepancies seen on imaging under certain clinical circumstances where the biochemical profile of the brain (i.e. in various neurological diseases) may differ. For example, the reported variations in distribution seen in certain brain tumors, in individuals with encephalitis or subacute stroke (Moretti et al., 1995).

5.4.2 Imaging Brain Perfusion in AD

In neurodegenerative diseases such as Alzheimer's disease (AD), functional neuroimaging with SPECT radiotracer ^{99m}Tc -Exametazime has been used as an ancillary test in AD diagnosis to evaluate regional cerebral perfusion. As cerebral blood flow is closely coupled to neuronal activity, the activity distribution of ^{99m}Tc -Exametazime has been used as a surrogate marker of neuronal activity levels in areas of the brain and specific hypoperfusion patterns have been established in AD and other dementias. In

general, perfusion SPECT has moderate diagnostic value in AD with sensitivity/specificity (80%/85%) (Bloudek et al., 2011).

Few studies of SPECT perfusion have been carried out in mouse models. Apostolova et al. (Apostolova et al., 2012) successfully implemented SPECT perfusion imaging in mice using ^{99m}Tc -Exametazime that provided sufficient sensitivity to detect age-related differences in rCBF in a mouse model. In comparing ^{99m}Tc -Exametazime and ^{99m}Tc -ECD retention in mice, they noted a rapid clearance of ^{99m}Tc -ECD whereas significant brain retention was observed with ^{99m}Tc -Exametazime. The interspecies differences in esterase activity between human and mouse brain was thought to explain the lack of retention of ^{99m}Tc -ECD in the brain (Apostolova et al., 2012). Given these findings, in the current study, we focused on brain perfusion imaging with ^{99m}Tc -Exametazime.

To the best of our knowledge, no evidence exists as to whether the patterns of human temporoparietal hypometabolism are conserved in animal models of AD commonly used for diagnostic and therapeutic drug development. Transgenic mouse models of AD have been developed, including the 5XFAD mouse model (Oakley et al., 2006), a model of amyloidosis based on familial AD (FAD) mutations. This model overexpresses the human amyloid precursor protein (*APP*) *APP*₆₉₅ with the Swedish (K670N, M671L), Florida (I716V), and London (V717I) FAD mutations, as well as human presenilin 1 (PS1) harboring two FAD mutations, M146L and L286V. This mouse model of brain amyloidosis has a very aggressive course, exhibiting A β deposition accompanied by astrogliosis and microgliosis as early as ~2 months of age (Oakley et al., 2006) with commensurate increases over disease progression. In addition, a number of

similarities between this AD animal model and human AD have been documented, including loss of synaptic markers observed at 9 months, cognitive impairment as early as 4 months (Eimer & Vassar, 2013; Oakley et al., 2006) and association of the AD-specific enzyme butyrylcholinesterase (BChE) with A β pathology (Darvesh & Reid, 2016; Reid & Darvesh, 2015).

The aim of the current study was to implement preclinical brain perfusion imaging methods with ^{99m}Tc-Exametazime to evaluate patterns of perfusion in the 5XFAD mouse model.

5.5 Methods

Formal approval to conduct the current experiments was obtained from the Dalhousie University Radiation Safety Committee and the Canadian Nuclear Safety Commission (license 07154-2-17.10). ^{99m}Tc-Exametazime was synthesized at the Department of Diagnostic Imaging, Nova Scotia Health Authority, using the precursor kit which was an unconditional gift from GE, Canada. Mice were cared for according to the guidelines set by the Canadian Council on Animal Care (Dalhousie University Committee on Laboratory Animals Protocol 15-070).

5.5.1 Animals

Pairs of female wild-type (C57BL/6J x SJL/J F1, Stock Number: 100012-JAX) and male transgenic hemizygous 5XFAD mice (B6SJL-Tg(APP^{Sw}FILon, PSEN1*^{M146L}*^{L286V})6799Vas/Mmjax, Stock Number: 006554-JAX) were obtained from Jackson Laboratory (Bar Harbor, ME), and cared for as

described previously (Reid & Darvesh, 2015). Imaging was performed during light phase of the light-dark cycle. A total of 9 5XFAD mice (M:n=3, F:=2) and 8 WT (M:n=3, F:=2) were imaged with an average age of 11.5 ± 0.2 months.

5.5.2 ^{99m}Tc -Exametazime Synthesis

Synthesis of ^{99m}Tc -Exametazime followed standard procedures for preparation of CeretecTM for evaluation of regional cerebral blood flow (GE Healthcare, Ill, USA).

5.5.3 SPECT-CT Imaging

Mice were weighed immediately prior to imaging, anaesthetized with 3% isoflurane in an induction chamber, restrained in a TailVeiner Restrainer (Braintree Scientific) while under a continuous stream of 1.5% isoflurane. A catheter line was placed in the lateral tail vein and mice subsequently received 1.188 ± 0.053 mCi of ^{99m}Tc -Exametazime in 205-260 μL (5XFAD, 1.065 ± 0.036 mCi; WT, 1.326 ± 0.081 mCi). Injection of ^{99m}Tc -Exametazime was followed by a saline flush of $\sim 10\mu\text{L}$. Mice were recovered with tracer uptake occurring in conscious mice over 20 minutes. Mice then were secured in prone position in a heated Magnetic Resonance (MR)-compatible bed, wrapped in a blanket and maintained under continuous stream of 1.5-2% isoflurane and respiration rate monitored for the duration of scan (SA Instruments Inc. Stony Brook, NY). The mouse head region was centered on a 14mm axial field of view (FOV) and a 3-dimensional (3D) static SPECT scan was acquired in super list mode (SLM) over 45 minutes (4 projections) on a SPARKTM SRT-50 single head standalone tabletop SPECT scanner (Cubresa Inc. MB, CA) integrated with a Triumph XO LabPET pre-clinical computed tomography (CT) scanner (Trifoil Imaging, CA).

Following SPECT imaging, a CT scan was acquired for anatomical reference and subsequently co-registered with anatomical magnetic resonance imaging (MRI) acquired in a separate scan (see below). CT images were collected in fly mode with a 70 kVp x-ray beam energy (160 μ A beam current), 512 projections, 4 summed frames/projection, with 2 \times 2 binning and magnification of 2.26X, providing complete whole brain coverage in a 56mm FOV. CT scan duration was 8.5min.

5.5.4 MR Imaging

MRI scans were performed in a separate session prior to SPECT/CT imaging to facilitate regional analyses of radiotracer retention in the brain. MR imaging was carried out as described previously (DeBay, Reid, Pottie, et al., 2017), acquiring 142 μ m isotropic images at 3.0T over 61min using a 3D balanced Steady-State Free Precession, (b-SSFP) imaging sequence (T2/T1-weighting).

5.5.5 Image Processing

Dynamic SPECT images were reconstructed as follows: SPECT SLM data were converted to list mode data using built-in Cubresa SPARKTM preprocessing routine at 140keV with a 20% energy window applied. List mode data was reconstructed using an iterative 3D Maximum-Likelihood Expectation Maximization (MLEM) algorithm (9 iterations) using HiSPECT software (SciVis GmbH, Göttingen, Germany). Resultant SPECT images yielded an effective in-plane resolution of 0.8mm. Dark image and quantitative calibrations were performed weekly for the duration of the study and applied to each image acquired.

CT images were reconstructed with a $512 \times 512 \times 512$ image matrix over a 56 mm FOV using built-in optimum noise reconstruction procedures with the Triumph XO CT acquisition software, yielding images with $102\mu\text{m}$ isotropic resolution. Fusion of SPECT and CT images was achieved using established coordinate transformations between two modalities, whose common coordinate frames were applied in AMIDE Imaging Analysis software (Loening & Gambhir, 2003). Images were assessed by visual inspection to ensure accurate fusion results. MRI images underwent 3D maximum intensity projection (MIP) processing of 4 phase cycle frequencies and resulting reconstructed images were zero-padded (interpolated to higher resolution grid to increase the effective resolution and image quality) in ImageJ (NIH, USA).

5.5.6 SPECT/CT/MRI Coregistration and SPECT Regional Analysis

Inter-modality registration performed between SPECT/CT/MRI and a MR-based 3D digital mouse atlas permitted parcellation of the brain for regional analyses as described previously (Macdonald et al., 2014). A 6-parameter rigid body registration was performed between mouse MR and a standard brain from which the digital atlas was derived using Automated Image Registration 5.3.0 (Woods et al., 1998). Higher spatial transformations (warping) were applied to standard brain and corresponding warped MR atlas. MRI and warped MR atlas, along with SPECT/CT fused images were imported into AMIDE, where affine registration between modalities was carried out (Loening & Gambhir, 2003).

To evaluate brain perfusion, SPECT volume of interest (VOI) statistics were generated for six brain structures defined by the MR atlas: i) whole brain (all structures

excluding cerebellum, brain stem and olfactory bulb), ii) cerebral cortex, iii) hippocampal formation, iv) amygdala, v) thalamus and vi) basal ganglia. Semiquantitative estimates of perfusion were determined for each of the structures via standardized uptake values (SUV), expressed as $SUV = (\text{activity}/\text{unit dose})/\text{g}$. Relative standardized uptake values (SUV_r) were also evaluated, using a whole brain reference region, determined as follows: $SUV_{r_{\text{roi}}} = SUV_{\text{roi}}/SUV_{r_{\text{wb}}}$. This normalized metric was employed to limit any possible inter-subject or inter-scan variability in the study.

5.5.7 Statistical Analysis

Average SUV and SUV_r brain perfusion metrics were compared between 5XFAD and WT group means for each brain structure using unpaired t-tests (two tailed, assuming unequal variances). Differences were concluded at a significance level of 5% ($p < 0.05$, *). All data are presented as group means \pm standard error of the mean (SEM). All statistical tests were performed in SPSS (IBM, Armonk, NY).

5.6 Results

Following administration of ^{99m}Tc-Exametazime and 20 minutes of uptake, a 40 minute static SPECT scan was performed followed by CT to evaluate regional brain perfusion in 5XFAD and WT strains, facilitated by MRI co-registration to a digital mouse atlas (Ma et al., 2005).

5.6.1 ^{99m}Tc-Exametazime Perfusion SPECT

^{99m}Tc-Exametazime SPECT scans generated sufficient image quality in both 5XFAD and WT mice. SPECT scans showed similar general patterns of uptake on visual

inspection (Figure 5.2). Whole brain and regional evaluation of ^{99m}Tc -Exametazime perfusion was carried out using SUV and relative SUVr metrics with a whole brain reference region, the results of which are described below.

5.6.1.1 Whole Brain Perfusion

Whole brain uptake of ^{99m}Tc -Exametazime revealed no significant differences in brain perfusion SUVs between 5XFAD (0.372 ± 0.254) and WT (0.640 ± 0.254) mice ($p=0.536$) (Figure 5.3). Three outliers were observed in whole brain SUV metrics (1 5XFAD and 2 WT), which were 2 standard deviations above the mean. Separate analysis comparing 5XFAD and WT with outliers removed was investigated, yielding the same results. For this reason, all data was included for the current analysis.

5.6.1.2 Regional Perfusion

A number of relevant brain structures were investigated including amygdala, caudate/putamen, globus pallidus, hippocampus, hypothalamus and neocortex. Among the structures evaluated, SUV values ranged from ($0.296 \pm 0.203 - 0.520 \pm 0.371$) for AD and from ($0.497 \pm 0.256 - 0.818 \pm 0.440$) for WT (Figure 5.4). For SUVr metrics of the same structures, SUVr values ranged from ($0.855 \pm 0.041 - 1.221 \pm 0.029$) for AD and from ($0.921 \pm 0.057 - 1.213 \pm 0.020$) for WT (Figure 5.4). Regardless of the ^{99m}Tc -Exametazime perfusion metric (SUV vs SUVr), no significant differences among brain structures were observed between 5XFAD and WT mice (SUV: $0.357 \leq p \leq 0.640$; SUVr: $0.595 \leq p \leq 0.936$) (Figure 5.4).

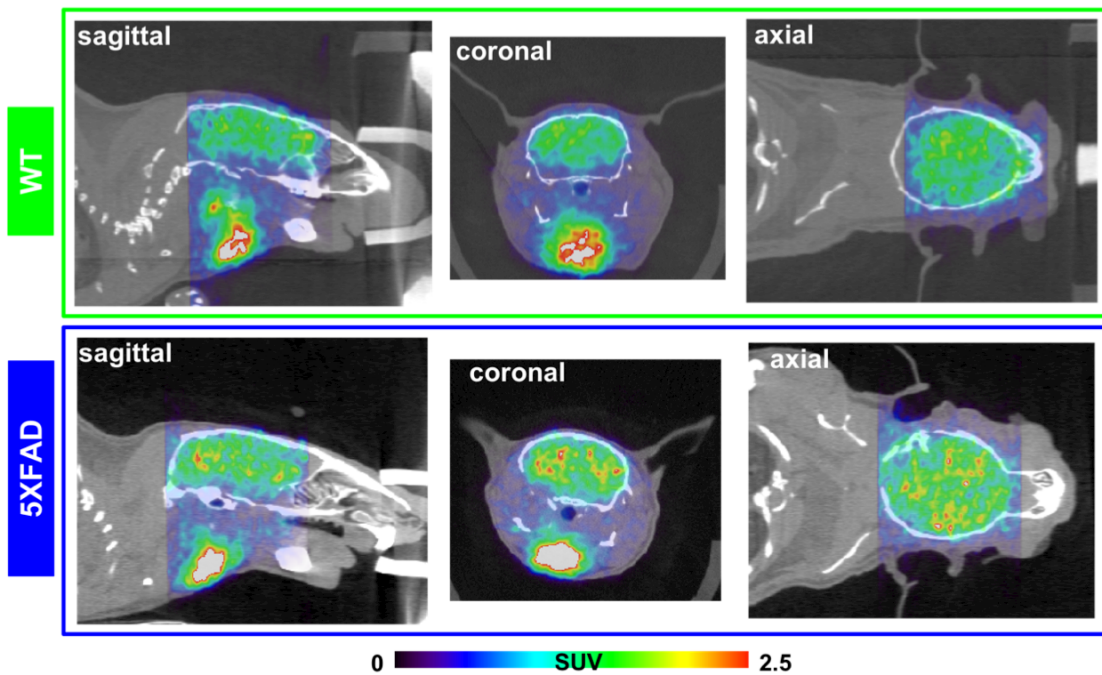


Figure 5.2 ^{99m}Tc -Exametazime Single Photon Emission Computed Tomography / Computed Tomography (SPECT/CT) images in sagittal, coronal and axial planes for a representative WT mouse (top) and 5XFAD mouse (bottom). A similar distribution of ^{99m}Tc -Exametazime radiotracer was seen in WT and 5XFAD mice. SPECT colour scale set to a common scale of 0-2.5 standardized uptake value (SUV) units.

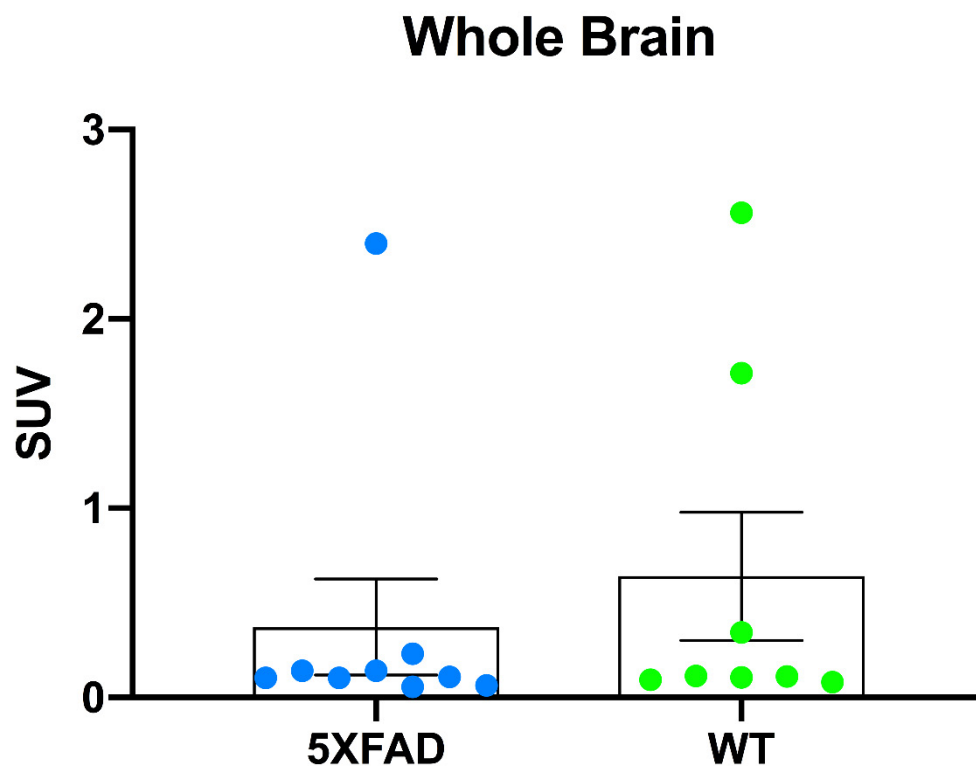


Figure 5.3 Whole brain ^{99m}Tc -Exametazime SPECT perfusion measured via standardized uptake value (SUV) in 5XFAD (blue) and WT (green) mice at 11.2 months of age. No significant differences in whole brain perfusion were observed between 5XFAD (0.372 ± 0.254) and WT (0.640 ± 0.338) mice ($p = 0.536$). Individual subjects represented by coloured circles and bar plot indicates Mean \pm SEM.

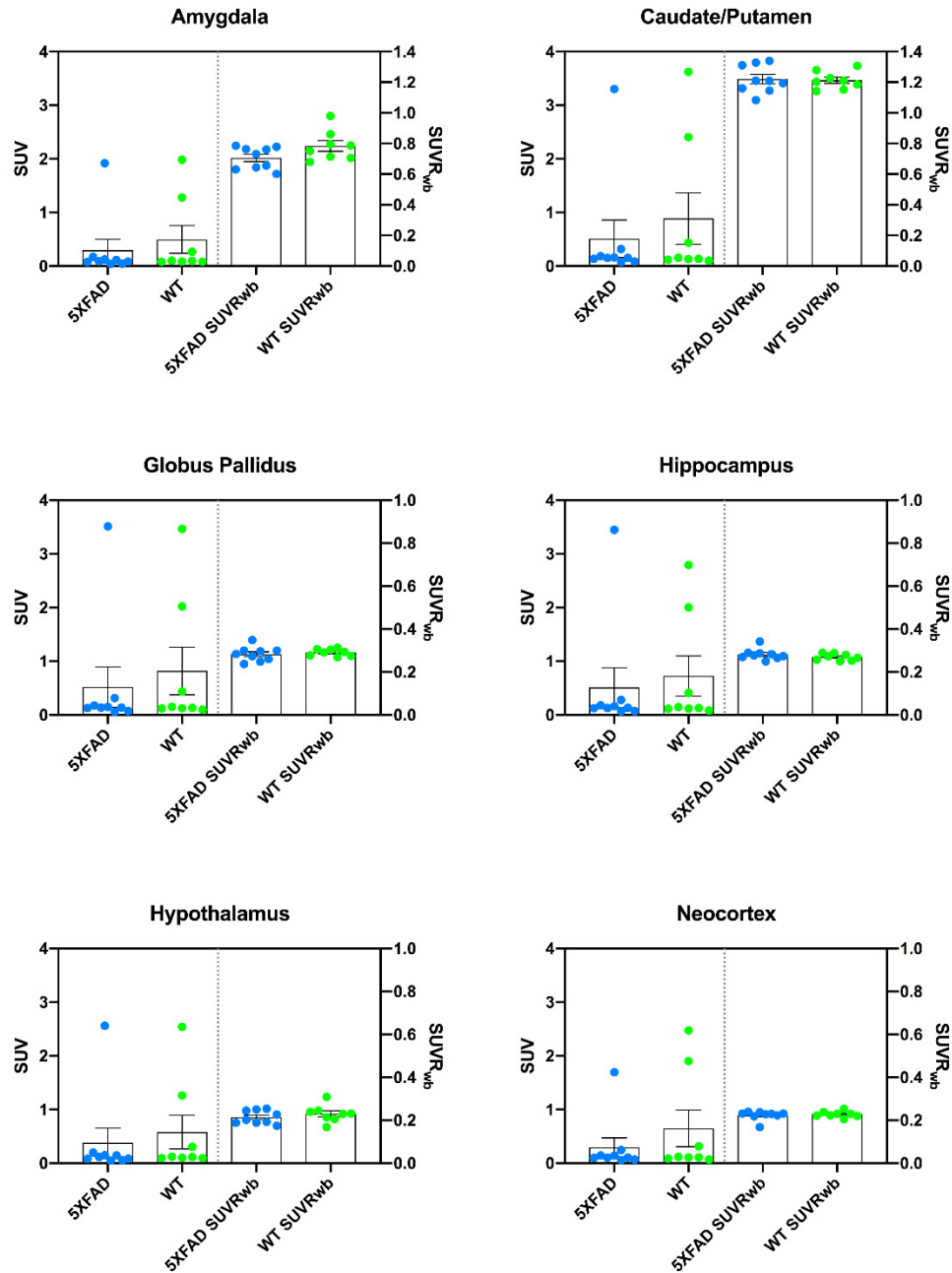


Figure 5.4 Regional ^{99m}Tc -Exametazime SPECT perfusion measured in 5XFAD (blue) and WT (green) mice at 11.2 months of age. Standardized uptake value (SUV) (left) and corresponding relative standardized uptake value (SUVR) with whole brain reference region (right) were evaluated in the amygdala, caudate/putamen, globus pallidus, hippocampus, hypothalamus and neocortex. No significant differences in regional perfusion were observed between 5XFAD and WT in any of the structures for either SUV or SUVR metrics ($0.357 \leq p \leq 0.936$) Individual subjects represented by coloured circles and bar plot indicates Mean \pm SEM.

5.7 Discussion

The objective of the current study was to implement preclinical brain perfusion imaging methods with ^{99m}Tc -Exametazime in the 5XFAD mouse model as part of a neuroimaging validation of the Cubresa SPARK™ tabletop SPECT scanner for our diagnostics program. Given the widespread use of the 5XFAD mouse model in our research program, characterizing its brain function is essential to further our understanding the effects of disease progression on important physiological parameters including cerebral blood flow. Cerebral blood flow is a particularly relevant parameter in radiotracer development as perfusion is directly related to tracer transfer from arterial blood to the brain. In order to reconcile the use of 5XFAD mice in our research program, it is important to uncover any inherent confounds that may exist including the possibility of differential patterns of perfusion between 5XFAD and corresponding WT counterparts, which could lead to the misinterpretation of results from prospective diagnostic radiotracer development studies.

In the current study, no differences in brain perfusion were observed between 5XFAD and WT at 11 months of age at the whole brain level or in subsequent regional analyses using SUV and SUVr metrics. Technical limitations, in part, may explain the absence of statistical differences observed between groups in the current study. Small differences in animal-to-animal and day-to-day variations in physiology could significantly impact the uptake of the tracer into various organs, including the brain. Though anesthetic and temperature was controlled and respiratory rates were measured consistently throughout the course of study, heart rate and other physiological parameters were not evaluated, which could introduce a significant amount of variance to tracer

uptake. The spatial resolution of SPECT may also be a limitation in evaluating some of the smaller structures of the brain and partial volume effects could be another source of error in the current study and the results should be interpreted with caution. Technical limitations notwithstanding, the current results may suggest an apparent disconnect between cerebral blood flow and glucose metabolism, a so-called neurovascular decoupling in the 5XFAD brain. We have consistently observed patterns of hypometabolism in the 5XFAD mouse brain of a similar age, predominantly seen later in disease progression as late as ~13 months (Macdonald et al., 2014), but also at earlier timepoints (DeBay, Reid, Macdonald, et al., 2017; Macdonald et al., 2014), depending on the [^{18}F]FDG metabolism metrics employed. These studies of brain metabolism ostensibly demonstrated global reductions in [^{18}F]FDG uptake with contributions from various structures including the cerebral cortex, hippocampal formation, amygdala, basal ganglia and thalamus (DeBay, Reid, Macdonald, et al., 2017; Macdonald et al., 2014) whereas in the current study no statistically separable differences were observed between 5XFAD and WT mice in the same brain regions. The interplay between brain perfusion and brain metabolism in the 5XFAD mouse model warrants further investigation.

5.8 Acknowledgements

D.R. DeBay was responsible for study conceptualization, the implementation of $^{99\text{m}}\text{Tc}$ -Exametazime SPECT imaging protocols, data acquisition and processing, analysis pipeline development, statistical design and interpretation and manuscript preparation. T.T Phi provided expertise in the interpretation of $^{99\text{m}}\text{Tc}$ -Exametazime SPECT images and S. Darvesh and S. Burrell provided guidance in study conceptualization and

interpretation of imaging findings.

This project has been funded, in part, from a Dalhousie Faculty of Medicine Collaborative Research Grant held by trainees Drew DeBay (Medical Neuroscience) and Dr. Tan Trao (Radiology) and supervised by Dr. Sultan Darvesh and Dr. Steve Burrell.

The authors would like GE Healthcare Canada for providing Ceretec™ and NSHA and IWK nuclear medicine technologists Cathy Grandy, Sandra Ellis, Sandra Macdonald, and Eleanor Power for their technical support in addition to Christa Davis for her technical support. This research was also supported by the Canadian Institutes of Health Research (MOP-82798, RNS- 117795, MOP-119343), Capital Health Research Fund, Nova Scotia Health Research Foundation (Scotia Scholar^{OM}, MED-MAT-2011-7512), Faculty and Department of Medicine of Dalhousie University, Natural Sciences and Engineering Research Council of Canada and Killam Trusts, Innovacorp, Mount Saint Vincent University Committee on Research and Publication, Dalhousie Medical Research Foundation Gunn Family Research Prize, DeWolfe Graduate Studentship, Mrs. Sadie MacLeod through the Dalhousie Medical Research Foundation Adopt-a-Researcher program and the Dalhousie Medical Research Foundation Irene MacDonald Sobey Endowed Chair in Curative Approaches to Alzheimer's Disease.

Chapter 6 Butyrylcholinesterase-Knockout Reduces Fibrillar β -amyloid and Conserves Cerebral Glucose Metabolism in 5XFAD Mouse Model of Alzheimer's Disease

6.1 Publication Status

Published and presented with permission.

DeBay DR, Reid GA, Macdonald IR, Mawko G, Burrell S, Martin E, Bowen CV, Darvesh S. *Butyrylcholinesterase-knockout reduces fibrillar β -amyloid and conserves [18 F]FDG retention in 5XFAD mouse model of Alzheimer's disease.* Brain Res. 2017 Sep 15;1671:102-110. doi: 10.1016/j.brainres.2017.07.009. PMID:28729192.

6.2 Overview

Work in the current chapter was dedicated to further the neuroimaging characterization of the mouse models regularly used in our AD diagnostics program. In this study, brain function in a BChE-knockout model of AD (5XFAD/BChE-KO) was evaluated with [18 F]FDG-PET imaging. This study sought to determine whether a BChE-induced reduction of fibrillar A β , as is seen in these knockout mice, translated into improved brain function when compared to 5XFAD and WT counterparts.

6.3 Abstract

Alzheimer's disease (AD) is the most common neurodegenerative disorder causing dementia. One hallmark of the AD brain is the deposition of β -amyloid (A β) plaques. AD is also a state of cholinergic dysfunction and butyrylcholinesterase (BChE) associates with A β pathology. A transgenic mouse (5XFAD) is an aggressive

amyloidosis model, producing A β plaques of which BChE also associates. A derived strain (5XFAD/BChE-KO), with the BChE gene knocked out, has significantly lower fibrillar A β than 5XFAD mice at the same age. Therefore, BChE may have a role in A β pathogenesis. Furthermore, in AD, diminished glucose metabolism in the brain can be detected *in vivo* with positron emission tomography (PET) imaging following [^{18}F] fluorodeoxyglucose ([^{18}F]FDG) administration. To determine whether hypometabolism is related to BChE-induced changes in fibrillar A β burden, whole brain and regional uptake of [^{18}F]FDG in 5XFAD and 5XFAD/BChE-KO mice was compared to corresponding wild-type (WT_{5XFAD} and WT_{BChE-KO}) strains at 5 months. Diminished fibrillar A β burden was confirmed in 5XFAD/BChE-KO mice relative to 5XFAD. 5XFAD and 5XFAD/BChE-KO mice demonstrated reduction in whole brain [^{18}F]FDG retention compared to respective wild-types. Regional analysis of relevant AD structures revealed reduction in [^{18}F]FDG retention in 5XFAD mice in all brain regions analyzed (save cerebellum) compared to WT_{5XFAD}. Alternatively, 5XFAD/BChE-KO mice demonstrated a more selective pattern of reduced retention in the cerebral cortex and thalamus compared to WT_{BChE-KO}, while retention in hippocampal formation, amygdala and basal ganglia remained unchanged. This suggests that in knocking out BChE and reducing fibrillar A β , a possible protective effect on brain function may be conferred in a number of structures in 5XFAD/BChE-KO mice.

6.4 Introduction

Alzheimer's disease (AD) is the most common neurodegenerative disorder that causes dementia (WHO, 2012). AD is accompanied by progressive cognitive impairment

(McKhann et al., 2011). Neurodegeneration over the course of AD progression ultimately manifests as brain atrophy visualized through structural magnetic resonance imaging (MRI) scans (Scheltens et al., 2016) and impaired neurometabolism, which can be readily measured via alterations in brain uptake of the radioactive glucose analogue, 2-deoxy-2-[¹⁸F]fluoro-deoxyglucose ([¹⁸F]FDG) using positron emission tomography (PET) imaging (Jack et al., 2016; Mosconi, 2005; Silverman et al., 2001). In AD, hypometabolism of glucose, indicating reduced neuronal function, is typically seen in a temporo-parietal lobar pattern (Kato et al., 2016; Mosconi, 2005).

Characteristic AD neuropathology includes the deposition of β -amyloid ($A\beta$) plaques and tau neurofibrillary tangles (NFTs) (Montine et al., 2012). It has been established that the AD brain also exhibits cholinergic dysfunction, contributing to the cognitive and behavioural symptoms of AD (Bartus et al., 1982; Coyle et al., 1983; Davies & Maloney, 1976). Cholinesterases, particularly butyrylcholinesterase (BChE), are found to associate with $A\beta$ plaques and neurofibrillary tangles (NFTs) (Darvesh et al., 2010; Mesulam & Geula, 1994), but their role(s) in disease pathogenesis remain unclear. However, putative roles include formation and/or maturation of $A\beta$ plaques (Guillozet et al., 1997; Mesulam & Geula, 1994). Furthermore, in a genome-wide association study of the Alzheimer's Disease Neuroimaging Initiative (ADNI), BChE is associated with AD progression (Ramanan et al., 2014), suggesting this enzyme contributes to AD pathogenesis.

Various hypotheses have been put forward to explain neurodegeneration in AD, including $A\beta$ plaque deposition (Selkoe & Hardy, 2016), NFT accumulation (Iqbal et al.,

2016) and cholinergic changes (Bartus et al., 1982; Coyle et al., 1983; Davies & Maloney, 1976). Under the amyloid cascade hypothesis, the early deposition of amyloid serves to initiate pathological events, including neuronal dysfunction and synaptic loss, ultimately leading to neuronal death (Selkoe & Hardy, 2016). However, a causal link between A β and neurodegenerative processes in AD is not well established (Cohen et al., 2009; Edison et al., 2007; Engler et al., 2006; Furst et al., 2012; Kemppainen et al., 2015; Klupp et al., 2015; Li et al., 2008; Lowe et al., 2014). Furthermore, AD drugs designed to target A β have been ineffective in AD treatment (Doody, Farlow, et al., 2014; Doody, Thomas, et al., 2014; Salloway et al., 2014). Similarly, strategies to inhibit NFT aggregation or phosphorylation have been unsuccessful in treating AD (Forlenza et al., 2014; Tariot et al., 2011). Cholinesterase inhibitors such as donepezil, galantamine and rivastigmine, on the other hand, have been the only therapeutic strategy to provide symptomatic benefit to those persons with mild to moderate AD (Birks, 2006).

Neuroimaging approaches have been devised to visualize AD pathology such as A β plaques in the living brain using PET analysis (Clark et al., 2012; Curtis et al., 2015; Klunk et al., 2004; Sabri et al., 2015; Villemagne et al., 2015). Neurodegenerative aspects such as atrophy have been assessed with structural MRI (Scheltens et al., 2016) and hypometabolism using [^{18}F]FDG-PET imaging (Jack et al., 2016). Several studies have shown associations between A β deposition and impaired glucose metabolism in various regions of the AD brain (Cohen et al., 2009; Edison et al., 2007; Engler et al., 2006; Lowe et al., 2014). However, other longitudinal studies have shown early transient correlations of A β and glucose hypometabolism in mild cognitive impairment (MCI) that are not maintained after conversion to AD (Kemppainen et al., 2015). Klupp et al. have

shown that hypometabolism in functionally connected regions that are abundant in A β deposits, may support an AD network-degeneration hypothesis (Klupp et al., 2015). Conversely, other studies have shown a lack of association between regional A β deposition and corresponding regionally-specific glucose metabolism metrics (Furst et al., 2012; Li et al., 2008). In contrast to regional effects, it has been suggested that impaired glucose metabolism may reflect overall global A β burden in the AD brain (Altmann et al., 2015).

Transgenic mouse models of brain amyloidosis have been developed, including the 5XFAD mouse model (Oakley et al., 2006), based on familial AD (FAD) mutations. This model overexpresses the human amyloid precursor protein (*APP*) *APP*₆₉₅ with the Swedish (K670N, M671L), Florida (I716V), and London (V717I) FAD mutations, as well as human presenilin 1 (PS1) harboring two FAD mutations, M146L and L286V. This mouse model of brain amyloidosis has a very aggressive course, exhibiting A β deposition as early as ~2 months of age (Oakley et al., 2006). In addition, a number of similarities between this AD animal model and human AD have been documented, including loss of synaptic markers, cognitive impairment (Eimer & Vassar, 2013; Oakley et al., 2006) and association of BChE with AD pathology (Darvesh & Reid, 2016; Reid & Darvesh, 2015). In addition to the putative role of BChE as an AD biomarker in humans (Darvesh, 2013), evidence exists indicating that BChE may have a modulatory role in A β accumulation. Recent work involving a novel BChE knock-out AD mouse model (5XFAD/BChE-KO) has revealed that the absence of BChE expression leads to diminished fibrillar A β plaque pathology in the brain (Darvesh & Reid, 2016; Reid & Darvesh, 2015).

This 5XFAD/BChE-KO strain provides a means to modulate A β deposition and therefore permits examination of the effect of such a change on brain function using [^{18}F]FDG-PET. [^{18}F]FDG -PET is an established, non-invasive imaging technique used clinically that has also been effectively implemented in pre-clinical research, providing direct *in vivo* context between human and animal models which is not as readily assessed by autoradiographic methods (e.g. [^{14}C]C-DG). The present study was undertaken to determine whether a BChE-induced reduction of fibrillar A β , as seen in 5XFAD/BChE-KO mice, translates into improved [^{18}F]FDG retention compared to 5XFAD mice. Further establishing the precise interplay between BChE, fibrillar A β deposition and brain function in AD, will be beneficial towards our understanding of AD pathogenesis and may be facilitated with the use of transgenic models of AD.

6.5 Experimental Methods

6.5.1 Animals

Female wild-type (WT_{5XFAD}; C57BL/6J x SJL/J F1; The Jackson Laboratories, Stock # 100012), male transgenic hemizygous 5XFAD (B6SJL- Tg (APPS^{wFILon},PSEN1*^{M146L}*^{L286V}) 6799Vas/Mmjax; Mutant Mouse Regional Resource Center, 034840-JAX) and heterozygous butyrylcholinesterase (B6.129S1-Bchetm1Loc/J; The Jackson Laboratories, Stock # 008087), referred to here as BChE-het mice, were purchased. Mice were housed in same-sex groups of 1– 5, within polyethylene cages (30x19x13cm), containing a wood-chip bedding and covered by a metal cage top and micro-isolator filter. Food (Purina rodent chow, #5001) and tap water

were available *ad libitum*. Animals were kept in normal light/dark cycle. Hemizygous 5XFAD mice, used for breeding and subsequent experiments, were produced from pairs of WT_{5XFAD} female mice bred with 5XFAD male mice. Homozygous BChE-knockout (BChE-KO) mice were produced from BChE-het males and females. A three generation breeding scheme was used to produce the desired transgenic hemizygous 5XFAD strain that were homozygous BChE-knockout (5XFAD/BChE-KO). Hemizygous male 5XFAD mice were bred with pairs of BChE-KO females to produce 5XFAD/BChE-het mice. Male 5XFAD/BChE-het mice were bred with female BChE-KO mice to produce 5XFAD/BChE-KO mice. 5XFAD/ BChE-KO males were bred with BChE-KO females to maintain the strain and produce mice for subsequent study.

In the present study, 5 month male mice were used and were comprised of the following strains; 5XFAD (n=3), 5XFAD/BChE-KO (n=5), WT_{5XFAD} (n=4) and WT_{BChE-KO} (n=6). Imaging studies were performed during the dark phase of the light-dark cycle. Mice were cared for according to the guidelines set by the Canadian Council on Animal Care. Formal approval to conduct these experiments was obtained from the Dalhousie University Committee on Laboratory Animals (protocol 15-070) and from the Dalhousie University Radiation Safety Committee, overseen by the Canadian Nuclear Safety Commission (license 07154-2-17.10).

6.5.2 Genotyping

All mice were genotyped for *APP*, *PS1* and *BCHE* genes. An ear punch was used to identify mice and collect a skin sample for genotyping. For DNA isolation, 80 μ L of 0.025 M sodium hydroxide and 0.2 mM EDTA disodium dihydrate was added to skin

samples and was incubated at 98°C for 1h with periodic vortexing to digest tissue. Following tissue digestion, 80 µL of a neutralization solution containing 40 mM Tris HCl at pH 5.5 was added, vortexed and centrifuged at 4000 rpm for 3min (Truett et al., 2000). The supernatant was removed and saved for polymerase chain reaction (PCR). To each PCR tube was added 2.5 µL PCR buffer (0.2M Tris–HCl and 0.5M KCl pH 8.4), 0.5 µL 10 mM dNTP mixture (Invitrogen; 10297–018), 0.75 µL MgCl₂, 0.625 µL primers 5 µL DNA isolate, 0.1 µL Taq (Invitrogen; 10342–020) and 14.9 µL ultrapure dH₂O. PCR samples were amplified on a BIORAD C1000 Touch thermal cycler. For *BCHE* the following protocol was used: 94 °C 2min, 34 times (94°C for 30s, 59°C for 30s, 72°C for 1min), 4°C for 5min. For *APP* and *PSI*, 94°C 2min, 34 times (94°C for 30s, 65°C for 30s, 72°C for 1 min), 4 °C for 5 min. PCR products were run on a 2% agarose gel made with TAE buffer, containing 0.04 M Tris–acetate and 0.001 M EDTA, with SYBRÓ safe DNA gel stain (Invitrogen; S33102, 1:10,000). Gels were run for 30 min and visualized on a Typhoon 9410 Molecular Imager (GE Healthcare).

6.5.3 PET/CT Imaging

PET/CT imaging was completed as previously reported (Macdonald et al., 2014). Mice in all 4 groups were weighed immediately prior to the imaging procedure, restrained in a TailVeiner Restraint (Braintree Scientific) and injected with [¹⁸F]FDG (573-829 µCi, in 140-160 µL saline) via lateral tail vein. [¹⁸F]FDG was obtained from the Department of Diagnostic Imaging, Nova Scotia Health Authority. Uptake of the tracer occurred in conscious mice in a novel cage over 30 min under a heat lamp and in the presence of a mobile battery powered mechanical mouse (Hurry Scurry Mouse, Toysmith) which the test mouse could interact with to facilitate uptake under controlled

conditions. Mice were then anaesthetized with 3% isoflurane (in 100% oxygen) in an induction chamber and secured in prone position in a custom built, Magnetic Resonance (MR)-compatible animal tray with an integrated nosecone and bite bar. Mice were wrapped in a blanket on a heated bed and maintained under a continuous stream of isoflurane gas anesthetic (1.5-2%) and respiratory rate was monitored for the duration of the scan (SA Instruments Inc. Stony Brook, NY). The head region of the mouse was centered on a 37 mm axial field of view (FOV) and PET coincidence events were acquired in list mode over a 30 min scan period, with a LabPET4 pre-clinical PET/CT scanner (Trifoil Imaging, CA).

Immediately following PET scanning, for anatomical reference, a computed tomography (CT) image was performed in fly mode with a 70 kVp x-ray beam energy (160 mA beam current), 512 projections, 4 summed frames/projection, with 2X2 binning and a magnification of 2.26X, providing complete whole brain coverage in a 56 mm FOV. CT scan duration was approximately 8.5 min. Once CT was acquired, mice were immediately transported in the MR compatible bed to the MR scanner located in a room adjacent to the PET/CT suite.

6.5.4 MR Imaging

MR imaging was completed as previously reported (Macdonald et al., 2014). All MR scans were performed at 3.0 T using a superconducting Magnex Scientific clinical MR “head only” scanner (Oxford, UK) retrofitted for small animal imaging (Magnex Scientific gradient coil, ID of 21 cm; maximum gradient strength of 200 mT/m) and interfaced with a Direct Drive spectrometer (Varian Inc., Palo Alto, CA). A 30 mm ID

“Litzcage” quadrature RF coil (Doty Scientific, Columbia, SC), tuned to 128.8 MHz, was used as a transmit/receive volume coil for imaging. *In vivo* anatomical images were obtained using a 3D balanced steady-state free precession, (b-SSFP) imaging sequence (T2/T1-weighting) acquired in a sagittal readout. Repetition time (T_R), echo time (T_E), flip angle and bandwidth (BW) were optimized for best brain image quality. The sequence consisted of $T_R/T_E = 9/4.5$ ms, flip angle = 30° , 4 frequencies, 4 signal averages and BW = 40.3 kHz. A FOV of $(22.1 \text{ mm})^3$ with matrix dimensions of 156^3 was used to acquire $(142 \text{ }\mu\text{m})^3$ isotropic resolution images with full brain coverage (~ 61 min/scan). During imaging, respiratory rate and internal body temperature of the mice were monitored using an MR compatible physiological monitoring and gating system (SA Instruments Inc., Stony Brook, NY). The temperature of the mouse was maintained at $37 \pm 1^\circ\text{C}$ via temperature control feedback loop controlling an air heating system.

6.5.5 Image Processing

PET list-mode data were spatially histogrammed as a single timeframe and binned according to their line of response. Coincidence events were rebinned over a maximum span field of 31 oblique planes using a single slice rebinning algorithm. An iterative reconstruction approach was employed via a 2D Maximum-Likelihood Expectation Maximization (MLEM) algorithm, which was performed 100 times and constrained to a 46 mm radial FOV. The resultant PET images yielded an effective isotropic resolution of 1.2 mm. Normalization correction (to account for variable count-rate sensitivity of sensors) and quantitative calibrations were performed weekly for the duration of the study and these corrections were applied in the reconstruction of the data sets. Processing of PET list mode data, reconstruction and corrections were performed in LabPET

software.

CT images were reconstructed with a 512X512X512 image matrix over a 56 mm FOV using the built-in optimum noise reconstruction procedure provided with the Triumph XO CT acquisition software, yielding images with 102 μm isotropic resolution. Fusion of PET and CT images was achieved using the Vivid™ Image Analysis Platform (Trifoil Imaging, CA and Visualization Sciences Group, MA), which aligns and overlays the common coordinate frames of each modality. Images were assessed by visual inspection by a single observer to ensure accurate fusion results. PET data was then interpolated to 102 μm in each plane (resolution- matched to the CT). MR images underwent 3D maximum intensity projection (MIP) processing of 4 phase cycle frequencies, and resulting reconstructed images were zero-padded (interpolated to higher resolution grid to increase the effective resolution and image quality) in ImageJ (NIH, USA).

6.5.6 Whole Brain and Regional ^{18}F FDG Uptake Analysis

For region of interest (ROI) analysis of [^{18}F]FDG uptake in the brain, an MR-based 3D digital mouse atlas (Ma et al., 2005; Ma et al., 2008) was employed and inter-modality registration between PET/CT/MRI was performed (see Figure 2 as example). Briefly, a semi-automated skull stripping algorithm using BrainSuite 11 (LONI UCLA) was performed on each mouse- specific MR image to remove all extraneous non-brain data. A linear, 6-parameter model rigid body registration was performed using Automated Image Registration 5.3.0 (Woods et al., 1998) between the skull stripped MR and the standard brain from which the digital atlas was derived. Subsequently, higher

order non-linear spatial transformations (warping) of the standard brain to the mouse-specific MR images acquired in this study were carried out to 3rd order polynomial. This provided the necessary transformations to be applied to the 3D digital mouse atlas. Visualization of the mouse-specific MR image and corresponding warped atlas mask overlay was carried out in RView (Studholme et al., 1996) to assess the goodness of fit. PET/CT fused data, mouse-specific MR image data and the warped digital atlas were imported into AMIDE (Loening & Gambhir, 2003), and underwent affine registration with CT and PET images (see Figure 2). ROI statistics were generated from the PET data for whole brain, amygdala, basal ganglia, cerebellum, hippocampal formation, cerebral cortex and thalamus. For the whole brain ROI, a composite mask of atlas ROIs was derived using fslmaths scripts employing threshold and subtraction commands carried out in FSL (Oxford, UK). Whole brain ROIs contained all atlas brain structures excluding the olfactory bulb, cerebellum and brainstem. [¹⁸F]FDG uptake values in each ROI are reported as SUVs (mean voxel value of activity, normalized to the injected dose per body weight of each mouse).

6.5.7 Thioflavin-S Histofluorescence

Following a 24 h period after imaging (to allow decay of radioactivity), mice were euthanized by a lethal intraperitoneal sodium pentobarbital injection, perfused transcardially with saline (25 mL, 0.9% NaCl, 0.1% NaNO₃) and 50 mL of 4% formaldehyde in 0.1M phosphate buffer (PB, pH 7.4). Brains were removed and post-fixed for 1.5 h in 4% formaldehyde in PH (pH 7.4), immersed in 30% sucrose in PB with 0.05% sodium azide and stored at 4 °C until used. Brains were frozen with dry ice and cut into 40 µm serial coronal sections on a Leica SM2000R microtome with Physitemp

freezing stage and BFS-30TC controller. Sections were stored at 4 °C in PB with 0.08% sodium azide until used for analysis of fibrillar A β with thioflavin-S histofluorescence as described previously (Reid & Darvesh, 2015). Briefly, sections were rinsed in 0.05 M Tris-buffered saline pH 7.6 for 30 min, mounted onto glass slides, air-dried overnight, rehydrated in dH₂O, dehydrated in a series of ethanol washes, cleared in xylene and rinsed in 50% ethanol. Sections were then incubated overnight in a solution of 0.05% Th-S (Sigma–Aldrich, St. Louis, MO, USA) in 50% ethanol, rinsed in 80% aqueous ethanol and dH₂O and coverslipped with an aqueous mounting medium.

6.5.8 Microscopy Analysis

The stained mouse brain sections were analyzed and photographed using a Zeiss Axioplan 2 motorized microscope with a Zeiss Axiocam HRC digital camera using AxioVision 4.6 software (Carl Zeiss Canada Ltd., Toronto, Ontario, Canada) at the Cellular Microscopy and Digital Imaging CORES facility at Dalhousie University. The photographs were assembled using Adobe Photoshop (CS 5 version 12.0) and the images were contrast enhanced and the brightness adjusted to a common background level. Plaque load quantification was performed in ImageJ 1.49d (NIH) and was recorded as a percentage of the total area, as described elsewhere (Darvesh et al., 2012). Briefly, gray-scale images of sections stained for Thioflavin-S were taken throughout the brain. An intensity threshold level was set such that stained plaques, but not background, was selected. The cortex was outlined with the polygon selection tool and measured for the percent area covered by plaque staining. On average, twelve Thioflavin-S-stained sections were quantified per brain. For each brain, data from each section were summed to give a cortical area and the total plaque area measured. This was used to determine the

percent plaque load in each brain. The percent area covered by plaque pathology was expressed as a group mean to allow comparison between the 4 groups.

6.5.9 Statistical Analysis

[¹⁸F]FDG uptake values are presented as mean activity values for each whole brain or parcellated structure, normalized to the injected dose per body weight of each individual animal (SUV). Parametric analysis of variance (ANOVA) was employed to compare group means (5XFAD, 5XFAD/BChE-KO, WT_{5XFAD} and WT_{BChE-KO}). If results of the ANOVA were determined to be significant ($p < 0.05$), subsequent Tukey HSD post-hoc tests were performed. Statistically significant differences were concluded at a significance level of 5% ($p < 0.05$ (*), $p < 0.01$ (**), and $p < 0.001$ (***)). All data are presented as group means with bars representing standard error of the mean (SEM). Unpaired t-tests were applied to determine the difference between means in the areas covered by fibrillar A β pathology in 5XFAD and 5XFAD/BChE- KO mice. Results were considered significant for $p < 0.05$. All statistical measures were calculated with SPSS (IBM Inc.)

6.6 Results

In the present study, two transgenic amyloid mouse models (5XFAD and 5XFAD/BChE-KO) and their respective WT's (WT_{5XFAD} and WT_{BChE-KO}) were examined to determine the effect of fibrillar amyloid deposition on [¹⁸F]FDG uptake in the brain. Although the animals were imaged first, prior to histological examination, for logical interpretation we present the fibrillar A β plaque staining first.

6.6.1 Brain Fibrillar A β Deposition

Fibrillar A β burden in the cerebral cortex of the 5 month 5XFAD and 5XFAD/BChE-KO mice was determined for each mouse with Th-S histofluorescence (Figure 6.1A). In 5XFAD/BChE-KO mice, fibrillar A β plaque deposition was found to be some 33% lower in the cerebral cortex than 5XFAD counterparts (Figure 6.1B). This is consistent with previous studies of male 5XFAD/BChE-KO mice at 6 months of age (Reid & Darvesh, 2015), confirming that the absence of BChE in this AD model leads to diminished A β pathology in the mouse cerebral cortex. Reduced fibrillar A β in subcortical structures has also been reported previously (Darvesh & Reid, 2016). No fibrillar plaques could be discerned in either WT strains.

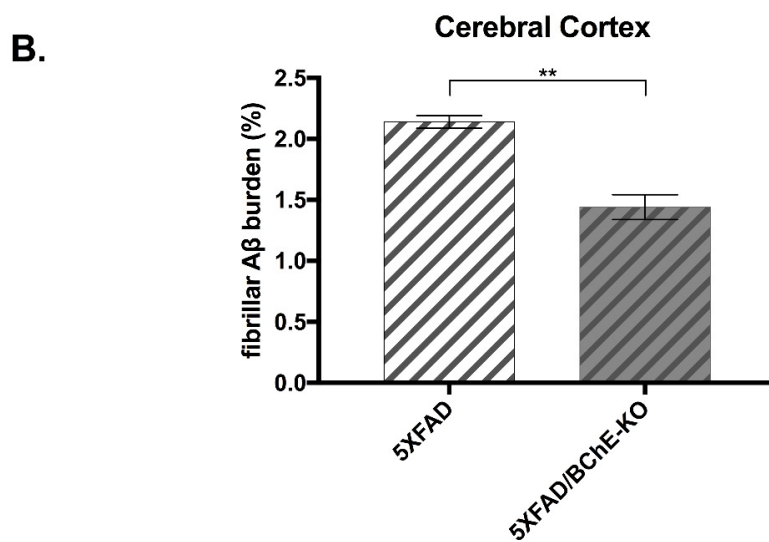
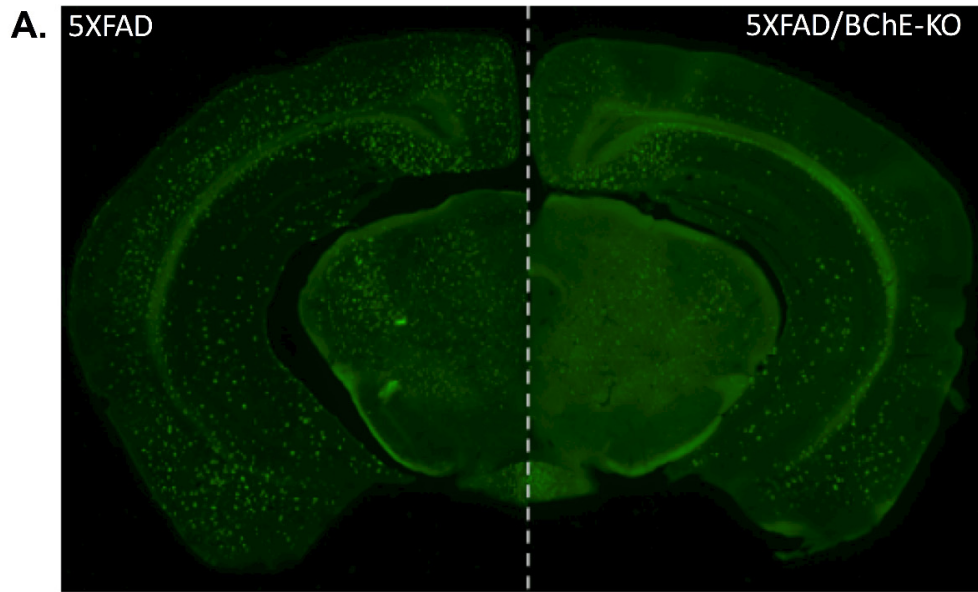


Figure 6.1 **A.** Fibrillar A β staining at 5 months in 5XFAD (left) and 5XFAD/BChE-KO (right) brains detected with thioflavin-S histofluorescence staining. **B.** Fibrillar A β plaque burden, as determined by the % area covered by pathology in cerebral cortex of 5month 5XF AD/BChE-KO ($1.44 \pm 0.10\%$) mice. A 33% decrease in fibrillar A β deposition was observed in 5XFAD/BChE-KO mice relative to 5XFAD counterparts plotted as mean \pm SEM where ** represents a p-value of 0.001.

6.6.2 Whole Brain ^{18}F FDG SUV Comparisons

^{18}F FDG PET scans were co-registered with CT and MRI to permit anatomical parcellation of the brain. Semi-quantitative measures of either whole brain or selected regional ^{18}F FDG standard uptake values (SUVs) were obtained in the brains of 5XFAD and 5XFAD/BChE-KO mice (Figure 6.2) and corresponding WT counterparts (WT images not shown).

Whole brain ANOVA indicated significant differences were present between study groups ($F=9.54$, $p<0.0005$). In 5XFAD mice, a decrease in whole brain ^{18}F FDG SUV was observed compared to $\text{WT}_{5\text{XFAD}}$ counterparts (28.4% decrease, $p<0.01$) (Figure 6.3). In 5XFAD/BChE-KO mice, a similar trend of reduced ^{18}F FDG retention was observed, where 5XFAD/BChE-KO whole brain SUVs were lower than their respective $\text{WT}_{\text{BChE-KO}}$ counterparts (21.9% decrease, $p<0.05$) (Figure 6.3). In spite of a 33% reduction of cortical fibrillar $\text{A}\beta$ plaque burden, no differences in whole brain ^{18}F FDG retention between 5XFAD and 5XFAD/BChE-KO mice was demonstrated (Figure 6.3). While $\text{WT}_{5\text{XFAD}}$ and $\text{WT}_{\text{BChE-KO}}$ whole brain SUVs were not statistically separable in our sample, it appears as though the baseline operating range of $\text{WT}_{\text{BChE-KO}}$ mice may be lower in terms of whole brain retention of ^{18}F FDG. This potential disparity may confound interpretation of the comparison of 5XFAD and 5XFAD/BChE-KO strains. In a similar way, no differences in whole brain ^{18}F FDG retention between 5XFAD and $\text{WT}_{\text{BChE-KO}}$ mice were observed, perhaps owed to this potential strain-related shift in baseline whole brain ^{18}F FDG retention. In addition, 5XFAD/BChE-KO whole brain SUVs were significantly less than the $\text{WT}_{5\text{XFAD}}$ group (34.3% decrease, $p < 0.001$).

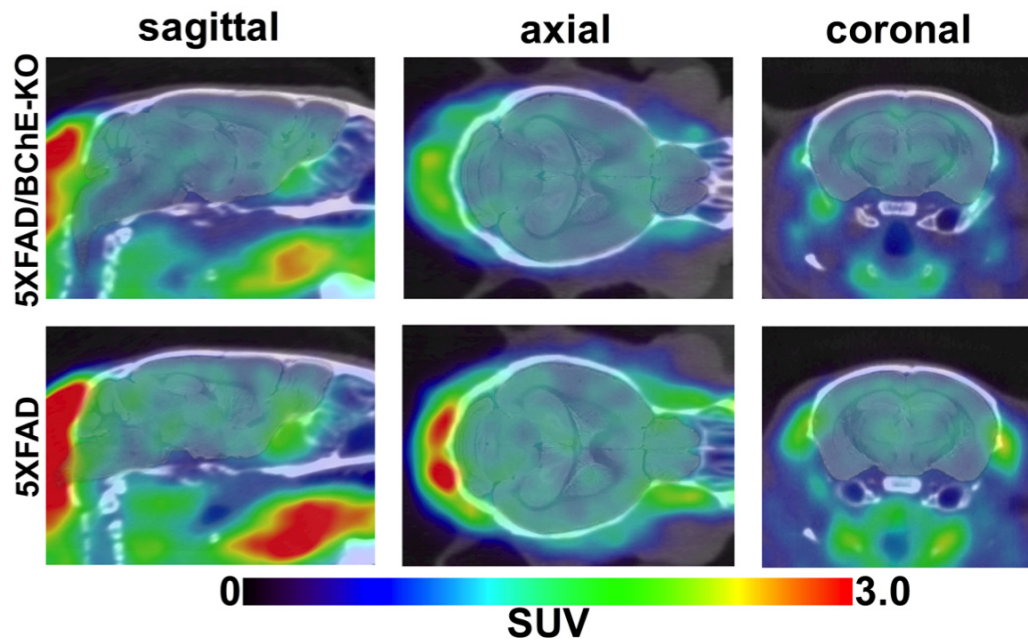


Figure 6.2 Co-registered PET/CT and standard MRI brains in representative 5XFAD/BChE-KO and 5XFAD brains used for analysis of [18F]FDG uptake. All mice received 18FDG injections (573-829 μ Ci, in 140-160 μ L saline) via lateral tail vein, and images were acquired over an equivalent 30 minute period, following 30 minute uptake of tracer. PET radioactivity source maps set to a common scale of 0 to 3.0 SUV units. Extra-cranial uptake showed some variability in regions of brown adipose tissue caudally and with salivary gland uptake ventrally.

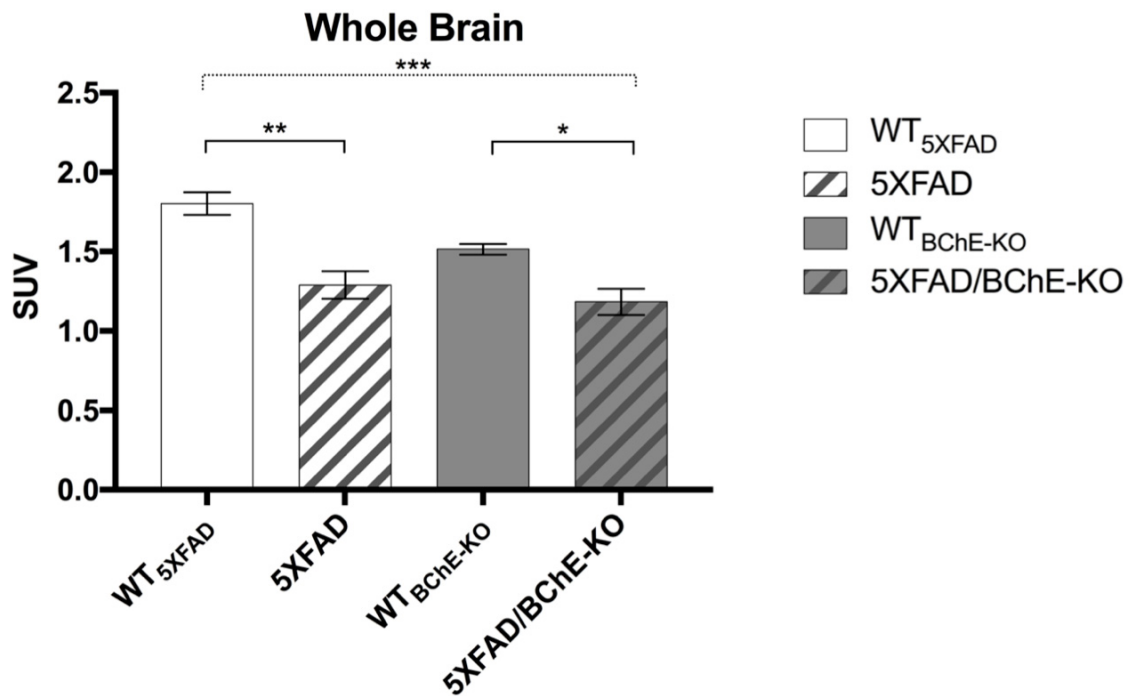


Figure 6.3 Standardized uptake values (SUVs) comparing whole brain [18F]FDG uptake in 5XFAD, 5XFAD/BChE-KO and corresponding WT_{BChE-KO} and WT_{5XFAD} mouse strains plotted as mean \pm SEM where *** = $p < 0.001$; ** = $p < 0.01$; * = $p < 0.05$. 5XFAD and 5XFAD/BChE-KO whole brain SUVs (1.29 ± 0.09 and 1.18 ± 0.08 , respectively) represent similar decreases in brain metabolism observed from respective WT_{5XFAD} (28.4% decrease, $p < 0.01$) and WT_{BChE-KO} (21.9% decrease, $p < 0.05$) counterparts. In addition, whole brain SUV values of WT_{5XFAD} and WT_{BChE-KO} were not statistically different from one another, nor were 5XFAD from 5XFAD/BChE-KO or WT_{BChE-KO}. Whole brain SUVs were significantly less than the WT_{5XFAD} group (34.3% decrease, $p < 0.001$).

6.6.3 [¹⁸F]FDG Regional SUV Comparisons

We sought to determine whether such a global whole brain measure might mask any regional differences in [¹⁸F]FDG retention between the groups investigated. Brain regions known to be affected in AD, including cerebral cortex, thalamus, hippocampal formation, amygdala and basal ganglia as well as cerebellum, were selected for comparison.

Regional ANOVAs indicated significant differences were present between study groups within each brain region (cerebral cortex: $F=9.29$, $p=0.0005$; thalamus: $F=8.93$, $p=0.0007$; hippocampal formation: $F=8.23$, $p=0.0001$; amygdala: $F=5.11$, $p=0.0084$; basal ganglia: $F=8.70$, $p=0.0007$; cerebellum: $F=4.89$, $p=0.01$). As in whole brain measurements, in 5XFAD mice, comparable statistically significant decreases in all regional SUVs (save cerebellum) were observed compared to WT_{5XFAD} (a reduction in regional retention of between 25.9-32.3%, $p<0.05$) (Figure 6.4). In 5XFAD/BChE-KO mice, however, a more selective regional pattern of reduced retention was observed (Figure 6.4). For example, while decreases in SUVs were observed in the cerebral cortex (22.8% decrease, $p<0.05$) and thalamus (23.6% decrease, $p<0.05$) compared to $WT_{BChE-KO}$, SUVs in the hippocampal formation, amygdala and basal ganglia (as well as cerebellum) were conserved when comparing $WT_{BChE-KO}$ and 5XFAD/BChE-KO and were not statistically different from one another (Figure 6.4).

As in whole brain, no significant differences could be discerned in [¹⁸F]FDG uptake between 5XFAD and 5XFAD/BChE-KO mice in these regions examined (Figure 6.4) nor were WT_{5XFAD} and $WT_{BChE-KO}$ statistically separable from one another. In a

similar way, no differences in whole brain [^{18}F]FDG retention between 5XFAD and $\text{WT}_{\text{BChE-KO}}$ mice were observed (Figure 6.4), perhaps again owed to this potential strain-related shift in baseline ^{18}F FDG retention. In addition, 5XFAD/BChE-KO SUVs in each region examined were significantly less than the $\text{WT}_{5\text{XFAD}}$ group (up to a 34.3% decrease, $p < 0.01$) (Figure 6.4).

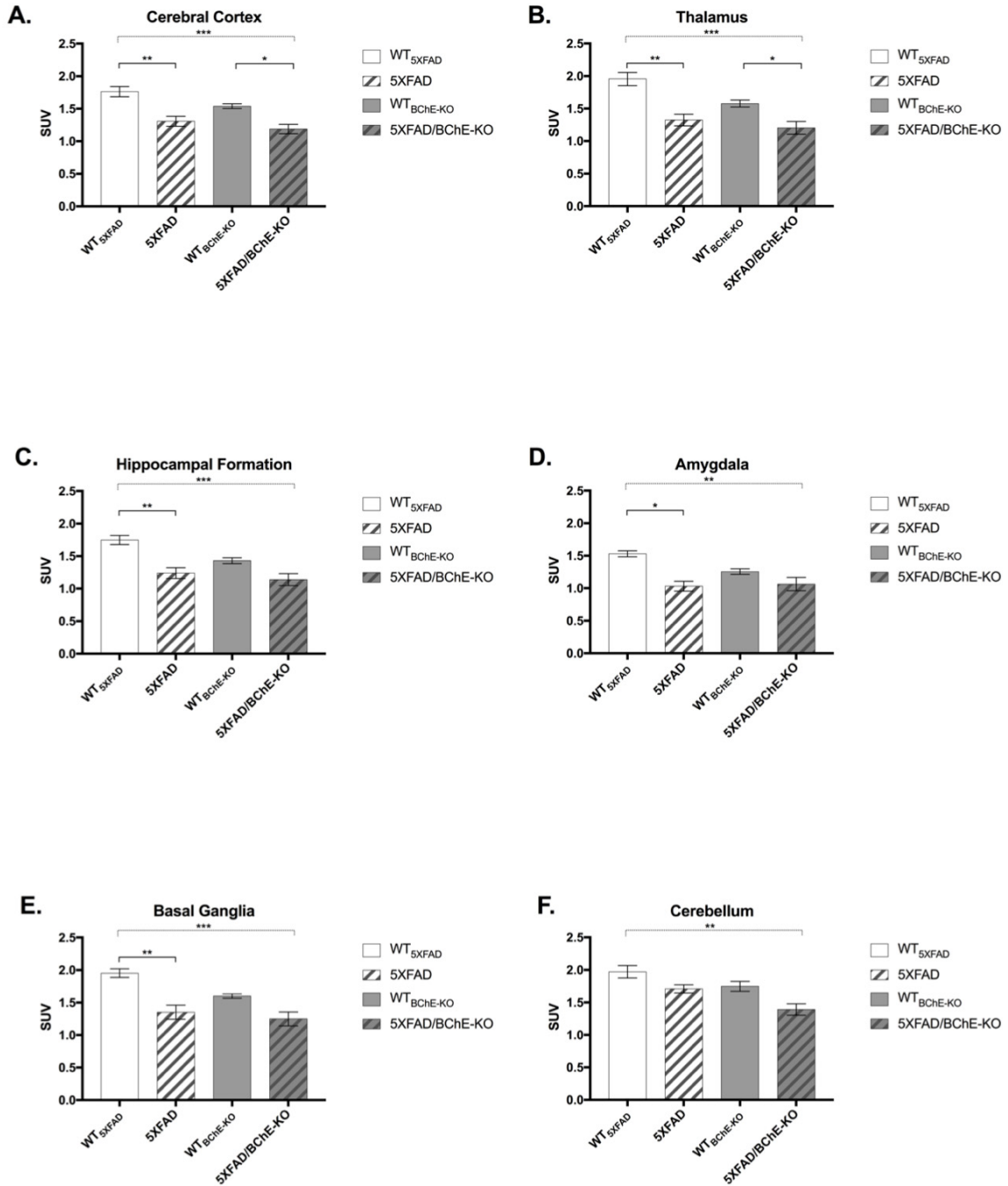


Figure 6.4 [18F]FDG regional SUVs for 5XFAD, WT5XFAD, 5XFAD/BChE-KO and WT BChE-KO mice in **A.** cerebral cortex, **B.** thalamus, **C.** hippocampal formation, **D.** amygdala, **E.** basal ganglia and **F.** cerebellum plotted as mean \pm SEM where * = $p < 0.05$; ** = $p < 0.01$; *** = $p < 0.001$.

6.7 Discussion

In AD, reduced glucose metabolism is thought to be due to neuronal dysfunction and/or loss. It has been hypothesized that neuronal dysfunction is due to A β deposition with fibrillar forms of A β being the toxic form (Selkoe & Hardy, 2016). To examine the effects of A β on the brain, a number of mouse models of amyloidosis have been developed, including the 5XFAD mouse model (Oakley et al., 2006). The present study examines the question as to whether there is a link between BChE-modulated fibrillar A β plaque burden and brain function by comparing [^{18}F]FDG retention in the brains of the 5XFAD mouse model and a derived strain, 5XFAD/BChE-KO. Previous studies using the 5XFAD/BChE-KO model have shown that the absence of BChE expression leads to diminished fibrillar A β in the brains of 5XFAD mice (Darvesh & Reid, 2016; Reid & Darvesh, 2015). The current study confirms these observations in male mice at 5 months of age (Figure 1). Other studies have also experimentally altered A β deposition *in vivo* by way of delivering ultrasound to reduce A β aggregation in the mouse brain (Leinenga & Gotz, 2015) and through immunotherapy-mediated A β clearance techniques (Hara et al., 2004; Kalra & Khan, 2015; Lee et al., 2006; Levites et al., 2006; Schenk et al., 1999; Sigurdsson et al., 2001). Some studies have reported functional improvements in learning and memory in response to lowering A β levels in the brain (Lee et al., 2006; Leinenga & Gotz, 2015). The present study was undertaken to assess cerebral [^{18}F]FDG retention with PET analysis in the 5XFAD mouse compared to the 5XFAD/BChE-KO mouse in which there is reduction in fibrillar A β due to the absence of BChE (Darvesh & Reid, 2016; Reid & Darvesh, 2015). 5XFAD and 5XFAD/BChE-KO mice were compared for uptake of ^{18}F FDG along with their respective WT counterparts. Clear

decreases in whole brain (Figure 6.3) and regional (Figure 6.4) [^{18}F]FDG retention were seen in 5XFAD mice compared to $\text{WT}_{5\text{XFAD}}$ (save cerebellum). This is consistent with the hypometabolism of glucose typically observed in human AD (Mosconi, 2005), in 5XFAD (Macdonald et al., 2014) as well as other models studied previously (Waldron et al., 2015; Waldron et al., 2017), though a more global pattern of metabolic dysfunction was present in 5XFAD in the current study. In 5XFAD/BChE-KO mice, whole brain SUVs demonstrated a pattern of decreased ^{18}F FDG retention compared to $\text{WT}_{\text{BChE-KO}}$ counterparts. Further regional analysis (Figure 6.4) revealed that this reduction in ^{18}F FDG retention is predominantly in the cerebral cortex and thalamus, while that in the hippocampal formation, basal ganglia and amygdala (as measured by regional SUVs) appears to be conserved in the 5XFAD/BChE-KO brain. One possible interpretation of these findings is that absence of BChE in the 5XFAD/BChE-KO brain may confer a protective effect on brain function in certain regions otherwise susceptible to metabolic deficits.

Similar levels of [^{18}F]FDG retention were observed in SUVs of 5XFAD mice and 5XFAD/BChE-KO counterparts when comparing SUV metrics in whole brain (Figure 6.3) and regional comparisons (Figure 6.4). In addition, while $\text{WT}_{5\text{XFAD}}$ and $\text{WT}_{\text{BChE-KO}}$ whole brain SUVs were not statistically separable in our sample, it appears as though the baseline operating range of $\text{WT}_{\text{BChE-KO}}$ mice may be lower in terms of whole brain retention (a statistical trend, $p < 0.1$, was observed). This potential disparity may confound interpretation of the comparison of 5XFAD and 5XFAD/BChE-KO strains. In a similar way, no differences in whole brain [^{18}F]FDG retention between 5XFAD and $\text{WT}_{\text{BChE-KO}}$ mice were observed, perhaps owed to this potential strain-related shift in baseline whole

brain retention. This may represent a limitation of the current study as subtle strain-related differences in baseline brain retention will require caution in the interpretation of comparisons of [^{18}F]FDG uptake. This preliminary study, while at relatively low sample size, was able to detect significant differences consistent with previous studies of fibrillar A β quantification (Darvesh & Reid, 2016; Reid & Darvesh, 2015) and [^{18}F]FDG -PET in the 5XFAD model (Macdonald et al., 2014) as well as generate, in some cases, highly significant differences in the current study design.

A more than 30% lower fibrillar A β plaque burden was observed in the cerebral cortex of 5XFAD/BChE-KO mice (Figure 6.1). With a reduction in fibrillar A β , conferred by knocking out BChE, certain structures in the 5XFAD/BChE-KO brain, including the hippocampal formation, basal ganglia and amygdala appear to maintain the baseline brain [^{18}F]FDG retention seen in WT_{BChE-KO} counterparts. This is in keeping with previous observations in TASTPM mice where there is reduced ^{18}F FDG uptake with increased A β deposition (Waldron et al., 2017).

A separate analysis (data not shown) was also performed to determine whether knocking out BChE had any effect on [^{18}F]FDG retention in otherwise healthy mice. This was done to assess any potential confounds in the selection of the WT_{BChE-KO} background strain versus the derived BChE-KO line bred with 5XFAD mice to generate 5XFAD/BChE-KO mice. Whole brain and regional SUV quantification in BChE-KO mice revealed that in each of these regions, SUV values were identical to that of WT_{BChE-KO} counterparts. This confirmed that the use of WT_{BChE-KO} was appropriate for WT_{BChE-KO} and 5XFAD/BChE-KO comparisons.

Comparison of WT_{BChE-KO} to BChE-KO mice also suggests that in otherwise healthy mice, the lack of BChE expression does not affect cerebral [¹⁸F]FDG retention. This is consistent with what has been shown previously in humans, where BChE silent healthy individuals show no overt clinically abnormal phenotype (Manoharan, Boopathy, et al., 2007), though upon rigorous testing, exhibit subtle impairment in cognitive performance in tasks subserved by thalamocortical circuits (Manoharan, Kuznetsova, et al., 2007). Although the lack of BChE under normal conditions may not have any measurable effect of phenotype, under disease conditions, in particular AD, the role of BChE in the brain may be different. Indeed, reduced [¹⁸F]FDG retention is a feature of 5XFAD and 5XFAD/BChE-KO mice when compared to their respective WT background strains. Regional assessment of 5XFAD/BChE-KO mice indicate that cerebral cortex and thalamus seem to be the dominant regions that drive a state of reduced retention in these AD animals which lack BChE expression, while hippocampal formation, amygdala and basal ganglia have unaltered [¹⁸F]FDG retention which is conserved in 5XFAD/BChE-KO mice. This result is of interest since thalamocortical circuits involved in higher cognitive processing in humans have been documented to be affected in BChE silent (those lacking BChE expression) individuals (Manoharan, Kuznetsova, et al., 2007). Whether the reduced retention observed in 5XFAD/BChE-KO cerebral cortex and thalamic brain regions is an analogous manifestation of the BChE silent phenomenon in humans requires further investigation. This notion may account for our current findings in 5XFAD/BChE-KO mice, where with a reduction in fibrillar A β in 5XFAD/BChE-KO mice there is conservation of [¹⁸F]FDG retention in a number of brain structures, while cerebral cortex and thalamus still remain susceptible to a reduction in [¹⁸F]FDG retention.

The 5XFAD/BChE-KO model is well suited for studies aimed at examining the effects of BChE and changes in fibrillar A β plaque deposition.

Under the conditions of the present study, we show that the absence of BChE in an AD mouse model leads to decreases fibrillar A β plaque deposition and may conserve brain function in certain regions otherwise susceptible to metabolic deficits in BChE-expressing AD brains. Indeed, the interplay between BChE, A β plaque deposition and cerebral glucose metabolism over the course of AD progression requires further scrutiny.

6.8 Acknowledgements

The authors would like to thank Christa Davis for her technical support. This research was supported in part by the Canadian Institutes of Health Research (MOP-119343, CSE-133358), Capital Health Research Fund, Nova Scotia Health Research Foundation, Faculty and Department of Medicine of Dalhousie University, Innovacorp, Dalhousie Medical Research Foundation, Nova Scotia Co-op Education Incentive, Gunn Family Research Prize, DeWolfe Graduate Studentship, the Dalhousie Medical Research Foundation Irene MacDonald Sobey Endowed Chair in Curative Approaches to Alzheimer's Disease, Ms. Sadie MacLeod and Brain Canada platform support grant.

Chapter 7 Conclusions

7.1 Overview

The current chapter aims to consolidate the overall findings and conclusions drawn from each of the preceding chapters of the thesis in the context of the development and *in vivo* evaluation of BChE radioligands. Future pursuits towards the clinical translation of BChE imaging and the significance of the current body of work will be addressed.

7.2 General Conclusions

Chapter 1 provided an overview of Alzheimer's disease, its clinical presentation and the neuropathological features that define the disease. Despite intense focus on establishing reliable biomarkers within the Amyloid, Tau and Neurodegeneration (AT(N)) framework, a definitive diagnosis of AD is not yet achievable during life. An emphasis was placed on early cholinergic system dysfunction that has been implicated in AD and specifically, our recent findings that the enzyme BChE is a highly sensitive and specific biomarker of AD and has greater predictive value as a diagnostic entity during life than currently used biomarkers. The current state of brain imaging of the cholinergic system is highlighted and the recent trajectories in BChE radioligand development are discussed. The fundamentals of nuclear medicine (PET and SPECT) imaging along with complimentary structural imaging modalities magnetic resonance imaging (MRI) and computed tomography (CT) were reviewed. The various analysis techniques currently

employed for brain imaging in nuclear medicine were outlined and general theory on the radioligand development in the central nervous system (CNS) was reviewed.

Chapter 2 described the synthesis and preliminary *in vivo* evaluation of lead candidate radioligand *N*-methylpiperidiny-4-^[123I]iodobenzoate (TRV6001), a SPECT imaging agent targeting BChE. This work represented the first *in vivo* images of our BChE radioligands acquired on a dedicated pre-clinical scanner, made possible through a research collaboration with medical device company Cubresa. TRV6001 readily crossed the BBB and SPECT imaging with this tracer was found to recapitulate the known histochemical distribution of BChE in mouse brain. Increased TRV6001 retention in the AD cerebral cortex was able to effectively distinguish the 5XFAD mouse brain from that of WT. These preliminary results provided important insight into the *in vivo* behaviour of these BChE radioligands and a solid foundation for further imaging and analysis technique development.

Chapter 3 focused on the development of 2D dynamic planar scintigraphy capabilities to evaluate six candidate BChE radioligands among pyridone, diphenyl carbamate and piperidine classes of molecules in various mouse models. The enhanced temporal resolution and sufficient sensitivity offered by this scintigraphy method provided an effective means to more closely evaluate each radioligand's biodistribution, their ability to cross the BBB and to determine their clearance characteristics, providing estimates of the *in vivo* kinetics between these radioligands. Differential rates of tracer clearance (thus retention) were observed between classes of tracers. This proof-of-concept work established this method as a rapid screening tool to evaluate putative radioligand candidates and positions itself as a method that can be combined with *in vitro*

kinetics and MPO evaluation to establish a radioligands product profile. Ultimately, this method provides valuable information that can be incorporated into a “go/no go” paradigm for in the development pipeline for candidate BChE radioligands.

In Chapter 4, the synthesis and *in vivo* evaluation of [^{18}F] PET BChE radioligand *N*-Methylpiperidin-4-yl *p*-[^{18}F]fluorobenzoate (TRV6501) was carried out. Kinetic modelling approaches were employed to evaluate *in vivo* pharmacokinetic characteristics of the radioligand, which included a single tissue compartment model (1TCM), a simplified reference tissue model (SRTM) and graphical analysis techniques. This permitted estimation of associated brain retention metrics including binding potential (BP_{ND}) and volume of distribution (V_{T}) which were compared in BChE-abundant 5XFAD mice and BChE-KO mice (mice lacking the expression of BChE). No significant differences were seen in these brain retention metrics between the two mouse strains at relatively low sample size. An established pharmacokinetic analysis framework is now in place for future evaluation of putative [^{18}F]-based BChE PET radioligands.

Chapter 5 and Chapter 6 were dedicated to further neuroimaging characterization of the mouse models regularly used in our AD diagnostics program. In Chapter 5, $^{99\text{m}}\text{Tc}$ -Exametazime SPECT was used to assess baseline perfusion in 5XFAD and WT mice. No differences in perfusion were observed between strains, suggesting an apparent disconnect (a so-called neurovascular decoupling) between cerebral blood flow and established patterns of glucose hypometabolism in 5XFAD mice. Characterizing brain perfusion in these models is essential to further our understanding of the effects of disease progression on important physiological parameters including cerebral blood flow, a particularly relevant parameter to monitor in radiotracer development using these mice.

In Chapter 6, brain function in a BCHE-knockout mouse model of AD was evaluated using [¹⁸F]FDG-PET imaging. This study sought to determine whether a BChE-induced reduction of fibrillar A β , as seen in these knockout mice, translated into improved brain function compared to BChE-expressing 5XFAD mice. Whereas a global reduction in ¹⁸F retention was observed in the 5XFAD mouse certain brain regions were conserved in the BCHE-knockout mouse. This suggested that in knocking out BChE and reducing fibrillar A β , a possible protective effect on brain function may be conferred in a number of structures in BCHE-knockout mice. Determining the precise interplay between BChE, fibrillar A β deposition and brain function in AD, will be beneficial towards our understanding of AD pathogenesis and may be facilitated with evaluation of these transgenic models of AD. An extension of this study in humans is currently underway, using a candidate gene-driven analyses to determine the effects of *BCHE-K* and *BCHE-A* genetic polymorphisms on AD neuroimaging biomarkers using data from the Alzheimer's Disease Neuroimaging Initiative (ADNI).

7.3 Current Perspectives and Future of BChE Imaging of the Brain in AD: Towards Clinical Translation

Cholinergic dysfunction is a central feature in the AD brain and has shown to be inextricably linked to the cognitive decline (Davies & Maloney, 1976) and A β and NFT deposition observed in the disease (Mesulam & Geula, 1994; Moran et al., 1994). The cholinergic enzyme BChE associates with A β and NFTs in the cerebral cortex in AD. We have recently shown that BChE is a highly sensitive and specific biomarker of AD and importantly, is virtually absent in other forms of dementia (Macdonald et al., 2017).

This positions BChE as an important diagnostic imaging target that has the potential to enhance the accuracy of an AD diagnosis during life. Based on the work described in this thesis, a variety of considerations must be addressed in order to effectively translate these radioligands into widespread clinical utility, which are highlighted below.

The target profile of BChE must be considered when developing radioligands for molecular imaging of the BChE enzyme. BChE is abundant in the cerebral cortex in AD reaching levels that have been reported to be 1.4-fold up to 9.3-fold greater than in cognitively normal individuals (Macdonald et al., 2017; Perry, Perry, et al., 1978). Studies in our lab have determined that this corresponds to an estimated concentration and density (B_{\max}) of approximately 3 nM in the human cerebral cortex in AD (Darvesh group, unpublished). Given the inherent sensitivity provided by PET and SPECT imaging, which is on the order of 10^{-12} (pM) concentrations, this suggests that sufficient concentrations of BChE enzymatic target are present for brain imaging. Taken together, this indicates that not only is BChE a viable diagnostic target for the disease, it's bioavailability is such that it is also technically feasible to visualize within the constraints of PET and SPECT imaging.

There are several important issues that will need to be addressed in order for these candidate BChE radioligands to reach exploratory Investigational New Drug (IND) clinical trials in humans. These issues primarily relate to the chemical and biochemical profile of these radioligands that ultimately dictate the pharmacokinetic performance of these agents *in vivo*, as detailed below.

Physicochemical Profile. In order to effectively reach the brain for imaging, favourable physicochemical properties of the radioligand must be present. The multiparameter optimization score (MPO) serves as a good predictor of the probability of crossing the BBB, with $MPO \geq 3.0$ indicating a high likelihood of a radioligand reaching the brain (Wager et al., 2016). MPO scores of a desirable CNS radioligand are governed by the following parameters: typically possesses a lower MW (≤ 360 g/mol), a topological polar surface area (TPSA) between 40-90 has fewer hydrogen bond donors (HBDs) (≤ 0.5) and favours smaller ClogP (≤ 3), (ClogD) (≤ 2) and pKa (≤ 8) values. Many of the currently developed radioligands evaluated in this thesis satisfy these criteria and have successfully generated PET and SPECT brain images in animal models.

Optimal BBB Penetration. Generally speaking, a radioligand with maximal BBB penetration (in combination with high affinity and selectivity for the target) would offer the best opportunity for efficient labeling of the enzyme, thus generating PET or SPECT images with high signal-to-noise ratio (SNR). For rodent imaging, this value has been suggested to be ~ 0.10 %ID/mL upon peak tracer accumulation in the brain (Van de Bittner et al., 2014). In the current TRV6501 PET study, this was considerably lower at ~ 0.01 %ID/mL, though clear accumulation of TRV6501 was apparent in PET images. Further optimization of BBB penetration in putative radioligands is warranted and may relate to minimizing radiometabolites that may be generated in the blood prior to reaching the brain.

Target Engagement Optimization. High affinity and selectivity for the target is essential in generating effective images that accurately represent the distribution of BChE in the brain. As BChE substrate radioligands, this is largely governed by the catalytic

efficiency (k_{cat}/K_m) of the enzyme which should be on the order of $10^2 - 10^8 \text{ M}^{-1}\cdot\text{min}^{-1}$ *in vitro*. The radioligands evaluated in this thesis all fall within this operating range.

Radiometabolites and Hydrolysis of Radioligands by BChE in the blood. Gaining further insight into the interaction of candidate radioligands in the blood will be an important future pursuit. The prospect of hydrolysis of these radioligands by circulating BChE is a distinct possibility, given that BChE is also present in the blood (Darvesh, Hopkins, et al., 2003). Reducing radioligand hydrolysis by altering the binding affinity of the molecule offers one possibility in limiting these interactions with BChE in the blood. If candidate radioligands are found to be hydrolyzed in the blood, it is important that the radiometabolites are either not active or do not cross the BBB. Extensive investigation is warranted to account for all possible radiometabolite species that may be contributing to the measured PET or SPECT signal for a given radioligand.

Off target and non-specific Binding. Candidate BChE radioligands should exhibit minimal off target and non-specific binding to generate high contrast images depicting true BChE distributions in the brain. In the future, the specificity of binding for candidate radioligands can be prioritized through *in vitro* autoradiographic methods using post-mortem mouse or human brain tissue. Incubation of BChE-positive (histochemical verified) brain tissue with candidate radioligands and subsequent self-blocking of adjacent slices BChE using cold (non-radioactive) ligands or a BChE inhibitor such as ethopropazine will discriminate regions of specific binding vs. off-target or non-specific binding. Similar *in vivo* imaging studies could be carried out, whereby an AD mouse could be imaged with a candidate radioligand and a follow up imaging session with candidate radioligand after administration of self-blocking non-radioactive ligand or

ethopropazine inhibition. Decreased signal accumulation in BChE-rich regions would indicate the specificity of the radioligand for BChE in the brain. These studies have been planned and are currently underway.

The current proof-of-concept work described in this thesis offers a significant advancement in the development and characterization of these BChE radioligands, that until now, has not been possible. Several of the candidate radioligands evaluated in this thesis possess many of these favourable attributes that ultimately confer effective uptake and retention of radioligand in the brain. Further evaluation of these PET and SPECT radioligands is warranted. With a neuroimaging analysis framework now in place, the *in vivo* evaluation of tracer biodistribution and key pharmacokinetic parameters related to brain uptake and clearance that define their *in vivo* performance can ultimately feed forward to the product profile of these radioligands. Pharmacokinetic modeling will serve as an important tool to evaluate the performance of current and future BChE radiotracers. Fine tuning (as required) of the radioligand parameters highlighted above in these radiotracers or structurally similar molecules will provide the best opportunity to advance the most promising candidates towards exploratory IND clinical trials in humans.

Certain additional criteria related to the safety and tolerability of prospective radioligands must be met on the road to clinical translation of these BChE imaging agents. These radiopharmaceuticals should exhibit no toxicity and have no pharmacological effects in patients (US-FDA, 2006). Minimizing the required dose to patients is also key and this can be accomplished, in part, by developing a radioligand with high specific activity. Preclinical safety studies, as required by FDA (US-FDA,

2006) and Health Canada (Health Canada, 2014) Guidelines, are carried out using pharmacological and toxicological data in animals to determine a safe radiation absorbed dose in humans and to evaluate which organs are potential targets of toxicity (Harapanhalli, 2010). For this, biodistribution and radiation dosimetry studies for a given candidate radioligand are carried out in animals to determine the concentration of radioactivity (e.g. %ID/g) in blood, brain and other organs at a suitable imaging dose. With this supporting information, one can infer an equivalent scaled (e.g. %kg/g) distribution in humans, providing estimates of human radiation dosimetry as has been described previously (Stabin et al., 2005; Toyohara et al., 2013). The total effective radiation dose incurred annually by a subject must not exceed 50mSv per year (Health Canada, 2014). By way of comparison, amyloid imaging agents ranging from 185-450MBq per dose and scan times of 40-130min generate 1.3-6.3 mSv of exposure per imaging dose (Herholz & Ebmeier, 2011). In addition, chemistry manufacturing and controls information pertaining to the composition, purity and stability are also evaluated to determine the quality and suitability of a radioligand for human use (Harapanhalli, 2010).

Once all of these above criteria are satisfied, a successful exploratory IND application permits early Phase I clinical trial evaluation in a small cohort of healthy subjects (typically 7 individuals) at low dosage to assess the general biodistribution, pharmacokinetics and mechanism of action of the candidate radiopharmaceutical in humans (Harapanhalli, 2010). This is to establish that the radioligand is safe and works as expected in humans. Interspecies differences may exist when translating preclinical

evaluations to humans. A radioligand that is effective in a mouse model, may not necessarily predict performance in humans.

If exploratory IND proves successful, Phase I clinical trials can commence to evaluate a preliminary safety assessment, initial dose and dose escalation studies in humans. This is followed by Phase II trials to demonstrate proof of concept and to evaluate efficacy in a limited number of human subjects. Finally, if successful, Phase III clinical trials demonstrate efficacy and continued safety in well-controlled clinical studies in large cohorts of human subjects (Harapanhalli, 2010).

7.4 Significance

BChE is a highly sensitive and specific biomarker of AD and holds great promise as a diagnostic target for molecular imaging of the brain. A critical step towards reaching experimental investigational new drug (IND) status for human BChE brain imaging in clinical trials is in the preclinical development and evaluation of radioligands in animal models. In the current work, an essential neuroimaging analysis framework has been developed and implemented, providing an *in vivo* radioligand development toolkit which will enable rigorous evaluation of candidate BChE radioligands for PET and SPECT AD diagnostics as they are developed. Ultimately, this will accelerate the radioligand research and development cycle, getting these radiopharmaceuticals to clinical trials and to market in a timely manner.

Brain imaging of BChE in humans may enhance the accuracy and timely detection of AD not yet possible with current brain imaging methods, with significant potential to augment the current AD biomarker armamentarium. An early and definitive

diagnosis of AD will be critical to help evaluate new treatment approaches as they become available. Confirming an AD diagnosis and distinguishing it from other forms of dementias (whose treatment approaches are likely different), will ultimately ensure accurate patient stratification, properly placing the right types of dementia patients in the right clinical trials to determine the effectiveness of AD drug therapies that may eventually lead to a cure for the disease. The timely diagnosis of AD, during life, will also provide clear advantages in the improvement of health management approaches and will help relieve the economic burden associated with the disease. If successful, this research has significant potential to impact the way we diagnose, manage and perhaps eventually, how we even treat Alzheimer's disease.

References

- Altmann, A., Ng, B., Landau, S. M., Jagust, W. J., Greicius, M. D., & Alzheimer's Disease Neuroimaging, I. (2015). Regional brain hypometabolism is unrelated to regional amyloid plaque burden. *Brain*, *138*(Pt 12), 3734-3746. doi:10.1093/brain/awv278
- Apostolova, I., Wunder, A., Dirnagl, U., Michel, R., Stemmer, N., Lukas, M., Derlin, T., Gregor-Mamoudou, B., Goldschmidt, J., Brenner, W., & Buchert, R. (2012). Brain perfusion SPECT in the mouse: normal pattern according to gender and age. *Neuroimage*, *63*(4), 1807-1817. doi:10.1016/j.neuroimage.2012.08.038
- Arendt, T., Bruckner, M. K., Lange, M., & Bigl, V. (1992). Changes in acetylcholinesterase and butyrylcholinesterase in Alzheimer's disease resemble embryonic development--a study of molecular forms. *Neurochem Int*, *21*(3), 381-396.
- Bartus, R. T., Dean, R. L., 3rd, Beer, B., & Lippa, A. S. (1982). The cholinergic hypothesis of geriatric memory dysfunction. *Science*, *217*(4558), 408-414.
- Birks, J. (2006). Cholinesterase inhibitors for Alzheimer's disease. *Cochrane Database Syst Rev*(1), CD005593. doi:10.1002/14651858.CD005593
- Blennow, K., & Zetterberg, H. (2018). Biomarkers for Alzheimer's disease: current status and prospects for the future. *J Intern Med*. doi:10.1111/joim.12816
- Bloudek, L. M., Spackman, D. E., Blankenburg, M., & Sullivan, S. D. (2011). Review and meta-analysis of biomarkers and diagnostic imaging in Alzheimer's disease. *J Alzheimers Dis*, *26*(4), 627-645. doi:10.3233/JAD-2011-110458
- Boellaard, R. (2009). Standards for PET image acquisition and quantitative data analysis. *J Nucl Med*, *50 Suppl 1*, 11S-20S. doi:10.2967/jnumed.108.057182
- Bormans, G., Sherman, P., Snyder, S. E., & Kilbourn, M. R. (1996). Synthesis of carbon-11- and fluorine-18-labeled 1-methyl-4-piperidyl-4'-fluorobenzoate and their biodistribution in mice. *Nucl Med Biol*, *23*(4), 513-517.
- Bushberg, J. T. (2002). *The Essential Physics of Medical Imaging* (2nd Edition ed.).
- Cash, D. M., Rohrer, J. D., Ryan, N. S., Ourselin, S., & Fox, N. C. (2014). Imaging endpoints for clinical trials in Alzheimer's disease. *Alzheimers Res Ther*, *6*(9), 87. doi:10.1186/s13195-014-0087-9
- Catafau, A. M. (2001). Brain SPECT in clinical practice. Part I: perfusion. *J Nucl Med*, *42*(2), 259-271.

- Clark, C. M., Pontecorvo, M. J., Beach, T. G., Bedell, B. J., Coleman, R. E., Doraiswamy, P. M., Fleisher, A. S., Reiman, E. M., Sabbagh, M. N., Sadowsky, C. H., Schneider, J. A., Arora, A., Carpenter, A. P., Flitter, M. L., Joshi, A. D., Krautkramer, M. J., Lu, M., Mintun, M. A., Skovronsky, D. M., & Group, A.-A. S. (2012). Cerebral PET with florbetapir compared with neuropathology at autopsy for detection of neuritic amyloid-beta plaques: a prospective cohort study. *Lancet Neurol*, *11*(8), 669-678. doi:10.1016/S1474-4422(12)70142-4
- Cohen, A. D., Price, J. C., Weissfeld, L. A., James, J., Rosario, B. L., Bi, W., Nebes, R. D., Saxton, J. A., Snitz, B. E., Aizenstein, H. A., Wolk, D. A., Dekosky, S. T., Mathis, C. A., & Klunk, W. E. (2009). Basal cerebral metabolism may modulate the cognitive effects of Aβ in mild cognitive impairment: an example of brain reserve. *J Neurosci*, *29*(47), 14770-14778. doi:10.1523/JNEUROSCI.3669-09.2009
- Coyle, J. T., Price, D. L., & DeLong, M. R. (1983). Alzheimer's disease: a disorder of cortical cholinergic innervation. *Science*, *219*(4589), 1184-1190.
- Curtis, C., Gamez, J. E., Singh, U., Sadowsky, C. H., Villena, T., Sabbagh, M. N., Beach, T. G., Duara, R., Fleisher, A. S., Frey, K. A., Walker, Z., Hunjan, A., Holmes, C., Escovar, Y. M., Vera, C. X., Agronin, M. E., Ross, J., Bozoki, A., Akinola, M., Shi, J., Vandenberghe, R., Ikonovic, M. D., Sherwin, P. F., Grachev, I. D., Farrar, G., Smith, A. P., Buckley, C. J., McLain, R., & Salloway, S. (2015). Phase 3 trial of flutemetamol labeled with radioactive fluorine 18 imaging and neuritic plaque density. *JAMA Neurol*, *72*(3), 287-294. doi:10.1001/jamaneurol.2014.4144
- Darreh-Shori, T., Brimijoin, S., Kadir, A., Almkvist, O., & Nordberg, A. (2006). Differential CSF butyrylcholinesterase levels in Alzheimer's disease patients with the ApoE ε4 allele, in relation to cognitive function and cerebral glucose metabolism. *Neurobiol Dis*, *24*(2), 326-333. doi:10.1016/j.nbd.2006.07.013
- Darvesh, S. (2013). Butyrylcholinesterase radioligands to image Alzheimer's disease brain. *Chem Biol Interact*, *203*(1), 354-357. doi:10.1016/j.cbi.2012.08.009
- Darvesh, S. (2016). Butyrylcholinesterase as a Diagnostic and Therapeutic Target for Alzheimer's Disease. *Curr Alzheimer Res*, *13*(10), 1173-1177.
- Darvesh, S., Cash, M. K., Reid, G. A., Martin, E., Mitnitski, A., & Geula, C. (2012). Butyrylcholinesterase is associated with beta-amyloid plaques in the transgenic APPSWE/PSEN1dE9 mouse model of Alzheimer disease. *J Neuropathol Exp Neurol*, *71*(1), 2-14. doi:10.1097/NEN.0b013e31823cc7a6
- Darvesh, S., Hopkins, D. A., & Geula, C. (2003). Neurobiology of butyrylcholinesterase. *Nat Rev Neurosci*, *4*(2), 131-138. doi:10.1038/nrn1035

- Darvesh, S., & Reid, G. A. (2016). Reduced fibrillar beta-amyloid in subcortical structures in a butyrylcholinesterase-knockout Alzheimer disease mouse model. *Chem Biol Interact.* doi:10.1016/j.cbi.2016.04.022
- Darvesh, S., Reid, G. A., & Martin, E. (2010). Biochemical and histochemical comparison of cholinesterases in normal and Alzheimer brain tissues. *Curr Alzheimer Res*, 7(5), 386-400.
- Darvesh, S., Walsh, R., Kumar, R., Caines, A., Roberts, S., Magee, D., Rockwood, K., & Martin, E. (2003). Inhibition of human cholinesterases by drugs used to treat Alzheimer disease. *Alzheimer Dis Assoc Disord*, 17(2), 117-126.
- Davies, P., & Maloney, A. J. (1976). Selective loss of central cholinergic neurons in Alzheimer's disease. *Lancet*, 2(8000), 1403.
- Davis, K. L., & American College of Neuropsychopharmacology. (2002). *Neuropsychopharmacology : the fifth generation of progress : an official publication of the American College of Neuropsychopharmacology* (Vol. Chapter 31). Philadelphia: Lippincott Williams & Wilkins.
- DeBay, D. R., Reid, G. A., Macdonald, I. R., Mawko, G., Burrell, S., Martin, E., Bowen, C. V., & Darvesh, S. (2017). Butyrylcholinesterase-knockout reduces fibrillar beta-amyloid and conserves (18)FDG retention in 5XFAD mouse model of Alzheimer's disease. *Brain Res*, 1671, 102-110. doi:10.1016/j.brainres.2017.07.009
- DeBay, D. R., Reid, G. A., Pottie, I. R., Martin, E., Bowen, C. V., & Darvesh, S. (2017). Targeting butyrylcholinesterase for preclinical single photon emission computed tomography (SPECT) imaging of Alzheimer's disease. *Alzheimers Dement (N Y)*, 3(2), 166-176. doi:10.1016/j.trci.2017.01.005
- Doody, R. S., Farlow, M., Aisen, P. S., Alzheimer's Disease Cooperative Study Data, A., & Publication, C. (2014). Phase 3 trials of solanezumab and bapineuzumab for Alzheimer's disease. *N Engl J Med*, 370(15), 1460. doi:10.1056/NEJMc1402193
- Doody, R. S., Thomas, R. G., Farlow, M., Iwatsubo, T., Vellas, B., Joffe, S., Kieburtz, K., Raman, R., Sun, X., Aisen, P. S., Siemers, E., Liu-Seifert, H., Mohs, R., Alzheimer's Disease Cooperative Study Steering, C., & Solanezumab Study, G. (2014). Phase 3 trials of solanezumab for mild-to-moderate Alzheimer's disease. *N Engl J Med*, 370(4), 311-321. doi:10.1056/NEJMoA1312889

- Dubois, B., Hampel, H., Feldman, H. H., Scheltens, P., Aisen, P., Andrieu, S., Bakardjian, H., Benali, H., Bertram, L., Blennow, K., Broich, K., Cavedo, E., Crutch, S., Dartigues, J. F., Duyckaerts, C., Epelbaum, S., Frisoni, G. B., Gauthier, S., Genthon, R., Gouw, A. A., Habert, M. O., Holtzman, D. M., Kivipelto, M., Lista, S., Molinuevo, J. L., O'Bryant, S. E., Rabinovici, G. D., Rowe, C., Salloway, S., Schneider, L. S., Sperling, R., Teichmann, M., Carrillo, M. C., Cummings, J., Jack, C. R., Jr., Proceedings of the Meeting of the International Working Group, the American Alzheimer's Association on "The Preclinical State of, A. D., July, & Washington Dc, U. S. A. (2016). Preclinical Alzheimer's disease: Definition, natural history, and diagnostic criteria. *Alzheimers Dement*, 12(3), 292-323. doi:10.1016/j.jalz.2016.02.002
- Edison, P., Archer, H. A., Hinz, R., Hammers, A., Pavese, N., Tai, Y. F., Hotton, G., Cutler, D., Fox, N., Kennedy, A., Rossor, M., & Brooks, D. J. (2007). Amyloid, hypometabolism, and cognition in Alzheimer disease: an [11C]PIB and [18F]FDG PET study. *Neurology*, 68(7), 501-508. doi:10.1212/01.wnl.0000244749.20056.d4
- Eimer, W. A., & Vassar, R. (2013). Neuron loss in the 5XFAD mouse model of Alzheimer's disease correlates with intraneuronal Aβ42 accumulation and Caspase-3 activation. *Mol Neurodegener*, 8, 2. doi:10.1186/1750-1326-8-2
- Engler, H., Forsberg, A., Almkvist, O., Blomquist, G., Larsson, E., Savitcheva, I., Wall, A., Ringheim, A., Langstrom, B., & Nordberg, A. (2006). Two-year follow-up of amyloid deposition in patients with Alzheimer's disease. *Brain*, 129(Pt 11), 2856-2866. doi:10.1093/brain/awl178
- Forlenza, O. V., De-Paula, V. J., & Diniz, B. S. (2014). Neuroprotective effects of lithium: implications for the treatment of Alzheimer's disease and related neurodegenerative disorders. *ACS Chem Neurosci*, 5(6), 443-450. doi:10.1021/cn5000309
- Frisoni, G. B., Fox, N. C., Jack, C. R., Jr., Scheltens, P., & Thompson, P. M. (2010). The clinical use of structural MRI in Alzheimer disease. *Nat Rev Neurol*, 6(2), 67-77. doi:10.1038/nrneurol.2009.215
- Furst, A. J., Rabinovici, G. D., Rostomian, A. H., Steed, T., Alkalay, A., Racine, C., Miller, B. L., & Jagust, W. J. (2012). Cognition, glucose metabolism and amyloid burden in Alzheimer's disease. *Neurobiol Aging*, 33(2), 215-225. doi:10.1016/j.neurobiolaging.2010.03.011
- Geula, C., Greenberg, B. D., & Mesulam, M. M. (1994). Cholinesterase activity in the plaques, tangles and angiopathy of Alzheimer's disease does not emanate from amyloid. *Brain Res*, 644(2), 327-330. doi:10.1016/0006-8993(94)91697-7
- Geula, C., & Mesulam, M. M. (1989). Cortical cholinergic fibers in aging and Alzheimer's disease: a morphometric study. *Neuroscience*, 33(3), 469-481.

- Geula, C., & Mesulam, M. M. (1995). Cholinesterases and the pathology of Alzheimer disease. *Alzheimer Dis Assoc Disord*, 9 Suppl 2, 23-28.
- Giacobini, E., & Pepeu, G. (2006). *The brain cholinergic system in health and disease*. Abingdon, Oxon England: Informa Healthcare.
- Grimmer, T., Wutz, C., Alexopoulos, P., Drzezga, A., Forster, S., Forstl, H., Goldhardt, O., Ortner, M., Sorg, C., & Kurz, A. (2016). Visual Versus Fully Automated Analyses of 18F-FDG and Amyloid PET for Prediction of Dementia Due to Alzheimer Disease in Mild Cognitive Impairment. *J Nucl Med*, 57(2), 204-207. doi:10.2967/jnumed.115.163717
- Grover, V. P., Tognarelli, J. M., Crossey, M. M., Cox, I. J., Taylor-Robinson, S. D., & McPhail, M. J. (2015). Magnetic Resonance Imaging: Principles and Techniques: Lessons for Clinicians. *J Clin Exp Hepatol*, 5(3), 246-255. doi:10.1016/j.jceh.2015.08.001
- Guillozet, A. L., Smiley, J. F., Mash, D. C., & Mesulam, M. M. (1997). Butyrylcholinesterase in the life cycle of amyloid plaques. *Ann Neurol*, 42(6), 909-918. doi:10.1002/ana.410420613
- Hara, H., Monsonego, A., Yuasa, K., Adachi, K., Xiao, X., Takeda, S., Takahashi, K., Weiner, H. L., & Tabira, T. (2004). Development of a safe oral Abeta vaccine using recombinant adeno-associated virus vector for Alzheimer's disease. *J Alzheimers Dis*, 6(5), 483-488.
- Harapanhalli, R. S. (2010). Food and Drug Administration requirements for testing and approval of new radiopharmaceuticals. *Semin Nucl Med*, 40(5), 364-384. doi:10.1053/j.semnuclmed.2010.05.002
- Health Canada. (2014). *Guidance Document - A Guide for the Preparation of Applications for Authorization of Positron-emitting Radiopharmaceuticals for Use in Basic Clinical Research*. (990). Ottawa, ON: Minister of Public Works and Government Services Canada
- Health Canada - Publications.
- Herholz, K., & Ebmeier, K. (2011). Clinical amyloid imaging in Alzheimer's disease. *Lancet Neurol*, 10(7), 667-670. doi:10.1016/S1474-4422(11)70123-5
- Hou, C. E., Carlin, D., & Miller, B. L. (2004). Non-Alzheimer's disease dementias: anatomic, clinical, and molecular correlates. *Can J Psychiatry*, 49(3), 164-171.
- Hyman, B. T., & Trojanowski, J. Q. (1997). Consensus recommendations for the postmortem diagnosis of Alzheimer disease from the National Institute on Aging and the Reagan Institute Working Group on diagnostic criteria for the neuropathological assessment of Alzheimer disease. *J Neuropathol Exp Neurol*, 56(10), 1095-1097.

- Iadecola, C. (2017). The Neurovascular Unit Coming of Age: A Journey through Neurovascular Coupling in Health and Disease. *Neuron*, 96(1), 17-42. doi:10.1016/j.neuron.2017.07.030
- Innis, R. B., Cunningham, V. J., Delforge, J., Fujita, M., Gjedde, A., Gunn, R. N., Holden, J., Houle, S., Huang, S. C., Ichise, M., Iida, H., Ito, H., Kimura, Y., Koeppe, R. A., Knudsen, G. M., Knuuti, J., Lammertsma, A. A., Laruelle, M., Logan, J., Maguire, R. P., Mintun, M. A., Morris, E. D., Parsey, R., Price, J. C., Slifstein, M., Sossi, V., Suhara, T., Votaw, J. R., Wong, D. F., & Carson, R. E. (2007). Consensus nomenclature for in vivo imaging of reversibly binding radioligands. *J Cereb Blood Flow Metab*, 27(9), 1533-1539. doi:10.1038/sj.jcbfm.9600493
- Iqbal, K., Liu, F., & Gong, C. X. (2016). Tau and neurodegenerative disease: the story so far. *Nat Rev Neurol*, 12(1), 15-27. doi:10.1038/nrneurol.2015.225
- Irie, T., Fukushi, K., Namba, H., Iyo, M., Tamagami, H., Nagatsuka, S., & Ikota, N. (1996). Brain acetylcholinesterase activity: validation of a PET tracer in a rat model of Alzheimer's disease. *J Nucl Med*, 37(4), 649-655.
- Jack, C. R., Jr., Bennett, D. A., Blennow, K., Carrillo, M. C., Dunn, B., Haeberlein, S. B., Holtzman, D. M., Jagust, W., Jessen, F., Karlawish, J., Liu, E., Molinuevo, J. L., Montine, T., Phelps, C., Rankin, K. P., Rowe, C. C., Scheltens, P., Siemers, E., Snyder, H. M., Sperling, R., & Contributors. (2018). NIA-AA Research Framework: Toward a biological definition of Alzheimer's disease. *Alzheimers Dement*, 14(4), 535-562. doi:10.1016/j.jalz.2018.02.018
- Jack, C. R., Jr., Bennett, D. A., Blennow, K., Carrillo, M. C., Feldman, H. H., Frisoni, G. B., Hampel, H., Jagust, W. J., Johnson, K. A., Knopman, D. S., Petersen, R. C., Scheltens, P., Sperling, R. A., & Dubois, B. (2016). A/T/N: An unbiased descriptive classification scheme for Alzheimer disease biomarkers. *Neurology*, 87(5), 539-547. doi:10.1212/WNL.0000000000002923
- Jacquier-Sarlin, M. R., Polla, B. S., & Slosman, D. O. (1996a). Cellular basis of ECD brain retention. *J Nucl Med*, 37(10), 1694-1697.
- Jacquier-Sarlin, M. R., Polla, B. S., & Slosman, D. O. (1996b). Oxido-reductive state: the major determinant for cellular retention of technetium-99m-HMPAO. *J Nucl Med*, 37(8), 1413-1416.
- James, M. L., & Gambhir, S. S. (2012). A molecular imaging primer: modalities, imaging agents, and applications. *Physiol Rev*, 92(2), 897-965. doi:10.1152/physrev.00049.2010

- Jansen, W. J., Ossenkoppele, R., Knol, D. L., Tijms, B. M., Scheltens, P., Verhey, F. R., Visser, P. J., Amyloid Biomarker Study, G., Aalten, P., Aarsland, D., Alcolea, D., Alexander, M., Almdahl, I. S., Arnold, S. E., Baldeiras, I., Barthel, H., van Berckel, B. N., Bibeau, K., Blennow, K., Brooks, D. J., van Buchem, M. A., Camus, V., Cavedo, E., Chen, K., Chetelat, G., Cohen, A. D., Drzezga, A., Engelborghs, S., Fagan, A. M., Fladby, T., Fleisher, A. S., van der Flier, W. M., Ford, L., Forster, S., Fortea, J., Foskett, N., Frederiksen, K. S., Freund-Levi, Y., Frisoni, G. B., Froelich, L., Gabryelewicz, T., Gill, K. D., Gkatzima, O., Gomez-Tortosa, E., Gordon, M. F., Grimmer, T., Hampel, H., Hausner, L., Hellwig, S., Herukka, S. K., Hildebrandt, H., Ishihara, L., Ivanoiu, A., Jagust, W. J., Johannsen, P., Kandimalla, R., Kapaki, E., Klimkiewicz-Mrowiec, A., Klunk, W. E., Kohler, S., Koglin, N., Kornhuber, J., Kramberger, M. G., Van Laere, K., Landau, S. M., Lee, D. Y., de Leon, M., Lisetti, V., Lleo, A., Madsen, K., Maier, W., Marcusson, J., Mattsson, N., de Mendonca, A., Meulenbroek, O., Meyer, P. T., Mintun, M. A., Mok, V., Molinuevo, J. L., Mollergard, H. M., Morris, J. C., Mroczko, B., Van der Mussele, S., Na, D. L., Newberg, A., Nordberg, A., Nordlund, A., Novak, G. P., Paraskevas, G. P., Parnetti, L., Perera, G., Peters, O., Popp, J., Prabhakar, S., Rabinovici, G. D., Ramakers, I. H., Rami, L., Resende de Oliveira, C., Rinne, J. O., Rodrigue, K. M., Rodriguez-Rodriguez, E., Roe, C. M., Rot, U., Rowe, C. C., Ruther, E., Sabri, O., Sanchez-Juan, P., Santana, I., Sarazin, M., Schroder, J., Schutte, C., Seo, S. W., Soetewey, F., Soininen, H., Spuru, L., Struyfs, H., Teunissen, C. E., Tsolaki, M., Vandenberghe, R., Verbeek, M. M., Villemagne, V. L., Vos, S. J., van Waalwijk van Doorn, L. J., Waldemar, G., Wallin, A., Wallin, A. K., Wiltfang, J., Wolk, D. A., Zboch, M., & Zetterberg, H. (2015). Prevalence of cerebral amyloid pathology in persons without dementia: a meta-analysis. *JAMA*, *313*(19), 1924-1938. doi:10.1001/jama.2015.4668
- Johnson, K. A., Minoshima, S., Bohnen, N. I., Donohoe, K. J., Foster, N. L., Herscovitch, P., Karlawish, J. H., Rowe, C. C., Carrillo, M. C., Hartley, D. M., Hedrick, S., Pappas, V., & Thies, W. H. (2013). Appropriate use criteria for amyloid PET: a report of the Amyloid Imaging Task Force, the Society of Nuclear Medicine and Molecular Imaging, and the Alzheimer's Association. *J Nucl Med*, *54*(3), 476-490. doi:10.2967/jnumed.113.120618
- Johnson, K. A., Minoshima, S., Bohnen, N. I., Donohoe, K. J., Foster, N. L., Herscovitch, P., Karlawish, J. H., Rowe, C. C., Carrillo, M. C., Hartley, D. M., Hedrick, S., Pappas, V., Thies, W. H., Alzheimer's, A., Society of Nuclear, M., Molecular, I., & Amyloid Imaging, T. (2013). Appropriate use criteria for amyloid PET: a report of the Amyloid Imaging Task Force, the Society of Nuclear Medicine and Molecular Imaging, and the Alzheimer's Association. *Alzheimers Dement*, *9*(1), e-1-16. doi:10.1016/j.jalz.2013.01.002
- Kalra, J., & Khan, A. (2015). Reducing Abeta load and tau phosphorylation: Emerging perspective for treating Alzheimer's disease. *Eur J Pharmacol*, *764*, 571-581. doi:10.1016/j.ejphar.2015.07.043

- Kang, H. M., Sohn, I., Jung, J., Jeong, J. W., & Park, C. (2016). Age-related changes in pial arterial structure and blood flow in mice. *Neurobiol Aging*, *37*, 161-170. doi:10.1016/j.neurobiolaging.2015.09.008
- Kato, T., Inui, Y., Nakamura, A., & Ito, K. (2016). Brain fluorodeoxyglucose (FDG) PET in dementia. *Ageing Res Rev*, *30*, 73-84. doi:10.1016/j.arr.2016.02.003
- Kemppainen, N., Joutsa, J., Johansson, J., Scheinin, N. M., Nagren, K., Rokka, J., Parkkola, R., & Rinne, J. O. (2015). Long-Term Interrelationship between Brain Metabolism and Amyloid Deposition in Mild Cognitive Impairment. *J Alzheimers Dis*, *48*(1), 123-133. doi:10.3233/JAD-150190
- Kikuchi, T., Okamura, T., Fukushi, K., Takahashi, K., Toyohara, J., Okada, M., Zhang, M. R., & Irie, T. (2007). Cerebral acetylcholinesterase imaging: development of the radioprobes. *Curr Top Med Chem*, *7*(18), 1790-1799.
- Kikuchi, T., Zhang, M. R., Ikota, N., Fukushi, K., Okamura, T., Suzuki, K., Arano, Y., & Irie, T. (2004). N-[¹⁸F]fluoroethylpiperidin-4-ylmethyl butyrate: a novel radiotracer for quantifying brain butyrylcholinesterase activity by positron emission tomography. *Bioorg Med Chem Lett*, *14*(8), 1927-1930. doi:10.1016/j.bmcl.2004.01.080
- Klunk, W. E., Engler, H., Nordberg, A., Wang, Y., Blomqvist, G., Holt, D. P., Bergstrom, M., Savitcheva, I., Huang, G. F., Estrada, S., Ausen, B., Debnath, M. L., Barletta, J., Price, J. C., Sandell, J., Lopresti, B. J., Wall, A., Koivisto, P., Antoni, G., Mathis, C. A., & Langstrom, B. (2004). Imaging brain amyloid in Alzheimer's disease with Pittsburgh Compound-B. *Ann Neurol*, *55*(3), 306-319. doi:10.1002/ana.20009
- Klupp, E., Grimmer, T., Tahmasian, M., Sorg, C., Yakushev, I., Yousefi, B. H., Drzezga, A., & Forster, S. (2015). Prefrontal hypometabolism in Alzheimer disease is related to longitudinal amyloid accumulation in remote brain regions. *J Nucl Med*, *56*(3), 399-404. doi:10.2967/jnumed.114.149302
- Knopman, D. S., DeKosky, S. T., Cummings, J. L., Chui, H., Corey-Bloom, J., Relkin, N., Small, G. W., Miller, B., & Stevens, J. C. (2001). Practice parameter: diagnosis of dementia (an evidence-based review). Report of the Quality Standards Subcommittee of the American Academy of Neurology. *Neurology*, *56*(9), 1143-1153.
- Kuhl, D. E., Koeppe, R. A., Snyder, S. E., Minoshima, S., Frey, K. A., & Kilbourn, M. R. (2006). In vivo butyrylcholinesterase activity is not increased in Alzheimer's disease synapses. *Ann Neurol*, *59*(1), 13-20. doi:10.1002/ana.20672
- Lammertsma, A. A., & Hume, S. P. (1996). Simplified reference tissue model for PET receptor studies. *Neuroimage*, *4*(3 Pt 1), 153-158. doi:10.1006/nimg.1996.0066

- Landau, S. M., Breault, C., Joshi, A. D., Pontecorvo, M., Mathis, C. A., Jagust, W. J., Mintun, M. A., & Alzheimer's Disease Neuroimaging, I. (2013). Amyloid-beta imaging with Pittsburgh compound B and florbetapir: comparing radiotracers and quantification methods. *J Nucl Med*, *54*(1), 70-77. doi:10.2967/jnumed.112.109009
- Lassen, N. A., Andersen, A. R., Friberg, L., & Paulson, O. B. (1988). The retention of [^{99m}Tc]-d,l-HM-PAO in the human brain after intracarotid bolus injection: a kinetic analysis. *J Cereb Blood Flow Metab*, *8*(6), S13-22. doi:10.1038/jcbfm.1988.28
- Layer, P. G. (1983). Comparative localization of acetylcholinesterase and pseudocholinesterase during morphogenesis of the chicken brain. *Proc Natl Acad Sci U S A*, *80*(20), 6413-6417.
- Lee, E. B., Leng, L. Z., Zhang, B., Kwong, L., Trojanowski, J. Q., Abel, T., & Lee, V. M. (2006). Targeting amyloid-beta peptide (Aβ) oligomers by passive immunization with a conformation-selective monoclonal antibody improves learning and memory in Aβ precursor protein (APP) transgenic mice. *J Biol Chem*, *281*(7), 4292-4299. doi:10.1074/jbc.M511018200
- Leinenga, G., & Gotz, J. (2015). Scanning ultrasound removes amyloid-beta and restores memory in an Alzheimer's disease mouse model. *Sci Transl Med*, *7*(278), 278ra233. doi:10.1126/scitranslmed.aaa2512
- Levin, C. S. (2005). Primer on molecular imaging technology. *Eur J Nucl Med Mol Imaging*, *32 Suppl 2*, S325-345. doi:10.1007/s00259-005-1973-y
- Levites, Y., Das, P., Price, R. W., Rochette, M. J., Kostura, L. A., McGowan, E. M., Murphy, M. P., & Golde, T. E. (2006). Anti-Aβ₄₂- and anti-Aβ₄₀-specific mAbs attenuate amyloid deposition in an Alzheimer disease mouse model. *J Clin Invest*, *116*(1), 193-201. doi:10.1172/JCI25410
- Li, Y., Rinne, J. O., Mosconi, L., Pirraglia, E., Rusinek, H., DeSanti, S., Kemppainen, N., Nagren, K., Kim, B. C., Tsui, W., & de Leon, M. J. (2008). Regional analysis of FDG and PIB-PET images in normal aging, mild cognitive impairment, and Alzheimer's disease. *Eur J Nucl Med Mol Imaging*, *35*(12), 2169-2181. doi:10.1007/s00259-008-0833-y
- Lockridge, O. (2015). Review of human butyrylcholinesterase structure, function, genetic variants, history of use in the clinic, and potential therapeutic uses. *Pharmacol Ther*, *148*, 34-46. doi:10.1016/j.pharmthera.2014.11.011
- Lockridge, O., Bartels, C. F., Vaughan, T. A., Wong, C. K., Norton, S. E., & Johnson, L. L. (1987). Complete amino acid sequence of human serum cholinesterase. *J Biol Chem*, *262*(2), 549-557.

- Loening, A. M., & Gambhir, S. S. (2003). AMIDE: a free software tool for multimodality medical image analysis. *Mol Imaging*, 2(3), 131-137.
- Logan, J., Fowler, J. S., Volkow, N. D., Wolf, A. P., Dewey, S. L., Schlyer, D. J., MacGregor, R. R., Hitzemann, R., Bendriem, B., Gatley, S. J., & et al. (1990). Graphical analysis of reversible radioligand binding from time-activity measurements applied to [N-11C-methyl]-(-)-cocaine PET studies in human subjects. *J Cereb Blood Flow Metab*, 10(5), 740-747. doi:10.1038/jcbfm.1990.127
- Lowe, V. J., Weigand, S. D., Senjem, M. L., Vemuri, P., Jordan, L., Kantarci, K., Boeve, B., Jack, C. R., Jr., Knopman, D., & Petersen, R. C. (2014). Association of hypometabolism and amyloid levels in aging, normal subjects. *Neurology*, 82(22), 1959-1967. doi:10.1212/WNL.0000000000000467
- Ma, Y., Hof, P. R., Grant, S. C., Blackband, S. J., Bennett, R., Slate, L., McGuigan, M. D., & Benveniste, H. (2005). A three-dimensional digital atlas database of the adult C57BL/6J mouse brain by magnetic resonance microscopy. *Neuroscience*, 135(4), 1203-1215. doi:10.1016/j.neuroscience.2005.07.014
- Ma, Y., Smith, D., Hof, P. R., Foerster, B., Hamilton, S., Blackband, S. J., Yu, M., & Benveniste, H. (2008). In Vivo 3D Digital Atlas Database of the Adult C57BL/6J Mouse Brain by Magnetic Resonance Microscopy. *Front Neuroanat*, 2, 1. doi:10.3389/neuro.05.001.2008
- Macdonald, I. R., DeBay, D. R., Reid, G. A., O'Leary, T. P., Jollymore, C. T., Mawko, G., Burrell, S., Martin, E., Bowen, C. V., Brown, R. E., & Darvesh, S. (2014). Early detection of cerebral glucose uptake changes in the 5XFAD mouse. *Curr Alzheimer Res*, 11(5), 450-460.
- Macdonald, I. R., Maxwell, S. P., Reid, G. A., Cash, M. K., DeBay, D. R., & Darvesh, S. (2017). Quantification of Butyrylcholinesterase Activity as a Sensitive and Specific Biomarker of Alzheimer's Disease. *J Alzheimers Dis*, 58(2), 491-505. doi:10.3233/JAD-170164
- Macdonald, I. R., Reid, G. A., Joy, E. E., Pottie, I. R., Matte, G., Burrell, S., Mawko, G., Martin, E., & Darvesh, S. (2011). Synthesis and preliminary evaluation of piperidinyl and pyrrolidinyl iodobenzoates as imaging agents for butyrylcholinesterase. *Mol Imaging Biol*, 13(6), 1250-1261. doi:10.1007/s11307-010-0448-0
- Macdonald, I. R., Reid, G. A., Pottie, I. R., Martin, E., & Darvesh, S. (2016). Synthesis and Preliminary Evaluation of Phenyl 4-123I-Iodophenylcarbamate for Visualization of Cholinesterases Associated with Alzheimer Disease Pathology. *J Nucl Med*, 57(2), 297-302. doi:10.2967/jnumed.115.162032

- Manoharan, I., Boopathy, R., Darvesh, S., & Lockridge, O. (2007). A medical health report on individuals with silent butyrylcholinesterase in the Vysya community of India. *Clin Chim Acta*, 378(1-2), 128-135. doi:10.1016/j.cca.2006.11.005
- Manoharan, I., Kuznetsova, A., Fisk, J. D., Boopathy, R., Lockridge, O., & Darvesh, S. (2007). Comparison of cognitive functions between people with silent and wild-type butyrylcholinesterase. *J Neural Transm (Vienna)*, 114(7), 939-945. doi:10.1007/s00702-007-0631-x
- Massoulie, J., Pezzementi, L., Bon, S., Krejci, E., & Vallette, F. M. (1993). Molecular and cellular biology of cholinesterases. *Prog Neurobiol*, 41(1), 31-91.
- McKhann, G. M., Knopman, D. S., Chertkow, H., Hyman, B. T., Jack, C. R., Jr., Kawas, C. H., Klunk, W. E., Koroshetz, W. J., Manly, J. J., Mayeux, R., Mohs, R. C., Morris, J. C., Rossor, M. N., Scheltens, P., Carrillo, M. C., Thies, B., Weintraub, S., & Phelps, C. H. (2011). The diagnosis of dementia due to Alzheimer's disease: recommendations from the National Institute on Aging-Alzheimer's Association workgroups on diagnostic guidelines for Alzheimer's disease. *Alzheimers Dement*, 7(3), 263-269. doi:10.1016/j.jalz.2011.03.005
- McRobbie, D. (2004). *MRI From Picture to Proton*.
- Mesulam, M. M. (2013). Cholinergic circuitry of the human nucleus basalis and its fate in Alzheimer's disease. *J Comp Neurol*, 521(18), 4124-4144. doi:10.1002/cne.23415
- Mesulam, M. M., & Geula, C. (1994). Butyrylcholinesterase reactivity differentiates the amyloid plaques of aging from those of dementia. *Ann Neurol*, 36(5), 722-727. doi:10.1002/ana.410360506
- Mikalsen, A., Andersen, R. A., & Alexander, J. (1986). Use of ethopropazine and BW 284C51 as selective inhibitors for cholinesterases from various species. *Comp Biochem Physiol C*, 83(2), 447-449.
- Mitra, E., & Quon, A. (2009). Positron emission tomography/computed tomography: the current technology and applications. *Radiol Clin North Am*, 47(1), 147-160. doi:10.1016/j.rcl.2008.10.005
- Montine, T. J., Phelps, C. H., Beach, T. G., Bigio, E. H., Cairns, N. J., Dickson, D. W., Duyckaerts, C., Frosch, M. P., Masliah, E., Mirra, S. S., Nelson, P. T., Schneider, J. A., Thal, D. R., Trojanowski, J. Q., Vinters, H. V., Hyman, B. T., National Institute on, A., & Alzheimer's, A. (2012). National Institute on Aging-Alzheimer's Association guidelines for the neuropathologic assessment of Alzheimer's disease: a practical approach. *Acta Neuropathol*, 123(1), 1-11. doi:10.1007/s00401-011-0910-3

- Moran, M. A., Mufson, E. J., & Gomez-Ramos, P. (1994). Cholinesterases colocalize with sites of neurofibrillary degeneration in aged and Alzheimer's brains. *Acta Neuropathol*, 87(3), 284-292. doi:10.1007/bf00296744
- Moretti, J. L., Caglar, M., & Weinmann, P. (1995). Cerebral perfusion imaging tracers for SPECT: which one to choose? *J Nucl Med*, 36(3), 359-363.
- Morris, E., Chalkidou, A., Hammers, A., Peacock, J., Summers, J., & Keevil, S. (2016). Diagnostic accuracy of (18)F amyloid PET tracers for the diagnosis of Alzheimer's disease: a systematic review and meta-analysis. *Eur J Nucl Med Mol Imaging*, 43(2), 374-385. doi:10.1007/s00259-015-3228-x
- Mosconi, L. (2005). Brain glucose metabolism in the early and specific diagnosis of Alzheimer's disease. FDG-PET studies in MCI and AD. *Eur J Nucl Med Mol Imaging*, 32(4), 486-510. doi:10.1007/s00259-005-1762-7
- Mosconi, L., De Santi, S., Li, Y., Li, J., Zhan, J., Tsui, W. H., Boppana, M., Pupi, A., & de Leon, M. J. (2006). Visual rating of medial temporal lobe metabolism in mild cognitive impairment and Alzheimer's disease using FDG-PET. *Eur J Nucl Med Mol Imaging*, 33(2), 210-221. doi:10.1007/s00259-005-1956-z
- Namba, H., Fukushi, K., Nagatsuka, S., Iyo, M., Shinotoh, H., Tanada, S., & Irie, T. (2002). Positron emission tomography: quantitative measurement of brain acetylcholinesterase activity using radiolabeled substrates. *Methods*, 27(3), 242-250.
- National Institute of Mental Health. (April, 2019). NIH/NIMH Therapeutics Discovery Research, CNS Radiotracer Table. Retrieved from <https://www.nimh.nih.gov/research/research-funded-by-nimh/therapeutics/cns-radiotracer-table.shtml>
- Neirinckx, R. D., Burke, J. F., Harrison, R. C., Forster, A. M., Andersen, A. R., & Lassen, N. A. (1988). The retention mechanism of technetium-99m-HM-PAO: intracellular reaction with glutathione. *J Cereb Blood Flow Metab*, 8(6), S4-12. doi:10.1038/jcbfm.1988.27
- Neirinckx, R. D., Canning, L. R., Piper, I. M., Nowotnik, D. P., Pickett, R. D., Holmes, R. A., Volkert, W. A., Forster, A. M., Weisner, P. S., Marriott, J. A., & et al. (1987). Technetium-99m d,l-HM-PAO: a new radiopharmaceutical for SPECT imaging of regional cerebral blood perfusion. *J Nucl Med*, 28(2), 191-202.
- Nicolet, Y., Lockridge, O., Masson, P., Fontecilla-Camps, J. C., & Nachon, F. (2003). Crystal structure of human butyrylcholinesterase and of its complexes with substrate and products. *J Biol Chem*, 278(42), 41141-41147. doi:10.1074/jbc.M210241200

- Noble, J. M., & Scarmeas, N. (2009). Application of pet imaging to diagnosis of Alzheimer's disease and mild cognitive impairment. *Int Rev Neurobiol*, 84, 133-149. doi:10.1016/S0074-7742(09)00407-3
- Nowotnik, D. P., Canning, L. R., Cumming, S. A., Harrison, R. C., Higley, B., Nechvatal, G., Pickett, R. D., Piper, I. M., Bayne, V. J., Forster, A. M., & et al. (1985). Development of a ⁹⁹Tcm-labelled radiopharmaceutical for cerebral blood flow imaging. *Nucl Med Commun*, 6(9), 499-506.
- Oakley, H., Cole, S. L., Logan, S., Maus, E., Shao, P., Craft, J., Guillozet-Bongaarts, A., Ohno, M., Disterhoft, J., Van Eldik, L., Berry, R., & Vassar, R. (2006). Intraneuronal beta-amyloid aggregates, neurodegeneration, and neuron loss in transgenic mice with five familial Alzheimer's disease mutations: potential factors in amyloid plaque formation. *J Neurosci*, 26(40), 10129-10140. doi:10.1523/JNEUROSCI.1202-06.2006
- Olsson, B., Lautner, R., Andreasson, U., Ohrfelt, A., Portelius, E., Bjerke, M., Holtta, M., Rosen, C., Olsson, C., Strobel, G., Wu, E., Dakin, K., Petzold, M., Blennow, K., & Zetterberg, H. (2016). CSF and blood biomarkers for the diagnosis of Alzheimer's disease: a systematic review and meta-analysis. *Lancet Neurol*, 15(7), 673-684. doi:10.1016/S1474-4422(16)00070-3
- Ota, T., Shinotoh, H., Fukushi, K., Kikuchi, T., Sato, K., Tanaka, N., Shimada, H., Hirano, S., Miyoshi, M., Arai, H., Suhara, T., & Irie, T. (2010). Estimation of plasma IC50 of donepezil for cerebral acetylcholinesterase inhibition in patients with Alzheimer disease using positron emission tomography. *Clin Neuropharmacol*, 33(2), 74-78. doi:10.1097/WNF.0b013e3181c71be9
- Ota, T., Shinotoh, H., Fukushi, K., Nagatsuka, S., Namba, H., Iyo, M., Aotsuka, A., Tanaka, N., Sato, K., Shiraiishi, T., Tanada, S., Arai, H., & Irie, T. (2004). A simple method for the detection of abnormal brain regions in Alzheimer's disease patients using [¹¹C]MP4A: comparison with [¹²³I]IMP SPECT. *Ann Nucl Med*, 18(3), 187-193.
- Pappata, S., Tavitian, B., Traykov, L., Jobert, A., Dalger, A., Mangin, J. F., Crouzel, C., & DiGiambardino, L. (1996). In vivo imaging of human cerebral acetylcholinesterase. *J Neurochem*, 67(2), 876-879.
- Park, S. H., Han, P. K., & Choi, S. H. (2015). Physiological and Functional Magnetic Resonance Imaging Using Balanced Steady-state Free Precession. *Korean J Radiol*, 16(3), 550-559. doi:10.3348/kjr.2015.16.3.550
- Patlak, C. S., Blasberg, R. G., & Fenstermacher, J. D. (1983). Graphical evaluation of blood-to-brain transfer constants from multiple-time uptake data. *J Cereb Blood Flow Metab*, 3(1), 1-7. doi:10.1038/jcbfm.1983.1

- Perry, E., McKeith, I., & Ballard, C. (2003). Butyrylcholinesterase and progression of cognitive deficits in dementia with Lewy bodies. *Neurology*, *60*(11), 1852-1853. doi:10.1212/01.wnl.0000068336.84399.9e
- Perry, E. K. (1980). The cholinergic system in old age and Alzheimer's disease. *Age Ageing*, *9*(1), 1-8.
- Perry, E. K., Perry, R. H., Blessed, G., & Tomlinson, B. E. (1978). Changes in brain cholinesterases in senile dementia of Alzheimer type. *Neuropathol Appl Neurobiol*, *4*(4), 273-277.
- Perry, E. K., Tomlinson, B. E., Blessed, G., Bergmann, K., Gibson, P. H., & Perry, R. H. (1978). Correlation of cholinergic abnormalities with senile plaques and mental test scores in senile dementia. *Br Med J*, *2*(6150), 1457-1459.
- Pike, G. B. (2012). Quantitative functional MRI: concepts, issues and future challenges. *Neuroimage*, *62*(2), 1234-1240. doi:10.1016/j.neuroimage.2011.10.046
- Pike, V. W. (2009). PET radiotracers: crossing the blood-brain barrier and surviving metabolism. *Trends Pharmacol Sci*, *30*(8), 431-440. doi:10.1016/j.tips.2009.05.005
- Pike, V. W. (2016). Considerations in the Development of Reversibly Binding PET Radioligands for Brain Imaging. *Curr Med Chem*, *23*(18), 1818-1869.
- Ramanan, V. K., Risacher, S. L., Nho, K., Kim, S., Swaminathan, S., Shen, L., Foroud, T. M., Hakonarson, H., Huentelman, M. J., Aisen, P. S., Petersen, R. C., Green, R. C., Jack, C. R., Koeppe, R. A., Jagust, W. J., Weiner, M. W., Saykin, A. J., & Alzheimer's Disease Neuroimaging, I. (2014). APOE and BCHE as modulators of cerebral amyloid deposition: a florbetapir PET genome-wide association study. *Mol Psychiatry*, *19*(3), 351-357. doi:10.1038/mp.2013.19
- Rasmussen, J. M., Lakatos, A., van Erp, T. G., Kruggel, F., Keator, D. B., Fallon, J. T., Macciardi, F., Potkin, S. G., & Alzheimer's Disease Neuroimaging, I. (2012). Empirical derivation of the reference region for computing diagnostic sensitive (1)(8)fluorodeoxyglucose ratios in Alzheimer's disease based on the ADNI sample. *Biochim Biophys Acta*, *1822*(3), 457-466. doi:10.1016/j.bbadis.2011.09.008
- Reid, G. A., & Darvesh, S. (2015). Butyrylcholinesterase-knockout reduces brain deposition of fibrillar beta-amyloid in an Alzheimer mouse model. *Neuroscience*, *298*, 424-435. doi:10.1016/j.neuroscience.2015.04.039
- Rempel, B. P., Price, E. W., & Phenix, C. P. (2017). Molecular Imaging of Hydrolytic Enzymes Using PET and SPECT. *Mol Imaging*, *16*, 1536012117717852. doi:10.1177/1536012117717852

- Roivainen, A., Rinne, J., Virta, J., Jarvenpaa, T., Salomaki, S., Yu, M., & Nagren, K. (2004). Biodistribution and blood metabolism of 1-11C-methyl-4-piperidinyl n-butyrates in humans: an imaging agent for in vivo assessment of butyrylcholinesterase activity with PET. *J Nucl Med*, *45*(12), 2032-2039.
- Sabri, O., Sabbagh, M. N., Seibyl, J., Barthel, H., Akatsu, H., Ouchi, Y., Senda, K., Murayama, S., Ishii, K., Takao, M., Beach, T. G., Rowe, C. C., Leverenz, J. B., Ghetti, B., Ironside, J. W., Catafau, A. M., Stephens, A. W., Mueller, A., Koglin, N., Hoffmann, A., Roth, K., Reininger, C., Schulz-Schaeffer, W. J., & Florbetaben Phase 3 Study, G. (2015). Florbetaben PET imaging to detect amyloid beta plaques in Alzheimer's disease: phase 3 study. *Alzheimers Dement*, *11*(8), 964-974. doi:10.1016/j.jalz.2015.02.004
- Salloway, S., Sperling, R., Fox, N. C., Blennow, K., Klunk, W., Raskind, M., Sabbagh, M., Honig, L. S., Porsteinsson, A. P., Ferris, S., Reichert, M., Ketter, N., Nejadnik, B., Guenzler, V., Miloslavsky, M., Wang, D., Lu, Y., Lull, J., Tudor, I. C., Liu, E., Grundman, M., Yuen, E., Black, R., Brashear, H. R., Bapineuzumab, & Clinical Trial, I. (2014). Two phase 3 trials of bapineuzumab in mild-to-moderate Alzheimer's disease. *N Engl J Med*, *370*(4), 322-333. doi:10.1056/NEJMoal304839
- Saxena, A., Redman, A. M., Jiang, X., Lockridge, O., & Doctor, B. P. (1997). Differences in active site gorge dimensions of cholinesterases revealed by binding of inhibitors to human butyrylcholinesterase. *Biochemistry*, *36*(48), 14642-14651. doi:10.1021/bi971425+
- Scheltens, P., Blennow, K., Breteler, M. M., de Strooper, B., Frisoni, G. B., Salloway, S., & Van der Flier, W. M. (2016). Alzheimer's disease. *Lancet*, *388*(10043), 505-517. doi:10.1016/S0140-6736(15)01124-1
- Schenk, D., Barbour, R., Dunn, W., Gordon, G., Grajeda, H., Guido, T., Hu, K., Huang, J., Johnson-Wood, K., Khan, K., Kholodenko, D., Lee, M., Liao, Z., Lieberburg, I., Motter, R., Mutter, L., Soriano, F., Shopp, G., Vasquez, N., Vandeventer, C., Walker, S., Wogulis, M., Yednock, T., Games, D., & Seubert, P. (1999). Immunization with amyloid-beta attenuates Alzheimer-disease-like pathology in the PDAPP mouse. *Nature*, *400*(6740), 173-177. doi:10.1038/22124
- Selkoe, D. J., & Hardy, J. (2016). The amyloid hypothesis of Alzheimer's disease at 25 years. *EMBO Mol Med*, *8*(6), 595-608. doi:10.15252/emmm.201606210
- Sigurdsson, E. M., Scholtzova, H., Mehta, P. D., Frangione, B., & Wisniewski, T. (2001). Immunization with a nontoxic/nonfibrillar amyloid-beta homologous peptide reduces Alzheimer's disease-associated pathology in transgenic mice. *Am J Pathol*, *159*(2), 439-447.
- Silver, A. (1974). *The Biology of Cholinesterases*. . Amsterdam: North Holland Publishing.

- Silverman, D. H., Small, G. W., Chang, C. Y., Lu, C. S., Kung De Aburto, M. A., Chen, W., Czernin, J., Rapoport, S. I., Pietrini, P., Alexander, G. E., Schapiro, M. B., Jagust, W. J., Hoffman, J. M., Welsh-Bohmer, K. A., Alavi, A., Clark, C. M., Salmon, E., de Leon, M. J., Mielke, R., Cummings, J. L., Kowell, A. P., Gambhir, S. S., Hoh, C. K., & Phelps, M. E. (2001). Positron emission tomography in evaluation of dementia: Regional brain metabolism and long-term outcome. *JAMA*, *286*(17), 2120-2127.
- Snowdon, D. A., & Nun, S. (2003). Healthy aging and dementia: findings from the Nun Study. *Ann Intern Med*, *139*(5 Pt 2), 450-454.
- Snyder, S. E., Gunupudi, N., Sherman, P. S., Butch, E. R., Skaddan, M. B., Kilbourn, M. R., Koeppe, R. A., & Kuhl, D. E. (2001). Radiolabeled cholinesterase substrates: in vitro methods for determining structure-activity relationships and identification of a positron emission tomography radiopharmaceutical for in vivo measurement of butyrylcholinesterase activity. *J Cereb Blood Flow Metab*, *21*(2), 132-143. doi:10.1097/00004647-200102000-00004
- Snyder, S. E., Tluczek, L., Jewett, D. M., Nguyen, T. B., Kuhl, D. E., & Kilbourn, M. R. (1998). Synthesis of 1-[¹¹C]methylpiperidin-4-yl propionate ([¹¹C]PMP) for in vivo measurements of acetylcholinesterase activity. *Nucl Med Biol*, *25*(8), 751-754.
- Stabin, M. G., Sparks, R. B., & Crowe, E. (2005). OLINDA/EXM: the second-generation personal computer software for internal dose assessment in nuclear medicine. *J Nucl Med*, *46*(6), 1023-1027.
- Stahl, A., Ott, K., Schwaiger, M., & Weber, W. A. (2004). Comparison of different SUV-based methods for monitoring cytotoxic therapy with FDG PET. *Eur J Nucl Med Mol Imaging*, *31*(11), 1471-1478. doi:10.1007/s00259-004-1626-6
- Studholme, C., Hill, D. L., & Hawkes, D. J. (1996). Automated 3-D registration of MR and CT images of the head. *Med Image Anal*, *1*(2), 163-175.
- Sussman, J. L., Harel, M., Frolow, F., Oefner, C., Goldman, A., Toker, L., & Silman, I. (1991). Atomic structure of acetylcholinesterase from *Torpedo californica*: a prototypic acetylcholine-binding protein. *Science*, *253*(5022), 872-879.
- Tariot, P. N., Schneider, L. S., Cummings, J., Thomas, R. G., Raman, R., Jakimovich, L. J., Loy, R., Bartocci, B., Fleisher, A., Ismail, M. S., Porsteinsson, A., Weiner, M., Jack, C. R., Jr., Thal, L., Aisen, P. S., & Alzheimer's Disease Cooperative Study, G. (2011). Chronic divalproex sodium to attenuate agitation and clinical progression of Alzheimer disease. *Arch Gen Psychiatry*, *68*(8), 853-861. doi:10.1001/archgenpsychiatry.2011.72
- Thie, J. A. (2004). Understanding the standardized uptake value, its methods, and implications for usage. *J Nucl Med*, *45*(9), 1431-1434.

- Tien, R. D., & Ashdown, B. C. (1992). Crossed cerebellar diaschisis and crossed cerebellar atrophy: correlation of MR findings, clinical symptoms, and supratentorial diseases in 26 patients. *AJR Am J Roentgenol*, *158*(5), 1155-1159. doi:10.2214/ajr.158.5.1566683
- Toyohara, J., Sakata, M., Fujinaga, M., Yamasaki, T., Oda, K., Ishii, K., Zhang, M. R., Moriguchi Jeckel, C. M., & Ishiwata, K. (2013). Preclinical and the first clinical studies on [¹¹C]ITMM for mapping metabotropic glutamate receptor subtype 1 by positron emission tomography. *Nucl Med Biol*, *40*(2), 214-220. doi:10.1016/j.nucmedbio.2012.11.008
- Truett, G. E., Heeger, P., Mynatt, R. L., Truett, A. A., Walker, J. A., & Warman, M. L. (2000). Preparation of PCR-quality mouse genomic DNA with hot sodium hydroxide and tris (HotSHOT). *Biotechniques*, *29*(1), 52, 54.
- US-FDA, C. f. D. E. a. R. (2006). *Guidance for Industry, Investigators, and Reviewers – Exploratory IND Studies*. (1024). Rockville, MD: Office of Training and Communication, Division of Drug Information, HFD-240, Center for Drug Evaluation and Research.
- Van de Bittner, G. C., Ricq, E. L., & Hooker, J. M. (2014). A philosophy for CNS radiotracer design. *Acc Chem Res*, *47*(10), 3127-3134. doi:10.1021/ar500233s
- Villemagne, V. L. (2016). Amyloid imaging: Past, present and future perspectives. *Ageing Res Rev*, *30*, 95-106. doi:10.1016/j.arr.2016.01.005
- Villemagne, V. L., Fodero-Tavoletti, M. T., Masters, C. L., & Rowe, C. C. (2015). Tau imaging: early progress and future directions. *Lancet Neurol*, *14*(1), 114-124. doi:10.1016/S1474-4422(14)70252-2
- Villemagne, V. L., & Okamura, N. (2016). Tau imaging in the study of ageing, Alzheimer's disease, and other neurodegenerative conditions. *Curr Opin Neurobiol*, *36*, 43-51. doi:10.1016/j.conb.2015.09.002
- Vroman Battle, M., Cowan, G. S. M., & Rakow, E. A. (2000). Statistical Power: Planning for It, Estimating It Post Hoc and Reporting It. *IEEE Transactions on Professional Communication*, *43*, 345-354.
- Wager, T. T., Hou, X., Verhoest, P. R., & Villalobos, A. (2010). Moving beyond rules: the development of a central nervous system multiparameter optimization (CNS MPO) approach to enable alignment of druglike properties. *ACS Chem Neurosci*, *1*(6), 435-449. doi:10.1021/cn100008c
- Wager, T. T., Hou, X., Verhoest, P. R., & Villalobos, A. (2016). Central Nervous System Multiparameter Optimization Desirability: Application in Drug Discovery. *ACS Chem Neurosci*, *7*(6), 767-775. doi:10.1021/acscchemneuro.6b00029

- Waldron, A. M., Wintolders, C., Bottelbergs, A., Kelley, J. B., Schmidt, M. E., Stroobants, S., Langlois, X., & Staelens, S. (2015). In vivo molecular neuroimaging of glucose utilization and its association with fibrillar amyloid-beta load in aged APPPS1-21 mice. *Alzheimers Res Ther*, 7(1), 76. doi:10.1186/s13195-015-0158-6
- Waldron, A. M., Wyffels, L., Verhaeghe, J., Richardson, J. C., Schmidt, M., Stroobants, S., Langlois, X., & Staelens, S. (2017). Longitudinal Characterization of [18F]-FDG and [18F]-AV45 Uptake in the Double Transgenic TASTPM Mouse Model. *J Alzheimers Dis*, 55(4), 1537-1548. doi:10.3233/JAD-160760
- Wang, L., Benzinger, T. L., Su, Y., Christensen, J., Friedrichsen, K., Aldea, P., McConathy, J., Cairns, N. J., Fagan, A. M., Morris, J. C., & Ances, B. M. (2016). Evaluation of Tau Imaging in Staging Alzheimer Disease and Revealing Interactions Between beta-Amyloid and Tauopathy. *JAMA Neurol*, 73(9), 1070-1077. doi:10.1001/jamaneurol.2016.2078
- Wang, Z., Jiang, Y., Wang, X., Du, Y., Xiao, D., Deng, Y., & Wang, J. (2015). Butyrylcholinesterase K variant and Alzheimer's disease risk: a meta-analysis. *Med Sci Monit*, 21, 1408-1413. doi:10.12659/MSM.892982
- Watabe, H., Ikoma, Y., Kimura, Y., Naganawa, M., & Shidahara, M. (2006). PET kinetic analysis--compartmental model. *Ann Nucl Med*, 20(9), 583-588.
- Wernick, M. N., & Aarsvold, J. N. (2004). *Emission tomography : the fundamentals of PET and SPECT*. Amsterdam ; Boston: Elsevier Academic Press.
- WHO (Ed.) (2012). *Dementia: A Public Health Priority*. . Geneva, CH.
- Wiebusch, H., Poirier, J., Sevigny, P., & Schappert, K. (1999). Further evidence for a synergistic association between APOE epsilon4 and BCHE-K in confirmed Alzheimer's disease. *Hum Genet*, 104(2), 158-163.
- Woods, R. P., Grafton, S. T., Holmes, C. J., Cherry, S. R., & Mazziotta, J. C. (1998). Automated image registration: I. General methods and intrasubject, intramodality validation. *J Comput Assist Tomogr*, 22(1), 139-152.
- Wright, C. I., Geula, C., & Mesulam, M. M. (1993). Neurological cholinesterases in the normal brain and in Alzheimer's disease: relationship to plaques, tangles, and patterns of selective vulnerability. *Ann Neurol*, 34(3), 373-384. doi:10.1002/ana.410340312
- Xiao, Y., Guan, Z. Z., Wu, C. X., Li, Y., Kuang, S. X., & Pei, J. J. (2012). Correlations between cholinesterase activity and cognitive scores in post-ischemic rats and patients with vascular dementia. *Cell Mol Neurobiol*, 32(3), 399-407. doi:10.1007/s10571-011-9770-6

- Yeo, J. M., Lim, X., Khan, Z., & Pal, S. (2013). Systematic review of the diagnostic utility of SPECT imaging in dementia. *Eur Arch Psychiatry Clin Neurosci*, 263(7), 539-552. doi:10.1007/s00406-013-0426-z
- Zanotti-Fregonara, P., Chen, K., Liow, J. S., Fujita, M., & Innis, R. B. (2011). Image-derived input function for brain PET studies: many challenges and few opportunities. *J Cereb Blood Flow Metab*, 31(10), 1986-1998. doi:10.1038/jcbfm.2011.107
- Zetterberg, H. (2017). Review: Tau in biofluids - relation to pathology, imaging and clinical features. *Neuropathol Appl Neurobiol*, 43(3), 194-199. doi:10.1111/nan.12378

Appendix A Copyright Permission Letters



[Home](#) (<https://w...>) > [About](#) (<https://...>) > [Policies](#) (<https...>) > [Copyright](#) (<htt...>) > [Permissions](#) (...)

Permissions

As a general rule, permission should be sought from the rights holder to reproduce any substantial part of a copyrighted work. This includes any text, illustrations, charts, tables, photographs, or other material from previously published sources. Obtaining permission to re-use content published by Elsevier is simple. Follow the guide below for a quick and easy route to permission.

[Permission guidelines](#)

[ScienceDirect content](#)

[Tutorial videos](#)

[Help and suppo](#)

Permission guidelines

For further guidelines about obtaining permission, please review our Frequently Asked Questions below:

[When is permission required?](#)

[When is permission not required?](#)

[From whom do I need permission?](#)

[How do I obtain permission to use photographs or illustrations?](#)

[Do I need to obtain permission to use material posted on a website?](#)

What rights does Elsevier require when requesting permission?

How do I obtain permission from another publisher?

What is Rightslink?

What should I do if I am not able to locate the copyright owner?

Can I obtain permission from a Reproduction Rights Organization (RRO)?

Is Elsevier an STM signatory publisher?

Do I need to request permission to re-use work from another STM publisher?

Do I need to request permission to text mine Elsevier content?

Can I include/use my article in my thesis/dissertation? –

Yes. Authors can include their articles in full or in part in a thesis or dissertation for non-commercial purposes.

[J Alzheimers Dis.](#) 2017; 58(2): 491–505.

PMCID: PMC5438481

Published online 2017 May 11. Prepublished online 2017 Apr 28.

PMID: [28453492](#)

doi: [10.3233/JAD-170164](#)

Quantification of Butyrylcholinesterase Activity as a Sensitive and Specific Biomarker of Alzheimer's Disease

[Ian R. Macdonald](#),^a [Selena P. Maxwell](#),^a [George A. Reid](#),^a [Meghan K. Cash](#),^a [Drew R. DeBay](#),^a and [Sultan Darvesh](#)^{a,b,c,*}

Debomoy Lahiri, Handling Associate Editor

▾ [Author information](#) ▾ [Article notes](#) ▾ [Copyright and License information](#) [Disclaimer](#)

^aDepartment of Medical Neuroscience, Dalhousie University, Halifax, NS, Canada

^bDepartment of Medicine (Neurology and Geriatric Medicine), Dalhousie University, Halifax, NS, Canada

^cDepartment of Chemistry and Physics, Mount Saint Vincent University, Halifax, NS, Canada

*Correspondence to: Sultan Darvesh, Room 1308, Camp Hill Veterans' Memorial, 5955 Veterans' Memorial Lane, Halifax, NS, B3H 2E1, Canada. Tel.: +1 902 473 2490; Fax: +1 902 473 7133; E-mail: sultan.darvesh@dal.ca.

Accepted 2017 Mar 12.

[Copyright](#) IOS Press and the authors. All rights reserved

This is an open access article distributed under the terms of the [Creative Commons Attribution Non-Commercial \(CC BY-NC 4.0\) License](#), which permits unrestricted non-commercial use, distribution, and reproduction in any medium, provided the original work is properly cited.



RightsLink®

Home

Account Info

Help



Title: Targeting butyrylcholinesterase for preclinical single photon emission computed tomography (SPECT) imaging of Alzheimer's disease

Logged in as:
Drew DeBay
Mr. Drew DeBay
Account #:
3001501545

LOGOUT

Author: Drew R. DeBay,George A. Reid,Ian R. Pottie,Earl Martin,Chris V. Bowen,Sultan Darvesh

Publication: Alzheimer's & Dementia: Translational Research & Clinical Interventions

Publisher: Elsevier

Date: June 2017

© 2017 The Authors. Published by Elsevier Inc. on behalf of the Alzheimer's Association.

Please note that, as the author of this Elsevier article, you retain the right to include it in a thesis or dissertation, provided it is not published commercially. Permission is not required, but please ensure that you reference the journal as the original source. For more information on this and on your other retained rights, please visit: <https://www.elsevier.com/about/our-business/policies/copyright#Author-rights>

BACK

CLOSE WINDOW

Copyright © 2019 [Copyright Clearance Center, Inc.](#) All Rights Reserved. [Privacy statement](#). [Terms and Conditions](#). Comments? We would like to hear from you. E-mail us at customer@copyright.com



RightsLink®

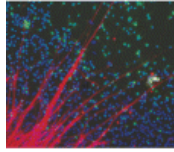
Home

Account Info

Help



Brain Research



Title: Butyrylcholinesterase-knockout reduces fibrillar β -amyloid and conserves 18FDG retention in 5XFAD mouse model of Alzheimer's disease

Author: Drew R. DeBay, George A. Reid, Ian R. Macdonald, George Mawko, Steve Burrell, Earl Martin, Chris V. Bowen, Sultan Darvesh

Publication: Brain Research

Publisher: Elsevier

Date: 15 September 2017

© 2017 Elsevier B.V. All rights reserved.

Logged in as:

Drew DeBay

Mr. Drew DeBay

LOGOUT

Please note that, as the author of this Elsevier article, you retain the right to include it in a thesis or dissertation, provided it is not published commercially. Permission is not required, but please ensure that you reference the journal as the original source. For more information on this and on your other retained rights, please visit: <https://www.elsevier.com/about/our-business/policies/copyright#Author-rights>

BACK

CLOSE WINDOW

Copyright © 2019 Copyright Clearance Center, Inc. All Rights Reserved. [Privacy statement](#). [Terms and Conditions](#). Comments? We would like to hear from you. E-mail us at customer@copyright.com